Korrelierte Dynamik hoch-angeregter Mehrteilchen-Systeme

Habilitationsschrift

zur Erlangung des akademischen Grades
Dr. rer. nat. habil.

vorgelegt der

Mathematisch-Naturwissenschaftlich-Technischen Fakultät
der Martin-Luther-Universität Halle-Wittenberg

von

Herrn Dr. rer. nat. Jamal Berakdar
geb. am: 20. Januar 1964 in: Damaskus

Gutachter:
1. Gutachter: Prof. Dr. P. Bruno
2. Gutachter: Prof. Dr. P.H. Dederichs
3. Gutachter: Prof. Dr. I. Mertig

Tag der Verteidigung der Schrift: 20.05.2003

urn:nbn:de:gbv:3-000005379
[http://nbn-resolving.de/urn/resolver.pl?urn=nbn%3Ade%3Agbv%3A3-000005379]

Inhaltsverzeichnis

1 Einleitung **5**

2 Wechselwirkende Mehr-Teilchen-Systeme im äußeren Potential **9**
  2.1 Approximative Lösungen der N-Teilchen-Schrödinger-Gleichung 9

3 Greensfunktionstheorie endlicher Systeme **15**
  3.1 Formale Behandlung 15
  3.2 Anwendung auf ein Vierteilchen-System 17
  3.3 Thermodynamik und Phasenübergänge endlicher Systeme 18

4 Kollektive Antwort und kurz-reichweitige Dynamik **21**
  4.1 Die Signatur kollektiver Antwort in endlichen elektronischen Systemen . . . 22

5 Die Quantenfeldmethoden: Konzepte und Anwendungen **25**
  5.1 Die Einteilchen-Greensfunktion ausgedehnter Systeme 25
  5.2 Spektrale Teilchen-Teilchen und Loch-Loch-Funktionen 28
  5.3 Der Zweiteilchen-Photostrom 30
    5.3.1 Praktische Implementierung für Metalloberflächen 31
    5.3.2 Beschreibung der Einteilchen-Bandstruktur 31
    5.3.3 Winkelabhängigkeit der Paar-Korrelationsfunktion 32
    5.3.4 Energieabhängigkeit der Paar-Korrelationsfunktion 36
  5.4 Aspekte der korrelierten Zweielektronen-Emission induziert bei Elektronenstoß 36

6 Zusammenfassung und Ausblick **41**

Literaturverzeichnis **43**

7 Auswahl eigener Arbeiten als Anhang **47**
  7.1 Theoretische Behandlung korrelierter Systeme mit endlicher Teilchenzahl . . 47
  7.2 Kollektive Antwort endlicher Systeme auf äußere Störungen 48
  7.3 Zweiteilchen-Anregung von Oberflächen 48
  7.4 Spektroskopie der Spin-Korrelationen in Ferromagneten 48
  7.5 Die Abbildung elektronischer Korrelationen in Festkörpern mittels der Photodoppelemission 49

8 Eidesstattliche Erklärung

9 Lebenslauf

Abstract.-

The understanding of elementary excitations in many-body correlated systems is of a fundamental importance for a variety of branches in physics [1, 2, 3, 4, 5]. This work gives an overview on recent theoretical treatments of correlated electronic collisions in non-relativistic many-body systems. In particular, concepts are presented that unravel the role of electronic correlation in finite few-body (atomic) systems and large extended systems, such as large molecules, metal clusters, and surfaces. For a finite system consisting of N correlated particles a method is suggested for the derivation of correlated many-body wave functions. Furthermore, a Green's function concept is introduced to investigate correlated electronic excitations as well as to trace down effects related to the thermodynamic and to the collective behaviour of finite systems. For the treatment of one and two-particle excitations in extended electronic systems, such as in solids and surfaces, the Green's function method as developed in field theory is utilized and a procedure is presented for the numerical calculations of the single and the two-particle Green's functions. The predictions of the theoretical concepts are contrasted with available experimental findings.

1 Einleitung

Die elektronische Struktur der Materie birgt den Schüssel zum Verständnis einer Reihe wichtiger Materialeigenschaften, wie z. B. der elektrischen Leitfähigkeit, des Magnetismus oder des optischen Verhaltens [5]. Ein verbreiteter und auch in vielen Fällen befriedigender Ansatz zur Beschreibung der Elektronen im Festkörper geht davon aus, dass die Elektronenbewegung im Rahmen einer Einteilchentheorie beschreibbar ist [2, 6]. Die Korrelationen der Elektronen führen dann zu einer Renormierung der Einteilcheneigenschaften [7, 8]. Andererseits hat sich gezeigt, dass die Wechselwirkung der Elektronen miteinander für die Erklärung einer Reihe von Phänomenen, wie beispielsweise der Supraleitung, dem Metall-Isolator-Übergang oder dem Ferromagnetismus unerlässlich ist [5]. Vor diesem Hintergrund sind theoretische und experimentelle Methoden, die verschiedene Aspekte der elektronischen Korrelation sowie deren Einfluss untersuchen, von großem Interesse.

Für ein N-Teilchen-System liefert die Größe $U = E_{N-2} - 2E_{N-1}$ einen ersten Einblick in die Stärke der Korrelation. Dabei sind E_{N-1} und E_{N-2} die Energien, die notwendig sind, um dem System ein bzw. zwei Teilchen zu entziehen. Für unkorrelierte Teilchen verschwindet U. Dagegen stellt man experimentell fest, dass für atomare Systeme die qualitative Beziehung $E_{N-2} \approx 3E_{N-1}$ gilt. Der Grenzübergang vom atomaren Limit bis hin zu thermodynamischen, delokalisierten Elektronen-Systemen, bei denen $E_{N-2} \approx 2E_{N-1}$ zu erwarten ist, wird durch Untersuchungen an Clustern beleuchtet [9]: Während für kleine Cluster atomares Verhalten überwiegt ($E_{N-2} \approx 3E_{N-1}$), zeigen große Cluster typische Merkmale ($E_{N-2} \approx 2E_{N-1}$) thermodynamischer Systeme [9]. Die Feststellung, dass in einem System $E_{N-2} \approx 2E_{N-1}$, also $U \approx 0$ gilt, ist aber kein notwendiges Zeichen für eine untergeordnete Rolle der elektronischen Korrelationen. Denn, im thermodynamischen Grenzwert (also für großes Volumen, große Teilchenzahl und endliche Teilchendichten) treten neue dynamische Erscheinungsformen der elektronischen Wechselwirkung zutage. So führen korrelierte Fluktuationen in der elektronischen Dichte zum Auftreten ausgeprägter (Plasma-) Resonanzen sowie zu einer charakteristischen Antwort auf äußere Störungen. Zum Beispiel, wie in dieser Arbeit dargelegt ist, ist die ionisierende Streuung geladener Teilchen von großen Metallclustern hauptsächlich durch die kollektive Antwort des Clusters bestimmt, die sich als eine Abschirmung der äußeren Störung manifestiert. Für kleine (atomare) Cluster sind die Abschirmeffekte vernachlässigbar.

Handelt es sich um kleine äußere Störungen bzw. um kleine Anregungen oder Fluktuationen um den Grundzustand, so kann man solche kollektiven Effekte der elektronischen Korrelation durch die Theorie der linearen Antwort (linear response) bzw. der so genannten random-phase approximation (RPA) theoretisch erfassen. Dagegen werden für die Behandlung von (ein, zweifach oder mehrfach) hoch-angeregten N-Teilchen-Systemen andere Methoden benötigt, die nicht nur E_{N-1} und E_{N-2} richtig wiedergeben, sondern auch in der Lage sind, die korrelierte Dynamik des hoch-angeregten Systems zu beschreiben.

In dieser Arbeit werden Konzepte entworfen, die eine systematische Untersuchung angeregter korrelierter Zustände erlauben. Ein Hauptaugenmerk gilt dem Vergleich von endlichen (Atomen, Clustern) und thermodynamischen, nicht-relativistischen Systemen (großen Molekülen und Metallclustern sowie Festkörpern und Oberflächen).

Für endliche atomare N-Teilchen-Systeme wird eine Methode zur Herleitung korrelierter N-Teilchen-Wellenfunktionen vorgeschlagen, die für die Berechnung von Reaktionswahrscheinlichkeiten benötigt werden [10, 11]. Das Verfahren beruht auf eine direkte approximative Lösung der nicht-relativistischen Schrödinger-Gleichung.

Einen Zugang zu thermodynamischen Eigenschaften in korrelierten endlichen Systemen bietet eine kumulative Greensfunktionsmethode, die hier vorgestellt wird. Diese Methode erlaubt eine systematische Untersuchung der Abhängigkeit der N-Teilchen-Greensfunktion sowie des Spektrums von der Stärke der Inner-Teilchen-Korrelationen. Im Rahmen der kanonischen Gesamtheit ergibt sich aus diesem Verfahren eine Rekursivformel für die Zustandssumme, aus der das thermodynamische Verhalten des Systems abgeleitet werden kann.

Weiterhin wird gezeigt, wie sich kollektive Effekte auf die Anregungsspektren in einem endlichen System auswirken und wie dies theoretisch zu erfassen ist. Als Beispiel betrachten wir die Elektronen-Stoßionisation von C_{60}-Molekülen sowie von Li-Clustern und untersuchen die Abhängigkeit der Wirkungsquerschnitte von der Größe der Cluster.

Zur theoretischen Behandlung von Mehrteilchen-Anregung in einem ausgedehnten System, wie bei einem Festkörper oder einer Oberfläche wird die Greensfunktionstheorie in ihrer feld-theoretischen Formulierung herangezogen. Insbesondere werden die Einteilchen- und Zweiteilchen-Greensfunktionen diskutiert und neue Methoden zur numerischen Berechnung aufgezeigt. Als Anwendung werden die Ein- und Zweiteilchen-Emission von Oberflächen untersucht. Während die Einteilchen-Emissionsspektren aussagekräftige Informationen über die elektronische Bandstruktur des Targetmaterials liefern, bietet das Zweiteilchen-Anregungsspktrum einen detaillierten Einblick in die Energie-, Winkel- und Spin-Abhängigkeit der Material-abhängigen Paar-Korrelationsfunktionen. Diese Aussage wird durch numerische Berechnungen für Kupfer-, Nickel- und Wolfram-Targetoberflächen sowie durch einen entsprechenden Vergleich mit verfügbaren experimentellen Befunden untermauert.

2 Wechselwirkende Mehr-Teilchen-Systeme im äußeren Potential

Ziel dieses Kapitels ist die Darlegung einer allgemeinen Methode zur Herleitung von korrelierten Mehrteilchen-Wellenfunktionen. Dazu betrachten wir ein wechselwirkendes N Teilchen-System, das sich in einem externen Potential U befindet. Wir nehmen weiterhin an, dass U als eine Summe von Einteilchen -Potentialen dargestellt werden kann, d.h. $U = \sum_j^N u_j$, wobei u_j nur auf das Teilchen j wirkt. Die Korrelationen zwischen den Teilchen werden durch eine paarweise Wechselwirkung $v_{ij} \equiv v_{ji}$ hervorgerufen.

Zur quantenmechanischen, nicht-relativistischen Beschreibung des Systems wird eine geeignete Lösung Ψ der N-Teilchen-Schrödinger-Gleichung benötigt. Da das Mehrteilchen-Problem ($N \geq 3$) in der Regel nicht separabel ist, sind solche Lösungen nur näherungsweise bekannt. Die Güte der approximativen Wellenfunktionen hängt stark vom Lösungsverfahren sowie von den Eigenschaften des betreffenden Zustandes ab. So liefert z.B. die Dichte-Funktional-Theorie (DFT) [12] adäquate Grundzustände für eine Reihe von Systemen (Atome, Moleküle und kondensierter Materie) [2, 6, 12]. Hingegen sind die angeregten Zustände im Rahmen der konventionellen DFT [12] im Prinzip nicht beschreibbar. In nächsten Abschnitt wird ein allgemeines Verfahren zur Lösung der N-Teilchen-Schrödinger-Gleichung vorgestellt, das die Korrelation der Teilchen berücksichtigt und eine Beschreibung angeregter Zustände erlaubt.

2.1 Approximative Lösungen der N-Teilchen-Schrödinger-Gleichung

Die Theorie wird im Rahmen der ersten Quantisierung formuliert. Die Symmetrie der Teilchen wird durch die (Anti)symetrisierung der hergeleiteten Wellenfunktionen wiedergegeben.

Der Einfachheit halber nehmen wir an, dass alle Teilchen die gleiche Masse m besitzen. Die nicht-relativistische, zeit-unabhängige Schrödinger-Gleichung für das N-Körper-Problem hat im Ortsraum die Gestalt [1]

$$\left[H_0 + \sum_{j=1}^{N} u_j + \sum_{\substack{i,j \\ j>i=1}}^{N} v_{ij} - E \right] \Psi(\mathbf{r}_1, \cdots, \mathbf{r}_N) = 0, \tag{2.1}$$

Die Ortskoordinate $\mathbf{r}_j$ legt die Position des Teilchens j in Bezug auf einen geeignet gewählten Koordinatenursprung fest (z.B. im Falle eines N-Elektronenatoms bietet sich der Kern als eine gute Wahl für den Ursprung an). Der Operator der kinetischen Energie H_0 hat die Form $H_0 = -\sum_{\ell=1}^{N} \Delta_\ell / 2m$, wobei Δ_ℓ der Laplacian bzgl. der Koordinate $\mathbf{r}_\ell$ darstellt.

Zur Herleitung des N-Teilchenzustandes $\Psi(\mathbf{r}_1, \cdots, \mathbf{r}_N)$ mit den entsprechenden Randbedingungen machen wir den Ansatz

$$\Psi(\mathbf{r}_1, \cdots, \mathbf{r}_N) = \mathcal{N} \Phi_I(\mathbf{r}_1, \cdots, \mathbf{r}_N) \Phi_{II}(\mathbf{r}_1, \cdots, \mathbf{r}_N) \chi(\mathbf{r}_1, \cdots, \mathbf{r}_N). \tag{2.2}$$

Wie unten dargelegt ist, werden in einem ersten Schritt bekannte Eigenschaften des Systems durch eine spezielle Form der Funktionen $\Phi_I, \ \Phi_{II}$ berücksichtigt. Dies bedeutet keine Einschränkung, denn die Funktion $\chi(\mathbf{r}_1, \cdots, \mathbf{r}_N)$ hat eine beliebige noch zu bestimmende Gestalt. In Gl. (2.2) ist $\mathcal{N}$ eine Normierungskonstante.

Die Funktion Φ_I wird als die Lösung von Gl. (2.1) im Falle unabhängiger Teilchen, d.h.

$$\left(H_0 + \sum_{j=1}^{N} u_j - E \right) \Phi_I(\mathbf{r}_1, \cdots, \mathbf{r}_N) = 0. \tag{2.3}$$

Diese Gleichung ist separabel. Die Lösung $\Phi_I(\mathbf{r}_1, \cdots, \mathbf{r}_N)$ is das Produkt

$$\Phi_I(\mathbf{r}_1, \cdots, \mathbf{r}_N) = \prod_{j=1}^{N} \xi_\ell(\mathbf{r}_\ell) \varphi_j(\mathbf{r}_j), \tag{2.4}$$

wobei die Funktionen $\xi_\ell(\mathbf{r}_\ell)\varphi_\ell(\mathbf{r}_\ell)$ aus der Gleichung

$$\left[-\Delta_\ell/(2m) + u_\ell - \epsilon_\ell \right] \xi_\ell(\mathbf{r}_\ell) \varphi_\ell(\mathbf{r}_\ell) = 0$$

zu bestimmen sind. Die Gesamtenergie kann somit in der Form $E_I = \sum_\ell \epsilon_\ell$ angegeben werden. Die Art der Randbedingungen wird durch eine geeignete Wahl der Funktionen $\xi_\ell(\mathbf{r}_\ell)$ in Gl. (2.4) berücksichtigt: Im Falle gebundener Systeme ist $\xi_\ell(\mathbf{r}_\ell)$ eine asymptotisch exponentiell abfallende Funktion. Für Kontinuum-Probleme ist $\xi_\ell(\mathbf{r}_\ell)$ eine ebene Welle und die Funktion $\varphi_\ell(\mathbf{r}_\ell)$ beschreibt dann die Modifikation dieser ebenen Welle aufgrund des Potentials u_ℓ.

---

[1] Wenn nicht ausdrücklich erwähnt, werden atomare Einheiten benutzt. Relativistische Korrekturen werden nicht berücksichtigt.

Sind die Teilchen stark zum externen Feld gekoppelt $u_j \gg v_{ij};\ \forall\, i, j \in [1, N]$, so liefert die Funktion Φ_I einen guten Ausgangspunkt zur Lösung der Gl. (2.1), denn man kann in diesem Falle das Gesamtpotential nach $v_{ij}/(\sum_k u_k)$ entwickeln und Gl. (2.4) als die erste Näherung $v_{ij}/(\sum_k u_k) = 0$ erhalten. Werden höhere Ordnungen benötigt, so empfiehlt sich die Störungstheorie als ein systematisches Lösungsverfahren zur Behandlung der Terme v_{ij}.

Ein weiterer Extremfall, neben dem Model unabhängiger Teilchen, ist die Situation, wenn die Korrelation zwischen den Teilchen sehr stark im Vergleich zur Koppelung zum externen Feld sind. Dies ist der Fall, wenn $v_{ij} \gg u_j;\ \forall\, i, j \in [1, N]$. Um diesem besonderen Umstand Rechnung zu tragen, wählen wir Φ_{II} in der Form

$$\Phi_{II}(\mathbf{r}_1, \cdots, \mathbf{r}_N) := \left[\prod_{\ell=1}^{N} \xi_\ell(\mathbf{r}_\ell)\right] \prod_{j>i=1}^{N} \varphi_{ij}(\mathbf{r}_{ij}). \tag{2.5}$$

The Funktionen $\varphi_{ij}(\mathbf{r}_{ij})$ sind die Lösungen für die Schrödinger-Gl. (2.1) im Falle extrem starker Korrelation zwischen dem Teilchen i und dem Teilchen j ($v_{ij} \gg u_l,\ v_{ij} \gg v_{mn},\ \forall\, l, m, n \neq i, j$), in diesem Fall vereinfacht sich Gl. (2.1) zu

$$\Big(H_0 + v_{ij} \ - E\Big)\, \varphi_{ij}(\mathbf{r}_{ij}) \prod_{\ell=1}^{N} \xi_\ell(\mathbf{r}_\ell) = 0. \tag{2.6}$$

Es ist zu beachten, dass i.a. die Funktion (2.5) keine exakte bzw. keine gute Nährung zur Lösung von Gl. (2.1) in Abwesenheit externer Felder (also für $u_l \to 0$) ist. Der Grund dafür ist, dass die ($N(N-1)/2$)-Zweiteilchen-Systeme, die in einem N-Körper-Problem gebildet werden können, miteinander verkoppelt sind. Im Rahmen der Theorie des wechselwirkenden Elektronengases ist wohl bekannt [3], dass ein solches Problem kompliziert ist, und die Lösung bzw. Lösungsverfahren von der Stärke der mitteleren kinetischen Energie ($\bar{H}_0$) verglichen mit der potentiellen Energie abhängt. So liefert z.B. die Störungstheorie im Falle dichter Eletronengase einen geeigneten Zugang. Zur Herleitung approximativer Wellenfunktionen für ein endliches System beliebiger Dichte verfahren wir wie folgt. Man kann zeigen [13], dass

$$\Delta_m \prod_{j>i=1}^{N} \varphi_{ij}(\mathbf{r}_{ij}) \quad = \quad \sum_{l=1}^{m-1} \Delta_m \varphi_{lm} \prod_{\substack{j>i \\ i\neq l}}^{N} \varphi_{ij} \ + \sum_{n=m+1}^{N} \Delta_m \varphi_{mn} \prod_{\substack{j>i \\ j\neq n}}^{N} \varphi_{ij} + A_m, \quad m \in [1, N], \tag{2.7}$$

wobei der Differentialoperator A_m die Gestalt hat

$$\begin{aligned} A_m &= 2\sum_{l=1}^{m-1}\left[(\nabla_m\varphi_{lm})\cdot(\sum_{n=m+1}^{N}\nabla_m\varphi_{mn})\right]\prod_{\substack{j>i\\ j\neq n, i\neq l}}^{N}\varphi_{ij} \\ &+\sum_{l=1}^{m-1}\left[(\nabla_m\varphi_{lm})\cdot(\sum_{l\neq s=1}^{m-1}\nabla_m\varphi_{sm})\right]\prod_{\substack{j>i\\ s\neq i\neq l}}^{N}\varphi_{ij} \\ &+\sum_{n=m+1}^{N}\left[(\nabla_m\varphi_{mn})\cdot(\sum_{\substack{t=m+1\\ t\neq n}}^{N}\nabla_m\varphi_{mt})\right]\prod_{\substack{j>i\\ j\neq t\neq n}}^{N}\varphi_{ij} \qquad m\in[1,N]. \end{aligned} \tag{2.8}$$

Den Operator, der die Zweiteilchensubsysteme (d.h. im Falle $u_j = 0$) miteinander verkoppelt, erhält man durch die Substitution der Funktion (2.5) in Gl. (2.1) unter Berücksichtigung der Relation (2.7). Daraus folgern wir, dass der Term, der die Separabilität verhindert, die Form

$$A = \sum_{m=1}^{N} A_m \tag{2.9}$$

besitzt. Der Mischterm (2.8) ist ein Teil des kinetischen Energieoperators und als solches fällt asymptotisch wie $\sim r_j^{-2}$ ab.

Um die komplette Wellenfunktion (2.2) zu bestimmen, bedarf es einer Bestimmung der Funktion $\chi(\mathbf{r}_1,\cdots,\mathbf{r}_N)$. Eine Bestimmungsgleichung erhält man, wenn die Ausdücke (2.5,2.4) in die Gln. (2.2,2.1) eingesetzt werden, was zur Relation führt

$$\begin{aligned} &\left\{H_0 - \frac{A}{\prod_{j>i=1}^{N}\varphi_{ij}} - \sum_{\ell=1}^{N}\left[(\nabla_\ell\ln\Phi_I \;+\; \nabla_\ell\ln\Phi_{II})\cdot\nabla_\ell\right.\right. \\ &\left.\left. +(\nabla_\ell\ln\Phi_I)\cdot(\nabla_\ell\ln\Phi_{II})\right] + E\text{-}\right\}\chi(\mathbf{r}_1,\cdots,\mathbf{r}_N) = 0\,. \end{aligned} \tag{2.10}$$

Aus dieser Gleichung ist ersichtlich, dass das weitere Vorgehen von der Form der Funktionen Φ_I und Φ_{II} (und somit von $u_\ell,\ v_{ij}$) abhängt, deren Bestimmung in der Regel keine Schwierigkeiten bereitet.

Der Vorteil der oben skizzierten Methode liegt darin, dass bekannte Aspekte des Problems in die Lösung miteinbezogen werden können. So haben wir durch die obige Wahl von Φ_I und Φ_{II} erreicht, dass 1.) die Lösung für den Fall unabhängiger Teilchen korrekt wiedergegeben ist, und dass 2.) alle Zweiteilchen-Potentiale durch Φ_{II} exakt berücksichtigt sind. Somit ist die Zweiteilchen-Korrelation explizit in der Theorie enthalten. Mehrteilchen-Kopplungen werden durch die Gl. (2.10) beschrieben.

Die hier vorgestellte Methode wurde für die Berechnung von Mehrkörper-Kontinuumszuständen eines Systems herangezogen, das aus N geladene Teilchen besteht [13, 11]. Eine Kopie von der Arbeit [13] ist im Anhang beigefügt.

3 Greensfunktionstheorie endlicher Systeme

Mit steigender Teilchenzahl wird die Behandlung korrelierter Systeme komplizierter und neue Phänomene treten auf, deren Erkärung einer detaillierten Beschreibung der kollektiven Eigenschaften des Systems bedarf. Deswegen ist eine Methode notwendig, die über das Wellenfunktionsverfahren hinaus geht und das gesamte Spektrum des Systems beinhaltet. Die Greensfunktionsmethode (GF) hat sich für diesen Zweck als sehr flexibel, effizient und allgemein erwiesen. In diesem Kapitel werden wir diese Theorie für Wenigteilchen-Systeme kurz erläutern und eine neue Betrachtungsweise einführen. Im Kapitel (5.2) werden wir auf die GF im Falle unendlich ausgedehnter Systeme eingehen.

Die Hauptschwierigkeiten für die Theory stammen aus den Inner-Teilchen-Korrelationen, denn wären die Teilchen unabhängig, so könnte man existierende Standardlösungmethoden heranziehen und das Verhalten des Systems genau vorhersagen. Aus diesem Grunde wird in diesem Kapitel eine nicht-perturbative Methode entwickelt [14], die es erlaubt, die Stärke der Innter-Teilchen-Korrelationen für eine kanonische Gesamtheit systematisch soweit zu reduzieren, dass eine Behandlung mit konventionellen Methoden, wie Störungstheorie oder Molekular-Feld-Näherung, sinnvoll wird. Dies wird durch eine kumulative Prozedur erreicht, die ein wechselwirkendes N-Teilchen-System auf Systeme abbildet, in denen nur $N - M$ Teilchen miteinander korreliert sind, dabei ist $M \in [1, N - 2]$. Das heißt die Stärke der Korrelationsenergie wird schrittweise reduziert.

3.1 Formale Behandlung

Die fundamentale Größe für die Beschreibung der mikroskopischen Eigenschaften eines N-Körper-Quantumsystems ist die Resolvente des Hamiltonoperators, die auch als der Greensoperator $G^{(N)}$ bezeichnet wird. $G^{(N)}$ erfüllt die Lippmann-Schwinger-Integralgleichung $G^{(N)} = G_0 + G_0 U^{(N)} G^{(N)}$, wobei G_0 der Greensoperator eines Referenzsystems mit N voneinander unabhängigen Teilchen ist. Eine äquivalente Prozedur ist die Benutzung vom so genannten Übergangsoperator $T^{(N)}$, der durch die Integralgleichung $T^{(N)} = U^{(N)} + U^{(N)} G_0 T^{(N)}$ definiert ist. Diese Integralgleichungen für $G^{(N)}$ und $T^{(N)}$ sind die Basis für störungstheoretische

Methoden. Für $N \geq 3$ ist aber die Anwendung dieser Lippmann-Schwinger-Gleichungen mit zwei wesentlichen Schwierigkeiten behaftet: 1.) Wie in den Arbeiten [15, 16] gezeigt wurde, liefern die Lippmann-Schwinger-Gleichungen für die Zustandsvektoren keine eindeutige Lösung. 2.) Wie Faddeev gezeigt hat [17, 18], ist der Kern dieser Integralgleichungen $K = G_0 U^{(N)}$ für $N \geq 3$ nicht integrabel, d.h. die Norm $\|K\| = [\mathrm{Tr}(KK^\dagger)]^{1/2}$ ist nicht integrabel. Weiterhin ist der Kern K auch nicht kompakt.

In diesem Abschnitt wird ein neuer Zugang vorgestellt. Wir nehmen an, dass das totale Potential die Form $U^{(N)} = \sum_{j>i=1}^{N} v_{ij}$ besitzt, wobei die Zweiteilchen-Potentiale v_{ij} an dieser Stelle nicht auf eine spezielle analytische Form beschränkt sind. Der Punkt ist nun, dass das Potential $U^{(N)}$ die Rekursionsformel

$$U^{(N)} = \frac{1}{N-2} \sum_{j=1}^{N} u_j^{(N-1)}, \quad u_j^{(N-1)} = \frac{1}{N-3} \sum_{k=1}^{N-1} u_{jk}^{(N-2)}, \; j \neq k \tag{3.1}$$

erfüllt, wobei $u_j^{(N-1)}$ das totale Potential des Systems ist, in dem $N-1$ Teilchen miteinander wechselwirken. Der Index j deutet darauf hin, dass das Teilchen mit der Bezeichnung j nicht mit dem Rest des Systems korreliert ist, denn man kann leicht zeigen, dass $u_j^{(N-1)} = \sum_{m>n=1}^{N} v_{mn}, \; m \neq j \neq n$ gilt. Wie in der im Anhang beigefügten Arbeit gezeigt ist [14], kann man die Formel (3.1) heranziehen, um eine ähnliche Rekursionsformel für den Übergangsoperator $T^{(N)}$ sowie für den Greensoperator $G^{(N)}$ herzuleiten. Es gilt nämlich

$$T^{(N)} = \sum_{j=1}^{N} T_j^{(N-1)}, \; j \in [1, N], \tag{3.2}$$

wobei sich die Operatoren $T_j^{(N-1)}$ aus der Matrix-Integralgleichung

$$\begin{pmatrix} T_1^{(N-1)} \\ T_2^{(N-1)} \\ \vdots \\ T_{N-1}^{(N-1)} \\ T_N^{(N-1)} \end{pmatrix} = \begin{pmatrix} t_1^{(N-1)} \\ t_2^{(N-1)} \\ \vdots \\ t_{N-1}^{(N-1)} \\ t_N^{(N-1)} \end{pmatrix} + [\mathbf{K}^{(N-1)}] \begin{pmatrix} T_1^{(N-1)} \\ T_2^{(N-1)} \\ \vdots \\ T_{N-1}^{(N-1)} \\ T_N^{(N-1)} \end{pmatrix} \tag{3.3}$$

ergeben. Der Operator $t_j^{(N-1)}$ ist der Übergangsoperator eines Systems, in dem nur $N-1$ Teilchen miteinander korreliert sind. Der Kern $[\mathbf{K}^{(N-1)}]$ der obigen Integralgleichung hängt nur von den reduzierten Operatoren $t_j^{(N-1)}$ [14] ab, es gilt nämlich

$$[\mathbf{K}^{(N-1)}] = \begin{pmatrix} 0 & t_1^{(N-1)} & t_1^{(N-1)} & \ldots\ldots & t_1^{(N-1)} \\ t_2^{(N-1)} & 0 & t_2^{(N-1)} & \ldots\ldots & t_2^{(N-1)} \\ \ldots & \ldots & \ldots & \ldots & \ldots \\ t_{N-1}^{(N-1)} & \ldots\ldots & t_{N-1}^{(N-1)} & 0 & t_{N-1}^{(N-1)} \\ t_N^{(N-1)} & \ldots\ldots & t_N^{(N-1)} & t_N^{(N-1)} & 0 \end{pmatrix} G_0, \tag{3.4}$$

wobei G_0 der Referenz-Greensoperator ist (der Greensoperator in Abwesenheit von $U^{(N)}$). Aus Gl. (3.1) wird klar, dass $t_j^{(N-1)}$ als Funktion von Übergangsoperatoren von Systemen ausgedrückt werden kann, in denen nur $N-2$ Teilchen miteinander wechselwirken. Somit ergibt sich ein iteratives Schema für die Herleitung vom Mehrteilchen-Übergangsoperatoren. Durch ähnliche Überlegungen für die Greensoperatoren $G^{(N)}$ sowie durch die Relation $G^{(N)} = G_0 + G_0 T^{(N)} G_0$ kommt man zur Schlußfolgerung, dass

$$G^{(N)} = G_0 + \sum_{j=1}^{N} G_j^{(N-1)}. \tag{3.5}$$

Die Operatoren $G_j^{(N-1)}$ sind mit den Greensoperatoren $g_j^{(N-1)}$ von Systemen verknüpft, in denen nur $N-1$ Teilchen miteinander korreliert sind, es gilt nämlich [14]

$$\begin{pmatrix} G_1^{(N-1)} \\ G_2^{(N-1)} \\ \vdots \\ G_{N-1}^{(N-1)} \\ G_N^{(N-1)} \end{pmatrix} = \begin{pmatrix} g_1^{(N-1)} - G_0 \\ g_2^{(N-1)} - G_0 \\ \vdots \\ g_{N-1}^{(N-1)} - G_0 \\ g_N^{(N-1)} - G_0 \end{pmatrix} + [\tilde{\mathbf{K}}^{(N-1)}] \begin{pmatrix} G_1^{(N-1)} \\ G_2^{(N-1)} \\ \vdots \\ G_{N-1}^{(N-1)} \\ G_N^{(N-1)} \end{pmatrix}, \tag{3.6}$$

wobei $[\tilde{\mathbf{K}}^{(N-1)}] = G_0[\tilde{\mathbf{K}}^{(N-1)}]G_0^{-1}$.

Die obigen Ergebnisse können so zusammengefasst werden, ist der Greensoperator des $(N-1)$-Teilchen-Systems bekannt, so ergibt sich der Greensoperator für N wechselwirkende Teilchen durch die Lösung von N linear, gekoppelten Integralgleichungen (nämlich Gln. (3.3,3.6)). Ist aber nur die Lösung des $(N-M)$-Teilchen-Problem bekannt ($M \in [1, N-2]$), so bedarf es der Durchführung von einer Hierarchie von Rechnungen beginnend mit der Herleitung der Lösung des $(N-M+1)$-Teilchen-Problems. Die Prozedur muss dann solange wiederholt werden, bis sich die Lösung des N-Teilchen-Problems ergibt.

3.2 Anwendung auf ein Vierteilchen-System

Für ein Vierteilchen-System kann man den Greensoperator $G^{(4)}$ in Abhängigkeit von Dreiteilchen-Greensfunktionen ausdrücken, nämlich $G^{(4)} = \sum_{j=1}^{4} g_j^{(3)} - 3G_0$, wobei $g_j^{(3)}$ ist der Greensoperator eines System, in dem nur drei Teilchen miteinander wechselwirken. Dies ergibt für die Zustandsvektoren die Relation

$$|\Psi^{(4)}\rangle = |\psi_{234}^{(3)}\rangle + |\psi_{134}^{(3)}\rangle + |\psi_{124}^{(3)}\rangle + |\psi_{123}^{(3)}\rangle - 3|\phi_{\text{free}}^{(4)}\rangle, \tag{3.7}$$

wobei $|\psi^{(3)}_{ijk}\rangle$ ist der Zustandsvektor eines Systems, in dem die Teilchen i, j und k korreliert sind. $|\phi^{(4)}_{\mathrm{free}}\rangle$ ist der Zustandsvektor eines nicht-wechselwirkenden Vierteilchen-Systems. Anhand von Gl. (3.7) wird der rechen-technische Vorteil des vorgeschlagenen Verfahrens deutlich: Aus Dreiteilchen-Wellenfunktionen, die wir z.B. durch die Methode von Kap. 2 herleiten, lassen sich Vierteilchen-Wellenfunktionen mit Hilfe von Gl. (3.7) direkt konstruieren. Eine Anwendung dieser Ideen auf konkrete physikalische Reaktionen sowie ein Vergleich mit den Experimenten befinden sich in Ref. [14] (Diese Arbeit ist im Anhang beigefügt).

3.3 Thermodynamik und Phasenübergänge endlicher Systeme

Endliche Systeme zeigen keine Phasenübergänge im strikten Sinne [19]. So sind z.B. die Fluktuationen in solchen Systemen natürlicherweise beschränkt, wogegen Phaseübergangen in einem thermodynamischen System durch unendliche Fluktuationen am kritischen Punkt gekennzeichnet sind. Nichtdestotrotz würde man erwarten, dass mit steigender Größe des Systems Spuren kritischer Phänomene immer mehr in Erscheinung treten. Traditionell werden solche Fragen im Rahmen der *f*inite-size scaling Theorie abgehandelt [20]. Für ein endliches, wechselwirkendes N-Teilchen-System ist die hier vorgestellte GF-Methode auch geeignet, um thermodynamische und quantenstatistische Fragen zu untersuchen. Zu diesem Zweck machen wir uns die in den Refn. [19, 21] vorgeschlagenen Ideen zunutze und schreiben die kanonische Zustandssumme als $Z(\beta) = \int dE\ \Omega(E)\ e^{-\beta E}$. Dabei ist $\Omega(E)$ die Zustandsdichte, die aus dem Imaginäranteil der Spur der Greensfunktion $G^{(N)}$ erhalten werden kann: $\Omega(E) = -\frac{1}{\pi}\mathbf{Tr}\,\Im\,G^{(N)}(E)$. Die in dieser Arbeit hergeleitete Rekursionsformel für die N-Teilchen-Greensfuncktion kann nun zur Berechnung von $\Omega(E)$ herangezogen werden. In erster Ordnung ergibt dieses Verfahren für die kanonische Zustandssumme die Formel

$$Z^{(N)} = \sum_{j=1}^{N} Z_j^{(N-1)} - (N-1)Z_0. \tag{3.8}$$

Z_0 ist die kanonische Zustandssumme eines aus N unabhängigen Teilchen bestehenden Referenzsystems. Weiterhin is $Z_j^{(N-1)}$ die kanonische Zustandssumme eines Systems, in dem die Stärke der Korrelationen dadurch reduziert sind, dass alle Wechselwirkungen mit dem Teilchen j ausgeschaltet sind.

Gl. (3.8) erlaubt das Studium thermodynamische Eigenschaften endlicher korrelierter Systeme auf mikroskopischer Ebene. Insbesondere, bietet die obige Gl. (3.8) eine Möglichkeit, den Einfluß der Stärke der Korrelationen auf die Thermodynamik des Systems systematisch zu untersuchen.

Kritische Phänomene können mit Hilfe der Methoden von Yang und Lee [19, 21] untersucht werden. Gehen wir z.B. der Frage nach, wann eine Kondensation in einem Quanten-Bose-Gas einsetzt, so ist die Grundzustandspopulation $\eta_0(N, \beta)$ die relevante Größe, die sich aus

$$\eta_0(N, \beta) = -\frac{1}{\beta} \frac{\partial_{\epsilon_0} Z^{(N)}(\beta)}{Z^{(N)}(\beta)} \quad = \quad -\frac{1}{\beta} \frac{\sum_{j=1}^{N} \partial_{\epsilon_0} Z_j^{(N-1)} - (N-1)\partial_{\epsilon_0} Z_0}{Z^{(N)}} \tag{3.9}$$

ergibt. ϵ_0 ist die Grundzustandsenergie. Mit Hilfe dieser Gleichung kann man systematisch die Wirkung der Inner-Teilchen-Korrelationen auf das Auftreten von kritischem Verhalten, oder man kann alternativ dazu die Nullstellen von Gl. (3.8) in der komplexen β-Ebene untersuchen. Eine Menge von Nullstellen von $Z^{(N)}(\beta)$, die systematisch der reellen β-Achse nahe kommen, ist eine Signatur eines kritischen Verhaltens im thermodynamischen Grenzfall.

4 Kollektive Antwort und kurz-reichweitige Dynamik

Im thermodynamischen Grenzfall (also für großes Volumen V, große Teilchenzahl N, aber für endliche Teilchendichten $n = N/V$) wird die charakteristische Antwort eines Systems durch ein kooperatives Zusammenspiel aller Elektronen hervorgerufen. Zum Beispiel, die Fluktuationen in der elektronischen Dichte sind durch den so genannten Polarisationsoperator $\Pi(\mathbf{q}, \omega)$ bestimmt. Dabei sind ω und $\mathbf{q}$, die von einer äußeren Störung auf das System übertragene Frequenz und Impuls. $\Pi(\mathbf{q}, \omega)$ beschreibt die Anregung und die Relaxation von den Teilchen-Loch-Paaren, was in der Summe globale Dichtefluktuationen erzeugt.

Der kollektiven Antwort des Systems steht die kurz-reichweitige Dynamik gegenüber. Dies wird am Beispiel von $\Pi(\mathbf{q}, \omega)$ ersichtlich: Die Polarisation des Mediums modifiziert die Eigenschaften der Zweiteilchen-Wechselwirkung $U(\mathbf{q}, \omega)$. Das modifizierte Potential U_{eff} ist eng mit U und $\Pi(\mathbf{q}, \omega)$ durch die Integralgleichung [2, 3]

$$\begin{aligned} U_{\mathit{eff}} &= U + U\Pi U_{\mathit{eff}}, && (4.1) \\ &= U\left(1 - U\Pi\right)^{-1} && (4.2) \end{aligned}$$

verknüpft. Die durch das Medium verursachte *Abschirmung* von U kann somit durch $\kappa(\mathbf{q}, \omega) := 1/(1 - U\Pi)$, die so genannte generalisierte dielektrische Funktion [3], quantifiziert werden. Um U_{eff} und κ zu bestimmen, bedarf es der Kenntnis der Polarisationsfunktion Π. Ein verbreitetes Näherungsverfahren zur Berechnung von Π ist die so genannte *random phase approximation* (RPA). In RPA wird Π durch Π_0 genähert, wobei Π_0 durch die Relation gegeben ist

$$i\Pi_0(\mathbf{q}, \omega) = \frac{2}{(2\pi)^4} \int d\mathbf{p} d\xi G_0(\mathbf{q} + \mathbf{p}, \omega + \xi) G_0(\mathbf{p}, \xi). \tag{4.3}$$

G_0 ist das freie Einteilchen-Greensfunktion. Die Berechnung von Π_0 kann für ein homogenes Elektronengas analytisch durchgeführt werden. Im Grenzwert langer Wellenlängen erhält man $\Pi_0 \approx -2N(\mu)$, wobei $N(\mu)$ die Zustandsdichte beim Fermi-Zustand μ ist. Das bedeutet, dass in Anwesenheit eines Mediums die Elektron-Elektron-Wechselwirkung die Form $U_{TF} = 4\pi/[q^2 + 8\pi N(\mu)]$ besitzt. Im Konfigurationsraum erhält man $U_{TF} = e^{-r/\lambda}/r$. Deswegen, im Gegensatz zu atomaren Systemen, in denen Streuprozesse mit kleinem Impulsübertrag dominierend sind (wegen $U \propto 1/q^2$), sind in einem Medium Streuereignisse mit kleinem q von untergeordneter Bedeutung. Dies ist eine Folge der kurzen Reichweite des re-normierten Streupotentials U_{eff} (4.2).

Außer für ein homogenes, unendlich ausgedehntes Elektronengas, (das ebene Wellen als unkorrelierte Eigenzustände besitzt) ist die Berechnung von U_{eff} i.a. eine schwierige Aufgabe. Für ein inhomogenes elektronisches System, wie eine Oberflächen, bietet die so genannte GW-Näherung [22] eine direkte Erweiterung der RPA (G steht für die Greensfunktion und $W \equiv U_{eff}$ für die abgeschirmte Wechselwirkung). In Ref.[23] befinden sich mehr Einzelheiten zu diesem Verfahren sowie eine Diskussion der Beziehung zur RPA.

4.1 Die Signatur kollektiver Antwort in endlichen elektronischen Systemen

Für endliche Systeme ist das Spektrum diskret, was eine signifikante Fluktuation um den Grundzustand verhindert. Mit steigender Größe und Teilchenzahldichte n treten aber kollektive Effektse immer mehr in Erscheinung. Um dieses Verhalten zu illustrieren sind große Moleküle oder Metall-Cluster besonders geeignet. Wir studieren hier den Einfluß der Fluktuationen in diesen Systemen auf den Prozess der Elektronenstoßionisation. Das Projektilelektron spielt die Rolle einer Testladung, die als eine wohldefinierte äußere Störung die elektronische Dichteverteilung des Targets anregt. Die Antwort des Systems wird in der Form von Ionisationswirkungsquerschnitten experimentell gemessen.

Im Rahmen der RPAE (RPA mit Austausch (engl. exchange)) schreibt sich die abgeschirmte Wechselwirkung U_{eff} zwischen dem Projektilelektron (also der Testladung) und dem Target als

$$\begin{aligned}
\Big\langle\, \mathbf{k}_1\mathbf{k}_2 \,\Big|\, U_{\mathit{eff}} \,\Big|\, \phi_\nu \mathbf{k_0} \,\Big\rangle \;&=\; \Big\langle\, \mathbf{k}_1\mathbf{k}_2 \Big|\, U \,\Big|\, \phi_\nu \mathbf{k_0} \,\Big\rangle \\
&+ \sum_{\substack{\varepsilon_p \le \mu \\ \varepsilon_h > \mu}} \left(\frac{\Big\langle\, \varphi_p \mathbf{k_2} \,\Big|\, U_{\mathit{eff}} \,\Big|\, \phi_\nu \varphi_h \,\Big\rangle \Big\langle\, \varphi_h \mathbf{k_1} \,\Big|\, U \,\Big|\, \mathbf{k_0} \varphi_p \,\Big\rangle}{\epsilon_0 - (\varepsilon_p - \varepsilon_h - i\delta)} \right. \\
&\qquad \left. - \frac{\Big\langle\, \varphi_h \mathbf{k_2} \,\Big|\, U_{\mathit{eff}} \,\Big|\, \phi_\nu \varphi_p \,\Big\rangle \Big\langle\, \varphi_p \mathbf{k_1} \,\Big|\, U \,\Big|\, \mathbf{k_0} \varphi_h \,\Big\rangle}{\epsilon_0 + (\varepsilon_p - \varepsilon_h - i\delta)} \right) .
\end{aligned} \tag{4.4}$$

φ_p und φ_h sind die intermediaren Teilchen- und Lochzustände mit den Energien ε_p bzw. ε_h. δ ist eine kleine positive reelle Zahl und μ ist das chemische Potential.

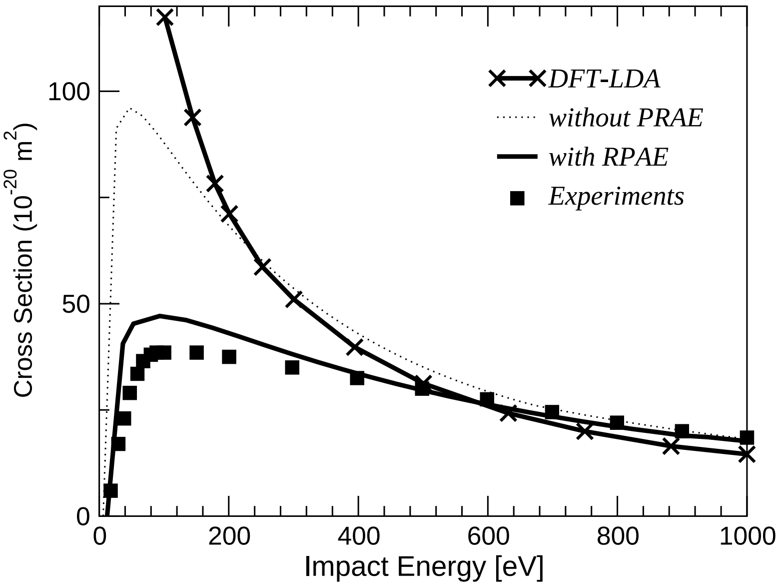

Abbildung 4.1: Der totale Wirkungsquerschnitt für die Elektronstoßionisation von C_{60} als Funktion der Projektilenergie. Die *absoluten* experimentellen Daten (volle Quadrate) für die Produktion von stabilen C_{60}^{+}-Ionen [24, 25] sind gezeigt. Die durchgezogene Kurve mit Kreuzen ist das Resultat einer DFT-Rechnung [26], die punktierte Kurve steht für das Resultat der in dieser Arbeit vorgestellten Theorie ohne RPAE. Dagegen ist das Resultat der Theorie mit RPAE durch die durchgezogene Kurve dargestellt.

Würde man die Elektron-Loch-Anregung vernachlässigen, dann würde sich Gl. (4.4) auf den ersten Term auf der rechten Seite reduzieren. Diese Näherung wurde in Ref.[27] angewandt, wobei die Einteilchenzustände mit Hilfe der Dichtefunktionaltheorie im Rahmen der lokalen Dichte-Näherung (DFT-LDA) [12] berechnet wurden. Gl. (4.4) wurde in der Arbeit[1] [28] selbst-konsistent für ein C_{60}-Target gelöst. Anschließend wurden damit die Ionisationswirkungsquerschnitte errechnet. Die Resultate sind im Abb. 4.1 gezeigt. Aus dieser Abbildung entnehmen wir, dass die durch die Dichtefluktuationen verursachte Abschirmung zu einer Absenkung der Ionisationswirkungsquerschnitte führt. Dies ist verständlich, denn durch die Abschirmung schrumpft die effektive Größe des Bereiches, in dem das Streupotential aktiv ist, was wiederum in eine verminderte Streuwahrscheinlichkeit resultiert.

---

[1] Dieser Artikel ist im Anhang beigefügt

Fig. (4.2) bietet einen Einblick in die Abhängigkeit der Abschirmung von der Größe von Li-Metallclustern: Vernachlässigt man die kollektive Abschirmung [Fig. (4.2) (a)], so steigt der auf die Anzahl der Elektronen normierte Wirkungsquerschnitt mit wachsender Größe der Cluster. Auf der anderen Seite ist es klar, dass für größer werdende Cluster kollektive Abschirmeffekte immer mehr in den Vordergrund treten, was zu einem vermindereten Streuvolumen, und somit zu kleiner werdenden Streuwirkungsquerschnitten führt [Fig. (4.2) (b)]. Für kleine Cluster liefern die Rechnungen mit und ohne RPAE ähnliche Ergebnisse.

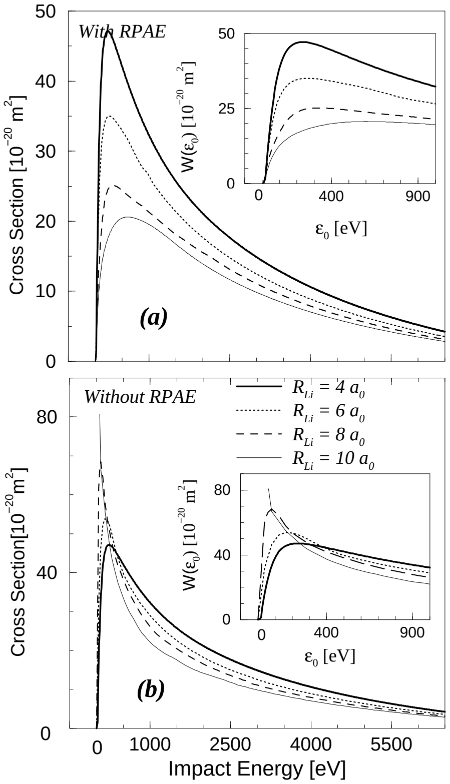

Abbildung 4.2: Der normierte totale Wirkungsquerschnitt für die Elektronen-Stoßionisation von sphärischen Li-Clustern mit verschiedenen Clusterradien R_{Li}. (a) enthält die Resultate der RPAE-Rechnung. (b) zeigt die Ergebnisse der Rechnung ohne Berücksichtigung der Teilchen-Loch-Anregung. (a) und (b) zeigen auch eine Vergrösserung des niederenergetischen Bereiches.

5 Die Quantenfeldmethoden: Konzepte und Anwendungen

Für die theoretische Behandlung stark korrelierter Systeme oder mehrfacher Anregung bedarf es Methoden, die über RPA hinaus gehen. Zu diesem Zweck wurden mehrere Theorien entworfen [3, 4, 29], die aber meistens auf die Behandlung von Grundzustandseigenschaften beschränkt sind. Zur Untersuchung von angeregten korrelierten Zuständen hat sich die Greensfunktionsmethode als ein sehr nützlich erwiesen. Diese Methode haben wir in Kapitel (3) eingeführt. Dies geschah allerdings im Rahmen der ersten Quantisierung, d.h. die Symmetrie der Teilchen ist durch entsprechende (anti)symmetrische Wellenfunktionen berücksichtigt, mit Hilfe derer relevante Matrixelemente der Greensfunktion zu berechnen sind. Mit steigender Teilchenzahl N, wird dieses Verfahren sehr umständlich. Eine alternative Methode bietet die Greensfunktionstheorie, die von Migdal & Galitskii sowie von Martin und Schwinger [30, 31] im Rahmen der Quantenfeldtheorie entwickelt wurde. Die Grundidee ist die Anwendung der Regel der Feynman-Diagrame, um eine Verbindung der Propagatoren höher Ordnung mit dem Einteilchen-Propagator (engl.*single-particle propagator*) herzustellen. Der sp-Propagator erhält man mittels einer Integralgleichung (Dyson-Gleichung) aus dem ungestörten (freien) Propagator. Der Symmetrie der Teilchen (Fermionen oder Bosonen) wird durch entsprechende Vertauschungsrelationen der Operatoren Rechnung getragen [3, 7, 8]. Dieses störungstheoretische Verfahren wurde sehr intensiv untersucht und für die Beschreibung von einer Reihe physikalischer Probleme verwendet. In diesem Kapitel werden wir nur auf die Aspekte eingehen, die für die Ein- und die Zweiteilchen-Anregung von unmittelbarer Bedeutung sind.

5.1 Die Einteilchen-Greensfunktion ausgedehnter Systeme

Die sp-Greensfunktion $g(\alpha t, \beta t')$ kann als der Erwartungswert eines zeit-geordneten Produktes von zwei Operatoren betrachtet werden

$$\mathrm{i}\, g(\alpha t, \beta t') = \langle \Psi_0 | \mathcal{T}[a_{\mathrm{H}\alpha}(t)\, a^{\dagger}_{\mathrm{H}\beta}(t')] | \Psi_0 \rangle, \tag{5.1}$$

wobei $|\Psi_0\rangle$ der korrelierte, exakte sowie normierte Grundzustand des N-Teilchen-Systems ist. $\mathcal{T}$ ist ein Zeitordnungsoperator. Weiterhin bezeichnen $a^\dagger_{\mathrm{H}\beta}(t')$ und $a_{\mathrm{H}\alpha}(t)$ die Fermionischen Erzeugungs- und Vernichtungsoperatoren im Heisenberg-Bild, die in einer Basis repräsentiert sind, deren Elemente mit den Quantenzahlen α und β charakterisiert sind. Für ein translationsinvariantes System bieten die Impulseigenzustände (mit den Quantenzahlen $\mathbf{k}$) eine geeignete Basis. Der Effekt des chronologischen Operators $\mathcal{T}$ kann durch die Stufenfunktion $\Theta(t-t')$ beschrieben werden, d.h.

$$\begin{aligned} \mathrm{i}g(k,t-t') &= \Theta(t-t')\langle\Psi_0|a_{\mathrm{H}k}(t)a^\dagger_{\mathrm{H}k}(t')|\Psi_0\rangle - \Theta(t'-t)\langle\Psi_0|a^\dagger_{\mathrm{H}k}(t')a_{\mathrm{H}k}(t)|\Psi_0\rangle \\ &= \Theta(t-t')\sum_\gamma e^{-\mathrm{i}[E^{(N+1)}_\gamma - E^{(N)}_0](t-t')}\left|\langle\Psi^{(N+1)}_\gamma|a^\dagger_k|\Psi_0\rangle\right|^2 \\ &\quad -\Theta(t'-t)\sum_\delta e^{-\mathrm{i}[E^{(N)}_0 - E^{(N-1)}_\delta](t-t')}\left|\langle\Psi^{(N-1)}_\delta|a_k|\Psi_0\rangle\right|^2 . \end{aligned} \tag{5.2}$$

$\Psi^{(N+1)}_\gamma$ und $\Psi^{(N-1)}_\delta$ bezeichnen einen kompletten Satz von Eigenzuständen des $(N+1)$- bzw. des $(N-1)$-Teilchen-Systems. Die Energien $E^{(N)}_0$, $E^{(N+1)}_\gamma$, und $E^{(N-1)}_\delta$ beziehen sich auf die exakten Energien des korrelierten Grundzustandes des N, des $(N+1)$, bzw. des $(N-1)$-Teilchen-Systems. The Exponentialfunktionen in Gl. (5.2) stammen aus den Exponentialfunktionen (mit den Hamiltonians als Argument), die in der Definition der Heisenberg-Operatoren eingehen. Da die Stufenfunktion die Integraldarstellung $\Theta(t) = -\lim_{\eta\to 0}\frac{1}{2\pi\mathrm{i}}\int_{-\infty}^{\infty}\mathrm{d}\omega\frac{e^{-\mathrm{i}\omega t}}{\omega+\mathrm{i}\eta}$, besitzt, erhählt man die Greensfunktion im Energieraum mittels einer Fourier-Transformation bzgl. des Zeitunterschiedes $t-t'$. Dies führt auf die Frequenz (ω)-abhängige, spektrale (oder Lehmann-) Darstellung der sp-Greensfunktion [32],

$$g(k,\omega) = \lim_{\eta\to 0}\left[\sum_\gamma \frac{\left|\langle\Psi^{(N+1)}_\gamma|a^\dagger_k|\Psi_0\rangle\right|^2}{\omega - [E^{(N+1)}_\gamma - E^{(N)}_0] + \mathrm{i}\eta} + \sum_\delta \frac{\left|\langle\Psi^{(N-1)}_\delta|a_k|\Psi_0\rangle\right|^2}{\omega - [E^{(N)}_0 - E^{(N-1)}_\delta] - \mathrm{i}\eta}\right] . \tag{5.3}$$

Diese Relation unterstreicht die physikalische Bedeutung der sp-Greensfunktion: Die Pole von $g(k,\omega)$ korrespondieren zur Änderung der Energie (bezogen auf $E^{(N)}_0$), wenn dem N-Teilchen-System ein zusätzliches Teilchen hizugefügt ($E^{(N+1)}_\gamma - E^{(N)}_0$) bzw. ein Teilchen entnommen ($E^{(N)}_0 - E^{(N-1)}_\delta$) wird. Die Residuen dieser Pole sind durch die so genannten *spektroskopischen Faktoren* gegeben. Diese liefern die messbare Wahrscheinlichkeit für die Addition bzw. für die Entnahme eines Teilchen mit dem Wellenvektor $\mathbf{k}$, um den mit den Quantenzahlen γ (δ) bezeichneten Zustand zu erreichen.

Offensichtlich sind solche Wahrscheinlichkeiten von direkter Bedeutung für den (e,2e)-Prozess.

Es hat sich eingebürgert, die spektrale Darstellung der sp-Greensfunktion in Abhngigkeit der spektralen Funktionen der Löcher bzw. der Teilchen darzustellen. Diese sind definiert als

$$S_{\mathrm{h}}(k,\omega) = \frac{1}{\pi}\Im\, g(k,\omega) = \sum_{\gamma} \left|\langle\Psi_{\gamma}^{(N-1)}|a_k|\Psi_0\rangle\right|^2 \delta(\omega - (E_0^{(N)} - E_{\gamma}^{(N-1)})), \quad \text{for } \omega \leq \epsilon_{\mathrm{F}}; \tag{5.4}$$

$$S_{\mathrm{p}}(k,\bar{\omega}) = \frac{1}{\pi}\Im\, g(k,\bar{\omega}) = \sum_{\gamma} \left|\langle\Psi_{\gamma}^{(N+1)}|a_k^{\dagger}|\Psi_0\rangle\right|^2 \delta(\bar{\omega} - (E_{\gamma}^{(N+1)} - E_0^{(N)})), \quad \text{for } \bar{\omega} > \epsilon_{\mathrm{F}}. \tag{5.5}$$

Die sp-Greensfunktion kann dann in der Form geschrieben werden

$$g(k,\omega) = \lim_{\eta\to 0}\left(\int_{-\infty}^{\epsilon_{\mathrm{F}}} \mathrm{d}\omega' \frac{S_{\mathrm{h}}(k,\omega')}{\omega - \omega' - \mathrm{i}\eta} + \int_{\epsilon_{\mathrm{F}}}^{\infty} \mathrm{d}\omega' \frac{S_{\mathrm{p}}(k,\omega')}{\omega - \omega' + \mathrm{i}\eta}\right). \tag{5.6}$$

In einer Reihe von Experimenten wurde eingehend demonstriert [33], dass für hohe Energien die $(e,2e)$-Spektroskopie die Funktion $S_{\mathrm{h}}(k,\omega)$ direkt abbildet. Die Bedeutung der Untersuchung von $S_{\mathrm{h}}(k,\omega)$ wird aus der Tatsache ersichtlich, dass der Erwartungswert von einem *beliebigen* Einteilchen-Operator $\hat{O}$ aus der Relation $\langle\hat{O}\rangle = \sum_{\alpha\beta}\int_{-\infty}^{E_{\mathrm{F}}} \mathrm{d}\omega S_{\mathrm{h}}(\alpha\beta,\omega)\langle\alpha|O|\beta\rangle$ berechnen läßt, wobei $\langle\alpha|O|\beta\rangle$ die Matrixdarstellung von $\hat{O}$ in der Basis $|\alpha\rangle$ ist. Dies wiederum unterstreicht die Wichtigkeit von Spketroskopien, die auf die Emission eines Teilchens beruhen, wie die einfache Photoemission [34, 35] oder die (e,2e)-Reaktion. Ein weiterer Vorteil der Methode der Greensfunktion ist die Existenz einer systematischen Vorgehensweise, die mit Hilfe der Diagramm-Technik geeignete Näherungen zu g liefert [8].
In der diagrammatischen Entwicklung von g führt man das Konzept der Selbstenergie Σ ein [22]. Die Kenntnis von Σ erlaubt die Bestimmung von g mittels der Dyson-Gleichung

$$g(\alpha\beta;\omega) = g_0(\alpha\beta;\omega) + \sum_{\gamma\,\delta} g_0(\alpha\gamma;\omega)\,\Sigma(\gamma\delta;\omega)\,g(\delta\beta;\omega), \tag{5.7}$$

wobei g_0 die Greensfunktion eines (nicht-wechselwirkenden) Referenzsystems ist. Die Selbstenergie Σ beschreibt alle Anregungen aufgrund der Wechselwirkung des Teilchens mit dem umgebenden Mediums und spielt die Rolle eines nicht-lokalen, energie-abhängigen, komplexen Einteilchen-Potentials.

5.2 Spektrale Teilchen-Teilchen und Loch-Loch-Funktionen

Die Dyson-Gleichung (5.7) kann mit algebraischen Methoden hergeleitet werden [8], die auch belegen, dass der sp-Propagator $g(\alpha t, \alpha' t')$ in einem engen Zusammenhang mit der Zwei-Teilchen-Greensfunktion $g^{\mathrm{II}}(\beta t_1, \beta' t_1', \gamma t_2, \gamma t_2')$ steht. Diese Abhängigkeit ist die erste in einer Hierarchie, die den N-Teilchen-Propagator mit dem $(N+1)$-Teilchen-Propagator [31, 30] verbindet. Von direkter Bedeutung für unsere Untersuchungen ist der Zwei-Teilchen-Propagator $g^{\mathrm{II}}(\beta t_1, \beta' t_1', \gamma t_2, \gamma t_2')$.

Ähnliche Überlegungen wie im Falle des sp-Propagators führen auf die Lehmann-Darstellung der Zweiteilchen-Greensfunktion in Abhängigkeit der Energien und Zuständen der Systeme mit N Teilchen und $N \pm 2$ Teilchen[1]

$$\begin{aligned} g^{\mathrm{II}}(\alpha\beta, \gamma\delta; \Omega) \quad &= \quad \sum_n \frac{\langle \Psi_0^{(N)} | a_\beta a_\alpha | \Psi_n^{(N+2)} \rangle \langle \Psi_n^{(N+2)} | a_\gamma^\dagger a_\delta^\dagger | \Psi_0^{(N)} \rangle}{\Omega - [E_n^{(N+2)} - E_0^{(N)}] + \mathrm{i}\eta} \\ &\quad - \sum_m \frac{\langle \Psi_0^{(N)} | a_\gamma^\dagger a_\delta^\dagger | \Psi_m^{(N-2)} \rangle \langle \Psi_m^{(N-2)} | a_\beta a_\alpha | \Psi_0^{(N)} \rangle}{\Omega - [E_0^{(N)} - E_m^{(N-2)}] - \mathrm{i}\eta}. \end{aligned} \tag{5.8}$$

Durch analoge Überlegungen wie im Einteilchenfall läßt sich die spektrale Zwei-Loch-Funktion $S_{\mathrm{hh}}(\mathbf{k}_1, \mathbf{k}_1, \Omega)$ aus g^{II} gewinnen, nämlich $S_{\mathrm{hh}}(\mathbf{k}_1, \mathbf{k}_1, \Omega) = \Im\, g^{\mathrm{II}}(\mathbf{k}_1, \mathbf{k}_1, \Omega)$, $\Omega \leq 2\epsilon_{\mathrm{F}}/\pi$. Spektroskopien, die auf der Emission zweier Teilchen gründen, wie z.B. die doppelte Photoemission [oder die (γ,2e)-Reaktion], sind direkt mit $S_{\mathrm{hh}}(\mathbf{k}_1, \mathbf{k}_1, \Omega)$ verknüpft.

Die Zweiteilchen-Greensfunktion beinhaltet zwei Klassen von Diagrammen: Der erst Typ wird von zwei nicht-wechselwirkenden sp-Propagatoren [vergl. Gl. (5.7)] generiert und ist erweitert mit ähnlichen Diagrammen, die alle möglichen Selbstenergie-Einschübe darstellen [3]. Der zweite Typ definiert die so genannte Vertex-Funktion Γ. Diese beinhaltet alle Verallgemeinerungen der Korrekturen zu der simplen Näherung für den Zweiteilchen-Propagator, in der nur eine einzige Wechselwirkung zwischen den zwei Teilchen berücksichtigt wird.

Um die Rolle von Γ zu erläutern, schreiben wir g^{II} in der Form

$$\begin{aligned} g^{\mathrm{II}}(\alpha t_1, \alpha' t_1', \beta t_2, \beta' t_2') \quad &= \quad \mathrm{i}\,[g(\alpha\beta, t_1 - t_2)\, g(\alpha'\beta', t_1' - t_2') - g(\alpha\beta', t_1 - t_2')\, g(\alpha'\beta, t_1' - t_2)] \\ &\quad \times \int \mathrm{d}t_a\, \mathrm{d}t_b\, \mathrm{d}t_c\, \mathrm{d}t_d \sum_{abcd} g(\alpha\, a, t_1 - t_a)\, g(\alpha'\, b, t_1' - t_b) \times \\ &\quad \times \langle ab | \Gamma(t_a, t_b; t_c, t_d) | cd \rangle\, g(c\, \beta, t_c - t_2)\, g(d\, \beta', t_d - t_2'). \end{aligned} \tag{5.9}$$

---

[1] In diesem Zusammenhang sei erwähnt, dass die $(N-2)$-Teilchen-Zustände das Endprodukt der doppelten Photoemission (γ,2e) sind.

Diese Gleichung verdeutlicht, dass Γ als eine effektive Wechselwirkung zwischen zwei Quasiteilchen angesehen werden kann. Weiterhin hängt Γ sehr eng mit der (Einteilchen-) Selbstenergie Σ [3] zusammen.

Im Energieraum ergibt sich für das Produkt zweier nicht-wechselwirkender Propagatoren in einfachster Näherung, also die nullte Ordnung in der Entwicklung der Gl. (5.9) bzgl. Γ, die Relation

$$\begin{aligned} g_{\mathrm{f}}^{\mathrm{II}}(\alpha\beta,\gamma\delta;\Omega) &= \frac{\mathrm{i}}{2\pi}\int \mathrm{d}\omega\, [g(\alpha,\gamma;\omega)\, g(\beta\,\delta;\Omega-\omega) - g(\alpha,\delta;\omega)\, g(\beta\,\gamma;\Omega-\omega)] \\ &= \sum_{mm'} \frac{\langle\Psi_0^{(N)}|a_\alpha|\Psi_m^{(N+1)}\rangle\langle\Psi_m^{(N+1)}|a_\gamma^\dagger|\Psi_0^{(N)}\rangle\langle\Psi_0^{(N)}|a_\beta|\Psi_{m'}^{(N+1)}\rangle\langle\Psi_{m'}^{(N+1)}|a_\delta^\dagger|\Psi_0^{(N)}\rangle}{\Omega - \{[E_m^{(N+1)} - E_0^{(N)}] + [E_{m'}^{(N+1)} - E_0^{(N)}]\} + \mathrm{i}\eta} \\ &- \sum_{nn'} \frac{\langle\Psi_0^{(N)}|a_\gamma^\dagger|\Psi_n^{(N-1)}\rangle\langle\Psi_n^{(N-1)}|a_\alpha|\Psi_0^{(N)}\rangle\langle\Psi_0^{(N)}|a_\delta^\dagger|\Psi_{n'}^{(N-1)}\rangle\langle\Psi_{n'}^{(N-1)}|a_\beta|\Psi_0^{(N)}\rangle}{\Omega - \{[E_0^{(N)} - E_n^{(N-1)}] + [E_0^{(N)} - E_{n'}^{(N-1)}]\} + \mathrm{i}\eta} \\ &- (\gamma \longleftrightarrow \delta). \end{aligned} \tag{5.10}$$

Die Leiterapproximation zur Zweiteilchen-Propagator lautet

$$g_{\mathrm{L}}^{\mathrm{II}}(\alpha\beta,\gamma\delta;\Omega) = g_{\mathrm{f}}^{\mathrm{II}}(\alpha\beta,\gamma\delta;\Omega) + \frac{1}{4}\sum_{\epsilon\eta\theta\zeta} g_{\mathrm{f}}^{\mathrm{II}}(\alpha\beta,\epsilon\eta;\Omega)\langle\epsilon\eta|V|\theta\zeta\rangle g_{\mathrm{L}}^{\mathrm{II}}(\theta\zeta,\gamma\delta;\Omega), \tag{5.11}$$

wobei V die nackte Zweiteilchen-Wechselwirkung ist. Diese Integralgleichung kann nun iteriert werden, was auf eine Serie von Leiterdiagrammen führt. Die entsprechende Leitersumme für die effektive Wechselwirkung Γ, die in Gl. (5.9) vorkommt, sieht wie folgt aus

$$\begin{aligned} \langle\alpha_1,\beta_2|\Gamma_{\mathrm{L}}(\Omega)|\alpha_1',\beta_2'\rangle &= \langle\alpha_1\,\beta_2|V|\alpha_1'\,\beta_2'\rangle \\ &+ \frac{1}{4}\sum_{\epsilon\eta\theta\zeta}\langle\alpha_1\,\beta_2|V|\epsilon\,\eta\rangle g_{\mathrm{f}}^{\mathrm{II}}(\epsilon\,\eta,\theta\,\zeta;\Omega)\langle\theta,\zeta|\Gamma_{\mathrm{L}}(\Omega)|\alpha_1',\beta_2'\rangle. \end{aligned} \tag{5.12}$$

Die RPA Näherung für den im Kapitel (4) eingeführten Teilchen-Loch-Propagator (oder den Polarisationspropagator) Π bedeutet, dass nur der Term (5.10) berücksichtigt ist. Darüber hinaus führende Approximationen (Vertex-Korrekturen) ergeben sich durch die Mitnahme weiterer Terme in der Summe (5.11).

Wie oben erwähnt, g^{II} ist von größter Bedeutung für die (γ,2e) Reaktion. Wir merken weiterhin an, dass die Leiter-Entwicklung (5.11) für die Zweiteilchen-Greensfunktion ein wichtige Rolle in der Bestimmung der Selbstenergie Σ spielt [8, 30], die ihrerseits benötigt wird, um die Einteilchen-Greensfunktion mittels Gl. (5.7) herzuleiten. Auf der anderen Seite geht die Einteilchen-Greensfunktion in die Definition von g^{II} ein, wie aus Gln. (5.10,5.11) ersichtlich ist. Deshalb sollten im Prinzip die Dyson Gln. (5.7) und (5.11) für die Einteilchen- und Zweiteilchen-Greensfunktionen in selbst-konsistenter Weise gelöst werden.

Dieser Zusammenhang zwischen g und g^{II} verdeutlicht zugleich die Beziehung zwischen den Informationen, die man durch die (e,2e) und die (γ,2e) Experimente erhält:

Im Einteilchenfall haben wir die Beziehung der (e,2e)-Reaktionswahrscheinlichkeiten zu der spektralen Darstellung von g hervorgehoben. In gleicher Weise zeigt man anhand von Gl. (5.8) die Bedeutung von g^{II} für den (γ,2e)-Prozess, nämlich g^{II} besitzt Pole bei den (relativ zum Grundzustandsenergie gemessenen) Energien, die zur Addition $[E_n^{(N+2)} - E_0^{(N)}]$ bzw. Entnahme $[E_0^{(N)} - E_n^{(N-2)}]$ von zwei Teilchen vom Grundzustand korrespondieren. Die Residuen dieser Pole sind ein Maß für die messbaren spektroskopischen Faktoren der entsprechenden Prozesse [in (γ,2e)-Experimenten [36] werden zwei Elektronen aus dem System herausgeschlagen]. Dies zeigt, dass (γ,2e) und (e,2e) verschiedene Informationen liefern, die dennoch in der Weise miteinander verknüpft sind, wie g mit g^{II} verflochten ist.

5.3 Der Zweiteilchen-Photostrom

Die ersten $(\gamma, 2e)$-Experimente an Oberflächen wurden 1998 veröffentlicht [36]. Von theoretischer Sicht misst man in einem $(\gamma, 2e)$-Experiment einen Zwei-Photoelektronen-Strom $\mathcal{J}$, der durch Wellenvektoren $\mathbf{k}_1$ und $\mathbf{k}_2$ charakterisiert ist. $\mathcal{J}$ hat die From [37]

$$\mathcal{J} \propto \langle \mathbf{k}_1, \mathbf{k}_2 | g^{\mathrm{IIr}} \, \Delta \, S^{\mathrm{II}}_{\mathrm{hh}}(\mathbf{k}'_1, \mathbf{k}'_2, E) \, \Delta^\dagger \, g^{\mathrm{IIa}} | \mathbf{k}_1, \mathbf{k}_2 \rangle, \tag{5.13}$$

wobei Δ den Dipoloperator bezeichnet. $S^{\mathrm{II}}_{\mathrm{hh}}$ ist die Loch-Loch spektrale Funktion, während g^{IIa} (g^{IIr}) für die avancierte (retardierte) Zweiteilchen-Greensfunktion steht. Wie im Falle der einfachen Photoemission, der Photostrom kann durch ein Zweiteilchen-Caroli-Diagramm [37] repräsentiert werden, das keine Signatur einer Zeitordnung zeigt. Dies ist darauf zurückzuführen, dass die experimentelle Zeitauflösung (typischerweise 200 ns) viel länger als alle Zeitskalen im System ist, weswegen eine Zeitintegration notwendig wird, um Gl. (5.13) zu erhalten. Dies schließt den $(\gamma, 2e)$-Prozess als Mittel zur Untersuchung der zeit-abhängigen korrelierten Dynamik der Elektronen aus. Nichtdestotrotz erlaubt die$(\gamma, 2e)$-Methode eine gezielte Untersuchung der Effekte der Korrelationen im Anfangs- bzw. im Endzustand. Dies wird durch eine geeignete Wahl von $\mathbf{k}_{1/2}$ erreicht. Sind z.B. $\mathbf{k}_1$ und $\mathbf{k}_2$ sehr groß, verglichen mit dem Fermi Wellenvektor, so wird erwartet, dass die Endzustandskorrelation nur in einem Bereich des Phasenraums eine Rolle spielt, wo die zwei Photoelektronen mit fast gleicher Geschwindigkeit emittiert werden.

5.3.1 Praktische Implementierung für Metalloberflächen

Wie aus Gl. (5.13) hervorgeht ist die Berechnung von $g^{\rm II}$ ein wesentliches Element in der numerischen Realisierung von (5.13). Auf der anderen Seite haben wir in Kapitel (5.2) gezeigt, dass die Einteilchen-Greensfunktion g für die Bestimmung von $g^{\rm II}$ benötigt wird, und $g^{\rm II}$ bestimmt u.a. auch Σ und somit auch g. Bis jetzt ist es nicht gelungen diese selbst-konsistente Schleife im Rahmen einer realistischen Beschreibung der Oberfläche numerisch umzusetzen. Da aber die Eigenschaften des Targets das wesentliche Ziel der theoretischen und experimentellen Untersuchungen sind, werden wir g selbst-konsistent und präzise bestimmen. Mit Hilfe von g wird dann $g^{\rm II}$ durch eine Methode bestimmt, die wir im nächsten Abschnitt skizzieren.

5.3.2 Beschreibung der Einteilchen-Bandstruktur

Um $\mathcal{J}$ numerisch zu berechnen, gehen wir wie folgt vor: Wären die zwei Photoelektronen unabhängig, dann ergibt Gl. (5.11) für die Zweiteilchen -Greensfunktion $g^{\rm II}$ die vereinfachte Form $g^{\rm II} = g_{\rm f}^{\rm II}$. Das heißt, dass in diesem Fall, wie in der RPA-Näherung für Π, $g^{\rm II}$ sich zu einem anti-symmetrischen Produkt von Einteilchen-Greensfunktion $g_j(\mathbf{k}_i, E_i),\ i = 1, 2$ vereinfacht. Die Greensfunktion $g_j(\mathbf{k}_i, E_i),\ i = 1, 2$ (sowie den einfachen Photoelektronenstrom) berechnen wir mit Hilfe der Schicht-Korringa-Kohn-Rostoker-Methode (layer Korringa-Kohn-Rostoker method, LKKR) [2]. Dazu wird die Density-Funktional Theorie (DFT) [2] kombiniert mit einer semi-empirischen Funktion für den komplexen Anteil der Selbstenergie herangezogen.

Für die Implementierung der elektronischen Korrelation in der Berechnung von $\mathcal{J}$ machen wir uns das Wechselwirkungspotential U_{TF} zunutze, wobei die Zustandsdichte $N(\mu)$ mit Hilfe der (ab-initio) LKKR berechnet wird. Weiterhin schreiben wir um

$$U_{TF} = \frac{Z_1}{r_1} + \frac{Z_2}{r_2} \text{ with } Z_j = a_j^{-1}\, \exp\,(-\frac{2a_j}{\lambda} r_j),\ j = 1, 2, \tag{5.14}$$

wobei $a_j = r_{12}/(2r_j)$. Gl. (5.14) kann dahin gehend interpretiert werden, dass der Effekt der Elektron-Elektron-Wechselwirkung als eine Modifikation Z_j/r_j der Einteilchen-Potentiale angesehen werden kann. Die inner-elektronischen Korrelationen werden als eine dynamische nicht-lokale Abschirmung der Wechselwirkung w_j der Elektronen mit dem Kristall berücksichtigt. Das Verhalten der Abschirmfunktion ist durch die Funktionen Z_j bestimmt, die folgende Merkmale zeigen: Wenn die zwei Elektronen in die gleiche Richtung emittiert werden, wird das Potential w_j abstoßend, um der starken, kurz-reichweitigen Abstoßung der zwei Elektronen Rechnung zu tragen. Sind die zwei Elektronen weit von einander entfernt

($r_i \gg r_j,\ i \neq j \in [1,2]$), so kann man die Abschirmeffekte vernachlässigen. Für die numerische Berechnung der Zweiphotoelektronenstromes ist es notwendig, Z_j durch $\bar{Z}_j$ anzunähern, wobei $\bar{Z}_j = \bar{a}_j^{-1} \exp(-2\bar{a}_j r_j/\lambda)$ und $\bar{a}_j = k_{12}/(2k_j)$ sind. $\mathbf{k}_{12} = \mathbf{k}_1 - \mathbf{k}_2$ ist der relative Wellenvektor der zwei Photoelektronen. Mit dieser Abschirmung werden die Veränderungen $\bar{Z}_j/r_j$ zu den ursprünglichen Einteilchen-Potentialen w_j berücksichtigt und eine korrelierte Greensfunktion $\bar{g}_j$ generiert. Im Gegensatz zu g hängen die Funktionen $\bar{g}_j$ von den Wellenvektoren der *zwei* Elektronen, sowie von $\mathbf{k}_{12}$ ab. Als die Zweiteilchen-Greensfunktion wird $\bar{g}^{\mathrm{II}}$ benutzt, die sich aus dem anti-symmetrisierten, direkten Produkt der modifizierten Einteilchen-Greensfunktionen $\bar{g}_j$ ergibt [also der erste Term in der Leiterapproximation, Gl. (5.11)]. Diese Idee wurde auch mit beachtlichem Erfolg zur Berechnung der (e,2e)-Reaktionswahrscheinlichkeiten herangezogen [38, 39, 40].

5.3.3 Winkelabhängigkeit der Paar-Korrelationsfunktion

In diesem Abschnitt werden numerische Ergebnisse für die ($\gamma, 2e$)-Reaktion präsentiert. Die Diskussion konzentriert sich auf die Abbildung von Korrelationseffekten sowie auf die Unterschiede und Gemeinsamkeiten zur einfachen Photoemission (single photoemission, SPE). Der Einteilchen-Grundzustand der Probe wird zuerst durch eine selbst-konsistente lineare muffin-tin-Orbitalmethode (LMTO) behandelt, die auf der lokalen Dichtenäherung der Dichtefunktionaltheorie basiert. Darauf bauen die Rechnungen für den SPE-Prozess im Rahmen des Einstufenmodells der Photoemission auf. Die durch das elektromagnetische Feld des Photons induzierte Störung wird dabei im Rahmen der Dipolnäherung behandelt. Die numerischen Berechnungen des Photoelektronenstroms $\mathcal{J}_1$ und $\mathcal{J}_2$ erfolgen mittels der Schichtmethode nach Korringa-Kohn-Rostoker (layer-KKR), wie oben dargelegt ist.

Abbildung (5.1) veranschaulicht den entscheidenden Unterschied zwischen SPE und DPE: Abb. (5.1)(a) zeigt die gemessene Intensitätsverteilung des Photostroms eines Cu(001)-Kristalls als Funktion der zur Oberfläche parallelen Komponenten des Photoelektronenwellenvektors, der durch Energie und Austrittsrichtung bestimmt ist. Dass die Ergebnisse für $\mathcal{J}_1$ [Abb. (5.1)(b)] gut mit den gezeigten Experimenten übereinstimmen, weist darauf hin, dass der Einteilchenanteil des Problems adäquat beschrieben wird. Für die SPE [Abb. (5.1)(a,b)] sind Symmetrie und Struktur der Kristalloberfläche bestimmende Faktoren für das Photoelektronenspektrum. Wir vergleichen diesen Befund mit der Intensitätsverteilung in DPE, wobei die Energie und die Emissionswinkel eines Photoelektrons fixiert sind [markiert durch den weißen Punkt], und das zweite mit derselben Energie wie in SPE detektiert wird [Abb. (5.1)(c) und (d)]. Wird das fixierte Elektron in Richtung der Oberflächennormalen emittiert [Abb. (5.1)(c)], so haben die SPE- und die DPE-Impulsverteilung gleiche Symmetrieeigenschaften. Bei schräger Detektion jedoch [Abb. (5.1)(d)], wird die Symmetrie des Prozesses gebrochen. Im DPE-Prozess weist die Photoelektronenverteilung eine neuartige Struktur auf: ein um das fixierte Elektron zentriertes Loch [Abb. (5.1)(c) und (d)]. Dieses Coulomb-Korrelationsloch (CL) ist eine direkte Folge der Korrelationen der zwei Photoelektronen und ist nicht isotrop. Seine Form wird durch zwei Faktoren bestimmt: 1. Die Elektron-Elektron-Wechselwirkung und die Austauschwechselwirkung diktieren seine Symmetrie und verhindern, dass die zwei Elektronen mit gleichen Wellenvektoren innerhalb eines Gebiets emittiert werden, dessen Ausdehnung durch die Abschirmlänge gegeben ist. Deshalb ist die Ausdehnung des Loches ein qualitatives Maß für die Stärke der Wechselwirkung zweier Elektronen miteinander, die durch gegebene Wellenvektoren, Energien und Spins charakterisiert sind. 2. Sind die zwei Photoelektronen (im Impulsraum) weit voneinander getrennt, so ist die Korrelation dieser Elektronen schwach. Da der DPE-Prozess bei Abwesenheit elektronischer Korrelationen verboten ist, verschwindet das DPE-Signal in diesem Fall. Durch Kombination dieser beiden Effekte wird die Form der Verteilungen in Abb. (5.1)(c) und (d) nachvollziehbar. Hervorzuheben ist die Tatsache, dass die Ausdehnung des CL energieabhängig ist: Bei niedrigen Photoelektronenenergien ist sie groß und dominiert das Spektrum, während das CL bei höheren Energien nur in einer beschränkten Region sichtbar ist [vergl. Abb. (5.1)(d) und 2(b')]. Dieses Verhalten ergibt sich daraus, dass für schnelle Photoelektronen eine kleine Änderung der Emissionsrichtung mit einem großen relativen Impuls der Photoelektronen einhergeht, was wiederum die Elektron-Elektron-Wechselwirkung signifikant abschwächt. Die Abbildungen (1) und (2) veranschaulichen weitere Merkmale des DPE-Prozesses: 1. Die Form des CL ist stark von den Photoelektronenenergien abhängig, da das interelektronische Wechselwirkungspotential dynamisch in die Übergangsmatrixelemente eingeht. Die Photoelektronenbeugung, die im Falle der DPE von den elektronischen Korrelationen abhängt, tritt mit wachsender Energie der Photoelektronen stärker in Erscheinung. 2. Sowohl in Abb. (5.1) als auch in Abb. (5.2) beobachten wir in den DPE-Spektren eine schwache Reminiszenz zu den entsprechenden SPE-Spektren. Das läßt sich damit erklären, dass in einer groben Näherung der DPE-Photostrom durch die Selbstfaltung der Einteilchenzustandsdichten [density of states (DOS)] bestimmt ist, während in derselben Näherung der SPE-Photostrom durch die DOS selbst gegeben ist. Demzufolge erwarten wir in Regionen mit niedriger DOS geringe Emissionen von Photoelektronen in SPE und DPE. 3. Da in der DPE zwei Elektronen die Oberfläche verlassen müssen, ist zu erwar-

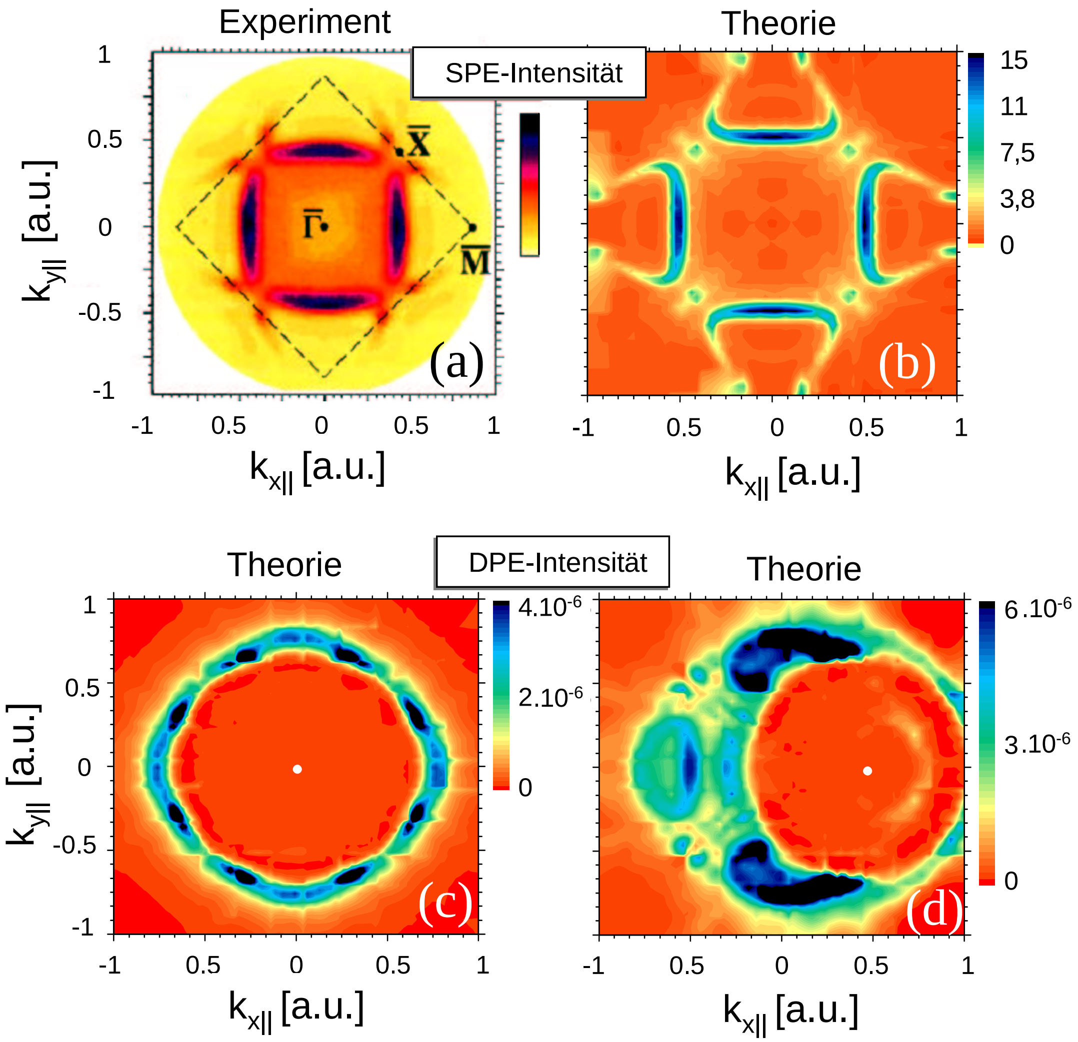

Abbildung 5.1: (a) Experimentelle Intensität der Einzelphotoelektronenemission [single photoemission (SPE)] vom Fermi-Niveau von Cu(001) als Funktion der oberflächenparallelen Komponenten $k_{x\|}, k_{y\|}$ des Photoelektronenwellenvektors. Die Photonenenergie ist ω = 21,2 eV. (b) Entsprechende theoretische Intensitäten für den Fall (a). Das unpolarisierte Licht fällt senkrecht zur Oberfläche ein. (c) Intensität der Doppelphotoemission für die gleiche Probe und für die gleichen Photoneneigenschaften wie in (a) und (b), und ω = 42,4 eV. Die zwei Photoelektronen haben identische Energien von 16 eV, jedoch sind Energie und Austrittsrichtung eines Photoelektrons festgehalten [markiert durch den weißen Punkt bei 0° in (c) und 30° Polarwinkel in (d)]. Die DPE-Intensität wird dann als Funktion der Oberflächenkomponente des Wellenvektors des zweiten Photoelektrons dargestellt.

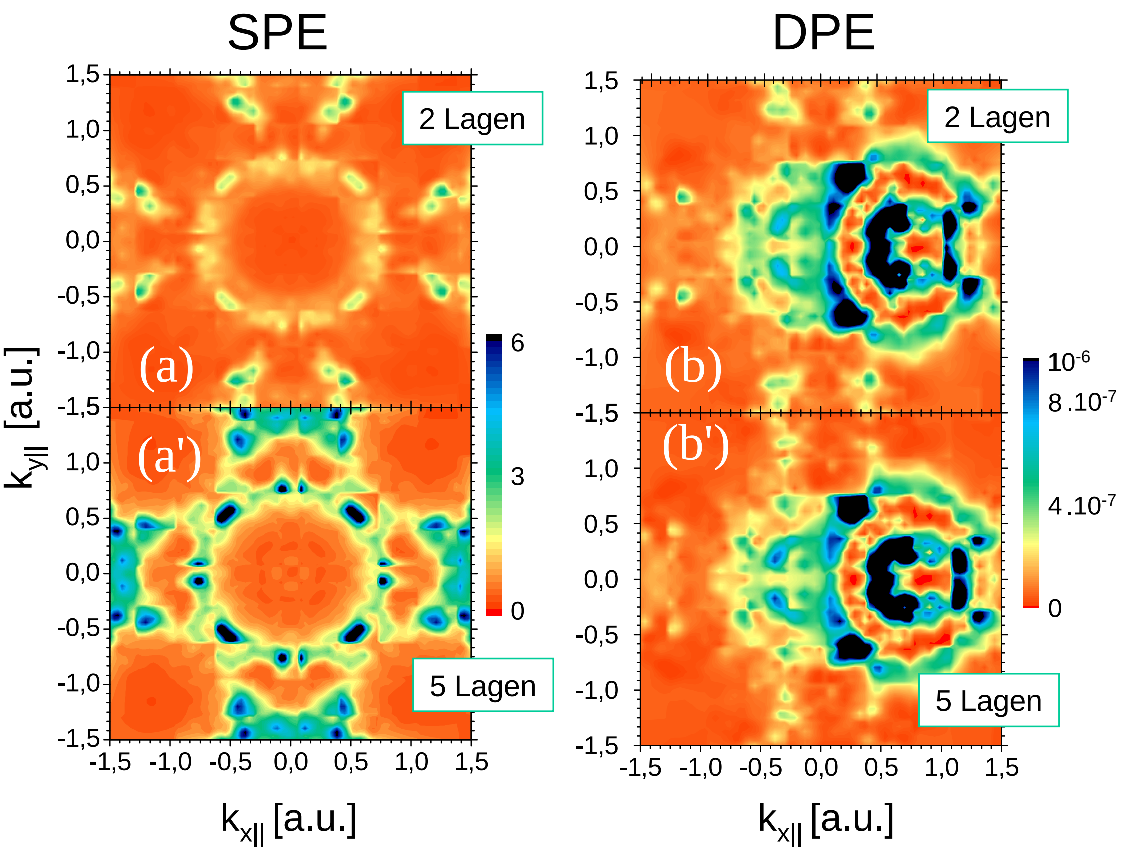

Abbildung 5.2: (a) Schichttiefenabhängigkeit der SPE- [(a) und (a')] und DPE- [(b) und (b')] Intensität für die Anordnung in Abb. (5.1)(d). Die Photoelektronenenergien betragen jeweils 30 eV. Die Photonenenergie beträgt ω = 35,2 eV für die SPE und ω = 70,4 eV für die DPE. Die Anteile der ersten zwei bzw. fünf Oberflächenschichten zum Photoelektronenstrom werden in (a) und (b) bzw. in (a') und(b') gezeigt.

ten, dass die DPE oberflächenempfindlicher ist als die SPE. Dieses läßt sich demonstrieren, indem die Anzahl der oberflächennahen Kristallschichten, die zum Photostrom beitragen, variiert wird [Abb. (2)]. In der DPE sind Form und Stärke des Photoelektronenstromes bereits durch die ersten zwei Oberflächenschichten bestimmt, während in der SPE auch die tieferen Schichten erheblich zum Photostrom beitragen.

5.3.4 Energieabhängigkeit der Paar-Korrelationsfunktion

Bei den bislang veröffentlichten DPE-Experimenten an Oberflächen werden die Emissionswinkel θ_1 und θ_2 der zwei Photoelektronen festgehalten und die Energien E_1 und E_2 der Photoelektronen variiert, d. h. man studiert die Energie-Korrelationsfunktionen. Die Abbildungen 3(a) und (b) decken deutliche Strukturen in den gemessenen und berechneten Energie-Korrelationen auf, deren Ursache die Elektronenbeugung ist. In Abb. (5.3)(b') ist der DPE-Photostrom für E_1 = E_2 , und θ_1=θ_2 als Funktion der Anzahl n der gebeugten Strahlen gezeigt, die in die Berechnungen einbezogen wurden: $\mathcal{J}_2$ verschwindet für abnehmendes n. Dieses Verhalten ist typisch für DPE von Atomen, wie in Abb. (5.3)(c) verdeutlicht wird. In Fall von Helium im Grundzustand fehlt die Elektronenpaarbeugung und nur ein einziges (Zweiteilchen-) Niveau, nämlich He(1Se), trägt zur DPE bei. Der Wirkungsquerschnitt von He verschwindet, wenn der Schwerpunktimpuls des Elektronenpaars senkrecht zum elektrischen Feld des Photons steht [das ist genau der Fall bei E_1 = E_2 in Abb. (5.3)(c)]. Ein weiterer wesentlicher Unterschied zwischen DPE von atomaren und molekularen Systemen im Vergleich zu DPE von Oberflächen ist die unterschiedliche elektronische Struktur der Probe. Wenn die Photonenenergie ω und die Elektronenpaarenergie $E = E_1$ + E_2 festgehalten sind, ist die Anfangsenergie $\epsilon = \omega - E$ des emittierten Elektronenpaars eindeutig bestimmt. Somit stammt das in Abb. (5.3)(c) gezeigte Spektrum für He von einem einzigen atomaren Niveau. Im Gegensatz dazu hängt bei Oberflächen die elektronische Struktur nicht nur von der Energie ϵ ab, sondern auch von den Bloch'schen Wellenvektoren der Elektronen. Wird in Abb. (5.3) die Energieverteilung (E_1 - $E_2)/E$ (bei fester Energie E) variiert, so ändern sich diese, und somit entstammen die Photoelektronen aus verschiedenen Anfangszuständen, die sich in ausgeprägten Strukturen in den DPE-Spektren manifestieren.

5.4 Aspekte der korrelierten Zweielektronen-Emission induziert bei Elektronenstoß

Neben der $(\gamma, 2e)$ hat sich die $(e, 2e)$-Spektroskopie als nützliches Mittel zur Untersuchung der elektronischen Korrelationen erwiesen [41]. In diesem Fall werden zwei Elektronen gleichzeitig nachgewiesen, die nach dem Beschuß mit nieder-energetischen Elektronen von einer Oberfläche emittiert werden. In jüngster Zeit wurden eine Reihe von Materialien mit dieser Methode untersucht [42, 43, 44, 45, 46, 47, 48, 49, 50, 51, 52, 53, 54]. In diesem Abschnitt werden wir auf die wesentlichen Aspekte der $(e, 2e)$-Theorie eingehen.

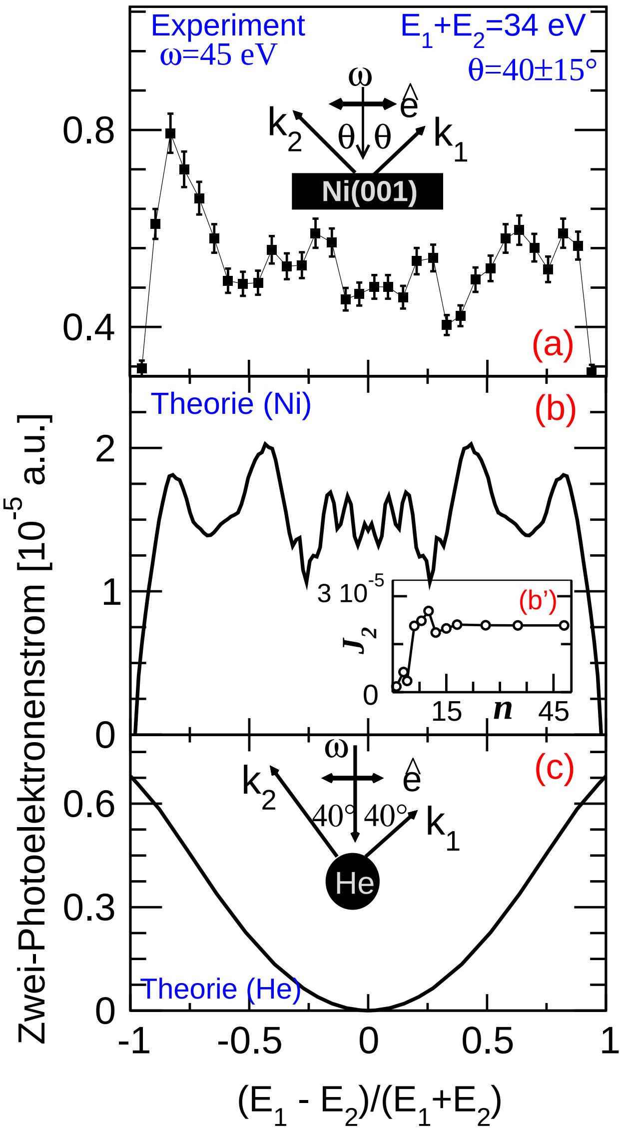

Abbildung 5.3: (a) Gemessene Energie-Korrelation zwischen zwei Photoelektronen, die in einem DPE-Prozess von Ni(001) emittiert werden. Die Wellenvektoren $\mathbf{k}_1$ und $\mathbf{k}_2$ der zwei Photoelektronen und der Feldvektor des linear polarisierten Lichts sind koplanar (siehe graphische Darstellung). Die Gesamtenergie des Elektronenpaars $E = E_1 + E_2$ =34 eV ist festgehalten, wobei ω = 45 eV. Der DPE-Photoelektronenstrom wird als Funktion von $(E_1 - E_2)/E$ aufgenommen. Die zwei Elektronendetektoren mit Winkelauflösung von 15° liegen an äquivalenten Positionen (40° bzgl. der Oberflächennormale). (b) Theoretische Ergebnisse für den Fall (a). Die Grafik (b') in (b) verdeutlicht die Abhängigkeit des DPE-Stromes $\mathcal{J}_2$ (bei $E_1 = E_2$) bzgl. der Anzahl n der gebeugten Strahlen, die in die Rechnung einbezogen wurden. (c) zeigt $\mathcal{J}_2$ in der entsprechenden Situation zu (a) und (b) für E = 34 eV, wenn anstelle von Ni(001) atomares Helium als Probe verwendet wird. Um die Doppelionisationsschwelle von He auszugleichen, wird ω angepasst.

Im Eingangskanal betrachten wir zwei Elektronen, ein einfallendes Elektron (1) und ein Valenzelektron (2). Die zwei Vakuum Elektronen im Endkanal werden mit (3) und (4) bezeichnet. Der Anfangszustand ist ein antisymmetrisiertes Produkt $\Big\langle\, 1,2 \,\Big| = \Big\langle\, 1 \,\Big| \otimes \Big\langle\, 2 \,\Big|$ von zwei LEED-Zuständen $\Big\langle\, 1 \,\Big|$ und $\Big\langle\, 2 \,\Big|$ (low-energy electron-diffraction state), jeder von denen beschreibt die Bewegung eines Elektrons mit Quantenzahlen $(E_j, k_{j,\|}, \sigma_j),\ j = 1-4$. E_j und $k_{j,\|}$ sind die Energien sowie die zur Oberfläche parallelen Wellenvektoren der Elektronen. σ_j charakterisiert den Spinzustand. Der korrelierte Endzustand $\Big\langle\, 3,4 \,\Big|_c$ der Elektronen (3) und (4) wird in der gleichen Weise hergeleitet, wie dies im Falle von $(\gamma, 2e)$ in Abschnitt (5.3.1) erklärt wurde. Eine Vernachlässigung der Korrelation bedeutet, dass man in Gl. (5.14) $U_{TF} \equiv 0$ setzt. In diesem Fall ist $\Big\langle\, 3,4 \,\Big|_c \approx \Big\langle\, 3,4 \,\Big| = \Big\langle\, 3 \,\Big| \otimes \Big\langle\, 4 \,\Big|$. Die Übergangsamplitude für die $(e, 2e)$-Reaktion ergibt sich aus Termen der Form

$$\Big\langle\, 3,4 \,\Big|_c U_{TF} \Big|\, 1 \,\Big\rangle \Im g_2^r \Big\langle\, 1 \,\Big| U_{TF} \Big|\, 3,4 \,\Big\rangle_c ,$$

wobei g_2^r die retardierte Einteilchen-Greensfunktion ist, die, wie im Falle von $(\gamma, 2e)$, mit Hilfe von DFT-LDA und LMTO hergeleitet werden kann. Die LEED-Zustände werden mit Hilfe von LKKR berechnet.

Abb. (5.4) zeigt ein typisches Beispiel der Spektren, die man in einem $(e, 2e)$ erhält. Die Emissionsrichtungen der zwei Elektronen sind durch eine gewählte Position der Detektoren im Raum festgehalten. Man variiert dann für eine feste Einschußenergie die Energien E_3 und E_4 der zwei auslaufenden Elektronen. Der Vergleich mit dem Experiment zeigt, dass die elektronische Korrelation dazu führt, dass die Elektonen vorzugsweise mit gleicher Energie emittiert werden. Weiterhin wird die Emission von nieder-energetischen Elektronen unterdrückt. Dies liegt daran, dass die Abstoßung innerhalb des Elektronenpaares mit sinkenden Energien $E_{3/4}$ stärker wird. Dieser Effekt wird, im Gegensatz zum unkorrelierten Fall [Abb. (5.4)a], durch den Zustand $\Big\langle\, 3,4 \,\Big|_c$ richtig erfaßt [Abb. (5.4)b], wie der Vergleich mit den experimentellen Daten [Abb. (5.4)c] belegt.

In Fig.(5.4) haben wir die spin-gemittelte Energie-Paar-Korrelation untersucht. In diesem Zusammenhang sei es erwähnt, dass die Auflösung des Spin-Zustands der Vakuumelektronen bzw. die Benutzung von Ferromagneten einen Einblick in die Spin-Paar-Koorelationen erlaubt, sowie eine analytische Methode zur Untersuchung von magnetischen Eigenschaften von Oberflächen bietet. Dies wurde in den Arbeiten [46, 52, 55] ausführlich diskutiert.

Weiterhin wurde gezeigt [54], dass sich die (e,2e)-Methode besonders eignet, die elektronischen Eigenschaften von Legierungen und ungeordneten Oberflächen zu untersuchen.

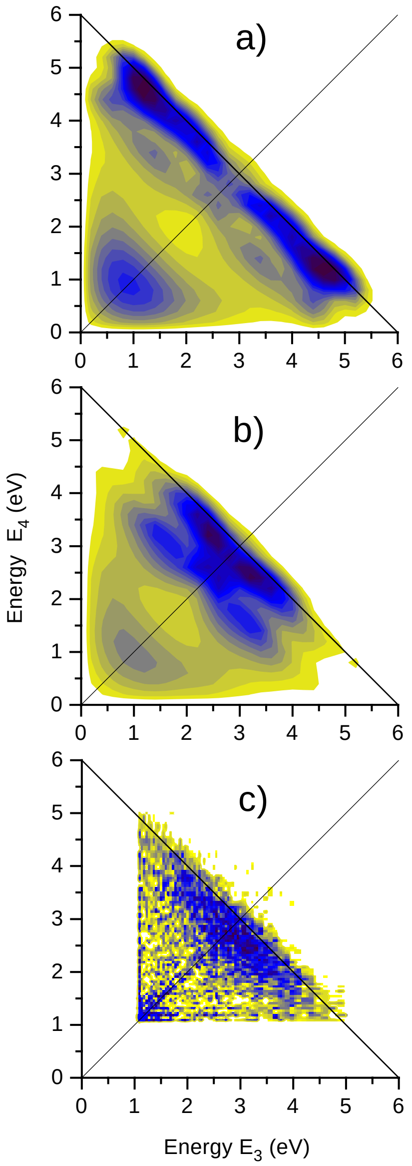

Abbildung 5.4: Die Energie-Korrelation der theoretisch berechneten Intensität für die Emission von zwei korrelierten Elektronen aus einer W(001) Oberfläche nach dem Beschuß mit Elektronen der Energie 10.6 eV. Die Einfallsrichtung des Projektils ist entlang der $z-$Richtung, die senkrecht zur Oberfläche gewählt ist. Die Richtung [100] definiert die $x-$Richtung. Die zwei emittierten Elektronen sind in der $(z-x)$ Ebene nachgewiesen. Der Emissionswinkel dieser Elektronen beträgt jeweils 40° bzgl. der $z-$Achse, wobei der Zwischenwinkel 80° ist. Die Abbildung zeigt die Resultate ohne (Teil a) und mit (Teil b) Berücksichtigung der Coulomb-Korrelation, wie diese durch Gl. (5.14) beschrieben ist. Teil (c) der Abbildung zeigt die entsprechenden Experimente. Die konträr-diagonalen Linie ist die Bindungsenergie des Valenzelektrons E_F. Entlang der eingezeichneten Diagonalen haben die zwei emittierten Elektronen die gleichen Energien.

6 Zusammenfassung und Ausblick

Ziel dieser Arbeit ist die Entwicklung und die Anwendung theoretischer Konzepte zur Behandlung von Anregungsprozessen in korrelierten, nicht-relativistischen N-Teilchen-Systemen. Für Wenigteilchen-Systeme wurde ein Verfahren zur Herleitung von korrelierten N-Teilchen-Wellenfunktionen vorgeschlagen und diskutiert.
Einen allgemeineren Zugang bietet die kumulative Greensfunktionsmethode, die in der Lage ist, dynamische und thermodynamischen Eigenschaften korrelierter Systeme zu untersuchen. Desweiteren wurde im Rahmen der *random-phase approximation* auf die Rolle kollektiver Antwort in endlichen Systemen eingegangen. Insbesondere wurde gezeigt, dass die durch Dichte-Fluktuationen verursachte Abschirmung einer äußeren Störung eine dominante Rolle bei Anregungsprozessen in großen Molekülen und Metallclustern spielt.
Für die theoretische Beschreibung von Mehrteilchen-Anregungen in einem ausgedehnten System wurde die Greensfunktionstheorie in der Feld-theoretischen Formulierung herangezogen. Ein Hauptaugenmerk galt der spektralen Eigenschaften der Einteilchen- und Zweiteilchen-Greensfunktionen sowie deren Verbindung zu der einfachen und zweifachen Teilchenemission. Weiterhin wurden Methoden zur numerischen Berechnung dieser Greensfunktionen im Rahmen der Dichte-Funktional-Theorie aufgezeigt und diskutiert.

Als Anwendung haben wir die einfache Ionisation in Fullerenen und Metallclustern betrachtet. Diese Arbeit wird z.Z. auf die mehrfache Ionisation verallgemeinert, um Einblicke in die elektronischen Korrelationen in diesen Systemen zu gewinnen. Weiterhin, haben wir gezeigt, wie die Energie- und Winkelabhängigkeit der Paar-Korrelationsfunktionen in Kupfer, Nickel und Wolfram mit Hilfe der hier entworfenen Techniken visualisiert werden können. Ziel laufender sowie zukünkftiger Projekte ist die Untersuchung von Mischkomplexen, in denen physikalische Eigenschaften endlicher und ausgedehnter Systeme zusammenwirken, wie z.B. von an Oberflächen adsorbierten Molekülen und Legierungen [54].

Literaturverzeichnis

[1] Pines, D. 1953, Phys. Rev., 92, 626; Abrahams, E. 1954, Phys. Rev., 95, 839; Pines, D., Nozieres, P. 1966, *The Theory of Quantum Liquids*, (Addison-Wesley, Reading, MA), und die darin enthaltenen Referenzen.

[2] Gonis, A. 2000, *Theoretical materials science: tracing the electronic origins of materials behavior*, (Warrendale, Materials Research Society).

[3] Fetter, A. L., Walecka J. D. 1971, *Quantum theory of many-particle systems*, (New York, McGraw-Hill).

[4] Lindgren, I., Morrison J. 1982, *Atomic Many-Body Theory* (Springer Verlag, Berlin).

[5] Fulde, P. 1991,*Electron Correlation in Molecules and Solids*, Springer Series in Solid-State Sciences, Vol. 100, (Springer Verlag, Berlin, Heidelberg, New York).

[6] Turek, I., Drchal, V., Kudrnovský, J., Šob, M., Weinberger, P. 1997, *Electronic Structure of Disordered Alloys, Surfaces, and Interfaces*, (Kluwer Academic Pub., Boston, London, Dordrecht).

[7] Mahan G. D. 1993, *Many-Particle Physics*, second ed., (Plenum Press, London).

[8] Abrikosov A. A., Korkov L. P., Dzyaloshinski I. E. 1975, *Methods of Quantum Field Theory in Statistical Physics*, (Dover).

[9] Ruhl E., *et al.* 1992, Chem. Phys. Lett., 191, 430,

[10] Berakdar, J. 1996, Phys. Lett. A, 220, 237.

[11] Malcherek, A. W., Rost J.-M., Briggs, J. S. 1997, Phys. Rev. A, 55, R3979.

[12] Dreizler, R. M., Gross, E. K. U. 1990, *Density Functional Theory* (Springer Verlag, Berlin, Heidelberg, New York).

[13] Berakdar, J. 1996, Phys. Rev. A, 55, 1994.

[14] Berakdar, J. 2000, Phys. Rev. Lett., 85, 4036.

[15] Lippmann, B. A. 1956, Phys. Rev., 102, 264.

[16] Foldy, L.L., Tobocman, W. 1957, Phys. Rev., 105, 1099.

[17] Faddeev, L.D. 1961, Soviet Phys. JETP 12, 1014.

[18] Faddeev, L.D. 1965, *Mathematical Aspects of the Three-Body Problem* (Davey, New York).

[19] Yang, C.N., Lee, T.D. 1952 Phys. Rev., 97, 404; 1952, *ibid*, 87, 410 .

[20] Barber, M.N. 1983, *Phase Transitions and Critical Phenomena*, eds. Domb, C., Lebowity, J.L., pp. 145-266.

[21] Grossmann, S., Rosenhauer, W. 1967, Z. Phys., 207, 138; 1969, *ibid*, 218, 437.

[22] Hedin, L. 1999, J. Phys. C, 11, R489.

[23] Berakdar, J., Kidun, O., Ernst, A. 2002, in *Correlations, Polarization, and Ionization in Atomic Systems*, eds. D. H. Madison, M. Schulz (AIP, Melville, New York), pp. 64-69.

[24] Matt, S. *et al.* 1996, J. Chem. Phys., 105, 1880.

[25] Foltin V. *et al.* 1998, Chem. Phys. Lett., 289, 181.

[26] Keller, S., Engel, E. 1999, Chem. Phys. Lett., 299, 165.

[27] Keller, S. 2001, Eur. Phys. J. D, 13, 51.

[28] Kidun, O., Berakdar, J. 2001, Phys. Rev. Lett., 87, 263401.

[29] Brueckner, K.A. 1955, Phys. Rev., 97, 1353; Bethe, H.A. 1971, Ann. Rev. Nucl. Sci., 21, 93; Jeukenne, J.P., Legeunne, A., Mahaux, C. 1976, Physics Reports, 25, 83.

[30] Migdal, A. B. 1967, *Theory of finite Fermi Systems*, New York.

[31] Martin, P. C., Schwinger, J. 1959, Phys. Rev., 115, 1342.

[32] Lehmann, H. 1954, Nuovo Cimento A, 11, 342.

[33] Weigold, E., McCarthy, I. E. 1999, *Electron Momentum Spectroscopy* (Kluwer Academic/Plenum Publishers).

[34] Kevan, S. D. (Ed.) 1992, *Angle-Resolved Photoemission: Theory and Current Application*, Studies in Oberfläche Science and Catalysis (Elsevier Science).

[35] Hüfner, S. 1995, *Photoelectron Spectroscopy*, No. 82 in Springer Series in Solid-State Science, (Spinger Verlag, Berlin).

[36] Herrmann, R. *et al.* 1998, Phys. Rev. Lett., 81, 2148; 1999, J. Phys. (Paris) IV, 9, 127.

[37] Fominykh, N.,*et al.* 2000, Solid State Commun., 113, 665.

[38] Berakdar, J., Gollisch, H., Feder R. 1999, Solid State Commun. , 112, 587.

[39] Fominykh, N., *et al.* 2001, in *Many-particle spectroscopy of Atoms, Molecules, Clusters and Surfaces*,
Eds. Berakdar J., Kirschner J., (Kluwer Acad/Plenum Pub.).

[40] Fominykh, N., Berakdar, J., Henk, J., Bruno, P. 2002, Phys. Rev. Lett., 89, 086402-1.

[41] Berakdar, J., Kirschner, J. 2001, (Eds.) *Many-particle spectroscopy of Atoms, Molecules, Clusters and Surfaces,*
(Kluwer Acad/Plenum Pub., New York).

[42] Coplan, M. A., Moore, J. H., Doering, J. P. 1994, Rev. Mod. Phys., 66, 985.

[43] Iacobucci, S., Marassi, L., Camilloni, R., Nannarone, S., Stefani, G. 1995, Phys. Rev. B, **51**, 10252.

[44] Vos, M., McCarthy, I. E. 1995 Rev. Mod. Phys., 67, 713.

[45] Artamonov, O. M., Samarin, S. N., Kirschner, J. 1997, Applied Physics A, A65, 535.

[46] Berakdar, J., Samarin, S. N., Herrmann, R. Kirschner, J. 1998, Phys. Rev. Lett., 81, 3535.

[47] Feder, R., Gollisch, H., Meinert, D., Scheunemann, T., Artamonov, O. M., Samarin, S. N., Kirschner, J. 1998 *Phys. Rev. B*, 58, 16418.

[48] Kheifets, A. S., Iacobucci, S., Ruocco, A., Camiloni, R., Stefani, G. 1998, Phys. Rev. B, 57, 7360.

[49] Gollisch, H., Scheunemann, T., Feder, R. 2001, Solid State Commun., 117(12), 691.

[50] Weigold, E., Vos, M. 2001, *Many Particle Spectroscopy of Atoms, Molecules, Clusters, and Surfaces* eds. Berakdar, J., Kirschner, J., (New York: Kluwer Academic/Plenum Publishers), p 417.

[51] Berakdar, J., Das, M. P. 1997, *Phys. Rev. A*, 56, 1403.

[52] Morozov, A., Berakdar, J., Samarin, S. N., Hillebrecht, F. U., Kirschner, J. 2002, Phys. Rev. B, 65, 104425.

[53] Canney, S. A., Vos, M., Kheifets, A. S., Guo, X., McCarthy, I. E., Weigold, E. 1997, Surf. Sci., 382(1-3), 241.

[54] Kouzakov, K. A., Berakdar, J. 2002, Phys. Rev. B, *to be published*

[55] Berakdar, J. 1999, Phys. Rev. Lett., 83, 5150-5153.

7 Auswahl eigener Arbeiten als Anhang

Die beigefügten Arbeiten behandeln folgende Themen:

7.1 Theoretische Behandlung korrelierter Systeme mit endlicher Teilchenzahl

- *Correlated scattering states of N-body Coulomb systems*
  J. Berakdar
  Phys. Rev. A 55, 1994 (1997)

- *Energy-exchange effects in few-particle Coulomb scattering*
  J. Berakdar
  Phys. Rev. Letters 78, 2712 (1997)

- *Asymmetric formation of of the positronium continuum states following positron-impact ionization of H_2*
  J. Berakdar
  Phys. Rev. Letters 81, 1393 (1998)

- *Cluster expansion of the many-body Green operator*
  J. Berakdar
  Physics Letters A 277, 35-41 (2000)

- *Scattering path formalism for the propagation of interacting compounds in ordered and disordered materials*
  J. Berakdar
  Surface Reviews and Letters 7, 205-210 (2000)

- *Incremental approach to strongly correlated many-body finite systems*
  J. Berakdar
  Phys. Rev. Letters 85, 4036-4039 (2000)

7.2 Kollektive Antwort endlicher Systeme auf äußere Störungen

- *Manifestation of charge density fluctuations in metal clusters: Suppression of the ionization channel*
  O. Kidun, J. Berakdar
  Phys. Rev. Letters 87, 263401-263404 (2001)

- *Excitation spectra of free fulleren clusters*
  O. Kidun, J. Berakdar
  Surf. Science 507-510) 662-665 (2002)

7.3 Zweiteilchen-Anregung von Oberflächen

- *Manifestations of electronic correlations in the diffraction of electron pairs from crystals*
  J. Berakdar, S.N. Samarin, R. Herrmann, J. Kirschner
  Phys. Rev. Letters 81, 3535 (1998)

- *Pair correlation in two-electron emission from surfaces*
  J. Berakdar, H. Gollisch, R. Feder
  Solid-State Communications 112, 587-591 (1999)

7.4 Spektroskopie der Spin-Korrelationen in Ferromagneten

- *Probing the spin polarization in ferromagnets*
  J. Berakdar
  Phys. Rev. Letters 83, 5150-5153 (1999)

- *Visualizing spin dependent electronic collisions in ferromagnets*
  S. N. Samarin, J. Berakdar, O. Artamonov, J. Kirschner
  Phys. Rev. Letters 85, 1746-1749 (2000)

- *Spin-correlation imaging of electrons in ferromagnets*
  A. Morozov, J. Berakdar, S. N. Samarin, F. U. Hillebrecht, J. Kirschner
  Phys. Rev. B 65, 104425 (2002)

7.5 Die Abbildung elektronischer Korrelationen in Festkörpern mittels der Photo-doppelemission

- *Emission of correlated electron pairs following single-photon absorption by solids and surfaces*
  J. Berakdar
  Phys. Rev. B 58, 9808 (1998)
- *The theory of two-electron photoemission from surfaces*
  N. Fominykh, J. Henk, J. Berakdar, P. Bruno, H. Gollisch, R. Feder
  Solid-State Communications 113, 665-669 (2000)

- *Spectroscopy of the electron-electron interaction in solids*
  N. Fominykh, J. Berakdar, J. Henk, P. Bruno
  Phys. Rev. Letters 89, 086402- 086408 (2002)
- *Double Photoemission from the Surface State of Cu(111)*
  N. Fominykh, J. Henk, J. Berakdar, P. Bruno
  Surf. Science 507-510, 229-233 (2002)

PHYSICAL REVIEW A VOLUME 55, NUMBER 3 MARCH 1997

Correlated scattering states of N-body Coulomb systems

Jamal Berakdar
Atomic and Molecular Physics Laboratories, Research School of Physical Sciences and Engineering, Australian National University, Canberra, Australian Capital Territory 0200, Australia

(Received 8 July 1996)

For N charged particles of equal masses moving in the field of a heavy residual charge, an approximate analytical solution of the many-body time-independent Schrödinger equation is derived at a total energy above the complete fragmentation threshold. All continuum particles are treated on equal footing. The proposed correlated wave function represents, to leading order, an exact solution of the many-body Schrödinger equation in the asymptotic region defined by large interparticle separations. Thus, in this asymptotic region the N-body Coulomb modifications to the plane-wave motion of free particles are rigorously estimated. It is shown that the Kato cusp conditions are satisfied by the derived wave function at all two-body coalescence points. An expression of the normalization of this wave function is also given. To render possible the calculations of scattering amplitudes for transitions leading to a four-body scattering state, an effective-charge method is suggested in which the correlations between the continuum particles are completely subsumed into effective interactions with the residual charge. Analytical expressions for these effective interactions are derived and discussed for physical situations. [S1050-2947(97)01103-7]

PACS number(s): 34.80.Dp, 34.10.+x, 25.10.+s

I. INTRODUCTION

Many-body Coulomb scattering states arise in various fundamental reactions in atomic and molecular physics. Although the Coulomb interactions governing the motion of charged particles possess a simple analytical dependence, the theoretical treatment of Coulomb scattering states is a challenging task even in the asymptotic region. The main difficulties in the theoretical description of such states arise from the infinite-range behavior of the Coulomb interaction. This is already revealed in the exactly solvable two-body (Kepler) problem in which case the asymptotic free motion in the relative coordinate is modified by the notorious Coulomb phase. For the three-body system the theoretical treatment is much more involved due to the nonseparability of the many-body Schrödinger equation. Asymptotic states for the three-body problem have been reported at large interparticle separations [1–4]. Only recently [5,6] have asymptotic three-body scattering states been derived that are valid in the entire asymptotic region defined by large hyperradius. The introduction of coupling between individual two-body subsystems (in the form of local relative momenta in Ref. [5] and local Sommerfeld parameters in the case of Ref. [6]) in deriving these asymptotic states underlines the complexity in the theoretical descriptions of Coulomb systems in the continuum. For systems with more than three particles in the continuum only little is known. Employing hyperspherical coordinates in the $3N$-configuration space, Peterkop [2] has derived an estimate of the Coulomb phase modification to an outgoing $(3N-1)$-dimensional spherical free wave of N electrons receding from a massive nucleus. The Coulomb phase modifications to the asymptotic plane-wave motion of the individual N electrons as well as the propagation of such asymptotic scattering states to finite distances have not been given. Due to unpublished work by Redmond, an expression for the Coulomb distortions of the asymptotic plane-wave relative motions in N-body Coulomb scattering systems has been reported in Ref. [1], however, without derivation.

In this work we derive an approximate analytical expression for the solution of the non-relativistic, time-independent Schrödinger equation of N charged particles moving in the field of a residual ion. The total energy of the system is assumed to be above the complete breakup threshold. The study is restricted to continuum particles with comparable masses and, with respect to these masses, a very heavy mass of the residual charge so that mass-polarization terms can be neglected and the center-of-mass motion can be separated out in a relative-coordinate frame of reference. The wave function is determined by separately solving for the N-independent Coulomb particle motion in the residual ion field and the correlated motion between the continuum particles with disregard of the residual-charge field. These two solutions are then subsequently coupled by an arbitrary function that is determined from the Schrödinger equation of the system. The derived correlated N-body wave function coincides with known expressions [4,6–8] in the case of three-body system and, for a two-body system, with the exact two-body Coulomb wave function. It is shown that the proposed wave function constitutes an exact solution of the many-body problem in the asymptotic region of large interparticle distances. In this region the asymptotic expression of the derived wave function tends to the asymptotic form suggested in Ref. [1], hence providing the proof for this suggestion. In addition, the normalization of the proposed wave function is derived by requiring that the total flux, generated by the wave function derived here, through a large multidimensional manifold defined by large, but constant, interparticle separations should be the same as the flux due to normalized N plane waves of the receding particles.

The inclusion of the correlations between the continuum particles presents an obstacle in actual calculations of scattering amplitudes using the derived wave function since in this case a $3N$-dimensional integral has to be evaluated. The reactions for which such Coulomb scattering amplitudes are currently needed are the double ionization of atomic systems upon charged particle impact and the electron-impact single ionization of atomic inner shells followed by an Auger decay [9]. Both of these processes lead to a four-body Coulomb continuum states in the final channel. Measurements of such reactions have already been performed [10–14,16,15]. In light of the absence of theoretical descriptions under situations where the four-body problem cannot be reduced to three-body one using the Born approximation, it appears timely to investigate methods of simplifying the proposed wave function such that reaction cross sections can be calculated. In a method proposed in Ref. [17] the correlations between the continuum particles are taken into account as an effective interaction between the continuum particles and the nucleus. However, as shown below, the effective product charges given by the method of Ref. [17] exhibit some undesirable features. Therefore, maintaining the philosophy of effective charges, an alternative set of effective product charges is derived by requiring that the many-body wave function constructed by this method should analytically match the known solution of the many-body Schrödinger equation in some limiting cases. The derived product charges are then well behaved. Properties of the proposed effective product charges are discussed in the case of positron-impact double ionization of He($^1S^e$) . Using the method developed in this work, pilot calculations for the multiple differential cross sections of the electron- and positron-impact double ionization of He($^1S^e$) have already been reported [18].

The plan of the paper is as follows. In Sec. II, after formulating the theoretical framework, the correlated many-body wave function is derived and the asymptotic behavior of the Schrödinger equation is investigated. In Sec. III the proposed wave function is shown to satisfy the Kato cups conditions [19] at all $N(N-1)/2$ two-body collision points. Section IV deals with the normalization of the derived wave function, whereas in Sec. V the method is applied to the four-body Coulomb continuum problem. To render possible the calculations of scattering amplitudes, the proposed wave functions is simplified using a method based on the effective-product-charge method. Conclusions are drawn in Sec. VI. Atomic units are used throughout.

II. FORMULATION OF THE PROBLEM AND ASYMPTOTIC SCATTERING STATES

We consider N charged particles of equal masses m and with charges Z_j, $j\in[1,N]$ moving in the field of a residual charge Z. The mass M of the charge Z is assumed to be much larger than m ($M\gg m$). In this work only continuum states are considered, i.e., the total energy E of the system is larger than the complete fragmentation-threshold energy. Neglecting terms of the orders m/M, the center-of-mass system and the laboratory frame of reference can be chosen to be identical. The nonrelativistic time-independent Schrödinger equation of the N-body system can then be formulated in the relative-coordinate representation as

$$\left[H_0+\sum_{j=1}^{N}\frac{ZZ_j}{r_j}+\sum_{\substack{i,j\\ j>i=1}}^{N}\frac{Z_iZ_j}{r_{ij}}-E\right]\Psi(\mathbf{r}_1,\ldots,\mathbf{r}_N)=0, \tag{1}$$

where $\mathbf{r}_j$ is the position of particle j with respect to the residual charge Z and $\mathbf{r}_{ij}:=\mathbf{r}_i-\mathbf{r}_j$ denotes the relative coordinate between particles i and j. The kinetic-energy operator H_0 has the form (in the limit $m/M\to 0$) $H_0=-\sum_{L=1}^{N}\Delta_L/2m$, where Δ_L is the Laplacian with respect to the coordinate $\mathbf{r}_L$. We note here that for a system of general masses the problem is complicated by an additional mass-polarization term that arises in Eq. (1). Upon introduction of N-body Jacobi coordinates, H_0 becomes diagonal; however, the potential terms acquire a much more complex form. Assuming the continuum particles to escape with relative asymptotic momenta $\mathbf{k}_j$ (with respect to the charge Z), it has been suggested in Ref. [1], due to unpublished work by Redmond, that for large interparticle distances the wave function $\Psi(\mathbf{r}_1,\ldots,\mathbf{r}_N)$ takes on the form

$$\lim_{\substack{r_{lm}\to\infty\\ r_n\to\infty}}\Psi(\mathbf{r}_1,\ldots,\mathbf{r}_N)\to(2\pi)^{-3N/2}\prod_{s=1}^{N}\xi_s(\mathbf{r}_s)\psi_s(\mathbf{r}_s)$$

$$\times\prod_{\substack{i,j=1\\ j>i}}^{N}\psi_{ij}(\mathbf{r}_{ij})$$

$$\forall l,m,n\in[1,N];\quad m>l, \tag{2}$$

where the functions $\xi_j(\mathbf{r}_j),\psi_j(\mathbf{r}_j),\psi_{ij}(\mathbf{r}_{ij})$ are defined as

$$\xi_j(\mathbf{r}_j):=\exp(i\mathbf{k}_j\cdot\mathbf{r}_j), \tag{3}$$

$$\psi_j(\mathbf{r}_j):=\exp[\mp i\alpha_j\ln(k_jr_j\pm\mathbf{k}_j\cdot\mathbf{r}_j)], \tag{4}$$

$$\psi_{ij}(\mathbf{r}_{ij}):=\exp[\mp i\alpha_{ij}\ln(k_{ij}r_{ij}\pm\mathbf{k}_{ij}\cdot\mathbf{r}_{ij})]\ . \tag{5}$$

The $+$ and $-$ signs refer to outgoing and incoming boundary conditions, respectively, and $\mathbf{k}_{ij}$ is the momentum conjugate to $\mathbf{r}_{ij}$, i.e., $\mathbf{k}_{ij}:=(\mathbf{k}_i-\mathbf{k}_j)/2$. The Sommerfeld parameters α_j,α_{ij} are given by

$$\alpha_{ij}=\frac{Z_iZ_j}{v_{ij}},\quad \alpha_j=\frac{ZZ_j}{v_j}. \tag{6}$$

In Eq. (6) v_j denotes the velocity of particle j relative to the residual charge, whereas $\mathbf{v}_{ij}:=\mathbf{v}_i-\mathbf{v}_j$. In this work we restrict the considerations to outgoing-wave boundary conditions. The treatment of incoming-wave boundary conditions runs along the same lines. The total energy of the system E is given by

$$E=\sum_{l=1}^{N}E_l\quad\text{where}\quad E_l=\frac{k_l^2}{2m}. \tag{7}$$

To derive asymptotic scattering states in the limit of large interparticle separations and their propagations to finite distances we assume for $\Psi(\mathbf{r}_1,\ldots,\mathbf{r}_N)$ the ansatz

$$\Psi(\mathbf{r}_1,\ldots,\mathbf{r}_N)=\mathcal{N}\Phi_I(\mathbf{r}_1,\ldots,\mathbf{r}_N)\Phi_{II}(\mathbf{r}_1,\ldots,\mathbf{r}_N)$$

$$\times\chi(\mathbf{r}_1,\ldots,\mathbf{r}_N), \tag{8}$$

where Φ_I,Φ_{II} are appropriately chosen functions, $\mathcal{N}$ is a normalization constant, and $\chi(\mathbf{r}_1,\ldots,\mathbf{r}_N)$ is a function of an arbitrary form. The function Φ_I is chosen to describe the motion of N-independent Coulomb particles moving in the field of the charge Z at the total energy E, i.e., Φ_I is determined by the differential equation

$$\left(H_0+\sum_{j=1}^{N} \frac{ZZ_j}{r_j}-E \right) \Phi_I(\mathbf{r}_1, \ldots ,\mathbf{r}_N)=0. \tag{9}$$

Since we are interested in scattering solutions with outgoing-wave boundary conditions that describe N particles escaping with asymptotic momenta $\mathbf{k}_j, j\in[1,N]$, it is appropriate to factor out the plane-wave part and write for Φ_I

$$\Phi_I(\mathbf{r}_1, \ldots ,\mathbf{r}_N)=\overline{\Phi_I}(\mathbf{r}_1, \cdots ,\mathbf{r}_N)\prod_{j=1}^{N} \xi_j(\mathbf{r}_j). \tag{10}$$

Upon substitution of the ansatz (10) into Eq. (9) it is readily concluded that Eq. (9) is completely separable and the regular solution Φ_I can be written in closed form

$$\Phi_I(\mathbf{r}_1, \ldots ,\mathbf{r}_N)=\prod_{j=1}^{N} \xi_j(\mathbf{r}_j)\varphi_j(\mathbf{r}_j), \tag{11}$$

where $\varphi_j(\mathbf{r}_j)$ is a confluent-hypergeometric function in the notation of Ref. [20]

$$\varphi_j(\mathbf{r}_j)= {}_1F_1[\alpha_j,1,-i(k_jr_j+\mathbf{k}_j\cdot\mathbf{r}_j)]. \tag{12}$$

The function Φ_I describes the motion of the continuum particles in the extreme case of very strong coupling to the residual ion, i.e., $|ZZ_j|\gg|Z_jZ_i|\forall i,j\in[1,N]$. In order to incorporate the other extreme case of strong correlations among the continuum particles ($|Z_jZ_i|\gg|ZZ_j|\forall i,j\in[1,N]$) we choose Φ_{II} to possess the form

$$\Phi_{II}(\mathbf{r}_1, \ldots ,\mathbf{r}_N)=\overline{\Phi_{II}}(\mathbf{r}_1, \ldots ,\mathbf{r}_N)\prod_{j=1}^{N} \xi_j(\mathbf{r}_j), \tag{13}$$

with

$$\overline{\Phi_{II}}(\mathbf{r}_1, \ldots ,\mathbf{r}_N):=\prod_{j>i=1}^{N} \varphi_{ij}(\mathbf{r}_{ij}), \tag{14}$$

where $\varphi_{ij}(\mathbf{r}_{ij}):= {}_1F_1[\alpha_{ij},1,-i(k_{ij}r_{ij}+\mathbf{k}_{ij}\cdot\mathbf{r}_{ij})]$. It is straightforward to show that the expression $\varphi_{ij}(\mathbf{r}_{ij})\Pi_{l=1}^{N}\xi_l(\mathbf{r}_l)$ solves for the Schrödinger equation (1) in the case of extreme correlations between particle i and particle j, i.e., $|ZZ_l|\ll|Z_iZ_j|\gg|Z_mZ_n|\forall l,m,n\neq i,j$. In terms of differential equations this means

$$\left(H_0+\frac{Z_iZ_j}{r_{ij}}-E \right)\varphi_{ij}(\mathbf{r}_{ij})\prod_{j=1}^{N} \xi_j(\mathbf{r}_j)=0. \tag{15}$$

It should be stressed, however, that the function (13) does not solve for Eq. (1) in the case of weak coupling to the residual ion ($Z\to0$), but otherwise comparable strength of correlations between the continuum particles. This is due to the fact that two-body subsystems formed by the continuum particles are coupled to each other. To derive an expression for this coupling term we note first that

$$\Delta_m\overline{\Phi_{II}}=\sum_{l=1}^{m-1} \Delta_m\varphi_{lm}\prod_{\substack{j>i\\ i\neq l}}^{N} \varphi_{ij} \;+\sum_{n=m+1}^{N} \Delta_m\varphi_{mn}\prod_{\substack{j>i\\ j\neq n}}^{N} \varphi_{ij}$$
$$+A_m, \quad m\in[1,N], \tag{16}$$

where the differential operator A_m has the form

$$A_m=2\sum_{l=1}^{m-1}\left[(\boldsymbol{\nabla}_m\varphi_{lm})\cdot\left(\sum_{n=m+1}^{N} \boldsymbol{\nabla}_m\varphi_{mn}\right)\right]\prod_{\substack{j>i\\ j\neq n,i\neq l}}^{N} \varphi_{ij}$$
$$+\sum_{l=1}^{m-1}\left[(\boldsymbol{\nabla}_m\varphi_{lm})\cdot\left(\sum_{l\neq s=1}^{m-1} \boldsymbol{\nabla}_m\varphi_{sm}\right)\right]\prod_{\substack{j>i\\ s\neq i\neq l}}^{N} \varphi_{ij}$$
$$+\sum_{n=m+1}^{N}\left[(\boldsymbol{\nabla}_m\varphi_{mn})\cdot\left(\sum_{\substack{t=m+1\\ t\neq n}}^{N} \boldsymbol{\nabla}_m\varphi_{mt}\right)\right]\prod_{\substack{j>i\\ j\neq t\neq n}}^{N} \varphi_{ij},$$
$$m\in[1,N]. \tag{17}$$

To obtain the differential operator that couples the two-body subsystems in the absence of the charge Z we neglect in Eq. (1) the interactions between the residual charge and the continuum particles ($Z=0$) and substitute the function (13) into Eq. (1). Making use of the relation (16) it is straightforward, however cumbersome, to show that the coupling term that prevents separability has the form

$$A=\sum_{m=1}^{N} A_m. \tag{18}$$

Equations (17) and (18) warrant comment. The term A_m is a mixing operator. It couples an individual two-body subsystem formed by two continuum particles to all other two-body subsystems formed by the continuum particles in the absence of the residual ion. Hence it is clear that all the terms in the sum (17) vanish for the case of the three-body system since in this case only one two-body system exists in the field of the residual charge. The second remark concerns the structure of A_m and hence A. From Eq. (16) it is evident that the remainder term (17) is part of the kinetic-energy operator. Thus it is expected that, under certain circumstances, this term has a finite range, which indicates that asymptotic separability, in the sense specified below, exists for many-body continuum Coulomb systems. In fact, as the functional form of $\varphi_{ij}(\mathbf{r}_{ij})$ is known, the term A can be calculated explicitly, which will be done below.

Now with Φ_I and Φ_{II} determined, the exact wave function (8) is given by the expression $\chi(\mathbf{r}_1, \ldots ,\mathbf{r}_N)$. Upon substitution of the expressions (13) and (11) into the ansatz (8) and inserting in the Schrödinger equation (1), a differential equation for the determination of $\chi(\mathbf{r}_1, \ldots ,\mathbf{r}_N)$ is derived

$$\Bigg\{ H_0-\frac{A}{\overline{\Phi_{II}}}-\sum_{L=1}^{N} [(\boldsymbol{\nabla}_L\ln\Phi_I \;+\boldsymbol{\nabla}_L\ln\Phi_{II})\cdot\boldsymbol{\nabla}_L$$
$$+(\boldsymbol{\nabla}_L\ln\Phi_I)\cdot(\boldsymbol{\nabla}_L\ln\Phi_{II})]+E\Bigg\}\chi(\mathbf{r}_1, \ldots ,\mathbf{r}_N)=0 \;\;. \tag{19}$$

From the derivation of the functions Φ_I and Φ_{II} [Eqs. (9) and (13)] it is clear that all long-range two-body Coulomb interactions have already been diagonalized by Φ_I and Φ_{II} because the total potential is exactly treated by these wave functions. Hence the function χ, to be determined here, contains information on many-body couplings, which are, under certain conditions (see below), of finite range. To explicitly show that, and due to flux arguments we write the function χ in the form

$$\chi(\mathbf{r}_1,\ldots,\mathbf{r}_N)=\prod_{j=1}^{N}\xi^*(\mathbf{r}_j)[1-f(\mathbf{r}_1,\ldots,\mathbf{r}_N)], \tag{20}$$

where $f(\mathbf{r}_1,\ldots,\mathbf{r}_N)$ is a function of an arbitrary structure. Inserting the form (20) into Eq. (19) we arrive, after much differential analysis, at the inhomogeneous differential equation

$$\left\{H_0-\sum_{L=1}^{N}[\boldsymbol{\nabla}_L(\ln\Phi_I+\ln\Phi_{II})+i\mathbf{k}_L]\cdot\boldsymbol{\nabla}_L\right\}f+\mathcal{R}(1-f)=0, \tag{21}$$

where the inhomogeneous term $\mathcal{R}$ is given by

$$\begin{aligned}\mathcal{R}:=\sum_{m=1}^{N}\Bigg\{&(\boldsymbol{\nabla}_m\ln\overline{\Phi_I})\cdot(\boldsymbol{\nabla}_m\ln\overline{\Phi_{II}})\\&+\sum_{l=1}^{m-1}\sum_{p=m+1}^{N}(\nabla_m\ln\varphi_{lm})\cdot(\nabla_m\ln\varphi_{mp})\\&+\frac{1}{2}\sum_{l=1}^{m-1}\sum_{s\neq l}^{m-1}(\nabla_m\ln\varphi_{lm})\cdot(\nabla_m\ln\varphi_{sm})\\&+\frac{1}{2}\sum_{n=m+1}^{N}\sum_{n\neq q=m+1}^{N}(\nabla_m\ln\varphi_{mn})\cdot(\nabla_m\ln\varphi_{mq})\Bigg\}.\end{aligned} \tag{22}$$

It is the inhomogeneous term $\mathcal{R}$ that contains the coupling between all individual two-particle subsystems. For example, the first term in Eq. (22) describes the coupling of a two-body subsystems formed by particles i and j to all two-body subsystems formed by the individual continuum particles and the residual ion. The second term originates from Eq. (18) and, as explained above, is a measure for the coupling among two-body subsystems of the continuum particles (in the absence of Z). To these couplings to be negligible the norm of the term $\mathcal{R}$ must be small. To get some insight into the functional form of $\mathcal{R}$, given by Eq. (22), we note that

$$\boldsymbol{\nabla}_L\ln\overline{\Phi_I}=\alpha_L k_L\mathbf{F}_L(\mathbf{r}_L), \tag{23}$$

where

$$\mathbf{F}_L(\mathbf{r}_L):=\frac{{}_1F_1[1+i\alpha_L,2,-i(k_Lr_L+\mathbf{k}_L\cdot\mathbf{r}_L)]}{{}_1F_1[i\alpha_L,1,-i(k_Lr_L+\mathbf{k}_L\cdot\mathbf{r}_L)]}(\hat{\mathbf{k}}_L+\hat{\mathbf{r}}_L)\ . \tag{24}$$

In addition, we remark that

$$\begin{aligned}\nabla_m\ln\overline{\Phi_{II}}&=\sum_{n=m+1}^{N}\nabla_m\ln\varphi_{mn}+\sum_{l=1}^{m-1}\nabla_m\ln\varphi_{lm}\\&=\sum_{n=m+1}^{N}\alpha_{mn}k_{mn}\mathbf{F}_{mn}(\mathbf{r}_{mn})-\sum_{l=1}^{m-1}\alpha_{lm}k_{lm}\mathbf{F}_{lm}(\mathbf{r}_{lm}),\end{aligned} \tag{25}$$

where

$$\mathbf{F}_{ij}(\mathbf{r}_{ij}):=\frac{{}_1F_1[1+i\alpha_{ij},2,-i(k_{ij}r_{ij}+\mathbf{k}_{ij}\cdot\mathbf{r}_{ij})]}{{}_1F_1[i\alpha_{ij},1,-i(k_{ij}r_{ij}+\mathbf{k}_{ij}\cdot\mathbf{r}_{ij})]}(\hat{\mathbf{k}}_{ij}+\hat{\mathbf{r}}_{ij})\ . \tag{26}$$

Thus the behavior of the coupling term $\mathcal{R}$ is controlled by the generalized functions $\mathbf{F}_{ij}(\mathbf{r}_{ij}),\mathbf{F}_l(\mathbf{r}_l)$ since Eq. (22) can be written in the form

$$\begin{aligned}\mathcal{R}:=\sum_{m=1}^{N}\Bigg\{&\alpha_mk_m\mathbf{F}_m(\mathbf{r}_m)\cdot\Bigg[\sum_{n=m+1}^{N}\alpha_{mn}k_{mn}\mathbf{F}_{mn}(\mathbf{r}_{mn})\\&-\sum_{s=1}^{m-1}\alpha_{sm}k_{sm}\mathbf{F}_{sm}(\mathbf{r}_{sm})\Bigg]\\&-\sum_{l=1}^{m-1}\sum_{p=m+1}^{N}\alpha_{lm}\alpha_{mp}k_{lm}k_{mp}\mathbf{F}_{lm}\cdot\mathbf{F}_{mp}\\&+\frac{1}{2}\sum_{l=1}^{m-1}\sum_{s\neq l}^{m-1}\alpha_{lm}\alpha_{sm}k_{lm}k_{sm}\mathbf{F}_{lm}\cdot\mathbf{F}_{sm}\\&+\frac{1}{2}\sum_{n=m+1}^{N}\sum_{n\neq q=m+1}^{N}\alpha_{mn}\alpha_{mq}k_{mn}k_{mq}\mathbf{F}_{mn}\cdot\mathbf{F}_{mq}\Bigg\}.\end{aligned} \tag{27}$$

The simplest approximation is to neglect the term $\mathcal{R}$ altogether. In this case the function $f=0$ solves for Eq. (21). Then the solution of Eq. (1) takes on the approximate form

$$\Psi(\mathbf{r}_1,\ldots,\mathbf{r}_N)\approx\mathcal{N}\prod_{m>l,j=1}^{N}\xi_j(\mathbf{r}_j)\varphi_j(\mathbf{r}_j)\varphi_{lm}(\mathbf{r}_{lm}). \tag{28}$$

Thus the justification of the approximation (28) reduces to the validity of neglecting the inhomogeneous term (27). One region in which this term can be disregarded is the asymptotic region of large interparticle separations. This is immediately deduced from the asymptotic behavior of the generalized functions $\mathbf{F}_{ij}(\mathbf{r}_{ij}),\mathbf{F}_l(\mathbf{r}_l)$, which dictate the asymptotic properties of $\mathcal{R}$, as readily concluded from Eq. (27). From the asymptotic expansion of the hypergeometric functions [20] we infer that

$$\begin{aligned}\lim_{r_{ij}\to\infty}|\mathbf{F}_{ij}(\mathbf{r}_{ij})|\to&\left|\frac{\hat{\mathbf{k}}_{ij}+\hat{\mathbf{r}}_{ij}}{\mathbf{k}_{ij}\cdot(\hat{\mathbf{k}}_{ij}+\hat{\mathbf{r}}_{ij})r_{ij}}\right|\\&+O(|k_{ij}r_{ij}+\mathbf{k}_{ij}\cdot\mathbf{r}_{ij}|^{-2})\ .\end{aligned} \tag{29}$$

An asymptotic relation similar to Eq. (29) holds for $\mathbf{F}_l(\mathbf{r}_l)$. It should be noted that the functions $\mathbf{F}_{ij}(\mathbf{r}_{ij}),\mathbf{F}_l(\mathbf{r}_l)$ have to be considered in a distributive (operator) sense, which means that, asymptotically, only terms of $\mathbf{F}_{ij},\mathbf{F}_l$ that fall off faster than the Coulomb potentials can be disregarded. Since $\mathcal{R}$ is essentially a sum of products of $\mathbf{F}_{ij}, \mathbf{F}_l$, the expression $\mathcal{R}$ is of finite range, in the sense that it diminishes faster than the Coulomb potential in the asymptotic regime, only in the case where all particles are far apart from each other, i.e.,

$$\lim_{\substack{r_{ij}\to\infty \\ r_l\to\infty}} \mathcal{R} \;\to\; O(|k_{ij}r_{ij}+\mathbf{k}_{ij}\cdot\mathbf{r}_{ij}|^{-2},|k_l r_l+\mathbf{k}_l\cdot\mathbf{r}_l|^{-2})$$

$$\forall j>i, l\in[1,N]. \tag{30}$$

Therefore, in the limit (30), the term $\mathcal{R}$ can be asymptotically neglected and the approximation (28) is justified. In fact, it is straightforward to show that the wave function (28) tends to the asymptotic form (2) in the limit of large interparticle separations, which proves the assumption made in Ref. [1]. However, if two particles are close together, regardless of whether all other particles are well separated, the coupling term is of infinite range, as seen from Eqs. (29) and (27). In this case the relation (30) does not hold. Consequently, the wave function (28) is not an exact asymptotic eigenfunction of the total Hamiltonian in this limit. It is important to note that the limit Eq. (30) is energy dependent. With increasing momenta of the escaping particles the asymptotic region, i.e., the limit Eq. (30), is reached faster. In other words, at a certain interparticle separations, the remainder term $\mathcal{R}$, which has been neglected to arrive at the approximate form (28), diminishes with increasing velocities of the emerging particles. In this sense the approximation leading to the wave function (28) is a high-energy approximation.

III. TWO-BODY CUSP CONDITIONS

In the preceding section it has been shown that the approximation (28) is, to leading order, exact for large particles' separation. In addition, it is concluded below that this function exhibits a behavior compatible with Eq. (1) at all two-body coalescence points $r_{ij}\to 0, r_l\to 0$, with $j>i, l\in[1,N]$. To guarantee regular behavior of the wave function at these collision points, at which the corresponding Coulomb two-body potential is divergent, the solution $\Psi(\mathbf{r}_1,\ldots,\mathbf{r}_N)$ of Eq. (1) must satisfy the Kato cusp conditions [19,21] (provided the solution does not vanish at these points). At a collision point $r_i\to 0$ these conditions are

$$\left[\frac{\partial\ \tilde{\Psi}(\mathbf{r}_1,\ldots,\mathbf{r}_N)}{\partial r_i}\right]_{r_i=0} = k_i\alpha_i\Psi(\mathbf{r}_1,\ldots,r_i=0,\ldots,\mathbf{r}_N)$$

$$\forall (r_i/r_j)\to 0, (r_i/r_{lm})\to 0;\ \ m>l,\ \ i\neq j\in[1,N]\ \ . \tag{31}$$

The quantity $\tilde{\Psi}(\mathbf{r}_1,\ldots,\mathbf{r}_N)$ is the wave function $\Psi(\mathbf{r}_1,\ldots,\mathbf{r}_N)$ averaged over a sphere of small radius $r_\delta \ll 1$ around the singularity $r_i=0$. A relation similar to Eq. (31) holds in the case of the coalescence points $r_{ij}\to 0$. To prove that the wave function (28) satisfies the conditions (31) we linearize $\Psi(\mathbf{r}_1,\ldots,\mathbf{r}_N)$ around $r_i=0$ and average over a sphere of small radius $r_\delta\ll 1$ to arrive at

$$\tilde{\Psi}(\mathbf{r}_1,\ldots,\mathbf{r}_N)=\mathcal{N}\ D(\mathbf{r}_i)\prod_{\substack{i\neq j=1\\ l>m}}^{N}\ \xi_j\varphi_j(\mathbf{r}_j)\varphi_{lm}(\mathbf{r}_{lm}), \epsilon_{ilm}\neq 0, \tag{32}$$

where

$$\begin{aligned} D(\mathbf{r}_i) &= \frac{2\pi}{4\pi r_\delta^2}\int_{-1}^{1} r_\delta^2 d\cos\theta[1+ik_i\cos\theta+\alpha_i k_i r_i(1+\cos\theta)] \\ &= 1+\alpha_i k_i r_i\,. \end{aligned} \tag{33}$$

To arrive at Eq. (33) one takes the z axes as $\mathbf{k}_i$ and defines $\cos\theta=\hat{\mathbf{k}}_i\cdot\hat{\mathbf{r}}_i$. From Eqs. (33) and (32) it is obvious that

$$\begin{aligned} \left[\frac{\partial\ \tilde{\Psi}(\mathbf{r}_1,\ldots,\mathbf{r}_N)}{\partial r_i}\right]_{r_i=0} &= \alpha_i k_i \mathcal{N}\prod_{\substack{i\neq j=1\\ l>m}}^{N}\ \xi_j\varphi_j(\mathbf{r}_j)\varphi_{lm}(\mathbf{r}_{lm}) \\ &= \alpha_i k_i \Psi(\mathbf{r}_1,\ldots,r_i=0,\ldots,\mathbf{r}_N), \\ & \qquad \epsilon_{ilm}\neq 0. \end{aligned} \tag{34}$$

In deriving Eq. (34) we made use of the fact that in the limit $(r_i/r_{ij}\to 0)$ the distance r_{ij} tends to r_j. The proof that the wave function (28) fulfills the cusp conditions at the collision points of two continuum particles $(r_{ji}\to 0)$ runs along the same lines. Finally, we remark that the wave function (28) is not compatible with the expansion of the exact solution of the Schrödinger equation (1) at the three-body collision points (e.g., $r_i\to 0$ and $r_j\to 0, j\neq i$) since in this case the exact wave function is known to satisfy a Fock expansion [22] in the coordinate $\rho := \sqrt{(r_i^2+r_j^2)}$, which contains, in addition to powers in ρ, logarithmic terms in ρ, whereas the wave function (28) possesses a regular power-series expansion around $r_i\to 0$ and $r_j\to 0$.

IV. NORMALIZATION

The knowledge of the normalization factor $\mathcal{N}$ of the wave function (28) is imperative for the evaluation of scattering amplitudes using the wave function (28) as a representation of scattering states. In principle, $\mathcal{N}$ is derived from a $3N$-dimensional integral over the norm of the function (28) which, for large N, is an inaccessible task. Thus, for the determination of $\mathcal{N}$ we resort to the requirement that the flux through an asymptotic manifold defined by a constant large interparticle separations should be the same in the case of the wave function (28) and a normalized plane-wave representation of the scattering state, i.e.,

$$\mathbf{J}_{\rm PW}=\mathbf{J}_\Psi\,, \tag{35}$$

where the plane-wave flux is given by

$$\mathbf{J}_{\mathrm{PW}} = -\frac{i}{2}(2\pi)^{-3N}\left[\prod_{l}^{N}\xi_l^*(\mathbf{r}_l)\boldsymbol{\nabla}\prod_{l}^{N}\xi_l(\mathbf{r}_l) - \prod_{l}^{N}\xi_l(\mathbf{r}_l)\boldsymbol{\nabla}\prod_{l}^{N}\xi_l^*(\mathbf{r}_l)\right] = (2\pi)^{-3N}\sum_{l=1}^{N}\mathbf{k}_l . \tag{36}$$

In Eq. (36) the total gradient $\boldsymbol{\nabla} := \sum_{l=1}^{N}\boldsymbol{\nabla}_l$ has been introduced. To evaluate the flux generated by the wave function (28) we note that, by taking advantage of Eqs. (23) and (25), we can write for the total gradient of the wave function (28)

$$\begin{aligned}\nabla\Psi := P\mathcal{N}\sum_{m=1}^{N}\Bigg\{ & i\mathbf{k}_m\Psi + \alpha_m k_m \mathbf{F}_m\Psi \\ & + \Bigg[\sum_{n=m+1}^{N}\alpha_{mn}k_{mn}\overline{\mathbf{F}}_{mn}(\mathbf{r}_{mn})\prod_{\substack{j>i\\ j\neq n}}^{N}\varphi_{ij} \\ & - \sum_{l=1}^{m-1}\alpha_{lm}k_{lm}\overline{\mathbf{F}}_{lm}(\mathbf{r}_{lm})\prod_{\substack{j>i\\ i\neq l}}^{N}\varphi_{ij}\Bigg]\prod_{s=1}^{N}\xi_s(\mathbf{r}_s)\varphi_s(\mathbf{r}_s)\Bigg\},\end{aligned} \tag{37}$$

where $\overline{\mathbf{F}}_{mn}$ is given by $\mathbf{F}_{mn}\varphi_{mn}$. The decisive point now is that since we are considering the flux at large interparticle distances only the first term of Eq. (37) is relevant. This is readily deduced from Eqs. (24) and (26) which state that all other terms in Eq. (37), except for the first term, can be neglected asymptotically. Note, in this context, that terms in the wave function that are asymptotically of the order $O(1/r_j, 1/r_{lm})$ correspond to parts of the Hamiltonian falling off faster than the Coulomb potentials and hence can be disregarded in the asymptotic regime. Now making use of the asymptotic expansion of the confluent hypergeometric function [20] and taking leading order in the interparticle distances, the flux $\mathbf{J}_\Psi$ can be deduced

$$\mathbf{J}_\Psi = \mathcal{N}^2\prod_{j=1}^{N}\frac{\exp(\pi\alpha_j)}{\Gamma(1-i\alpha_j)\Gamma^*(1-i\alpha_j)} \times \prod_{m>l=1}^{N}\frac{\exp(\pi\alpha_{lm})}{\Gamma(1-i\alpha_{lm})\Gamma^*(1-i\alpha_{lm})}\sum_{n=1}^{N}\mathbf{k}_n , \tag{38}$$

where $\Gamma(x)$ is the Gamma function. From Eqs. (35), (36), and (38) it follows that

$$\mathcal{N} = (2\pi)^{-3N/2}\prod_{j=1,m>l=1}^{N}\exp[-\pi(\alpha_{lm}+\alpha_j)/2] \times\Gamma(1-i\alpha_j)\Gamma(1-i\alpha_{lm}). \tag{39}$$

For two charged particles moving in the field of a heavy nucleus the wave function (28) with the normalization, given by Eq. (39), simplifies to the three-body wave function proposed in Refs. [4,7].

V. APPLICATION TO THE FOUR-BODY COULOMB CONTINUUM PROBLEM

Apart from the Rutherford scattering, the simplest application of the theory presented in the previous sections is the description of three-body Coulomb continuum states that are, for example, achieved as final states of electron-impact ionization and doublephoto ionization of atomic and molecular systems. In this case the wave function (28) simplifies to the three-body wave function proposed in Refs. [4,7] and extensively used by various authors. The second step in complexity is the description of the four-body scattering states. These states arise in the final channel of various reactions such as the double ionization of atomic systems by electron and positron impact as well as the triplephoto ionization. Experimentally there has been an increased interest in such reactions due to recent advances in coincidence-detection techniques [10–13]. The measurement of fully differential cross sections of reactions leading to four-body Coulomb continuum states was reported in Refs. [10,11]. In this study argon and krypton targets have been double ionized by a fast projectile electron under conditions where little momentum is being transferred to the target atoms. To describe the final state, the standard theoretical treatment [23–30] has been to reduce the four-body Coulomb continuum problem to a three-body problem by employing a first-order Born-type approximation (FBA) in the projectile-target potential, which is justified for the conditions under which the experiment has been performed. Recently, measurements for electron-impact double ionization have been performed at intermediate incident energies using the cold-target recoil-ion momentum spectroscopy [12,14]. In this case the FBA model is inappropriate. The last statement was also inferred from recent measurements [15] of the cross section for the double ionization of magnesium by electron impact at moderate incident energy. In view of these recent experiments and the absence of adequate theoretical models it appears timely to consider the applicability of the theory developed in the previous sections for the case of the four-body problem.

A. Product charges according to Jetzke and Faisal

For N continuum particles the wave function (28) describes $N(N-1)/2$ two-body Coulomb subsystems. The coupling between these two-body subsystems through the relative coordinates presents a serious problem for the calculations of scattering amplitudes. To overcome these difficulties further simplifications are needed. In Ref. [17] a procedure has been proposed in which the correlations between the continuum particles are completely subsumed in an effective interactions of each continuum particle with the nucleus. This is achieved by rewriting the total Coulomb potential in the form

$$\sum_{j=1}^{N}\frac{ZZ_j}{r_j} + \sum_{\substack{i,j\\ j>i=1}}^{N}\frac{Z_iZ_j}{r_{ij}} = \sum_{i}^{N}\frac{Z_i^{\mathrm{JF}}}{r_i}, \tag{40}$$

where the local product charges Z_i^{JF} are given by

$$Z_i^{\mathrm{JF}}(\mathbf{r}_1,\ldots,\mathbf{r}_N) = ZZ_i + \sum_{j\neq i}^{N} Z_iZ_j\frac{\mathbf{r}_i\cdot\mathbf{r}_{ij}r_i}{r_{ij}^3}. \tag{41}$$

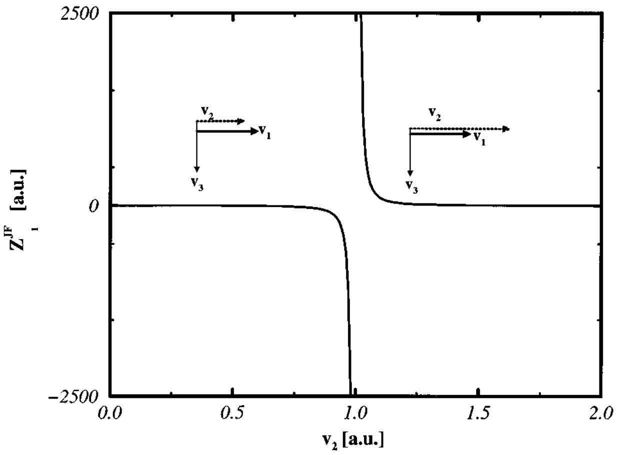

FIG. 1. Case where one positron and two electrons are moving in a nuclear field of a charge $Z=2$. The velocity vectors of all particles lie in the same plane. One electron, particle 2, and the positron, particle 1, are assumed to escape in the same direction with the positron having a fixed velocity $v_1=1$ a.u. The remaining electron, particle 3, is ejected in a direction perpendicular to $\mathbf{v}_1$, i.e., $\hat{\mathbf{v}}_1\cdot\hat{\mathbf{v}}_3=0$, with a fixed velocity $v_3=1$ a.u. The positron-nucleus product charge Z_1^{eff}, determined according to Eq. (42), is studied as function of v_2.

The position dependence of the product charges Z_i^{JF} is then converted into a velocity dependence by making use of the asymptotic approximation $\mathbf{r}_i=\mathbf{v}_i t$, where t is the time. This approximation is valid at large interparticle separations in which case Eq. (41) reduces to

$$Z_i^{\mathrm{JF}}(\mathbf{v}_1,\ldots,\mathbf{v}_N)=ZZ_i+\sum_{j\neq i}^{N} Z_iZ_j\frac{\mathbf{v}_i\cdot\mathbf{v}_{ij}v_i}{v_{ij}^3}. \tag{42}$$

Upon substitution of Eq. (42) in Eq. (40), the differential equation (1) becomes completely separable. The solution is obtained from the function (28) in the special case $\alpha_j=Z_j^{\mathrm{JF}}/v_j$ and $\alpha_{ij}\equiv 0$. When two continuum particles i,j approach each other in momentum space ($k_{ij}\to 0$) the effective charges, given by Eq. (41), diverge so as to simulate attractive (if $Z_iZ_j<0$) or repulsive (if $Z_iZ_j>0$) interaction between these particles. However, since these product charges contain scalar products between the velocity vectors of the escaping particles they exhibit unphysical behavior in the limit $\mathbf{v}_i\|\mathbf{v}_j$, $v_i\to v_j\pm\delta, 1\gg\delta>0$. This is clearly illustrated in Fig. 1, where we envisage the case of two electrons and one positron moving in the triple continuum of a residual charge $Z=2$. This is the final state achieved by positron-impact double ionization of He. We focus on the case in which one electron and the positron emerge in the same direction. When this electron approaches the positron (in momentum space) the positron-nucleus interaction (product charge) becomes strongly attractive in order to simulate the attractive electron-positron interaction. However, as the electron passes the positron the positron-nucleus interaction (product charge) varies rapidly from an attractive to a repulsive interaction. In other words, at the removable singularities $v_{ij}=0$ of the product charges (42) the functions $Z_i^{\mathrm{JF}}v_{ij}^2, Z_j^{\mathrm{JF}}v_{ij}^2$ are discontinuous in the limit $v_{ij}\to 0$. This behavior is quite unphysical and must be considered as a result of the way in which these product charges are constructed. We remark in passing that the same behavior of these product charges also arise for different charge states of the continuum particles as well as for a different number of these particles, in particular for a three-body system.

B. Product charges for the four-body Coulomb system in the continuum

In order to construct product charges $\overline{Z_j}, j\in[1,3]$, for a four-body system, that do not exhibit the unphysical behavior shown in Fig. 1, we maintain the philosophy of completely subsuming the correlations between the continuum particles into an effective interaction of these particles with the nucleus. In other words, the wave function (28) is written in the form

$$\Psi(\mathbf{r}_1,\ldots,\mathbf{r}_N)\approx\Psi^{\mathrm{eff}}(\mathbf{r}_1,\ldots,\mathbf{r}_N)=\overline{\mathcal{N}}\prod_{j=1}^{N}\xi_j(\mathbf{r}_j)\overline{\varphi_j}(\mathbf{r}_j), \tag{43}$$

where $\overline{\varphi_j}(\mathbf{r}_j)=\underline{\varphi_j}(\mathbf{r}_j)|_{\alpha_j=\overline{\alpha_j}}$ and $\overline{\mathcal{N}}=\mathcal{N}|_{\alpha_j=\overline{\alpha_j}}$, where $\overline{\alpha_j}(\mathbf{r}_1,\underline{\ldots},\mathbf{r}_N)=Z_j(\mathbf{r}_1,\ldots,\mathbf{r}_N)/v_j$. The local product charges $Z_j(\mathbf{r}_1,\ldots,\mathbf{r}_N)$ are then determined by requiring that the solution (43) should match the known solutions of the Schrödinger equation (1) in some limiting cases. In what follows we investigate these limiting cases of the four-body Schrödinger equation. However, for brevity, only the structure of Eq. (1) is discussed. The corresponding wave functions in these cases are easily deduced.

(a) Since all particles appear in the Schrödinger equation (1) in a symmetrical way all three continuum particles must be treated on equal footing, which results in the relations

$$\overline{Z_j}(Z_i,\mathbf{r}_i;Z_j,\mathbf{r}_j)=\overline{Z_i}(Z_j,\mathbf{r}_j;Z_i,\mathbf{r}_i). \tag{44}$$

(b) When two particles i,j approach each other ($r_{ij}\to 0, r_{ij}/r_k\to 0$) their mutual interaction increases as Z_iZ_j/r_{ij} and dominates the other interactions appearing in Eq. (1). Hence the interactions of particle i and particle j with the nucleus must change in a way that simulates their mutual Coulomb interaction regardless of the direction in which particle i is approached by particle j. The interaction of the remaining continuum particles with the nucleus must remain finite, i.e.,

$$\lim_{\substack{r_{ij}\to 0\pm\mathbf{d}\\ r_{ij}/r_l\to 0}}\overline{Z_i},\overline{Z_j}\to C\frac{Z_iZ_j}{r_{ij}},\overline{Z_l}\quad\text{finite},\quad|\mathbf{d}|\ll 0,\epsilon_{ijl}\neq 0, \tag{45}$$

where C is a positive real number. Condition (45) is violated by the product charges, given by Eq. (41).

(c) If one particle is moving in the vicinity of the nucleus it experiences the full nuclear charge. Assuming the remaining two continuum particles to be far away from the nucleus, their interaction with the nucleus must remain finite,

$$\lim_{r_i\to 0, r_i/r_j\to 0}\overline{Z_i}\to Z_iZ,\overline{Z_j}\quad\text{finite}\quad\forall\; i\neq j\in[1,3]. \tag{46}$$

(d) In order to treat the total potential V in an exact manner, V, and hence the Schrödinger equation (1), must be invariant under the local product charges $\overline{Z_j}$,

$$\sum_{j=1}^{3} \frac{\overline{Z_j}}{r_j} = V. \tag{47}$$

(e) From the Schrödinger equation (1) it is readily concluded that if one particle, say particle l, is far away from the remaining three particles, this particle (l) experiences a net charge of $Z+Z_i+Z_j$, i.e.,

$$\lim_{\substack{r_l\to\infty \\ r_l/r_i, r_l/r_j\to\infty}} \overline{Z_l}\to Z_l(Z+Z_i+Z_j), \epsilon_{ijl}\neq 0. \tag{48}$$

In addition, if in the three-body system, formed by the nucleus, particle i, and particle j, particle i approaches the nucleus, particle j experiences a net nuclear charge of $Z+Z_i$, as immediately concluded from Eq. (1). Mathematically this condition can be formulated as

$$\lim_{\substack{r_l\to\infty \\ r_i\to 0, (r_i/r_j, r_j/r_l)\to 0}} \overline{Z_j}\to Z_j(Z+Z_i). \tag{49}$$

(f) It is established that for three electrons moving in the field of a residual positive charge Z the gradient of the total potential vanishes when the three electrons recede equidistant from the nucleus forming an equilateral triangle with the nucleus residing in the center of this triangle [31]. In this case the force exerted on the three electrons by the nucleus vanishes and the interelectronic correlations are minimized. The Schrödinger equation (1) reduces in this configuration to

$$\left[H_0 + \sum_{j=1}^{3} \frac{-Z+\frac{1}{\sqrt{3}}}{r_j} - E \right] \Psi(\mathbf{r}_1, \mathbf{r}_2, \mathbf{r}_3) = 0. \tag{50}$$

The eigenfunction of Eq. (50) can be given in closed form. To account for this Wannier-type configuration [32], which is known to dominate the escape dynamics at lower excess energies E, we impose on the local charges $\overline{Z_j}$, $j\in[1,3]$, in the case of three continuum electrons, the relations

$$\lim_{\substack{r_i\to r_j\to r_l \\ \hat{\mathbf{r}}_i,\hat{\mathbf{r}}_j=\cos\pi/3}} \overline{Z_j}\to -Z+\frac{1}{\sqrt{3}}$$

$$\forall i,j,l\in[1,3], \quad \epsilon_{ijl}\neq 0, \quad Z_1=Z_2=Z_3=-1. \tag{51}$$

We note that all the conditions listed above are directly deduced from the Schrödinger equation (1) in the respective (dipole) limits. To incorporate the above relations into local product charges $\overline{Z_j}$, which are analytical functions in the whole configuration space, except for the poles given by Eq. (45), we define effective two-body potential $\overline{V_j}=\overline{Z_j}/r_j$ and introduce the linear transformation

$$\overline{V_j} = a_{j1}V_1 + a_{j2}V_2 + a_{j3}V_3 + a_{j4}V_{12} + a_{j5}V_{13} + a_{j6}V_{23},$$
$$j\in[1,3], \tag{52}$$

where $V_i = ZZ_i/r_i$ and $V_{ij}=Z_iZ_j/r_{ij}$ are the physical two-body potentials. Equivalent transformations of the charges $\overline{Z_j}=\overline{V_j}r_j$ immediately derive from Eq. (52). To determine the product charges $\overline{Z_j}$ the 6×3-matrix $\mathcal{A}$ with elements a_{ij} has to be derived. The conservation of the total potential [condition d] requires

$$\sum_{i=1}^{3} a_{ij} = 1 \quad \forall j\in[1,6]. \tag{53}$$

Relation (46) implies

$$a_{ii}=1 \quad \forall i\in[1,3], \quad a_{12}=a_{13}=a_{21}=a_{23}=a_{31}=a_{32}\equiv 0. \tag{54}$$

Imposing condition (45) leads to

$$a_{16}=0, \;\; a_{25}=0, \;\; a_{34}=0. \tag{55}$$

Thus the product charges are determined by the equations

$$\overline{Z_1} = ZZ_1 + \overline{a_{14}}\frac{r_1}{r_1+r_2}\,\frac{Z_1Z_2r_1}{r_{12}} + \overline{a_{15}}\frac{r_1}{r_1+r_3}\,\frac{Z_1Z_3r_1}{r_{13}}, \tag{56}$$

$$\overline{Z_2} = ZZ_2 + \overline{a_{24}}\frac{r_2}{r_1+r_2}\,\frac{Z_1Z_2r_2}{r_{12}} + \overline{a_{26}}\frac{r_2}{r_2+r_3}\,\frac{Z_2Z_3r_2}{r_{23}}, \tag{57}$$

$$\overline{Z_3} = ZZ_3 + \overline{a_{35}}\frac{r_3}{r_1+r_3}\,\frac{Z_1Z_3r_3}{r_{13}} + \overline{a_{36}}\frac{r_3}{r_2+r_3}\,\frac{Z_2Z_3r_3}{r_{23}}, \tag{58}$$

where the coefficients a_{ij} have been transformed to $\overline{a_{ij}}$ to simplify subsequent calculations. The relations, given by Eq. (48), yield, in the limits $(r_1/r_2, r_1/r_3)\to\infty$, $(r_2/r_1, r_2/r_3)\to\infty$, and $(r_3/r_2, r_3/r_1)\to\infty$, respectively,

$$Z_1(Z_2+Z_3) = \overline{a_{14}}Z_1Z_2 + \overline{a_{15}}Z_1Z_3, \tag{59}$$

$$Z_2(Z_1+Z_3) = \overline{a_{24}}Z_1Z_2 + \overline{a_{26}}Z_2Z_3, \tag{60}$$

$$Z_3(Z_1+Z_2) = \overline{a_{35}}Z_1Z_3 + \overline{a_{36}}Z_2Z_3. \tag{61}$$

Making use of Eq. (59), relation (56) reduces to

$$\overline{Z_1} = ZZ_1 + [Z_1(Z_2+Z_3) - \overline{a_{15}}Z_1Z_3]\frac{r_1^2}{(r_1+r_2)r_{12}}$$
$$+ \overline{a_{15}}\frac{r_1}{r_1+r_3}\,\frac{Z_1Z_3r_1}{r_{13}}. \tag{62}$$

Now we impose condition (49) on Eq. (62) and arrive at

$$\lim_{\substack{r_2\to\infty,\; r_3\to 0 \\ r_2\gg r_1\gg r_3}} \overline{Z_1} = Z_1(Z+Z_3) = ZZ_1 + \overline{a_{15}}Z_1Z_3 \tag{63}$$

which leads to $\overline{a_{15}}=1$. From Eq. (59) we deduce that $\overline{a_{14}}=1$. Similar considerations yield $\overline{a_{24}}=\overline{a_{26}}=\overline{a_{36}}=\overline{a_{35}}=1$. Thus the final form of the product charges is

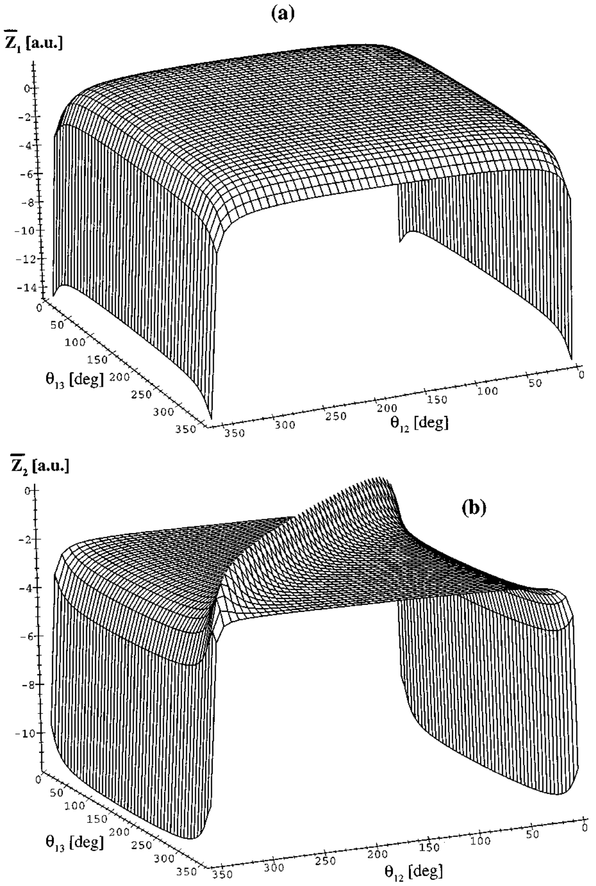

FIG. 2. For a four-body Coulomb system consisting of two electrons and one positron in the field of a residual charge $Z=2$, the effective charges, given by Eqs. (64) and (65), are depicted for the case where all particles escape in the same plane with velocities $v_1=v_2=1$ a.u. and $v_3=1.2$ a.u. The positron is taken to be particle 1. All angles are measured with respect to the direction $\hat{\mathbf{v}}_1$. (a) shows the angular dependence of the positron-nucleus effective product charge $\overline{Z_1}$, whereas in (b) the product charge of electron 1 with the nucleus ($\overline{Z_2}$) is investigated.

$$\overline{Z_1}=ZZ_1+\left[\frac{Z_1Z_2}{(r_1+r_2)r_{12}}+\frac{Z_1Z_3}{(r_1+r_3)r_{13}}\right]r_1^2, \tag{64}$$

$$\overline{Z_2}=ZZ_2+\left[\frac{Z_1Z_2}{(r_1+r_2)r_{12}}+\frac{Z_2Z_3}{(r_2+r_3)r_{23}}\right]r_2^2, \tag{65}$$

$$\overline{Z_3}=ZZ_3+\left[\frac{Z_1Z_3}{(r_1+r_3)r_{13}}+\frac{Z_2Z_3}{(r_2+r_3)r_{23}}\right]r_3^2. \tag{66}$$

It is straightforward to verify that all the conditions (44)–(51) are satisfied by the functions (64)–(66). For practical applications the position dependence of the effective charges (64)–(66) has to be converted into velocity dependence by applying the asymptotic approximation $\mathbf{r}_j=\mathbf{v}_j t$. Using this method, pilot calculations of the fully differential cross sections for the electron- and positron-impact double ionization of He($^1S^e$) have been reported [18]. A more extensive study of these reactions is in preparation [33]. For the case of positron impact the positron-nucleus product charge $\overline{Z_1}$ is depicted in Fig. 2(a), whereas Fig. 2(b) shows the electron-nucleus product charge in a typical scattering geometry where all momenta of the outgoing particles lie in the same plane. From Figs. 2(a) and 2(b) it is evident that when one of the electrons approaches the positron in velocity space the interaction of this electron with the nucleus and the positron-nucleus interaction become strongly attractive, which simulate the capture of the respective electron to the continuum of the positron. With diminishing interelectronic velocity the electron-nucleus interactions become strongly repulsive [see Fig. 2(b)] as to signify the repulsive electron-electron final-state interaction.

Three final remarks concerning the use of effective charges are due here. As our conditions (44)–(51), which have been used to determine the product charges $\overline{Z_j}$, are limits, there will naturally be other functional forms of local product charges that smoothly connect between these limits. The procedure used here is based on the transformation (52), which is motivated by physical arguments rather than by strict mathematical reasoning. A different procedure might well lead to different product charges $\overline{Z_j}$. Thus the benchmark for such approximate methods is that the derived effective product charges must be compatible with the physical picture of the dynamics of many-body continuum Coulomb states.

The second remark concerns the Kato cusp conditions at the collision point of two continuum particles. All effective-charge methods yield many-body wave functions of the form given by Eq. (43). Since $\partial\Psi^{\mathrm{eff}}/\partial r_{ij}=0$ such wave functions do not satisfy the Kato cups condition at the coalescence point of two continuum particles, as immediately concluded from Eq. (31).

The final remark concerns the applicability of this method for calculating scattering amplitudes. The basic idea of this work is to propagate (approximate) asymptotic solutions of the many-body Schrödinger equation to finite distances. The region around the origin where the reaction takes place, however, is not covered by this procedure. Therefore, the success or failure of employing this method to calculate reaction cross sections will decisively depend on how the process under consideration is treated at shorter distances around the origin. For example, in Refs. [34,35] the one-photon double ionization of helium has been considered. In both cases the wave function of the two electrons in the continuum of He^{2+} was taken, at large distances, in the form of Eq. (43). However, due to different treatments of the reaction around the origin, the cross section presented in Ref. [34] is in very good agreement with experimental finding, whereas the method used in Ref. [35] yielded quite disappointing results.

VI. CONCLUSION

In this work a many-body correlated scattering Coulomb wave function has been derived for N charged particles of equal masses moving in the N continuum of a massive residual charge. It has been shown that the derived wave function solves, to leading order, for the many-body Schrödinger equation in the asymptotic regime defined by large interparticle distances, which provides an expression for the asymptotic many-body Coulomb scattering states. It has been verified that the Kato cusp conditions at all two-body collision points are fulfilled by the derived wave function. In addition, the normalization of the proposed wave function has been deduced. The developed scattering states have been considered in the case of the four-body continuum Coulomb system. A method based on the effective-product-charge strategy has been suggested to simplify the proposed wave function so as to make feasible the calculations of reaction cross sections.

ACKNOWLEDGMENTS

I would like to thank Erich Weigold and Steve Buckman for helpful suggestions and comments on the manuscript. Financial support by the Alexander von Humboldt Foundation and the Australian National University is gratefully acknowledged.

---

[1] L. Rosenberg, Phys. Rev. D **8**, 1833 (1973).
[2] R. K. Peterkop, *Theory of Ionization of Atoms by the Electron Impact* (Colorado Associated University Press, Boulder, 1977).
[3] S. P. Merkuriev, Theor. Math. Phys. **32**, 680 (1977).
[4] M. Brauner, J. S. Briggs, and H. Klar, J. Phys. B **22**, 2265 (1989).
[5] E. O. Alt and A. M. Mukhamedzhanov, Phys. Rev. A **47**, 2004 (1993).
[6] J. Berakdar, Phys. Rev. A **53**, 2314 (1996).
[7] G. Garibotti and J. E. Miraglia, Phys. Rev. A **21**, 572 (1980).
[8] J. S. Briggs, Phys. Rev. A **41**, 539 (1990).
[9] M. Yu. Kuchiev and S. A. Scheinerman, Usp. Fiz. Nauk. SSSR **158**, 353 (1989) [Sov. Phys. Usp. **32**, 569 (1989)].
[10] A. Lahmam-Bennani, C. Dupré, and A. Duguet, Phys. Rev. Lett. **63**, 1582 (1989).
[11] A. Lahmam-Bennani, A. Duguet, A. M. Grisogono, and M. Lecas, J. Phys. B **25**, 2873 (1992).
[12] R. Dörner, V. Mergel, L. Spielberger, O. Jagutzki, S. Nuttgens, M. Unverzagt, H. Schmidt-Böcking, J. Ullrich, R. E. Olson, K. Tokesi, W. E. Meyerhof, W. Wu, and C. L. Cocke, Nucl. Instrum. Methods Phys. Res. Sect. B **99**, 111 (1995).
[13] B. El Marji, A. Duguet, A. Lahmam-Bennani, M. Lecas, and H. F. Wellenstein, J. Phys. B **26**, L733 (1995).
[14] O. Jagutzki, L. Spielberger, R. Dörner, S. Nüttgens, V. Mergel, H. Schmidt-Böcking, J. Ullrich, R. E. Olson, and U. Buck, Z. Phys. D **36**, 5 (1996).
[15] M. J. Ford, J. H. Moore, M. A. Coplan, J. W. Cooper, and J. P. Doering, Phys. Rev. Lett. **77**, 2650 (1996).
[16] L. Avaldi, P. Belotti, P. Bolognesi, R. Camilloni, and G. Stefani, Phys. Rev. Lett **75**, 1915 (1995).
[17] S. Jetzke and F. H. M. Faisal, J. Phys. B **25**, 1543 (1992).
[18] J. Berakdar, Phys. Lett. A **220**, 237 (1996).
[19] T. Kato, Commun. Pure Appl. Math. **10**, 151 (1957).
[20] M. Abramowitz and I. Stegun, *Pocketbook of Mathematical Functions* (Verlag Harri Deutsch, Frankfurt, 1984).
[21] C. R. Myers, C. J. Umrigar, J. P. Sethna, and J. D. Morgan, III, Phys. Rev. A **44**, 5537 (1991).
[22] V. A. Fock, K. Nor. Vidensk. Selsk. Frh. **31**, 138 (1958).
[23] B. Joulakian, C. Dal Cappello, and M. Brauner, J. Phys. B **25**, 2863 (1992).
[24] B. Joulakian and C. Dal Cappello, Phys. Rev. A **47**, 3788 (1993).
[25] C. Dal Cappello and H. Le Rouzo, Phys. Rev. A **43**, 1395 (1991).
[26] R. J. Tweed, J. Phys. B **6**, 270 (1973).
[27] Yu. F. Smirnov, A. V. Pavlitchenkov, V. G. Levin, and G. Neudatchin, J. Phys. B **11**, 20 (1978).
[28] J. Berakdar and H. Klar, J. Phys. B **26**, 4219 (1993).
[29] J. Berakdar, J. Phys. (France) IV **3**, C6-135 (1993).
[30] J. Berakdar, Phys. Rev. A **53**, 2281 (1996).
[31] H. Klar and W. Schlecht, J. Phys. B **9**, 1699 (1976).
[32] G. Wannier, Phys. Rev. **90**, 817 (1953).
[33] J. Berakdar and E. Weigold (unpublished).
[34] M. Pont and R. Shakeshaft, Phys. Rev. A **51**, R2676 (1995).
[35] H. Le Rouzo and C. Dal Cappello, Phys. Rev. A **43**, 318 (1991).

Energy-Exchange Effects in Few-Particle Coulomb Scattering

Jamal Berakdar
Atomic and Molecular Physics Laboratories, Research School of Physical Sciences and Engineering,
Australian National University, Canberra, ACT 0200, Australia
(Received 30 September 1996)

For the description of an arbitrary nonrelativistic three-body Coulomb system an analytical approximate wave function is designed which is correct for large interparticle separations. At shorter distances, where the potential energy dominates the kinetic one, the wave function is a linear mixture of products each consisting of three two-body Coulomb waves propagating *off the two-body* energy shell but *on the total* energy shell. The method is employed for the calculations of multiply differential cross sections for photo-double ionization of helium and for electron, positron, proton, and antiproton-impact ionization of atomic hydrogen. [S0031-9007(97)02917-7]

PACS numbers: 32.80.Fb, 34.10.+x, 34.80.Dp

The description of the correlated dynamics of few charged particles is one of the fundamental unsolved problems in atomic, molecular, and nuclear physics. In addition to the inherent nonseparability of many-body interacting systems, the infinite range of the Coulombic interaction poses a severe obstacle in theoretical treatments. For example, in resonant or direct fragmentation processes involving charged particles the long-range tail of Coulomb forces precludes free asymptotic states of the reaction fragments [1–4], which in turn seriously limits the applicability of standard methods of scattering theory. While the complicated dynamical nature of asymptotic Coulombic states has been unraveled in recent years [1–4], our knowledge of the fragmentation dynamics at finite interparticle distances is still scarce, in particular, if the strength of the different interactions involved is of the same order and a perturbative approach is inappropriate. An adequate description of the short-range dynamics is, however, imperative, since dissociation amplitudes involve the many-body scattering state in the entire Hilbert space.

This study aims at modeling the reaction dynamics of three arbitrary charged particles at finite interparticle separations while maintaining the requirement of exact treatment at infinite interparticle distances. For this purpose, following Refs. [5,6], we split the Hilbert space into an "inner" and a "far zone" depending on whether the total potential is larger or smaller than the kinetic energy. The scattering state in the inner zone is designed with special regard to the fragmentation dynamics. Subsequently, this state is mapped onto the asymptotic solution at the boundary between the inner and the far zone to arrive at an asymptotically correct behavior. Here we operate in a nonrelativistic time-independent framework. To decouple kinematic from dynamical properties we write the eigenfunction Ψ of the total Hamiltonian $\mathcal{H}$, at the total energy E, in the form (atomic units are used throughout)

$$\Psi(\mathbf{r}_{ij}, \mathbf{R}_k) = N \exp(i\mathbf{r}_{ij} \cdot \mathbf{k}_{ij} + i\mathbf{R}_k \cdot \mathbf{K}_k)\overline{\Psi}(\mathbf{r}_{ij}, \mathbf{R}_k), \tag{1}$$

where $\mathbf{k}_{ij}$ denote the momenta conjugate to the interparticle distances $\mathbf{r}_{ij}$, while $\mathbf{R}_k$ refers to the position of particle k with respect to the center of mass of the pair ij. $\mathbf{K}_k$ designates the momentum conjugate to $\mathbf{R}_k$, and N is a normalization factor. The distortion $\overline{\Psi}(\mathbf{r}_{ij}, \mathbf{R}_k)$ is solely due to the presence of the total potential. It can be determined as an eigensolution of an operator H whose properties are most transparent when expressed in the curvilinear coordinate system

$$\begin{aligned} &\{\xi_k = r_{ij} + \hat{\mathbf{k}}_{ij} \cdot \mathbf{r}_{ij}; \xi_m = r_{ij}\}, \\ &\epsilon_{ijk} \neq 0; \quad j > i, k \in [1,3]; \quad m \in [4,6]. \end{aligned} \tag{2}$$

In terms of (2) H decomposes into two *parametrically* coupled differential operators; an operator H_{par} which is differential in the *parabolic* coordinates $\xi_{1,2,3}$ only and an operator acts only on internal degrees of freedom r_{ij} [4]. An additional mixing term arises from the off-diagonal elements of the metric tensor. The parabolic operator H_{par} is exactly separable in the coordinates $\xi_{1\dots3}$ for it factorizes as

$$\begin{aligned} H_{\text{par}} &= \sum_{j=1}^{3} H_{\xi_j}, [H_{\xi_j}, H_{\xi_i}] \\ &= 0; \quad \forall\, i,j \in \{1,2,3\}, \end{aligned} \tag{3}$$

where

$$\begin{aligned} H_{\xi_j} &= \frac{2}{\mu_{lm} r_{lm}} [\partial_{\xi_j} \xi_j \partial_{\xi_j} + i k_{lm} \xi_j \partial_{\xi_j} - \mu_{lm} Z_{lm}]; \\ \epsilon_{jlm} &\neq 0, \quad j \in \{1,2,3\}. \end{aligned} \tag{4}$$

In Eq. (4) μ_{ij}, Z_{lm} denote the reduced mass of the pair ij and their product charge, respectively. Equation (4) is the Schrödinger equation for two-body Rutherford scattering expressed in parabolic coordinates [7]. Hence, within $H \approx H_{\text{par}}$, the three-body system is considered as the sum of three spatially decoupled two-body Coulomb systems on the *two-body energy shell* $E_{ij} = k_{ij}^2/2\mu_{ij}$. The exact regular eigenfunction of the operator H, within $H \approx$

$H_{\rm par}$, has thus the explicit form (outgoing wave boundary conditions are assumed)

$$\begin{aligned}\overline{\Psi}_{\rm par}(\xi_{1\cdots6};\mathbf{k}_{ij}) = {}& {}_1F_1(i\beta_{23},1,-ik_{23}\xi_1)\\ &\times {}_1F_1(i\beta_{13},1,-ik_{13}\xi_2)\\ &\times {}_1F_1(i\beta_{12},1,-ik_{12}\xi_3).\end{aligned} \tag{5}$$

Using Eq. (1), the eigenstate $\Psi_{\rm par}$ of $\mathcal{H}$ is then readily deduced. The Sommerfeld parameters β_{ij} are given by $\beta_{ij} = Z_{ij}\mu_{ij}/k_{ij}$. The asymptotic separability ($\lim_{\xi_{1,2,3}\to\infty} H \to H_{\rm par}$) and the parametric dependence of H_{ξ_j} [Eq. (4)] on internal degrees of freedom can be exploited to introduce coupling between the two-body subsystems [4]. This approach, however, does not account for transitions into intermediate virtual states and is applicable only to two electrons moving in the field of a residual ion [8]. To circumvent these shortcomings we adopt a strategy which is motivated by the measurement process and the analysis of Refs. [5,9]. In a scattering experiment the measurable quantities (observables) are the *asymptotic* momenta $\mathbf{k}_{ij}$ of the emerging reaction fragments (spin and spatial degrees of freedom are considered to be decoupled). In the "reaction zone" these quantum numbers are undetermined. To quantify this picture we define an inner, *momentum-exchange zone* and an outer, *asymptotic zone* depending on whether the total potential or the kinetic energy is the dominant quantity. As is well known [5,6], the boundary between these regimes is the Wannier radius R_w which is a scalar quantity. In the inner zone a two-body subsystem ij can assume any two-body quantum state defined by a particular $\mathbf{k}'_{ij}$, i.e., each two-body subsystem propagates *off the two-body energy shell* E_{ij}. The description of this is well facilitated by Eqs. (3)–(5) since the momenta $\mathbf{k}_{ij}$ enter in Eqs. (4) as dummy parameters and are determined only in the outer asymptotic zone where they are measured. To ensure the invariance of the Schrödinger equation under the introduction of intermediate momenta $\mathbf{k}'_{ij}$ we must operate under the constraint that the total energy E is conserved, i.e., the two-body subsystems exchange an indefinite amount of momentum in the momentum-exchange zone and virtually occupy all (two-body) continuum states available in the energy band $[0,E]$. As the system evolves towards the Wannier boundary R_w the reaction fragments take on the (asymptotic) momenta measured in a scattering reaction. In this model the directions $\hat{\mathbf{k}}_{ij}$ are fixed by the boundary conditions [see Eq. (2)]. The exact (regular) eigenfunctions $\Psi_{\rm par}$ of $\mathcal{H}$ (within $H \approx H_{\rm par}$) are known and characterized by k'_{ij}, with $E'_{ij} \in [0,E]$. The general solution in the inner zone is a linear superposition of $\Psi_{\rm par}(\xi_{1\cdots6};k'_{ij})$,

$$\begin{aligned}\Psi^{\rm in}(\xi_{1\cdots6}) = {}&\mathcal{N}\int d^3\mathbf{k}'_{ij}\, d^3\mathbf{K}'_k\, A_{\mathbf{k}'_{ij}}\Psi_{\rm par}(\xi_{1\cdots6};\mathbf{k}'_{ij})\\ &\times \delta(E-E')\delta^2(\hat{\mathbf{k}}_{ij}-\hat{\mathbf{k}}'_{ij})\delta^2(\hat{\mathbf{K}}_k-\hat{\mathbf{K}}'_k),\end{aligned} \tag{6}$$

where E' is the intermediate total energy. Since $\Psi^{\rm in}$ is a linear combination of eigenstates of $\mathcal{H}$ (within $H \approx H_{\rm par}$) it is obvious that $(\mathcal{H} - E)\Psi^{\rm in} = 0$. To account for the neglected part $H - H_{\rm par}$ the expansion coefficients $A_{\mathbf{k}'_{ij}}$ have to be deduced, e.g., variationally. For many-body continuum states, however, this procedure is intractable. Here only the low-energy part of $A_{\mathbf{k}'_{ij}}$ is needed since the wave function (6) is defined only in the inner, momentum-exchange zone whose boundary (R_w) scales inversely with E [6]. Within our model the expansion coefficients $A_{\mathbf{k}'_{ij}}(\xi_{4\cdots6})$ indicate the occupation probabilities for the intermediate states characterized by $E'_{ij} \in [0,E]$. According to the Wannier threshold analysis [5], the correlated motion in the interaction region is ergodic and hence our assumption $A_{\mathbf{k}'_{ij}}(\xi_{4\cdots6}) = 1$. At the boundary R_w the function $\Psi^{\rm in}$ has to be mapped onto the asymptotic state (5), which can be done as in the R-matrix approach [9]. Here we smoothly connect $\Psi^{\rm in}$ with the asymptotic states (5) at R_w by writing the three-body state in the entire Hilbert space in the form

$$\Psi_{\rm ex}(\xi_{1\cdots6};E) = f\Psi^{\rm in} + (1-f)\Psi_{\rm par}(\xi_{1\cdots6};\mathbf{k}_{ij}), \tag{7}$$

where $f := \exp(-R/R_w)$ is an exponential matching factor and $R := r_{12} + r_{13}$ measures the extent of the three-body system. Since R_w and R are scalar quantities, i.e., they depend on $\xi_{4\cdots6}$ only, the wave function $\Psi_{\rm ex}(\xi_{1\cdots6};E)$ is an eigensolution of the total Hamiltonian within the approximation $H \approx H_{\rm par} = \sum_{j=1}^{3} H_{\xi_j}$. As $\Psi_{\rm par}$ is asymptotically correct for large interparticle separations [2,4] and satisfy the Kato [10] cusp conditions [4] (R is always large in this case) it follows that these properties are directly reflected into $\Psi_{\rm ex}$ ($\lim_{R\gg1} f \to 0$). For $R \gg R_w$ we fall back to Eq. (5); i.e., in a high-energy scattering ($R_w \propto 1/E \to 0$) the escaping particles directly assume their experimentally measured momenta. For $R < R_w$ the two-body subsystems exchange an indefinite amount of energy. At low energies R_w extends to very large distances. The three particles then exchange energies up to infinity for $E \to 0$ and the transformation of the total wave function from $\Psi^{\rm in}$ to $\Psi_{\rm par}$ occurs at very large distances. This implies that properties of scattering amplitudes which are derived from asymptotic arguments are smeared out at threshold. If the integral in Eq. (7) runs over virtual bound states as well, highly excited Rydberg states provide, at lower energies, the major contribution to the wave function $\Psi_{\rm ex}$. If the Hamiltonian $\mathcal{H}$ contains short-range (nuclear) interactions, the second term of Eq. (7) remains unchanged while the signature of these interactions is carried by $\Psi^{\rm in}$.

In a reaction leading to three-body continuum states scattering amplitudes are determined by transition matrices of the form (prior form) $T = \langle\Psi_{\rm ex}|W|i\rangle$, where $|i\rangle$ is the initial state of the three-body system and W is the perturbation operator due to which the final state $\Psi_{\rm ex}$ is achieved. Introducing hyperspherical momenta $\kappa = E'$; $\tan\alpha = (K'_k/k'_{ij})\sqrt{\mu_{ij}/\mu_k}$ where $\mu_k =$

$m_k(m_i + m_j)/\sum_l m_l$, and performing the integrals involved in (6), the amplitude T reads

$$T = T^{\mathrm{asy}} + C \int_0^{\pi/2} d\alpha \sin^2 2\alpha T^{\alpha}, \tag{8}$$

where $C = \mathcal{N} \mu_{ij}^{3/2} \mu_k^{3/2} E^2$ and

$$T^{\alpha} = \langle f \Psi_{\mathrm{par}}(\xi_{1\cdots 6}; \alpha)|W|i\rangle,$$

$$T^{\mathrm{asy}} = \langle (1 - f)\Psi_{\mathrm{par}}(\xi_{1\cdots 6}; k_{ij})|W|i\rangle. \tag{9}$$

If virtual bound states are included the integral in Eq. (8) contains a sum over these states. From Eq. (8) it is obvious that a transition to an asymptotic state defined by the measured momenta $\mathbf{k}_{ij}$ occurs via an infinite number of intermediate virtual transitions, given by T^{α}, which may interfere to result in the measured cross section.

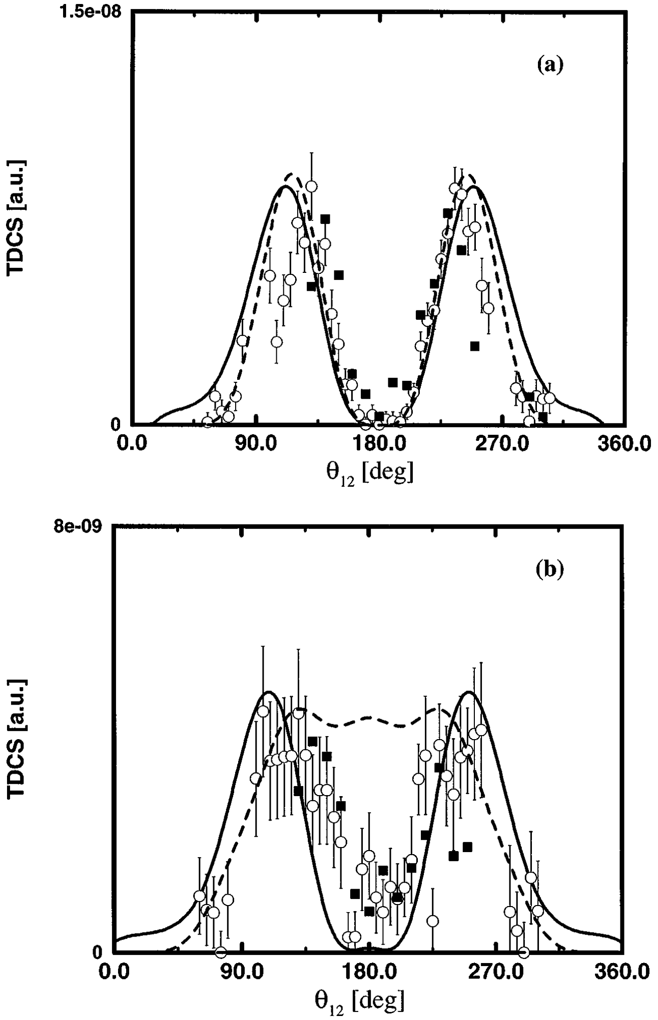

FIG. 1. (a) The triply differential cross section (TDCS) for the double ionization of He($^1S^e$) by a linearly polarized photon. One electron is detected along the direction of the polarization vector (ϵ) while the other electron is detected, in coincidence with the first one, under an angle θ_{12} with respect to ϵ. The two equal-energy electrons escape with a total excess energy of 4 eV. The relative experimental data are due to [16]. Representing the final state by Eq. (7) [or $\Psi_{\mathrm{ex}} \approx \Psi_{\mathrm{par}}$] results in the solid [dashed curve scaled down by 1.8]. The initial state is represented by a Hylleraas wave function which contains radial and angular correlations. (b) The same as in (a) but the electron fixed to ϵ is detected with an energy of 3.3 eV.

The present method is applicable to an arbitrary three-body Coulomb system. Here we investigate the one-photon double ionization of He($^1S^e$) (DPI) and include in the integral (6) continuum states only. As momentum-exchange effects occur at shorter distances ($R < R_w$) the velocity form of the dipole operator is employed (first-order perturbation theory for the radiation field is assumed). Neglecting energy exchange between the two-body subsystems results in the approximation $\Psi_{\mathrm{ex}} = \Psi_{\mathrm{par}}$, which has been employed for the calculations of the relative angular distributions of electrons following DPI with remarkable success [11,12]. From Figs. 1(a) and 1(b) it is evident that energy-exchange effects strongly depend on the configuration in which the two electrons are emitted. A drastic influence is observed when the two electrons escape with low and asymmetric energies [Fig. 1(b)] in which case the symmetry of the initial-state ($^1S^e$) and the final-state electronic repulsion imposes less severe restrictions on the angular distribution than in the case of equal-energy electrons [12]. In Fig. 2 the electron- and positron-impact ionization of atomic hydrogen is considered. For electron impact the approximation $H - H_{\mathrm{par}} = 0$ leads to some discrepancy between theory and experiment in the binary region. The recoil regime is well described. The present model provides no evidence for two additional shoulders predicted by the convergent close coupling (CCC) calculations [13]. Differences between electron and positron impact as observed in Fig. 2 can be traced to final-state interactions. For proton and antiproton impact [Figs. 3(a) and 3(b)] the projectile is mainly scattered into the forward direction and different

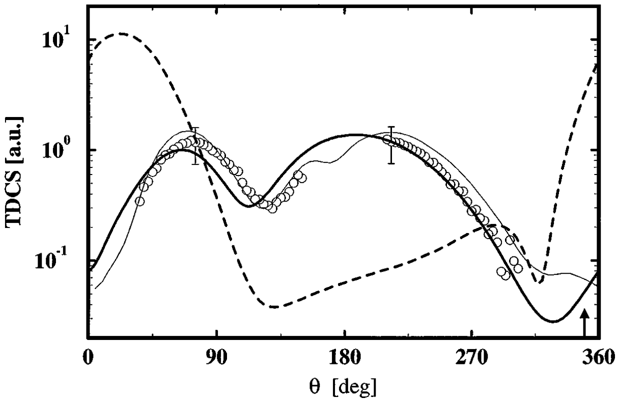

FIG. 2. The TDCS for the coplanar electron-impact ionization of atomic hydrogen calculated using the wave function (7) (solid curve). The incident energy is 54.4 eV. One electron is detected under an angle of 350° with respect to the incident direction $\mathbf{k}_i$, whereas the other one is detected under an angle θ with respect to $\mathbf{k}_i$ and with an energy of 5 eV. Experimental data are due to Ref. [17] with error bars indicating the uncertainty in the absolute value. The CCC results (solid light curve) are taken from Ref. [13] where comparison with a number of other models is made. Predictions of the present study for positron impact are included (dashed curve).

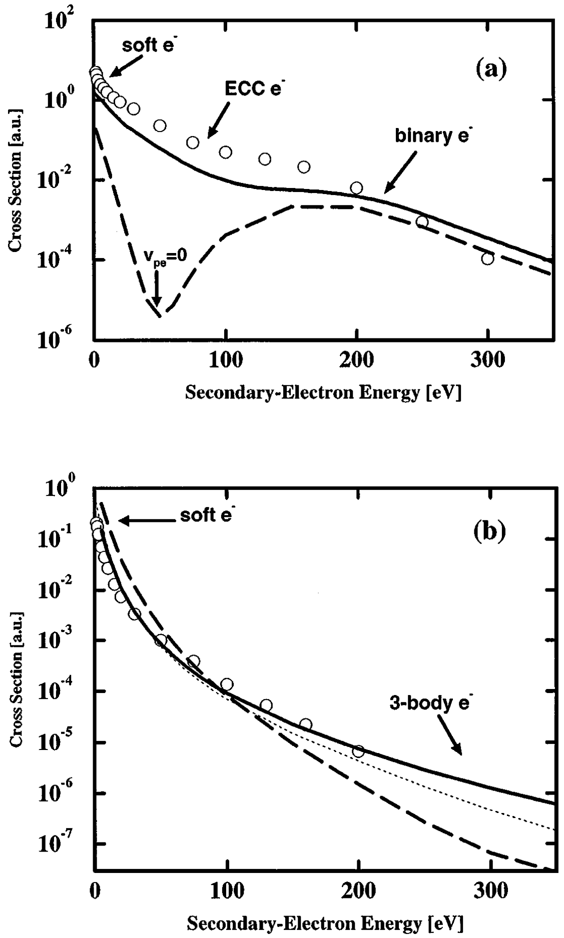

FIG. 3. The energy spectrum of secondary electrons ejected from atomic hydrogen upon proton (solid curve) and antiproton (dashed curve) impact with incident energy of 95 keV. In (a) the electrons are detected at an angle of 15° with respect to the incident beam, whereas in (b) this angle is fixed to 150°. In (b) calculations using $\Psi_{\mathrm{ex}} \approx \Psi_{\mathrm{par}}$ are included (dotted curve). The absolute experimental data are due to Ref. [18] where comparison with other theories can be found.

ionization mechanisms are distinguished via the particles' relative velocities (since $Z_{ij} = \pm 1$). The most notable difference between proton and antiproton impact appears at a diminishing relative velocity vector $\mathbf{v}_{\mathrm{pe}}$ of projectile-electron system [Fig. 3(a)]. This is due to the decisively different analytical behavior of the projectile-electron density of state which, for $v_{\mathrm{pe}} \to 0$, is of the form $\exp(-1/v_{\mathrm{pe}}) \to 0$ for antiproton and $1/v_{\mathrm{pe}} \to \infty$ for proton impact [14,15]. The ridge structure in Fig. 3(a) which appears at an electron velocity equal to twice the projectile's velocity (in the target frame) is due to a direct projectile-electron encounter [14]. Energy-exchange effects are prominent in the region where a high-energy electron is ejected backwards [Fig. 3(b)]. In this case the electron cannot be viewed as emitted in the field of the target (slow soft electrons) nor in the field of the projectile [electrons captured into the projectile's continuum (ECC), ECC electrons with $v_{\mathrm{pe}} \to 0$]. Detailed study showed that these electrons are ejected via multiple scattering from both nuclei in events with large deflection of the projectile.

In conclusion, transitions into two-body virtual states have been included for the first time into analytical correlated three-body wave functions with correct asymptotic behavior. To elucidate the effect of these transitions, scattering amplitudes for photo-double ionization and electron, positron, proton, and antiproton-impact ionization leading to three-body continuum final state have been calculated.

I am grateful to S. Buckman, E. Weigold, M. Hoogerland, and S. Mazevet for helpful comments and to A. Huetz for communicating his data. This work was supported by the Alexander von Humboldt Foundation and the Australian National University.

[1] L. Rosenberg, Phys. Rev. D **8**, 1833 (1973).
[2] M. Brauner, J. S. Briggs, and H. Klar, J. Phys. B **22**, 2265 (1989).
[3] E. O. Alt and A. M. Mukhamedzhanov, Phys. Rev. A **47**, 2004 (1993).
[4] J. Berakdar, Phys. Rev. A **53**, 2314 (1996); **54**, 1480 (1996); Phys. Lett. A **220**, 237 (1996).
[5] G. Wannier, Phys. Rev. **90**, 817 (1953).
[6] A. R. P. Rau, Phys. Rev. A **4**, 207 (1971); Phys. Rep. **110**, 369 (1984).
[7] H. A. Bethe and E. E. Salpeter, *Quantum Mechanics of One- and Two-Electron Atoms* (Springer, Berlin, 1957).
[8] J. Berakdar and J. S. Briggs, Phys. Rev. Lett. **72**, 3799 (1994); J. Phys. B **27**, 4271 (1994); **29**, 2289 (1996).
[9] K. A. Berrington, P. G. Burke, K. Butler, M. J. Seaton, P. J. Storey, K. T. Taylor, and Yu Yan, J. Phys. B **20**, 6379 (1987).
[10] T. Kato, Commun. Pure Appl. Math. **10**, 151 (1957).
[11] F. Maulbetsch, M. Pont, J. S. Briggs, and R. Shakeshaft, J. Phys. B **28**, L341 (1995).
[12] F. Maulbetsch, Ph.D. thesis, Freiburg University, 1995.
[13] I. Bray, D. A. Konovalov, I. E. McCarthy, and A. T. Stelbovics, Phys. Rev. A **50**, R2818 (1994).
[14] P. D. Fainstein, V. H. Ponce, and R. D. Rivarola, J. Phys. B **24**, 3091 (1991).
[15] J. Berakdar, J. S. Briggs, and H. Klar, Z. Phys. D **24**, 351 (1992).
[16] A. Huetz, L. Andric, A. Jean, P. Lablanquie, P. Selles, and J. Mazeau, in *Proceedings of XIX International Conference on the Physics of Electronic and Atomic Collisions, Whistler,* edited by L. Dube' *et al.* (AIP Press, New York, 1995).
[17] J. Röder (private communication).
[18] G. W. Kerby III, M. W. Gealy, Y.-Y. Hsu, and M. E. Rudd, Phys. Rev. A **51**, 2256 (1995).

Asymmetric Formation of Positronium Continuum States Following Positron-Impact Ionization of H_2

Jamal Berakdar*
Max-Planck Institute for Microstructure Physics, Weinberg 2, 06120 Halle, Germany

(Received 7 April 1998)

The fully differential cross section for the positron- and electron-impact ionization of H_2 is calculated. For positron impact the results are contrasted against a recent experiment which evidently shows the influence of the electron capture to a low-lying positronium continuum state. From a detailed analysis it is deduced that the capture probability is dependent on the orientation of the electron-positron relative momentum vector with respect to the residual ion. Within the used model, this asymmetric positronium formation is traced back to the distortion of the positron motion by the two-center potential formed by the residual ion and the secondary electron. [S0031-9007(98)06857-4]

PACS numbers: 34.85.+x, 34.10.+x, 34.80.Gs, 34.90.+q

A detailed understanding of correlated many-body scattering states is of fundamental importance for diverse fields of physics such as discharge and plasma physics, fusion physics, and physics of the upper atmosphere. Such continuum states are usually achieved as the final outcome of charged particle- and photon-impact ionization. Recent technological advances in multiple detection techniques have rendered possible an unprecedented insight into the properties of these states: the energy and momentum transfer to the many-body continuum can be probed independently by virtue of equivelocity heavy- and light-particle impact; for a fixed amount of energy and momentum transferred to the final state, the open reaction channels as well as the total potential surface can be varied using particle and antiparticle projectiles.

A unified description of all of these facets is a major challenge for current theoretical investigations.

The present study is motivated by a recent kinematically complete experiment [1] in which a H_2 molecule is ionized upon positron impact. The resulting final continuum states which consist of a positron and an electron moving in the field of H_2^+ [hereafter referred to as $(e^- e^+ H_2^+)$] have been simultaneously resolved in angle and energy.

Contrasting this final channel with that achieved in electron-impact ionization [two electrons in the double continuum of a residual ion, labeled hereafter by $(e^- e^- H_2^+)$], two distinctive differences can be noted.

(i) Evidently the total potential surface is markedly different in both cases [2] which results in completely different dynamics. This is particularly reflected by the decisively different threshold laws for total breakup (cf. [3–5] and references therein).

(ii) The indistinguishability of the two electrons introduces exchange effects in the case of $(e^- e^- H_2^+)$, i.e., the cross sections are statistical mixtures of triplet and singlet scattering cross sections. While this effect is absent in the case of $(e^- e^+ H_2^+)$, an additional channel opens, namely, that of positronium formation.

In the experiment of Kövér and Laricchia [1], capture of the ejected electron to low-lying positronium continuum states can be identified. This channel shows up as a rapid increase in the cross section when the electron approaches the positron in velocity space. The functional dependence of this enhancement is dictated by the electron-positron Coulomb density of states (CDS) (see below). Previous experimental and most of the theoretical work on positron-atom ionizing collisions concentrated on the analysis of the secondary electron spectra while the scattered positron is being undetected [6–15]. No unambiguous evidence as to the existence of the electron capture to the positron continuum has been found. On the other hand, the phenomenon of electron capture to the projectile's continuum (ECC) is well established in heavy ion-atom ionizing collisions both experimentally and theoretically [17–28]. From these studies it has been concluded that a theoretical description of the energy and angular distributions of the secondary electrons must account for the interaction of these electrons both with the residual ion and the projectile [29]. For light-particle impact, such as positron, the theoretical description is even more challenging, for in this case the projectile is deflected through very large angles [11,15]. In contrast, in the case of heavy-particle impact the projectile is scattered around the forward direction. Therefore, for the description of the $(e^- e^\pm H_2^+)$ final states, at least, a genuine three-body model is required. In this work we model the final state by a wave function originally derived for ion-atom collisions [16] and recently applied for electron and positron ionizing scattering [14] (atomic units, a.u., are used throughout; corrections due to finite electron mass as compared to that of the proton are neglected):

$$\begin{aligned}\Psi(\mathbf{r}_a, \mathbf{r}_b) \approx{}& (2\pi)^{-3} N_a N_b N_{ab} e^{i\mathbf{p}_a\cdot\mathbf{r}_a} e^{i\mathbf{p}_b\cdot\mathbf{r}_b} \\ &\times {}_1F_1[i\alpha_a, 1, -i(p_a r_a + \mathbf{p}_a \cdot \mathbf{r}_a)] \\ &\times {}_1F_1[i\alpha_b, 1, -i(p_b r_b + \mathbf{p}_b \cdot \mathbf{r}_b)] \\ &\times {}_1F_1[i\alpha_{ab}, 1, -i(p_{ab} r_{ab} + \mathbf{p}_{ab} \cdot \mathbf{r}_{ab})],\end{aligned} \quad (1)$$

where $\mathbf{r}_{a/b}$ are, respectively, the coordinates of the positron and the electron with respect to the residual ion,

$\mathbf{r}_{ab} = \mathbf{r}_a - \mathbf{r}_b$, and $\mathbf{p}_{ab}$ is its conjugate momentum. The vector momenta of the emerging positron and electron are, respectively, labeled $\mathbf{p}_a$ and $\mathbf{p}_b$, and ${}_1F_1[a,b,c]$ is the confluent hypergeometric function. The normalization factors N_j are given by

$$N_j = \exp(-\pi\alpha_j/2)\Gamma(1 - i\alpha_j), \qquad j = a, b, ab\,, \tag{2}$$

with the Sommerfeld parameters being $\alpha_a = Z_p Z_t/p_a$, $\alpha_b = -Z_t/p_b$, and $\alpha_{ab} = -Z_p/(2p_{ab})$, where Z_p and Z_t are the projectile and the final-state ion charge, respectively. The cross section, differential in the energies E_a, E_b and the solid angles Ω_a, Ω_b of the escaping particles, is then given by

$$\sigma(\Omega_a, \Omega_b, E_b) = C|\langle\Psi(\mathbf{r}_a, \mathbf{r}_b)|V|\varphi_{\mathbf{p}_0}(\mathbf{r}_a)\Phi(\mathbf{r}_b)\rangle|^2, \tag{3}$$

where $C = (2\pi)^4 p_a p_b/p_0$ and $\varphi_{\mathbf{p}_0}$ is a plane wave describing the projectile incident with momentum $\mathbf{p}_0$. The H_2 target, as described by $\Phi(\mathbf{r}_b)$, is assumed to be composed of two noninteracting hydrogen atoms. Furthermore, the relaxation time of the final-state ion H_2^+ is supposed to be much longer than the interaction time so that a frozen-core approximation can be applied. In Eq. (3) the perturbation operator V is the scattering potential of the incoming particle from the active electron and the residual ion.

The first Born approximation (FBA) is obtained from this scheme in the limit $\alpha_a \equiv 0 \equiv \alpha_{ab}$. It is well known that the FBA yields cross sections that depend on the velocity of the impinging projectile and the square of its charge. Therefore, the FBA does not distinguish between particle and antiparticle impact at the same impact velocity.

In contrast, the full calculations (Fig. 1) reveal a drastic difference between reactions leading to $(e^- e^- H_2^+)$ or $(e^- e^+ H_2^+)$ continuum, in particular, in the region where the escaping particles emerge with equal velocities. This difference is readily understood from the CDS of the electron-electron and electron-positron subsystems that is described by $|N_{ab}|^2 = 2\pi\alpha_{ab}[\exp(2\pi\alpha_{ab}) - 1]^{-1}$. In the limit of $p_{ab} \to 0$, $|N_{ab}|^2$ attains the behavior

$$\lim_{p_{ab}\to 0} |N_{ab}|^2 \to -2\pi\alpha_{ab} \to \infty\,, \qquad \text{for } Z_p > 0\ (e^+ \text{ impact})\,, \tag{4}$$

$$\lim_{p_{ab}\to 0} |N_{ab}|^2 \to 2\pi\alpha_{ab}\exp(-2\pi\alpha_{ab}) \to 0\,, \qquad \text{for } Z_p < 0\ (e^- \text{ impact})\,. \tag{5}$$

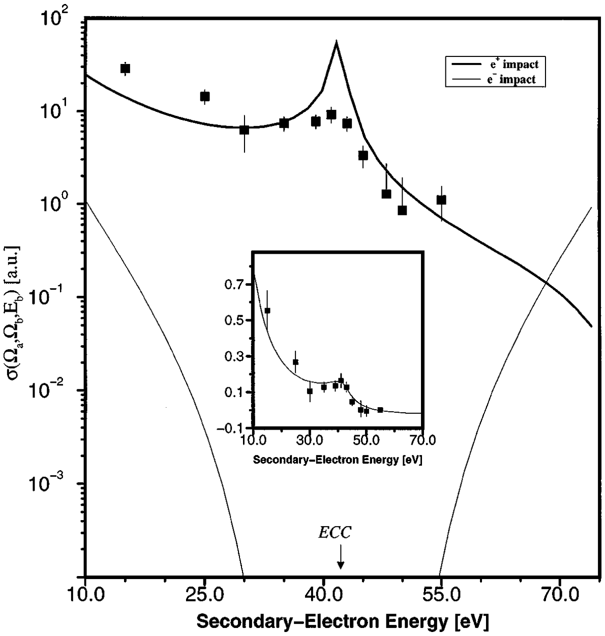

FIG. 1. The positron (thick curve) and electron (light curve) impact ionization cross sections of H_2 as a function of the secondary-electron energy. The solid squares are the experimental data of Ref. [1]. The incident energy is 100 eV. The absolute value of the experimental cross section is unknown. Both emerging particles are detected in the forward direction. The inset shows the positron calculations convoluted with the experimental resolution, as given by [1]. The position of the ECC peak is indicated.

From Eq. (4) it is clear that $\sigma(\Omega_a, \Omega_b, E_b)$ possesses a first order pole at $p_{ab} = 0$ in the case of e^+ impact that signifies the ECC channel. Because of the localized nature of this pole it is very important to account for the experimental resolution in order to compare with the experimental finding [30]. In fact, as shown in the inset (Fig. 1), the convolution with the experimental resolution, as given by Ref. [1], leaves only a small peak in the cross section at $p_{ab} = 0$. This is quite different from ion-atom collision where, due to the basically undeflected projectile, the ECC peak is much more pronounced even after convolution and with the scattered projectile being undetected (see, e.g., [27]).

For the following analysis it is important to note, however, that the general slope of σ around the ECC position is not much affected by the convolution, as can be observed in Fig. 1. Unfortunately, for the $(e^- e^- H_2^+)$ system there is no available experimental data in the present scattering geometry.

The obvious difference between e^- and e^+ impact, as seen in Fig. 1, is simply a reflection of the markedly different analytical behavior of (4) and (5). This effect also shows up in heavy-particle and antiparticle impact [31]. In our case, however, exchange introduces additional phenomena which can be unraveled by analyzing the quantity

$$\sigma^n(\Omega_a, \Omega_b, E_b) = \frac{\sigma(\Omega_a, \Omega_b, E_b)}{|N_{ab}|^2}\,. \tag{6}$$

For the case of Fig. 1 we depict in Fig. 2 the normalized cross section σ^n. As is more clear from Fig. 2, due to exchange in the case of e^- impact, σ^n (and σ) is symmetric with respect to the ECC position. Thus, for e^- impact exchange imposes a continuous σ^n at $p_{ab} = 0$.

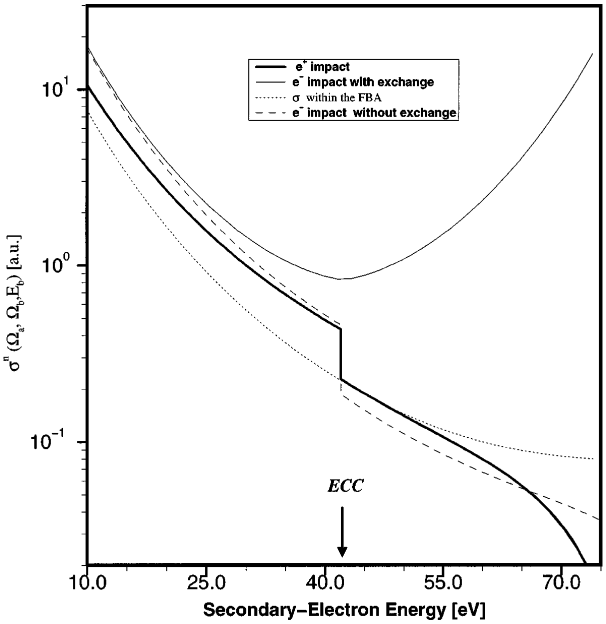

FIG. 2. The same as in Fig. 1, but the normalized cross section σ^n, as defined by (6), is considered. The cross sections σ^n for e^- impact with (light solid curve) and without (dashed curve) exchange are depicted along with σ^n for e^+ impact (solid thick curve). The cross section σ (3) (not σ^n) as predicted by the FBA is also shown (dotted curve, same results for e^- and e^+ impact).

Neglecting exchange reveals remarkable similarities between e^+ and e^- impact except for the region of very slow positrons in which case the repulsion between H_2^+ and the positron leads to a vanishing cross section [this is described by a positron-ion CDS, $|N_a|^2$, that behaves similar to Eq. (5) for slow e^+]. It is worthwhile to note that the slope of σ^n for e^+ and e^- (without exchange) is given by σ (not σ^n) as calculated within the FBA. In fact, even a plane-wave impulse approximation (PWIA) yields the same slope behavior of σ as within the FBA. The cross section σ^{PWIA} within the PWIA can be evaluated from the above model by setting $\alpha_a \equiv 0 \equiv \alpha_b, \alpha_{ab} \equiv 0$. The result is $\sigma^{\mathrm{PWIA}} = C/(2\pi^4 q^4)\,|\tilde{\Phi}(\mathbf{p}_{\mathrm{ion}})|^2$, where $\tilde{\Phi}(\mathbf{p}_{\mathrm{ion}})$ is the Fourier transform of Φ, $\mathbf{p}_{\mathrm{ion}}$ is the recoil momentum of the ion, and q is the momentum transfer. Thus the slopes of the σ as depicted in Fig. 1 are determined by the Compton profile of the initially bound state and the projectile-electron interaction potential in momentum space. Superimposed on that is then $|N_{ab}|^2$ and exchange requirements in the case of electron impact.

A much more delicate feature of the σ^n is the discontinuity at $p_{ab} \to 0$, i.e., the capture probability is dependent on whether $\mathbf{p}_a \to \mathbf{p}_b + \boldsymbol{\epsilon}$ or $\mathbf{p}_a \to \mathbf{p}_b - \boldsymbol{\epsilon}$, where $\epsilon \ll 1$. This behavior has also been encountered in ion-atom ionizing collisions (both experimentally and theoretically) [16,23,28,29,32–35] and has been dubbed *cusp asymmetry*. To my knowledge there is as yet no clear physical explanation of the origin of this asymmetry and, as will be shown below, this study sheds new light on this question but certainly does not resolve it.

Here we define the cusp asymmetry as

$$\Delta = \lim_{(E/2-E_b)\to 0^+} \sigma^n - \lim_{(E/2-E_b)\to 0^-} \sigma^n,$$

where E is the total excess energy. In the case of e^- impact the cusp asymmetry Δ is disguised by exchange (Fig. 2); its sign is the same as that observed in e^+ impact. This rules out an explanation of this asymmetry in terms of screening. Further calculations (not illustrated here for space limitations) showed the following: (a) The asymmetry diminishes at higher energies (>1 keV) and increases when the impact energy is lowered, and (b) the sign of the asymmetry is not dependent on the emission angles of the final-state products; i.e., if the ejected electron and the scattered projectile are detected both in the backward direction we end up with a behavior similar to that depicted in Fig. 2.

As mentioned above, the experimental data of Fig. 1 follow the slope of the calculated cross section and hence hint at the existence of Δ. Further ongoing experimental efforts should provide more insight into the exact value of Δ.

As realized in the early studies on ion-atom collision [32,33], a description of Δ requires a higher order treatment. This is obvious from Fig. 2. The FBA yields no asymmetry. In addition, if we neglect final-state

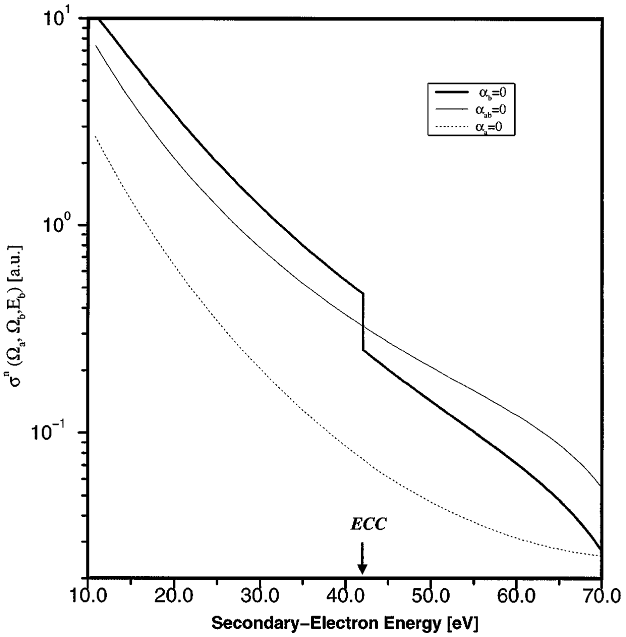

FIG. 3. The e^+-impact case for the same geometry as in Fig. 1 is studied. Neglect of the positron-residual ion final-state interaction [$\alpha_a \equiv 0$ in Eq. (1)] yields the dotted curve, whereas if we disregard the interaction between the emerging e^- and e^+ [$\alpha_{ab} \equiv 0$ in Eq. (1)] we end up with the solid light curve. The final-state interaction of the secondary electron with the ion has basically no influence on the cusp asymmetry [$\alpha_b \equiv 0$ in Eq. (1) leads to the thick solid curve].

interactions between the escaping particles (i.e., within an independent particle model) σ would be proportional to the FBA cross section [15] and we end up thus with vanishing Δ. Furthermore, as shown in Fig. 3, the final-state interaction of the ejected electron with the residual ion produces no contribution to Δ [i.e., Δ is invariant upon the substitution $\alpha_b \equiv 0$ in Eq. (1)]. In contrast, only the simultaneous final-state interaction of the positron with the emitted electron and the residual ion leads to an asymmetric ECC cusp. Neglecting one of these interactions results in a breakdown of Δ. In other words, within the present model, this asymmetric formation of positronium continuum states can be viewed as the result of the positron propagating in a two-center potential formed by the interaction with the continuum electron and the residual ion.

I am grateful to G. Laricchia for providing her experimental data and, together with J. S. Briggs and J. Macek, for stimulating discussions.

---

*Email address: jber@mpi-halle.de

[1] A. Kövér and G. Laricchia, Phys. Rev. Lett. **80**, 5309 (1998).
[2] C. D. Lin, Phys. Rep. **257**, 1–83 (1995).
[3] W. Ihra, J.H. Macek, F. Mota-Furtado, and P.F. O'Mahony, Phys. Rev. Lett. **78**, 4027 (1997).
[4] J.-M. Rost, J. Phys. B **28**, 3003 (1995).
[5] P. Ashly, J. Moxom, and G. LaricchiaPhys. Rev. Lett. **77**, 1250 (1996).
[6] M. Brauner and J.S. Briggs, J. Phys. B **19**, L325 (1986).
[7] A. Kövér, R.M. Finch, G. Laricchia, and M. Charlton, J. Phys. B **30**, L507 (1997), and references therein.
[8] A. Kövér, G. Laricchia, and M. Charlton, J. Phys. B **27**, 2409 (1994).
[9] A. Kövér, G. Laricchia, and M. Charlton, J. Phys. B **25**, L613 (1992).
[10] D.R. Schultz, R.E. Olson, and C.O. Reinhold, J. Phys. B **24**, 521 (1990).
[11] D.R. Schultz and C.O. Reinhold, J. Phys. B **23**, L9 (1990).
[12] P. Mandal, K. Roy, and N.C. Sil, Phys. Rev. A **33**, 756 (1986).
[13] R. A. Sparrow and R. E. Olson, J. Phys. B **27**, 2647 (1994).
[14] M. Brauner, J. Briggs, and H. Klar, J. Phys. B **22**, 2265 (1989).
[15] J. Berakdar and H. Klar, J. Phys. B **26**, 3891 (1993).
[16] C.R. Garibotti and J.E. Miraglia, J. Phys. B **14**, 863 (1981).
[17] A. Salin, J. Phys. B **2**, 631 (1969).
[18] J.H. Macek, Phys. Rev. A **1**, 235 (1970).
[19] Y. B. Band, J. Phys. B **18**, 2557 (1974).
[20] K. Dettmann, K.G. Harrison, and M.W. Lucas, J. Phys. B **7**, 269 (1974).
[21] M.M. Duncan, M.G. Menendez, F.L. Eisele, and J.H. Macek, Phys. Rev. A **15**, 1785 (1977).
[22] M. Suter, C.R. Vane, I.A. Sellin, S.B. Elston, G.D. Alton, R.S. Thoe, and R. Lauber, Phys. Rev. Lett. **41**, 399 (1978).
[23] G. A. Glas, P. Engar, S. D. Berry, M. Breining, R. Deserio, S. B. Elston, and I. A. Sellin, Nucl. Instrum. Methods Phys. Res., Sect. B **10/11**, 138 (1985).
[24] C.R. Vane, I.A. Sellin, M. Suter, G.D. Alton, S.B. Elston, P.M. Griffin, and R.S. Thoe, Phys. Rev. Lett. **40**, 1020 (1978).
[25] G. Bissinger, J.M. Joyce, and R. Mehta, Nucl. Instrum. Methods Phys. Res., Sect. B **40/41**, 33 (1989).
[26] J.O.P. Pederson, P. Hvelplund, A.G. Petersen, and P.D. Fainstein, J. Phys. B **24**, 4001 (1991).
[27] D.H. Lee, P. Richard, T.J.M. Zouros, J.M. Sanders, J.L. Shinpangh, and H. Hidmi, Phys. Rev. A **24**, 97 (1990).
[28] J. Berakdar, J.S. Briggs, and H. Klar, Z. Phys. D **24**, 351 (1992).
[29] N. Stolterfoht, D. Schneider, J. Tanis, H. Altevogt, A. Salin, P.D. Fainstein, R. Rivarola, J.P. Gradin, J.N. Scheurer, S. Andriamonje, D. Bertault, and J.F. Chemin, Europhys. Lett. **4**, 899 (1987).
[30] W. Oswald, R. Schramm, and H.D. Betz, Phys. Rev. Lett. **62**, 1114 (1989).
[31] P.D. Fainstein, V.H. Ponce, and R.D. Rivarola, J. Phys. B **21**, 2989 (1988).
[32] R. Shakeshaft and L. Spruch, Phys. Rev. Lett. **41**, 1037 (1978).
[33] R. Shakeshaft and L. Spruch, J. Phys. B **11**, L457 (1978).
[34] J.E. Miraglia and J.H. Macek, Phys. Rev. A **43**, 5919 (1991).
[35] P.D. Fainstein, V.H. Ponce, and R.D. Rivarola, J. Phys. B **24**, 3091 (1991).

PHYSICS LETTERS A

Physics Letters A 277 (2000) 35–41

www.elsevier.nl/locate/pla

Cluster expansion of the many-body Green operator

J. Berakdar

Max-Planck-Institut für Mikrostrukturphysik, Weinberg 2, 06120 Halle, Germany

Received 8 September 2000; received in revised form 16 October 2000; accepted 16 October 2000
Communicated by B. Fricke

Abstract

A scheme is presented for expressing the many-body Green operator of an interacting system in terms of Green operators of systems with a fewer number of interacting particles. The method relies on an exact algebraic operator identity proved in this work. Furthermore, we present a hierarchical approximation that reduces successively the many-body problem to a lower dimensional solvable problem. Recipes for higher order corrections are given and practical applications are pointed out. © 2000 Elsevier Science B.V. All rights reserved.

In recent years there has been an impressive progress in computational material science [1]. This development is driven by the unprecedented growth of computational resources and by the demand for yet more precise information on technologically relevant material properties, such as the optical, transport and magnetic characteristics. On the microscopic level, those properties can be obtained from the eigensolutions of the many-body quantum Hamiltonian of the system under study. Thus, one has to deal with the notoriously difficult many-body problem in a computationally acceptable manner. For this purpose remarkably successful and efficient conceptual schemes have been developed where the multi-particle system is mapped onto a one body problem for a particle moving in an effective (non-local) field created by all the other constituents of the system [2,3]. Usually, this effective field is further simplified according to certain recipes such as those provided by the local approximation within the density functional theory [4]. It is these theoretical concepts that rendered possible the calculation of the behavior of many particle systems. A wealth of static properties, such as the ground state energies are well described by such effective one particle methods for a considerable number of elements. However, static features of strongly correlated systems, such as transition metal oxides, still posse a challenge to single particle theories [3]. In addition, for the theoretical description of the many-body excitation spectrum [6] and for the treatment of dynamical processes, such as many particle reactive scattering, methods have to be envisaged that go beyond the single particle picture.

For example, correlated many-body states are a prerequisite for the theoretical formulation of recent measurements of the double and triple electronic excitation of localized or delocalized electronic compounds by one ultraviolet photon [5,7,8]. Recent technological advances have made it even possible to explore in full details the many-body continuum spectrum of four and more interacting particles [8–13] where numerical calculations are absent. Thus, it is desirable to develop, for many-body interacting systems, conceptually sound methods and schemes of approximations that can be numerically implemented.

E-mail address: jber@mpi-halle.de (J. Berakdar).

PII: S0375-9601(00)00676-9

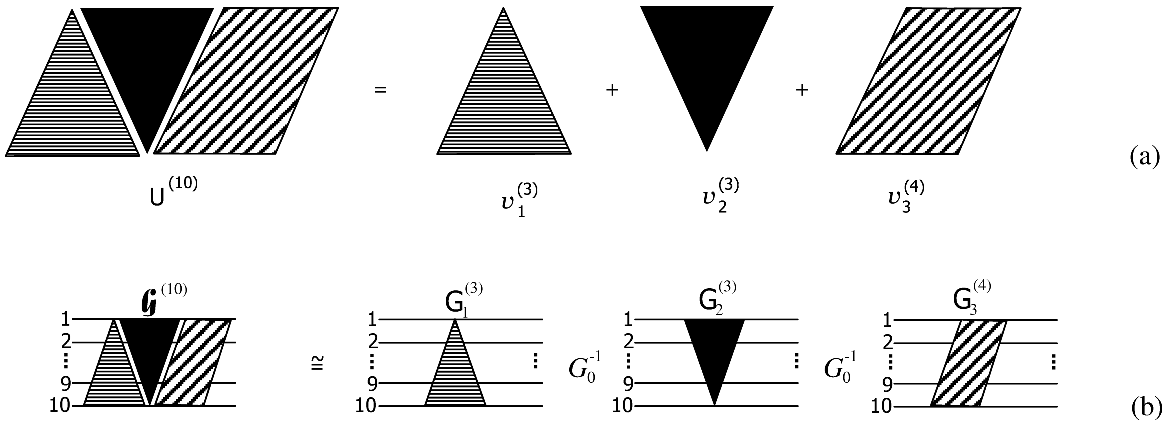

Fig. 1. (a) A pictorial representation of the potential decomposition (1) for a system consisting of three clusters. The coupled particles are located at the corners of the geometrical shapes. Thus, two of the clusters contain three interacting particles each, whereas one cluster encompasses four coupled particles. The shading of the shapes indicates that the various clusters might have different inherent internal dynamics. (b) A diagrammatic illustration of the Green operator expansion (16) which corresponds to the decomposition in (a). Each of the diagrams stands for a Green operator (written above it) with an interaction symbolized by the geometrical shapes (explained in (a)). The particles are indicated by straight lines.

In this study we design for an interacting many-body system a theoretical framework, within which the many-body state is derived cumulatively from the solution of a lower dimensional problem. To deal with strongly correlated systems, the treatment should not give a preference to a certain interaction. Furthermore, the method provides a systematic and mathematically sound scheme for approximations that are computationally manageable and allows, when desirable, to incorporate well established single particle and perturbative approaches.

The fundamental quantity that describes the behavior of the quantum N body system is the total Green operator $\mathcal{G}^{(N)}$ which is the resolvent of the respective Hamiltonian. Our goal is thus to find exact expressions for $\mathcal{G}^{(N)}$ in terms of quantities of lower dimensionality that are computationally accessible. To this end we consider two distinct cases.

Case 1. The N-body system can be broken down into L clusters. The cluster labeled by the number l contains m_l coupled particles. Thus, we require $\sum_l^L m_l = N$. The m_l particles within each subdivision are interacting via the potential $v_l^{(m_l)}$ so that the total interaction $U^{(N)}$ can be cast in the form

$$U^{(N)} = \sum_l^L v_l^{(m_l)}. \tag{1}$$

The non-relativistic total Hamiltonian of the system can be written as $H^{(N)} = K + U^{(N)}$, where K is the kinetic energy operator. Fig. 1(a) demonstrates geometrically decomposition (1).

Let us introduce the Green operator G_m of a system with the total potential $\sum_{j=1}^m v_j^{(m_j)}$, $m \in [1, L]$. Thus, $\mathsf{G}_L \equiv \mathcal{G}^{(N)}$, where $\mathcal{G}^{(N)}$ is the Green operator of the total system. As

$$H^{(N)} = \left(K + \sum_{j=1}^{m-1} v_j^{(m_j)} \right) + \sum_{j=m}^{L} v_j^{(m_j)}$$

we can treat G_{m-1} as a reference Green operator and deduce from the Lippmann–Schwinger equation the recurrence relations

$$\mathcal{G}^{(N)} \equiv \mathsf{G}_L = \mathsf{G}_{L-1}\big[\mathbf{1} + v_L^{(m_L)}\mathsf{G}_L\big], \tag{2}$$

$$\mathsf{G}_{L-1} = \mathsf{G}_{L-2}\big[\mathbf{1} + v_{L-1}^{(m_{L-1})}\mathsf{G}_{L-1}\big]. \tag{3}$$

These equations are reformulated in the simple but exact product expansion

$$\mathcal{G}^{(N)} = \prod_{j=1}^{L-1}\big[\tilde{\mathsf{G}}_j G_0^{-1}\tilde{\mathsf{G}}_{j+1}\big], \tag{4}$$

where

$$\tilde{\mathsf{G}}_j = G_0 + G_0 v_j^{(m_j)}\mathsf{G}_j. \tag{5}$$

Expansion (4) is derived for a system that can be naturally subdivided into clusters each of which possesses a characteristic internal dynamical structure (dictated by the terms in Eq. (1)). The total Green operator of the system is constructed from the Green operators of the individual clusters by means of Eq. (4). Here the question arises whether it is possible to perform similar analysis to systems that are completely coupled entities, such as the individual clusters themselves. The answer to this question leads us to the second case.

Case 2. We consider a strongly interacting finite system consisting of n particles. We attempt at expressing the many-body Green operator $G^{(n)}$ in terms of lower dimensional Green operators. For the further development we need assume a certain class for the interaction potentials. In what follows we treat the case where the total potential is of the form $U^{(n)} = \sum_{j>i=1}^{n} v_{ij}$, where v_{ij} have not to be further specified. The method can be generalized to more than two body interactions in a straightforward manner. The total potential $U^{(n)}$ can be decomposed as

$$U^{(n)} = \sum_{j=1}^{n} u_j^{(n-1)}, \tag{6}$$

$$u_j^{(n-1)} = \sum_{k=1}^{n-1} u_k^{(n-2)}, \quad j \neq k, \tag{7}$$

where $u_j^{(n-1)} = \tilde{u}_j^{(n-1)}/(n-2)$. Here $\tilde{u}_j^{(n-1)}$ is the total potential of a system consisting of $n-1$ interacting particles while the particle j is free (“disconnected”). In terms of the two-body interactions (v_{mn}) the collective potential $\tilde{u}_j^{(n-1)}$ is expressed as $\tilde{u}_j^{(n-1)} = \sum_{r>s=1}^{n} v_{rs}$, $r \neq j \neq s$. In Fig. 2(a) expansion (6) is explained geometrically.

The basic idea behind the exact relation (6) is to divide the completely interacting system into coupled clusters [cf. Eqs. (1), (6)] with an internal interaction.

Now, let us introduce the Green operator $G_m^{(n-1)}$ of a system with the total potential (sum of collective potentials) $\sum_{j=1}^{m} u_j^{(n-1)}$, $m \in [1, n]$ (note $G_n^{(n-1)} \equiv G^{(n)}$). As

$$H^{(n)} = \left(K + \sum_{j=1}^{m-1} u_j^{(n-1)}\right) + \sum_{j=m}^{n} u_j^{(n-1)}$$

we consider $G_{m-1}^{(n-1)}$ as a reference and conclude the recurrence relations

$$G^{(n)} = G_{n-1}^{(n-1)}\big[\mathbf{1} + u_n^{(n-1)} G_n^{(n-1)}\big], \tag{8}$$

$$G_{n-1}^{(n-1)} = G_{n-2}^{(n-1)}\big[\mathbf{1} + u_{n-1}^{(n-1)} G_{n-1}^{(n-1)}\big]. \tag{9}$$

Again, these equations can be compactly written in the form

$$G^{(n)} = \prod_{j=1}^{n-1} \left[\tilde{G}_j^{(n-1)} G_0^{-1} \tilde{G}_{j+1}^{(n-1)}\right], \tag{10}$$

where

$$\tilde{G}_j^{(n-1)} = G_0 + G_0 u_j^{(n-1)} G_j^{(n-1)}. \tag{11}$$

At first sight it seems that little has been gained by the above mathematical manipulation, since on the right-hand side of Eqs. (4), (10) the total Green operator appears. However, the following theorem can be shown (through lengthy but otherwise exact operator algebra):

Let $G_l^{(k)}$, $k, l \in [2, n]$, be the Green operator of a system with k interacting particles subject to the potential $\sum_{j=1}^{l} u_j^{(k)}$. The Green operator $G_l^{(k)}$ can be written in the form $G_l^{(k)} = G_0 + \sum_{j=1}^{l} \Gamma_j^{(k)}$. The operators $\Gamma_j^{(k)}$ are related to the Green operators $g_j^{(k)}$ of the systems in which the k particles are correlated by virtue of $u_j^{(n-1)}$ via the linear coupled integral equation

$$\begin{pmatrix} \Gamma_1^{(k)} \\ \Gamma_2^{(k)} \\ \vdots \\ \Gamma_{l-1}^{(k)} \\ \Gamma_l^{(k)} \end{pmatrix} = \begin{pmatrix} g_1^{(k)} - G_0 \\ g_2^{(k)} - G_0 \\ \vdots \\ g_{l-1}^{(k)} - G_0 \\ g_l^{(k)} - G_0 \end{pmatrix} + \left[\mathbf{K}^{(k)}\right] \begin{pmatrix} \Gamma_1^{(k)} \\ \Gamma_2^{(k)} \\ \vdots \\ \Gamma_{l-1}^{(k)} \\ \Gamma_l^{(k)} \end{pmatrix}. \tag{12}$$

The kernel $[\mathbf{K}^{(k)}]$ contains only Green operators with a reduced number of interactions and is given by

$$\left[\mathbf{K}^{(k)}\right] = \begin{pmatrix} 0 & g_1^{(k)} - G_0 & g_1^{(k)} - G_0 & \dots & g_1^{(k)} - G_0 \\ g_2^{(k)} - G_0 & 0 & g_2^{(k)} - g_0 & \dots & g_2^{(k)} - G_0 \\ \dots & \dots & \dots & \dots & \dots \\ g_{l-1}^{(k)} - G_0 & \dots & g_{l-1}^{(k)} - G_0 & 0 & g_{l-1}^{(k)} - G_0 \\ g_l^{(k)} - G_0 & \dots & g_l^{(k)} - G_0 & g_l^{(k)} - G_0 & 0 \end{pmatrix} G_0^{-1}. \tag{13}$$

It can be further shown that the kernel $[\mathbf{K}^{(k)}]$ is square integrable (i.e., the norm $\|[\mathbf{K}^{(k)}]\| = [\mathrm{Tr}([\mathbf{K}^{(k)}][\mathbf{K}^{(k)}]^\dagger)]^{1/2}$ is square integrable). Therefore, Eq. (12) can be solved by standard methods for treating integral equations of the Fredholm type. Here we just consider the first term (iteration) of Eq. (12) from which we deduce

$$G_l^{(k)} = G_0 + \sum_{j=1}^{l} g_j^{(k)} - l G_0. \tag{14}$$

The central quantity in Eqs. (4), (10) is of the form $G_0 + G_0 u_l^{(k)} G_l^{(k)}$. From Eq. (14) we conclude that

$$\begin{aligned} G_0 + G_0 u_l^{(k)} G_l^{(k)} &= G_0 + G_0 u_l^{(k)} g_l^{(k)} + G_0 u_l^{(k)} g_{l-1}^{(k)} + \cdots + G_0 u_l^{(k)} g_1^{(k)} - (l-1) G_0 u_l^{(k)} G_0 \\ &= g_l^{(k)} + G_0 u_l^{(k)} \big(G_0 + G_0 u_{l-1}^{(k)} g_{l-1}^{(k)}\big) + \cdots + G_0 u_l^{(k)} \big(G_0 + G_0 u_1^{(k)} g_1^{(k)}\big) - (l-1) G_0 u_l^{(k)} G_0 \\ &= g_l^{(k)} + G_0 u_l^{(k)} \big(G_0 u_{l-1}^{(k)} g_{l-1}^{(k)} + \cdots + G_0 u_1^{(k)} g_1^{(k)}\big). \end{aligned} \tag{15}$$

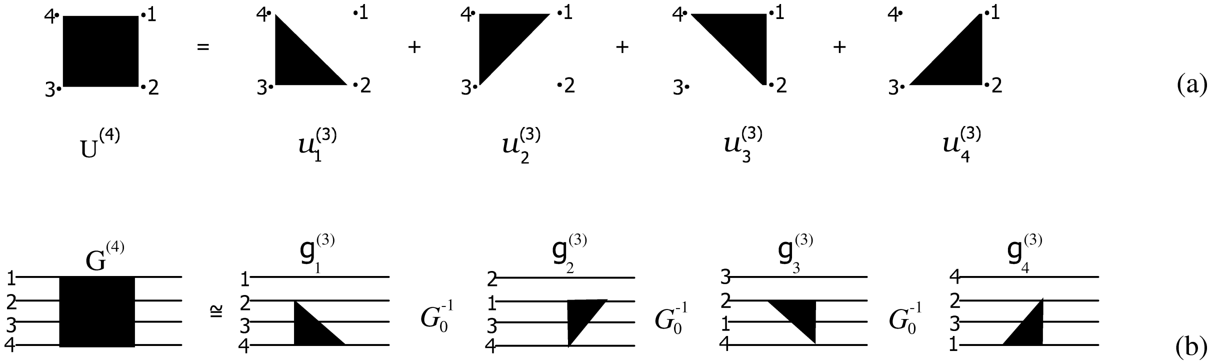

Fig. 2. (a) The reduction of a four interacting particle potential (indicated by a square) to a sum of three body potentials (depicted as triangles) according to Eq. (6). The interacting particles are located at the corners of the geometrical shapes. The orientation of the triangles signifies which particles are interacting. (b) According to Eq. (17), the interaction decomposition shown in (a) leads to a product expansion of the total Green operator in terms of Green operators with a reduced number of interacting particles. Each of the diagrams stands for the Green operator (indicated above it) that involves the interaction symbolized by the geometric shape. The particles are shown as straight lines. Only particles are interacting whose lines cross a triangle.

The leading term of Eq. (15) is identified as the Green operator $g_l^{(k)}$. All other terms are higher order multiple scattering between different subdivisions of the total system. Hence the first order terms in the exact expansions (4) and (10) attain respectively the forms

$$\mathcal{G}^{(N)} \overset{\text{1-order}}{=} \prod_{j=1}^{L-1} \mathsf{G}_j^{(m_j)} G_0^{-1} \mathsf{G}_{j+1}^{(m_{j+1})} \tag{16}$$

and

$$G^{(n)} \overset{\text{1-order}}{=} \prod_{j=1}^{n-1} g_j^{(n-1)} G_0^{-1} g_{j+1}^{(n-1)}, \tag{17}$$

$$g_j^{(n-1)} \overset{\text{1-order}}{=} \prod_{l=1}^{n-2} g_l^{(n-2)} G_0^{-1} g_{l+1}^{(n-2)}, \quad l \neq j. \tag{18}$$

In Eq. (16) only the Green operators $\mathsf{G}_j^{(m_j)}$ of the individual (isolated) clusters occur. Fig. 1(b) illustrates expansion (16) for the potential decomposition shown in Fig. 1(a). Note, that since each cluster j contains m_j interacting particles, $\mathsf{G}_j^{(m_j)}$ is in fact a correlated m_j particle Green operator. A recipes to deal with such interacting many-body Green operators is provided by Eqs. (17), (18) which allow to deduce the Green operator of a system of n interacting particles in a cumulative way from Green operators with a reduced dimensionality (lower number of interactions). An example is shown diagrammatically in Fig. 2(b) for the corresponding situation of Fig. 2(a). The correction terms beyond approximation (17), (18) are readily given by are readily given by Eq. (15). It should be noted here that for the case of a three interacting particle system the present results coincide with those obtained in Ref. [15].

The validity of the approximate expressions (17), (18) relies on the truncation of the multiple scattering series Eq. (15) after the first term. This first order approximation means that, within each individual cluster, multiple scattering events are taken into account to all order via g_l^k. However, scattering between various clusters is neglected. For example, in the three-body Coulomb case g_l^k in Eq. (15) is a two-body Green operator (known analytically). Eq. (17) accounts then for two-body interactions but excludes three-body ones which are of a shorter range (cf., e.g., second term of Eq. (15)). This is a first hint that the present proposal for approximation is reasonable, when for a particular physical system processes involving u_l^k are more important than those mediated by $u_l^k u_{l-1}^k$. Thus, the present method is not appropriate for the special case of zero-range potentials.

For practical application we operate as follows: The first step is to envisage whether the system can be separated in individual clusters as given by Eq. (1). If yes, we use Eq. (16) to deduce the total Green operator. The Green operators of the individual clusters with interacting m_l particle can then be deduced according to Eqs. (17), (18). If a solution of the m_l body problem is not possible we can reduce it to the $m_l - k$ problem using Eqs. (17), (18) for which the solution can be found, e.g., from other analytical or numerical procedures or from an effective field method. Thus, the method shown here is quite flexible and can be employed as a basis for a family of solutions.

Finally, the following general features should be noted: (1) Usually, the various Green operators of the reduced systems can be derived only approximately. The product expansions (16)–(18) have the advantage that no spurious interference terms can occurs due to different approximate treatment of the various reduced systems. (2) It is decisive to realize that relations (17), (18) are expansions in the number of *interactions* and not in the number of *particles*. The number of particles in each of the clusters is the same. It is only the number of *interacting* particles in the individual clusters which is reduced (with respect to the total number of interactions). Because of this the symmetry of a (fermionic, bosonic) system can be taken into account when calculating the desired observables from the Green operator. For example, the spectral function can be extracted from the trace of the imaginary part of $G^{(n)}$. The symmetry of the system enters then through the appropriate symmetry of the states used to obtain the trace of $G^{(n)}$. (3) Eqs. (4), (10) are algebraic operator identities and are valid for all abstract operator. Thus, the theory is readily applied to atomic, molecular, nuclear, and condensed matter systems [14]. (4) For many interacting particles $n \geqslant 3$ the Lippmann–Schwinger equations do not provide unique state vectors [16] and their kernel is not square integrable (and also not compact) [17]. As shown by Faddeev [17] the reason for this shortcoming is the occurrence of the so-called disconnected diagrams where one of the n particles is not interacting, i.e., not correlated with the other $n - 1$ particles. For the present case it can be shown that expansion (10) does not contain any disconnected terms. (5) The present model encompasses perturbative approaches in so far as the perturbative series for the reduced Green operators [$g_j^{(k)}$ in (17)] can be applied when necessary.

One of the simplest applications of Eq. (12) to condensed matter is the description of the propagation of two correlated hot electrons at surfaces. According to approximation (17), the total Green operator of two electrons moving in the surface crystal field is a product of three Green operators: the Green operators g_1 and g_2 of each of the individual electrons in absence of the inter-electronic coupling and the Green operator g_{12} of the electron pair in absence of the crystal. Expressions for g_1 and g_2 can be obtained from standard single particle band structure methods [2]. To evaluate g_{12} we need an expression for the electron electron interaction in extended systems. This can be derived from the *GW* [6] method within the random phase approximation. A simplified version of this scenario has been implemented to study the excitation spectrum of an electron pair in a ferromagnetic surface [18]. When compared with experiments, the results are very promising and strongly indicate the validity of approximation (17) for this specific case.

References

[1] K. Ohno, K. Esfarjani, Y. Kawazoe, Computational Material Science, Springer, Berlin, 1999.
[2] I. Turek, V. Drchal, J. Kudrnovský, M. Šob, P. Weinberger, Electronic Structure of Disordered Alloys, Surfaces, and Interfaces, Kluwer Academic, Boston, 1997.
[3] P. Fulde, Electron Correlation in Molecules and Solids, Springer Series in Solid-State Sciences, Vol. 100, Springer, Berlin, 1991.
[4] R.M. Dreizler, E.K.U. Gross, Density Functional Theory, Springer, Berlin, 1990.
[5] O. Schwartzkopf, B. Krässig, J. Elmiger, V. Schmidt, Phys. Rev. Lett 70 (1993) 3008.
[6] L. Hedin, J. Phys. C 11 (1999) R489.
[7] R. Herrmann, S.N. Samarin, H. Schwabe, J. Kirschner, Phys. Rev. Lett. 81 (1998) 2148.
[8] R. Wehlitz et al., Phys. Rev. Lett. 81 (1998) 1813.

[9] I. Taouil, A. Lahmam-Bennani, A. Duguet, L. Avaldi, Phys. Rev. Lett. 81 (1998) 4600.
[10] A. Dorn et al., Phys. Rev. Lett. 82 (1999) 2496.
[11] M. Unverzagt et al., Phys. Rev. Lett. 76 (1996) 1043.
[12] B. El-Marji, J.P. Doering, J.H. Moore, M.A. Coplan, Phys. Rev. Lett. 83 (1999) 1574.
[13] R. Moshammer et al., Phys. Rev. Lett. 84 (2000) 447.
[14] For Coulomb potentials Eqs. (4), (12) can be used. However, when deriving state vectors or tranistion amplitudes an appropriate renormalization is required, such as the one suggested in J. Macek, Phys. Rev. A 37 (1988) 2365.
[15] J.S. Briggs, Phys. Rev. A 41 (1990) 539.
[16] B.A. Lippmann, Phys. Rev. 102 (1956) 264.
[17] L.D. Faddeev, Sov. Phys. JETP 12 (1961) 1014.
[18] J. Berakdar, Phys. Rev. Lett. 83 (1999) 5150.

Surface Review and Letters, Vol. 7, No. 2 (2000) 000–000

SCATTERING PATH FORMALISM FOR THE PROPAGATION OF INTERACTING COMPOUNDS IN ORDERED AND DISORDERED MATERIALS

J. BERAKDAR*
Max-Planck-Institut für Mikrostrukturphysik, Weinberg 2,
06120 Halle, Germany

Received 15 February 2000

This study presents a theoretical framework for the propagation of a compound consisting of N interacting particles in a multicenter potential. A novel Green operator approach is proposed that disentangles the geometrical and dynamical properties of the scatterers from the internal evolution of the projectile compound. Furthermore, the transition operator for the scattering from the multicenter potential is expanded in terms of many-body scattering path operators, which in turn are expressed in terms of single site transition operators that are amenable to computations. To deduce the correlated many-body Green operator of the scattering compound, a cumulative method is designed that reduces the problem to the evaluation of Green operators of systems with a reduced number of interacting particles. This is particularly useful for efficient calculations and encompasses the usual perturbative approaches.

When an electronic system is subjected to an external perturbation, it may respond collectively by the emission of electrons. A variety of important structural and electronic properties of materials can then be deduced by analyzing the spectrum of the emitted electron flux. Prominent examples of such analytical techniques are electron energy loss spectroscopy,[1] the (low, high and medium energy) electron diffraction method[2] and single photoemission measurements.[3] Correspondingly, a number of reliable theoretical concepts have been put forward to deal with the single particle scattering from ordered and disordered matter.[4,5]

On the other hand, the propagation of a many-body system with coupled internal degrees of freedom through a multicenter potential is much less understood theoretically. Examples of such cases are the scattering of atoms, molecules and correlated electrons from surfaces (see Ref. 6 and references therein). A detailed analysis of such processes is, however, of great fundamental and technological importance, as a number of important catalytic reactions occur at surfaces.[7]

The difficulties in the theoretical treatment stem from the nonseparability introduced by the correlated many-body scattering compound and the subtle coupling of the internal motion (of the constituents of the compound) to the external multicenter potential.

This work aims at developing a systematic framework for the description of a compound with a finite number of interacting particles that propagates in the field created by a multicenter potential. This potential could be ordered or disordered, but it should be possible to cast it reasonably well in a nonoverlapping muffin tin form.

The fundamental quantity that describes the behavior of the correlated system in the presence of the external potential is the total Green operator $\mathcal{G}$, which is the resolvent of the respective Hamiltonian. Our goal is thus to find exact expressions for $\mathcal{G}$ in terms of single particle quantities that are

---

*E-mail: jber.mpi-halle.de

computationally accessible. Our strategy is to decouple formally the degrees of freedom of the compound with N interacting particles from the external scattering potential. For the Green operator of the N-body system we propose an incremental method due to which the Green operator is cumulatively reduced to Green operators of systems with a reduced number of interactions. This procedure can be successively repeated until a reduced interacting system is reached whose Green operator is known. In a second step the scattering compound is considered as a quasi-single-particle with an internal dynamical structure. For the scattering of this quasiparticle we design a scattering path operator formalism that expresses the multisite many-body transition operator in terms of single site transition operators.

For a mathematical formulation we consider a nonrelativistic compound consisting of N correlated particles. The total interaction within this system is assumed to be described by a potential of the form $U_{\text{int}}^{(N)} = \sum_{j>i=1}^{N} v_{ij}$, where v_{ij} have not been further specified at this stage. This structured projectile is then scattered from an external multicenter potential W_{ext} which can be cast in terms of a superposition of M individual nonoverlapping potentials, w_i, acting within specific distinguishable domains Ω_i, i.e. $W_{\text{ext}} = \sum_i^M w_i$, $\Omega_i \cap \Omega_j = 0,\ \forall j \neq i$. Thus, the correlated system is coupled to the external scattering potential via

$$W_{\text{ext}} = \sum_k^M \sum_l^N w_{kl}\,, \tag{1}$$

where w_{kl} is the interaction of particle l with the scattering site k. The total Hamiltonian of the system can be written as $\mathcal{H} = H_{\text{int}}^{(N)} + W_{\text{ext}}$, where $H_{\text{int}}^{(N)} = K + U_{\text{int}}^{(N)}$, and K being the kinetic energy operator. The behavior of the correlated system, characterized by $H_{\text{int}}^{(N)}$, when subjected to the external potential W_{ext} is described by the total Green operator (the resolvent of $\mathcal{H}$) which satisfies the relation

$$\mathcal{G} = G_{\text{int}}^{(N)} + G_{\text{int}}^{(N)} T_{\text{ext}} G_{\text{int}}^{(N)}\,, \tag{2}$$

$$T_{\text{ext}} = W_{\text{ext}} + G_{\text{int}}^{(N)} W_{\text{ext}} T_{\text{ext}}\,. \tag{3}$$

Here T_{ext} is the so-called transition operator and $G_{\text{int}}^{(N)}$ is the Green operator of the correlated system when the external potential is switched off. From Eqs. (2) and (3) it is clear that $\mathcal{G}$ can be formulated as $\mathcal{G} = AB$, where $A = \mathbf{1} + G_{\text{int}}^{(N)} T_{\text{ext}} = \mathbf{1} + G_{\text{int}}^{(N)} W_{\text{ext}} + G_{\text{int}}^{(N)} W_{\text{ext}} G_{\text{int}}^{(N)} W_{\text{ext}} + \cdots$ and $B = G_{\text{int}}^{(N)}$. These relations for $\mathcal{G}$ disentangle the internal degrees of freedom of the projectile, described by B, from the dynamical and geometrical properties of the external potential scattering that are described by A. The external motion is coupled to the internal one via $G_{\text{int}}^{(N)}$, which occurs in the expression for A. Thus, the task is focused on finding simple and mathematically sound expressions for $G_{\text{int}}^{(N)}$ and T_{ext}.

The total internal potential $U_{\text{int}}^{(N)}$ is decomposed as

$$U_{\text{int}}^{(N)} = \sum_{j=1}^{N} u_j^{(N-1)}\,, \tag{4}$$

$$u_j^{(N-1)} = \sum_{k=1}^{N-1} u_k^{(N-2)}\,, \quad j \notin [1,\, N-1]\,, \tag{5}$$

where $u_j^{(N-1)} = \tilde{u}_j^{(N-1)}/(N-2)$, with $\tilde{u}_j^{(N-1)}$ being the total potential of the correlated systems when $N-1$ particles are interacting while particle j is free. In Fig. 1 the expansion (4) is explained geometrically.

Let us introduce the Green operator $G_M^{(N-1)}$ of a system with the total potential $\sum_{j=1}^{M} u_j^{(N-1)}$, $M \in [1,\, N]$ (note that $G_N^{(N-1)} \equiv G_{\text{int}}^{(N)}$). As $H_{\text{int}}^{(N)} = (K + \sum_{j=1}^{M-1} u_j^{(N-1)}) + \sum_{j=M}^{N} u_j^{(N-1)}$, we can treat $G_{M-1}^{(N-1)}$ as the reference (known) Green operator and deduce from the Lippmann–Schwinger equation the recurrence relations

$$G_{\text{int}}^{(N)} = G_{N-1}^{(N-1)}[\mathbf{1} + u_N^{(N-1)} G_N^{(N-1)}] \tag{6}$$

$$G_{N-1}^{(N-1)} = G_{N-2}^{(N-1)}[\mathbf{1} + u_{N-1}^{(N-1)} G_{N-1}^{(N-1)}]\,. \tag{7}$$

These equations are reformulated in the simple but exact relation

$$G_{\text{int}}^{(N)} = G_0^{-N+1} \prod_{j=1}^{N} [G_0 + G_0 u_j^{(N-1)} G_j^{(N-1)}]\,. \tag{8}$$

The physical meaning of the operators $G_j^{(N-1)}$ which determine the expansion (8) is readily seen from Fig. 2 for a compound with six interacting constituents. It is clear from this diagram for the six-particle system that each of the reduced five-particle diagrams can be further expanded in terms of four-particle diagrams. To reach a simplified expression we note that $\sum_{i=1}^{j} u_i^{(N-1)} =$

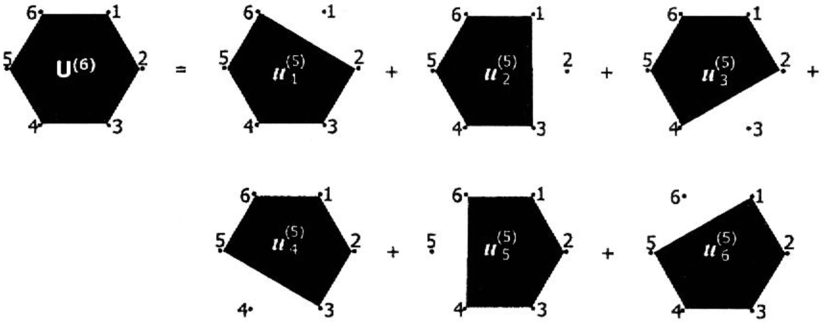

Fig. 1. Pictorial geometric sketch of the total potential expansion (4) for six interacting particles. The particles are enumerated and marked by the full dots at the corners of the hexagon. The hexagon stands for the full potential $U^{(6)}$ of the six correlated particles. According to Eq. (4), the hexagon can be broken down into six pentagons. Each pentagon symbolizes the full five-body potential $u_j^{(5)}$ of those five particles situated at the corners of the pentagon, whereas the particle not at a corner (particle j) is free.

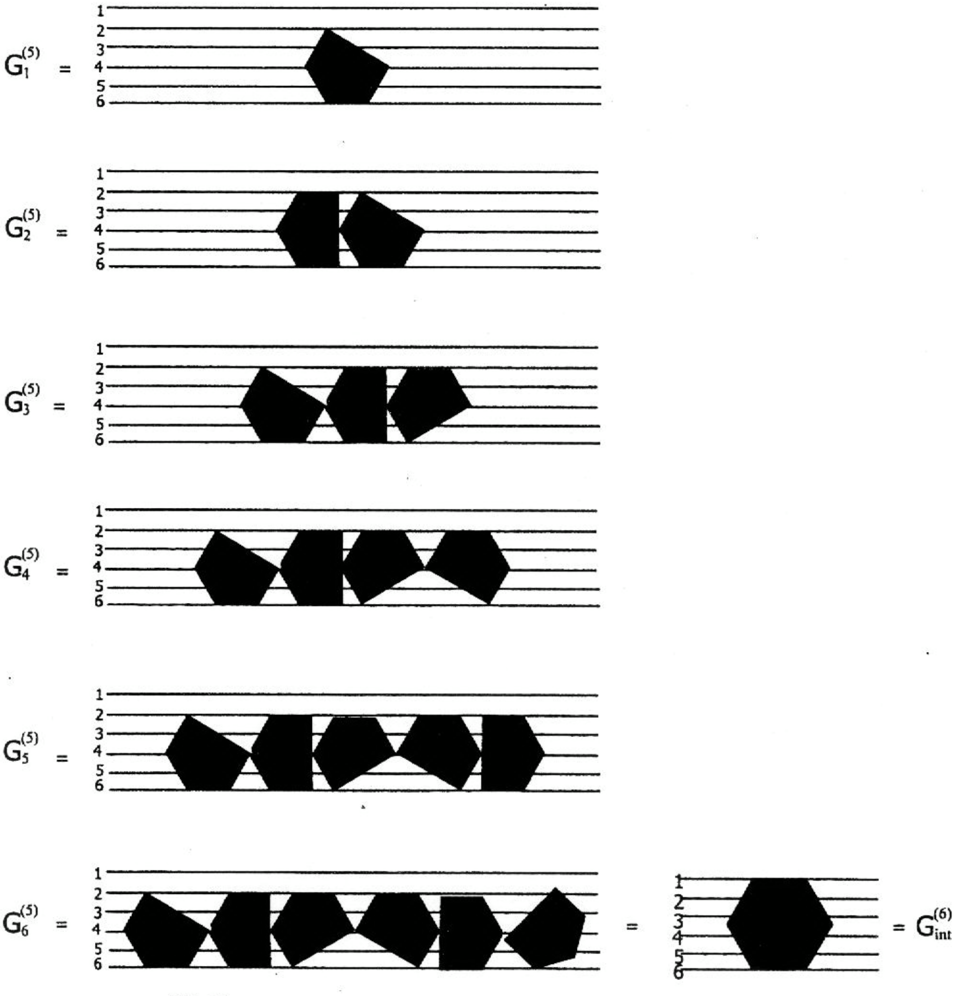

Fig. 2. The Green operators $G_j^{(N-1)}$ which occur in the expansion (6) are illustrated diagrammatically. As in Fig. 1, we choose an example of six interacting particles. The hexagons and the oriented pentagons stand for the same potentials, as explained in Fig. 1. The particles are indicated by straight lines. The interaction that occurs in each Green operator is the sum of the pentagons depicted in the respective diagrams. Only particles that cross a pentagon or a hexagon are interacting.

$u_j^{(N-1)} + \sum_{i=1}^{j-1} u_i^{(N-1)}$. Therefore, the Green operator $G_j^{(N-1)}$ satisfies the equation $G_j^{(N-1)} = g_j^{(N-1)} + g_j^{(N-1)}[\sum_{k=1}^{j-1} u_k^{(N-1)}]G_j^{(N-1)}$, where $g_j^{(N-1)}$ is the Green operator involving the interaction $u_j^{(N-1)}$ only. Inserting this relation into Eq. (8), we deduce that the leading term of the expansion (8) is given by the recurrence relations

$$\begin{aligned} G_{\text{int}}^{(N)} &= G_0^{-N+1} \prod_{j=1}^{N} \Big\{ G_0 + G_0 u_j^{(N-1)} g_j^{(N-1)} \\ &\quad + G_0 u_j^{(N-1)} g_j^{(N-1)} \\ &\quad \times \Big[\sum_{k=1}^{j-1} u_k^{(N-1)} \Big] G_j^{(N-1)} \Big\}, \end{aligned}$$

$$G_{\text{int}}^{(N)} \overset{\text{1.order}}{=} G_0^{-N+1} \prod_{j=1}^{N} g_j^{(N-1)} \tag{9}$$

$$g_j^{(N-1)} \overset{\text{1.order}}{=} G_0^{-N+2} \prod_{l=1}^{N-1} g_l^{(N-2)}, \quad j \notin [1, N-1]. \tag{10}$$

In other words, the Green operator of an N-body system is, in a first order approximation, a product of N Green operators of all the different interacting $N-1$ subsystems that can be combined within the N-body system. The Green operators of the $N-1$ subsystems can in turn be reduced in the same manner to a product of those of the $(N-2)$-body subsystems that exist in the $(N-1)$-particle system. Figure 3 gives a diagrammatic representation of this hierarchical procedure. In practice, one starts the incremental method as depicted in Fig. 3 from a system with a reduced number of interacting particles M for which the Green operator is known. Then, the recipe given above yields the solution (the Green operator) when $M+1$ particles are interacting. This procedure has to be further continued to reach the interacting N-body system. It is important to realize that this approach is not perturbative and that all interactions are treated on an equal footing. On the other hand, a perturbative treatment is encompassed in the expansion (9) through the Born series for $g_j^{(k)}$, $j, k \in [1, N]$.

Having established a reduction formula for the many-body Green operator, we turn now to dealing with the transition operator T_{ext}, as defined by Eq. (3). The aim is to express it in terms of single site transition operators. For this purpose we introduce $w^{(k)} := \sum_l^N w_{kl}$ as the interaction of all N interacting particles with the site k. The external potential (1) reads $W_{\text{ext}} = \sum_{k=1}^{M} w^{(k)}$. Thus, T_{ext} can be expanded in a sum as

$$T_{\text{ext}} = \sum_{k=1}^{M} q^{(k)} \tag{11}$$

$$q^{(k)} = w^{(k)} + w^{(k)} G_{\text{int}}^{(N)} T_{\text{ext}} \tag{12}$$

$$\begin{aligned} q^{(k)} &= w^{(k)} + w^{(k)} G_{\text{int}}^{(N)} q^{(k)} \\ &\quad + \sum_{l \neq k}^{M} w^{(k)} G_{\text{int}}^{(N)} q^{(l)} . \end{aligned} \tag{13}$$

Now we introduce the k site transition operator of the correlated compound as $t_k = w^{(k)} + w^{(k)} G_{\text{int}}^{(N)} t_k$ and rewrite Eq. (13) as

$$q^{(k)} = t_k + \sum_{l \neq k}^{M} t_k G_{\text{int}}^{(N)} q^{(l)} . \tag{14}$$

Combining this relation with Eq. (11) leads to

$$T_{\text{ext}} = \sum_{k}^{M} t_k + \sum_{l \neq k}^{M} t_k G_{\text{int}}^{(N)} (t_l + w_l G_{\text{int}}^{(N)} T_{\text{ext}}) . \tag{15}$$

Following the treatment by Gyorffy[8,9] of the single particle scattering from a multicenter potential, we introduce the *many-body scattering path operators*, τ^{ij}, as

$$\tau^{ij} = t_i \delta_{ij} + \sum_{k \neq i}^{M} t_i G_{\text{int}}^{(N)} \tau^{ik} = t_i \delta_{ij} + \sum_{k \neq j}^{M} \tau^{ik} G_{\text{int}}^{(N)} t_j \tag{16}$$

and sum over j. The comparison with Eq. (14) yields $q^{(i)} = \sum_j^M \tau^{ij}$, and from Eq. (11) we finally conclude that

$$T_{\text{ext}} = \sum_{i}^{M} q^{(i)} = \sum_{ij}^{M} \tau^{ij} . \tag{17}$$

The physical interpretation of t_k, $q^{(k)}$ and τ^{ij} is as follows. The operator t_k describes the scattering of the correlated system ($H_{\text{int}}^{(N)}$) as a whole from the site k in the absence of all the other scatterers, whereas $q^{(k)}$ characterizes the collision of this correlated system from the site k in the presence of all other scattering centers. The operators τ^{kl} describe the transition of the correlated projectile under the action

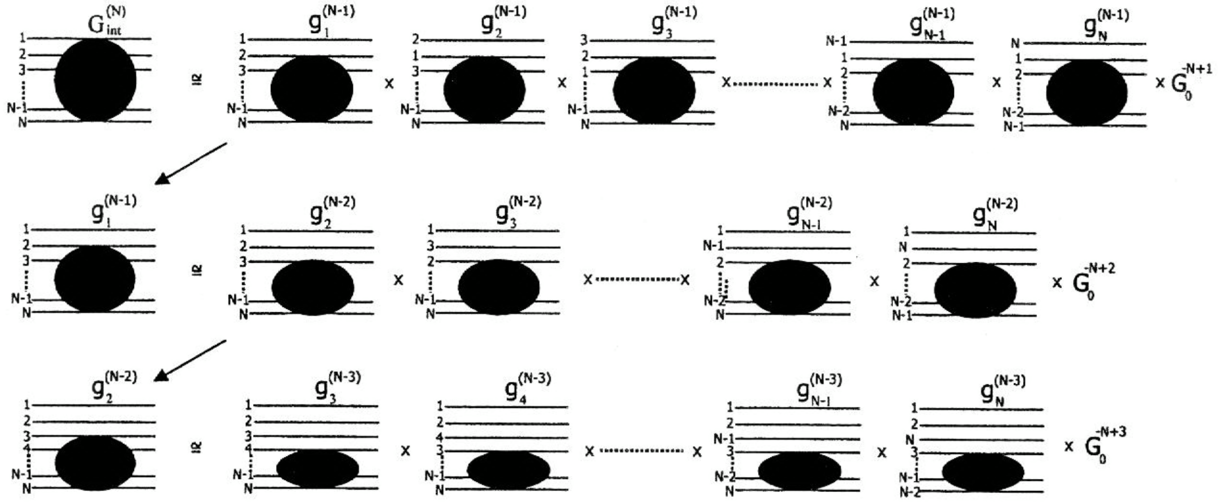

Fig. 3. Schematic representation of the approximation (9), (10) for N interacting particles. The total potential is labeled by the black circle and the $N-1$, $N-2$ and $N-3$ body potentials are indicated by ellipses with different eccentricities. The particles are shown by the solid lines. Only those particles that cross an ellipse are interacting. Each diagram stands for the Green operator (shown in the diagram) of a system with the potential symbolized by the circles and/or the ellipses.

of w_k following an initial scattering from the potential centered around the site l. Thus, the transition operator from the multicenter potential T_{ext} is broken down into successive single site transitions that are computationally more accessible. Combining Eqs. (17) and (8) we arrive at the final exact expression for the total Green operator (2):

$$\mathcal{G} = \left[1 + G_{\text{int}}^{(N)} \sum_{ij}^{M} \tau^{ij}\right] G_0^{-N+1} \times \prod_{k=1}^{N} \left[G_0 + G_0 u_j^{(N-1)} G_k^{(N-1)}\right]. \qquad (18)$$

As evident from Eqs. (10) and (16), the components of the main expression (18) can be obtained from established single particle theories. The first order term of the exact expansion (18) is

$$\mathcal{G} \approx \left[1 + G_0 \sum_{ij}^{M} \tau^{ij}\right] G_0^{-N+1} \prod_{j=1}^{N} g_j^{(N-1)}. \qquad (19)$$

In conclusion, we have proposed a nonperturbative scheme for the theoretical treatment of correlated many-body finite systems from a multicenter potential. The total Green operator is reduced to the evaluation of Green operators of systems with a reduced number of interactions and to the sequential scattering of these reduced systems as a whole from a single site. This has been achieved by the development of an incremental method that yields the Green operator of a system with N interactions from that for systems involving $N-l$ interactions, where $l \in [1, N-2]$. For the scattering from the external potential we designed a many-body scattering path formalism that relates the multicenter transition operator to single site transition operators.

References

1. H. Ibach and D. L. Mills, *Electron Energy Loss Spectroscopy and Surface Vibrations* (Academic, London, 1982).
2. M. A. van Hove, W. H. Weinberg and C.-M. Chan, *Low Energy Electron Diffraction*, Springer Series in Surface Science (Springer, Berlin, 1986).
3. S. Hüfner, *Photoelectron Spectroscopy*, No. 82, Springer Series in Solid-State Science (Spinger-Verlag, Berlin, 1995).
4. I. Turek, V. Drchal, J. Kudrnovský, M. Šob and P. Weinberger, *Electronic Structure of Disrodered Alloys, Surfaces, and Interfaces* (Kluwer, Boston, London, Dordrecht, 1997).
5. P. Weinberger, *Electron Scattering Theory for Ordered and Disordered Matter* (Clarendon, Oxford, 1990).
6. V. Bortolani, N. H. March and M. P. Tosi (eds.),

Interaction of Atoms and Molecules with Solid Surfaces (Plenum, New York, 1990).

7. D. A. King and D. P. Woodruff (eds.), *Chemical Physics of Solid Surfaces and Heterogeneous Catalysis* Vol. 3, *Chemisorption Systems, Part A* (Elsevier, Amsterdam, 1990).
8. B. L. Gyorffy, *Fondamenti di fisica dello stato solida, Scuola Nazionale di Struttura della Materia* (1971).
9. B. L. Gyorffy and M. J. Stott, in: D. J. Fabian and L. M. Watson (eds.), *Bandstructure Spectroscopy of Metals and Alloys* (Academic, London, 1973).

Incremental Approach to Strongly Correlated Many-Body Finite Systems

J. Berakdar*
Max-Planck-Institut für Mikrostrukturphysik, Weinberg 2, 06120 Halle, Germany

(Received 12 January 2000)

The transition and the Green operators of an interacting N body system are obtained from the solutions of the $N - M$ body problem where $M = 1, 2, \dots, N - 2$. This is achieved via the development of a cumulative, nonperturbative approach that makes use of existing knowledge on the system when the number of interacting particles is reduced. The method is applied to four interacting Coulomb particles where the Green operator is expressed as a sum of Green operators of all three body subsystems that can be combined within the four body system. The calculated four particle continuum spectrum is in a remarkable agreement with recent experimental findings.

PACS numbers: 34.10.+x, 25.10.+s, 34.80.Dp, 34.80.Ht

The description of the spectrum of many interacting particles is a problem of a long-standing history in theoretical physics. One of the efficient solution procedures has been to reduce the many-body problem to one for a single particle moving in an effective (nonlocal) field created by all other particles. For computationally tractable solutions approximate expressions for the effective field are employed according to certain recipes such as those provided by the local approximation within the density functional theory [1]. With the advent of many particle spectroscopy, however, it has been possible to probe in great detail the properties of many-body systems that are strongly dependent on the interparticle correlation. For example, the double and triple ionization and ionization/excitation of localized and delocalized electronic systems by an ultraviolet photon [2–4] cannot be described without the explicit use of correlated few-body states. Recently, experiments have pushed the limits to explore in full detail the many-body continuum spectrum of four or more interacting particles [4–10]. For this case, theory is lagging way behind. On the other hand, a system studied intensively in nuclear, atomic, and molecular physics is that consisting of three interacting particles. In 1961 Faddeev proposed coupled linear integral equations with a square integrable kernel to solve the three particle problem [11,12]. Nowadays, we have a wealth of further analytical and numerical methods at hand to deal with three body systems. In view of this situation it seems worthwhile to develop for the four body problem, in particular, and for N body systems in general, a cumulative method that takes advantage of previously accumulated knowledge on the solution of the $N - 1$ particle problem.

The fundamental quantity that describes the microscopic properties of N body quantum systems is the Green operator $G^{(N)}$ which is the resolvent of the total Hamiltonian. It can be deduced from the Lippmann-Schwinger equation $G^{(N)} = G_0 + G_0 U^{(N)} G^{(N)}$ where G_0 is the Green operator of a reference N particle system which is usually chosen as a noninteracting system. An equivalent approach to determine the dynamical behavior of a system is to derive the respective transition operator $T^{(N)}$ which satisfies the integral equation $T^{(N)} = U^{(N)} + U^{(N)} G_0 T^{(N)}$. These integral equations for $G^{(N)}$ and $T^{(N)}$ provide a natural framework for perturbative treatments. However, for $N \geq 3$ the application of the above Lippmann-Schwinger equations (and those for the state vectors) is hampered by mainly two difficulties: (1) as shown in Refs. [13,14] the Lippmann-Schwinger equations for the state vectors do not have a unique solution, and (2) as shown by Faddeev [11,12] the kernel of these integral equations $K = G_0 U^{(N)}$ is not a square integrable operator for $N \geq 3$, i.e., the norm $\|K\| = [\mathrm{Tr}(KK^\dagger)]^{1/2}$ is not square integrable. The kernel K is also not compact.

This study proceeds as follows: (a) We develop a recursive procedure to express the Hamiltonian of N interacting body systems in terms of Hamiltonians of systems with a reduced number of interactions. (b) In the spirit of the Faddeev approach [11,15,16] we derive nonperturbative integral equations with the following properties: (1) they treat all N particles on equal footing, and (2) they relate in a linear manner $G^{(N)}$ and $T^{(N)}$ to $G^{(N-M)}$ and $T^{(N-M)}$ where $M = 1, 2, \dots, N - 2$. (c) We develop a systematic and mathematically sound scheme for approximations and apply it to deduce the continuum spectrum of four interacting Coulomb particles.

To this end we consider a nonrelativistic system consisting of N interacting particles. We assume the total potential to be of the class $U^{(N)} = \sum_{j>i=1}^{N} v_{ij}$ without any further specification of the individual potentials v_{ij}. The potential $U^{(N)}$ satisfies the recurrence relations

$$U^{(N)} = \frac{1}{N-2} \sum_{j=1}^{N} u_j^{(N-1)}, \tag{1}$$

$$u_j^{(N-1)} = \frac{1}{N-3} \sum_{k=1}^{N-1} u_{jk}^{(N-2)}, \qquad j \neq k, \tag{2}$$

where $u_j^{(N-1)}$ is the total potential of a system of $N - 1$ interacting particles in which the j particle is missing, i.e., in terms of the physical pair potentials v_{mn} one can write $u_j^{(N-1)} = \sum_{m>n=1}^{N} v_{mn}, m \neq j \neq n$. It is straightforward to show that the potential expansions [Eqs. (1)

and (2)] are reflected in similar relations for the total Hamiltonian. Figure 1 illustrates how, according to Eqs. (1) and (2), the potential of a system of six interacting particles is expressed in terms of potentials of five correlated particles. The latter potentials can be further expressed in terms of four body potentials [cf. Eq. (2)]. This procedure is repeated until a potential with a desired number of interactions is achieved. From Fig. 1 it is clear that this "minimal geometric reduction" scheme [Eqs. (1) and (2)] treats all interactions on equal footing and provides maximal flexibility to reduce systematically the N body potential (Hamiltonian) to sums of $N - M$ potentials (Hamiltonians) with $M = 1, 2, \dots, N - 2$. This simple geometric observation has wide ranging consequences in that the transition and the Green operators can be expanded in the same way. This can be seen as follows: According to the decomposition (1), the integral equation for the transition operator can be written as

$$T^{(N)} = \sum_{j=1}^{N} T_j^{(N-1)}, \tag{3}$$

$$T_j^{(N-1)} = \tilde{u}_j^{(N-1)} + T^{(N)} G_0 \tilde{u}_j^{(N-1)}, \qquad j = 1, \dots, N. \tag{4}$$

Here we introduced the scaled potentials $\tilde{u}_j^{(N-1)} = (u_j^{(N-1)})/(N - 2)$. The physical meaning of the operators (4) is illustrated in Fig. 2 for the system depicted in Fig. 1.

The transition operator of the system, when $N - 1$ particles are interacting via the scaled potential $\tilde{u}_j^{(N-1)}$, is $t_j^{(N-1)} = \tilde{u}_j^{(N-1)} + \tilde{u}_j^{(N-1)} G_0 t_j^{(N-1)}$. With this relation Eq. (4) can be reformulated as

$$\begin{aligned} T_j^{(N-1)} &= t_j^{(N-1)} + t_j^{(N-1)} G_0 T^{(N)} - t_j^{(N-1)} G_0 (\tilde{u}_j^{(N-1)} + \tilde{u}_j^{(N-1)} G_0 T^{(N)}) = t_j^{(N-1)} + t_j^{(N-1)} G_0 (T^{(N)} - T_j^{(N-1)}) \\ &= t_j^{(N-1)} + t_j^{(N-1)} G_0 \sum_{k \neq j}^{N} T_k^{(N-1)}. \end{aligned} \tag{5}$$

Equation (5) can be expressed alternatively in a matrix form as

$$\begin{pmatrix} T_1^{(N-1)} \\ T_2^{(N-1)} \\ \vdots \\ T_{N-1}^{(N-1)} \\ T_N^{(N-1)} \end{pmatrix} = \begin{pmatrix} t_1^{(N-1)} \\ t_2^{(N-1)} \\ \vdots \\ t_{N-1}^{(N-1)} \\ t_N^{(N-1)} \end{pmatrix} + [\mathbf{K}^{(N-1)}] \begin{pmatrix} T_1^{(N-1)} \\ T_2^{(N-1)} \\ \vdots \\ T_{N-1}^{(N-1)} \\ T_N^{(N-1)} \end{pmatrix}. \tag{6}$$

The kernel $[\mathbf{K}^{(N-1)}]$ is a matrix operator whose elements consist of $t_j^{(N-1)}; j = 1 \cdots N$. From Eq. (2) it is clear that $t_j^{(N-1)}$ can also be expressed in terms of the transition operators of the $N - 2$ interacting subsystems as $t_j^{(N-1)} = \sum_{k \neq j}^{N-1} T_k^{(N-2)}$. The operators $T_k^{(N-2)}$ are deduced from Eq. (6) with N being replaced by $N - 1$.

From the relation $G^{(N)} = G_0 + G_0 T^{(N)} G_0$ we conclude that the Green operator of the interacting N particle system has the form $G^{(N)} = G_0 + \sum_{j=1}^{N} G_j^{(N-1)}$. The operators $G_j^{(N-1)}$ are related to the Green operators $g_j^{(N-1)}$ of the systems in which only $N - 1$ particles are correlated by virtue of $\tilde{u}_j^{(N-1)}$. This interrelation is given via

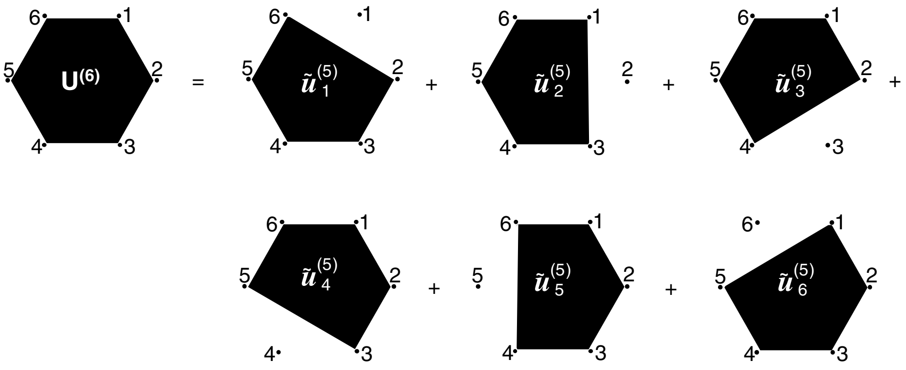

FIG. 1. A pictorial interpretation of the total potential expansion (1) for six interacting particles enumerated and marked by the full dots at the corners of the hexagon. The hexagon indicates the full potential $U^{(6)}$ of the six correlated particles. Each pentagon symbolizes the full five body potential $\tilde{u}_j^{(5)} = (u_j^{(5)})/4$ of those five particles that are at the corners of the pentagon. The particle being not at a corner of a pentagon is free (disconnected).

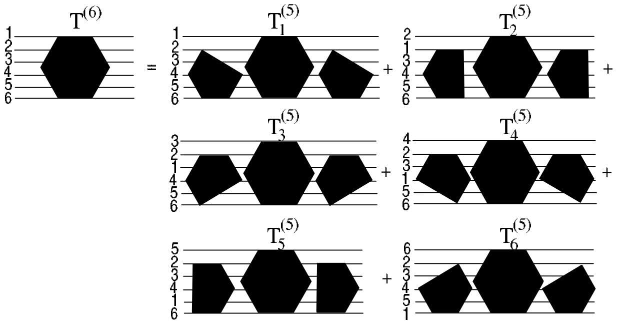

FIG. 2. A diagrammatic representation of Eq. (4) for a system of six correlated particles (cf. Fig. 1). The hexagons and the pentagons (with a specific orientation) label the same potentials as explained in Fig. 1. Each of the pictures stands for a transition operator of the six body system (the particles are labeled by straight lines). For example, the diagram $T_1^{(5)}$ means that the five particles 2, 3, 4, 5, and 6 interact first, propagate, and then all six particles interact with each other. The system then propagates and finally the five particles 2, 3, 4, 5, and 6 interact again.

$$\begin{pmatrix} G_1^{(N-1)} \\ G_2^{(N-1)} \\ \vdots \\ G_{N-1}^{(N-1)} \\ G_N^{(N-1)} \end{pmatrix} = \begin{pmatrix} g_1^{(N-1)} - G_0 \\ g_2^{(N-1)} - G_0 \\ \vdots \\ g_{N-1}^{(N-1)} - G_0 \\ g_N^{(N-1)} - G_0 \end{pmatrix} + [\tilde{\mathbf{K}}^{(N-1)}] \begin{pmatrix} G_1^{(N-1)} \\ G_2^{(N-1)} \\ \vdots \\ G_{N-1}^{(N-1)} \\ G_N^{(N-1)} \end{pmatrix}, \tag{7}$$

where $[\tilde{\mathbf{K}}^{(N-1)}] = G_0[\mathbf{K}^{(N-1)}]G_0^{-1}$. From Eqs. (6) and (7) we conclude that if the Green operator of the interacting $N - 1$ body system is known the Green operator of the N particles can then be deduced by solving a set of N linear, coupled integral equations [namely, Eqs. (6) and (7)]. According to the above equations, if only the solution of the $N - M$ problem is known where $M = 1, 2, \dots, N - 2$ we have to perform a hierarchy of calculations starting by obtaining the solution for the $N - M + 1$ problem and repeating the procedure to reach the solution of the N body problem. For $N = 3$ the present scheme reduces to the well-established Faddeev equations.

As an example we apply the method to the four body problem. This is particularly instructive, for a substantial body of knowledge on the three particle problem has been accumulated whereas theoretical studies on the four body problem are still scare. Moreover, an impressive amount of experimental data is available [4–8,10] that renders possible a detailed insight into the four body continuum spectrum. Therefore, using the present method, we express the four body Green operator in terms of known, approximate solutions of three body systems. For $N = 4$ the first iteration of Eq. (7) yields

$$G^{(4)} = \sum_{j=1}^{4} g_j^{(3)} - 3G_0, \tag{8}$$

where $g_j^{(3)}$ is the Green operator of the interacting three body system (particle j is noninteracting) and can be taken from other numerical or analytical studies. For example, it has been shown recently [17] that, under certain conditions specified in Ref. [17], the Hamiltonian of a general three body system reduces to a sum of three commuting Hamiltonians $h_k^{(2)}$ in which only two particles are interacting (particle k is free). The Green operators $g_j^{(3)}$ in Eq. (8) can therefore be written as $g_j^{(3)} \approx G_0^{-2} \prod_{k \neq j} g_k^{(2)}, k \in \{1, 2, 3, 4\} \ni j$ where $g_k^{(2)}$ is the resolvent of $h_k^{(2)}$. Thus we obtain from Eq. (8) $G^{(4)} = [\sum_{j=1}^{4} G_0^{-2} \prod_{k \neq j} g_k^{(2)}] - 3G_0, j \neq k \in \{1, 2, 3, 4\}$. In many situations it is possible to encompass in the reference Hamiltonian G_0 valuable and easily accessible preknowledge of the system which reduces the number of interactions in the potential (1). For example, we consider here the continuum dynamics of three electrons (or two electrons and a positron) in the Coulomb field of a heavy nucleus. Such a state is achieved following the electron and positron impact double ionization. As a reference we choose G_0 to be the Green operator of the three continuum particles moving independently in the Coulomb nuclear field. What remains in the potential (1) is then the interaction among the continuum particles which is treated according to the present method. Figures 3(a) and 3(b) show the results for the electron and the positron impact double ionization of ground state helium along with the experimental data [5,10] and a full numerical evaluation of the first Born term within a convergent close coupling (CCC) method [18]. The first Born approximation (FBA) corresponds to one term in Eq. (8) where the projectile motion is decoupled from the rest of the system. Thus, the results of the FBA are insensitive to the projectile charge state. The origin of the main peaks in the FBA spectrum has been unraveled in Ref. [10]. Thus we focus here on the novel additional structures predicted by the present theory. From Figs. 3 and 4 the following important implications are inferred: (i) The difference between the positron and the electron impact case indicates that the Born limit is not yet reached. We note that at such a high impact energy and a small momentum transfer as considered in Fig. 3 and 4 the Born limit is usually achieved in single ionization. This emphasizes the fundamental difference between single and double ionization as the latter having much higher ionization threshold and being basically correlation induced. (ii) The Born (and the optical) limit is approached differently depending on the emission angles and energies of the ejected electrons. (iii) In the author's view, the most remarkable prediction

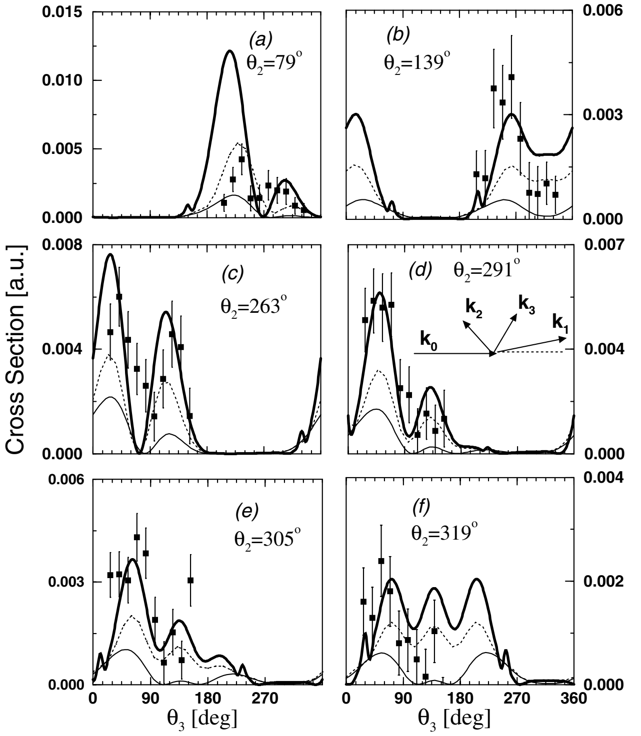

FIG. 3. The fully resolved double ionization cross section of He($1S^e$) following electron (solid lines) or positron (dotted line) impact. The scattering geometry is shown by the inset in (d). $\mathbf{k}_0$ and $\mathbf{k}_1$ are the initial and final state momenta of the projectile while $\mathbf{k}_2$ and $\mathbf{k}_3$ refer to the momenta of the two ejected electrons. The incident energy is 5.6 keV and $k_2^2/2 = k_3^2/2 = 10$ eV. All angles are measured with respect to $\hat{\mathbf{k}}_0$. The projectile is scattered through an angle of 0.45°. The emission angle θ_2 of one of the electrons is fixed at the value indicated on the figures while the cross section is scanned as a function of the emission angle θ_3 of the second electron. The thick solid (dotted) line is the result of the present model for electron (positron impact) whereas the light solid curve is the outcome of the CCC method within the first Born approximation [18]. The data (full square [10]) are on absolute scale.

of the present calculations is the presence of additional subsidiary peaks (in the spectrum shown in Figs. 3 and 4 which are absent in the FBA (CCC) results (cf. also Ref. [10]). An optimistic observer can identify these structures in the experimental data of Figs. 3(b), 3(e), and 3(f). In Fig. 4, however, these peaks are clearly observable. The origins of these peaks are interference effects between the various terms in the sum (8) when evaluating the cross sections. It is most interesting to recall here that the appearance of such interference effects in a Faddeev-type approach to Coulomb scattering problems [19] has been considered hitherto as a drawback and has not been confirmed experimentally [19]. The present study which is in the spirit of the Faddeev theory together with the notable agreement with experiment sheds a new light on Faddeev-type approaches as a useful route to few-body systems with long range correlations. In spite of this exciting result it should be noted that only the first iteration of (7) is used for the calculation of Figs. 3 and 4. The evaluation of higher order terms should remove the remaining discrepancies between theory and experiment. The compactness of the kernel of the integral equation (7) for *Coulomb* potentials is the subject of current research [20].

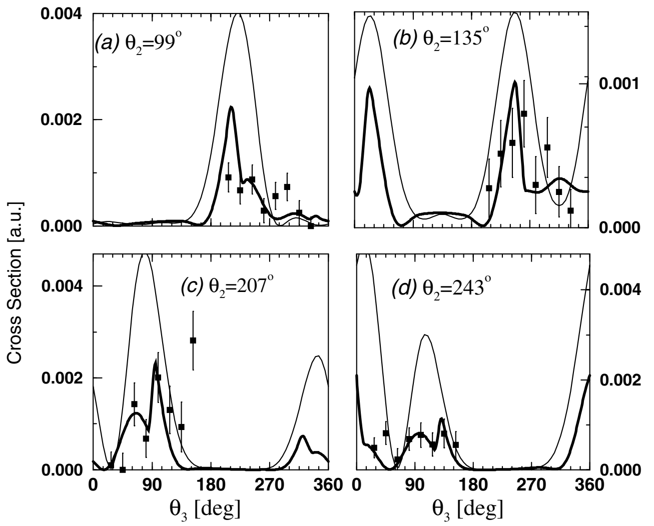

FIG. 4. The same as in Fig. 3 with the same labeling of curves, however the ejection energies are lowered to $k_2^2/2 = k_3^2/2 = 4$ eV. For shape comparison, the experimental data have been normalized by a single factor to the present theory.

I thank Anatoli Kheifets for communicating his results.

---

*Email address: jber@mpi-halle.de

[1] R. M. Dreizler and E. K. U. Gross, *Density Functional Theory* (Springer-Verlag, Berlin, 1990).
[2] O. Schwarzkopf *et al.,* Phys. Rev. Lett. **70**, 3008 (1993).
[3] R. Herrmann *et al.,* Phys. Rev. Lett. **81**, 2148 (1998).
[4] R. Wehlitz *et al.,* Phys. Rev. Lett. **81**, 1813 (1998).
[5] I. Taouil *et al.,* Phys. Rev. Lett. **81**, 4600 (1998).
[6] A. Dorn *et al.,* Phys. Rev. Lett. **82**, 2496 (1999).
[7] M. Unverzagt *et al.,* Phys. Rev. Lett. **76**, 1043 (1996).
[8] B. El-Marji *et al.,* Phys. Rev. Lett. **83**, 1574 (1999).
[9] R. Moshammer *et al.,* Phys. Rev. Lett. **84**, 447 (2000).
[10] A. Lahmam-Bennani *et al.,* Phys. Rev. A **59**, 3548 (1999).
[11] L. D. Faddeev, Sov. Phys. JETP **12**, 1014 (1961).
[12] L. D. Faddeev, *Mathematical Aspects of the Three-Body Problem* (Davey, New York, 1965).
[13] B. A. Lippmann, Phys. Rev. **102**, 264 (1956).
[14] L. L. Foldy and W. Tobocman, Phys. Rev. **105**, 1099 (1957).
[15] O. A. Yakubovsky, Sov. J. Nucl. Phys. **5**, 937 (1967).
[16] S. P. Merkuriev and L. D. Faddeev, *Quantum Scattering Theory for Systems of Few Particles* (Nauka, Moscow, 1985).
[17] J. Berakdar, Phys. Rev. A **53**, 2314 (1996).
[18] A. Kheifets *et al.,* J. Phys. B **32**, 5047 (1999).
[19] J. H. Macek, Phys. Rev. A **1**, 235 (1970); M. M. Duncan *et al., ibid.* **15**, 1785 (1977).
[20] A. M. Mukhamedzhanov, E. O. Alt, and G. V. Avakov, Phys. Rev. C **61**, 064006 (2000).

VOLUME 87, NUMBER 26 PHYSICAL REVIEW LETTERS 24 DECEMBER 2001

Manifestation of Charge-Density Fluctuations in Metal Clusters: Suppression of the Ionization Channel

Oleg Kidun* and Jamal Berakdar†
Max-Planck Institut für Mikrostrukturphysik, Weinberg 2, 06120 Halle, Germany

(Received 17 September 2001; published 6 December 2001)

The fluctuations in the electronic charge density of metallic clusters in response to an approaching electron suppress the single-ionization channel. This conclusion is made on the basis of numerical calculations for the total ionization cross sections using the random-phase approximation with exchange to describe the particle-hole (de)excitations. The general trends can be understood by means of the Thomas-Fermi model. The present theory explains, for the first time, the behavior of the measured total ionization cross section for C_{60}. The interplay between finite size and nonlocal screening effects is studied by tracing the changes in the ionization cross sections for Li clusters with an increasing cluster radius.

DOI: 10.1103/PhysRevLett.87.263401 PACS numbers: 36.40.Cg, 34.80.Gs, 36.40.Ei, 36.40.Mr

The primary source of knowledge on the structure and the dynamics of electronic systems is provided by their characteristic response to external perturbations. For systems with a large number of active electrons, such as clusters and surfaces, the collective response is determined basically by the cooperative behavior of the system's constituents, e.g., the delocalized electrons in a metallic surface shield, by an organized rearrangement, an external electric field which might be induced by an approaching test charge. These correlated fluctuations of the electronic density, i.e., the excitation and deexcitation of electron-hole pairs, can be described by the so-called polarization operator Π (or the particle-hole propagator) [1]. On the other hand, the spin and the charge density fluctuations of the medium modify the properties of the electron-electron interaction U. How the modified potential U_{eff} emerges from the naked interaction U is determined by Π through the integral equation [1] $U_{\text{eff}} = U + U\Pi U_{\text{eff}}$. This relation can be formally written as $U_{\text{eff}} = \frac{U}{1-U\Pi}$. Thus the *screening* of U is given by $\kappa := 1/(1 - U\Pi)$ which is referred to as the generalized dielectric function [1] and plays a central role in a variety of phenomena. To name one, the frequency (ω) and wave vector ($\boldsymbol{p}$) dependent electrical conductivity $\sigma(\boldsymbol{p}, \omega)$ of a plasma is obtained from $\kappa(\boldsymbol{p}, \omega)$ as $\sigma(\boldsymbol{p}, \omega) = i\omega(1 - \kappa)$. This is just one of numerous examples for the fundamental interest in the study of the dynamical screening in electronic systems.

The determination of the renormalized interaction U_{eff} and of the dielectric function κ entails the knowledge of Π. In essence, Π is a two-point Green function that describes the particle-hole excitations. Its lowest order approximation Π_0 is provided by the so-called random phase approximation (RPA) [1]. For a homogeneous system and in the long wavelength limit ($\lambda \gg \lambda_F$, where λ_F is the Fermi wave length) one obtains $\Pi_0 \approx -2N(\mu)$. Here $N(\mu)$ is the density of states at the Fermi level μ. Hence, for $\lambda \gg \lambda_F$, the screened potential of the bare electron-electron interaction $U(\boldsymbol{q}) = 4\pi/q^2$ is readily derived as $U_{\text{TF}} = 4\pi/[q^2 + 8\pi N(\mu)]$. In configuration space we recover thus the well-known Thomas-Fermi potential $U_{\text{TF}} = e^{-r/r_0}/r$ $[r_0 = 1/\sqrt{8\pi N(\mu)}]$. This form of the interaction gives a first hint of the nature of electronic collisions in many-particle systems, such as in metallic clusters: In an isolated scattering of two charged particles, events with a small momentum transfer q (far collisions) are predominant, for the naked potential behaves as $U \propto 1/q^2$. In contrast, these events are suppressed in the presence of a polarizable medium due to the finite range of the renormalized scattering potential U_{eff} which dictates that scattering can occur only at distances close enough such that the medium is not able to screen the external field ($\lim_{q\ll1} U_{\text{TF}}(q) \propto 1/[2N(\mu)] = \text{const}$). Hence, we conclude that the scattering probability as a function of the impact parameter saturates at a distance d determined by the extent r_0 of the scattering region ($\lim_{r_0\to\infty} d \to \infty$), these conclusions are endorsed by the full-numerical RPA calculations presented in this work.

The ideas sketched above are the key to resolving a yet open question of how metal clusters are ionized in response to an external perturbation induced by an approaching electron. In the experiments, which have been performed using free C_{60} clusters, one measures the absolute total ionization cross sections $W(\epsilon_0)$, i.e., the yield for the C_{60}^+ production, as a function of the energy (ϵ_0) of an incoming electron [2–4]. These measurements confirmed repeatedly that the cross section $W(\epsilon_0)$ possesses a plateau shape: Near the ionization threshold it rises strongly with increasing ϵ_0 and then falls off slowly at higher energies. This saturation effect is markedly different from what is known for atomic targets where $W(\epsilon_0)$ shows a pronounced peak at low ϵ_0 [cf. Fig. 1(a)].

Theoretical attempts to explain the behavior of $W(\epsilon_0)$ for C_{60} are scarce. For the energy region $\epsilon_0 < 100$ eV only semiempirical models exist [4,5], whereas for $\epsilon_0 > 100$ eV a quantum scattering approach has been proposed in Refs. [6,7]. All of these previous theories [4–7] were unable to explain the energy dependence of $W(\epsilon_0)$, basically because the problem has been approached from an atomic scattering point of view without accounting for the influence of the fluctuating electron density on the scattering process which is of a key importance at low energies ($\epsilon_0 < 1000$ eV) , as shown here in detail: The central quantity that determines $W(\epsilon_0)$ is the transition matrix element $T(\boldsymbol{k}_0, \phi_\nu; \boldsymbol{k}_1, \boldsymbol{k}_2)$. This matrix element is a measure for the probability that an incoming electron with momentum $\boldsymbol{k}_0$ ionizes a valence electron bound to the state ϕ_ν of the cluster with a binding energy ϵ_ν, where ν stands for a collective set of quantum numbers that quantify uniquely the electronic structure of the cluster. The emitted and the scattered electrons' states are labeled by the momenta $\boldsymbol{k}_1$ and $\boldsymbol{k}_2$. As outlined above the renormalized electron-electron interaction U_{eff} is determined by an integral equation with a kernel describing the particle-hole (de)excitation. Therefore, the evaluation of the T matrix entails a self-consistent solution of an integral equation. In the random-phase approximation with exchange (RPAE) [1] and within the *post* formulation [8] the T matrix has the form $T_{\mathrm{RPAE}} = \langle \boldsymbol{k}_1\boldsymbol{k}_2|U_{\mathrm{eff}}|\phi_\nu \boldsymbol{k_0}\rangle$, where

$$\langle \boldsymbol{k}_1\boldsymbol{k}_2|U_{\mathrm{eff}}|\phi_\nu \boldsymbol{k}_0\rangle = \langle \boldsymbol{k}_1\boldsymbol{k}_2|U|\phi_\nu \boldsymbol{k_0}\rangle + \sum_{\substack{\varepsilon_p\le\mu \\ \varepsilon_h>\mu}} \left(\frac{\langle \varphi_p \boldsymbol{k_2}|U_{\mathrm{eff}}|\phi_\nu \varphi_h\rangle \langle \varphi_h \boldsymbol{k_1}|U|\boldsymbol{k_0}\varphi_p\rangle}{\epsilon_0 - (\varepsilon_p - \varepsilon_h - i\delta)} - \frac{\langle \varphi_h \boldsymbol{k_2}|U_{\mathrm{eff}}|\phi_\nu \varphi_p\rangle \langle \varphi_p \boldsymbol{k_1}|U|\boldsymbol{k_0}\varphi_h\rangle}{\epsilon_0 + (\varepsilon_p - \varepsilon_h - i\delta)} \right). \tag{1}$$

The spin averaged cross section $W(\epsilon_0)$ is obtained from the weighted average of the singlet $\propto |T^{(S=0)}|^2$ [vanishing total spin ($S = 0$) of the electron pair] and the triplet $\propto |T^{(S=1)}|^2$ cross sections (we assume spin-flip processes to be irrelevant)

$$W(\epsilon_0) = \frac{(2\pi)^4}{k_0} \int d^3\boldsymbol{k}_1\, d^3\boldsymbol{k}_2 \left\{ \sum_\nu \frac{1}{4} |T^{(S=0)}(\boldsymbol{k}_0, \phi_\nu; \boldsymbol{k}_1, \boldsymbol{k}_2)|^2 + \frac{3}{4} |T^{(S=1)}(\boldsymbol{k}_0, \phi_\nu; \boldsymbol{k}_1, \boldsymbol{k}_2)|^2 \delta[\epsilon_0 + \epsilon_\nu - (k_1^2/2 + k_2^2/2)] \right\}. \tag{2}$$

In Eq. (1) φ_p and φ_h are, respectively, the intermediate particle's and hole's states with the energies ε_p, ε_h, whereas δ is a small positive real number. The first line of Eq. (1) amounts to a neglect of the electron-hole (de)excitations, as done in Ref. [7]. If U_{TF} is employed as an effective potential only the first line of Eq. (1) has to be evaluated, and we obtain the much simper expression $T_{\mathrm{TF}} = \langle \boldsymbol{k}_1\boldsymbol{k}_2|U_{\mathrm{TF}}|\phi_\nu \boldsymbol{k}_0\rangle$ from which the cross section W_{TF} follows according to Eq. (2). In contrast, as evident from Eqs. (1),(2), the numerical evaluation of $W(\epsilon_0)$ within RPAE is a challenging task. To tackle this problem we proceeded as follows: The quantum states of the metal clusters are constructed within the Hartree-Fock approximation and within the spherical jellium model [8,9]. The cluster potential which is a superposition of atomic potentials, is replaced by a shell confinement. The latter is formed by the delocalized valence electrons of carbon atoms and is modeled by the potential well: $V(r) = V_0$ within the region $R - \Delta < r < R + \Delta$, and $V = 0$ elsewhere. For C_{60} we use $R \approx 6.7a_0$ as the radius of the fullerene. The thickness of the shell is $2\Delta \approx 2a_0$ (a_0 is the Bohr radius). The height of the well was chosen such that the experimental value of the electron affinity of C_{60} and the number of valence electrons are correctly reproduced. Alternatively, one can employ a model cluster potential as derived from the density functional theory (DFT) within the local density approximation [7]. As shown below, the DFT potential leads basically to the same conclusions as the model potential outlined above.

As remarked in Refs. [6,7], the relatively large size of the cluster leads to severe convergence problems in evaluating the transition matrix elements. To circumvent this situation we utilized the nonlocal variable phase approach [10–12] for the numerical calculation of the Hartree-Fock states. In this method the electronic eigenfunctions and eigenvalues of the cluster are provided through scattering phase functions and through the poles of the scattering amplitudes in the complex plane of the particle's wave vectors. We find that this choice for the numerical realization renders a rapid and a reliable convergence of the self-consistent calculations. Upon the numerical summation over the states ϕ_ν in Eq. (2) we carry out the six-dimensional integral over the momenta $\boldsymbol{k}_1$ and $\boldsymbol{k}_2$ using a Monte Carlo procedure.

To get an insight into the effect of the screening we calculated $W_{\mathrm{TF}}(\epsilon_0)$ for different strengths of screening as quantified by r_0. As seen in Fig. 1(a), when approaching the unscreened limit ($r_0^{-1} = 0.01$ a.u.), the calculated $W_{\mathrm{TF}}(\epsilon_0)$ agree well both in shape and magnitude with the finding of Ref. [5] at lower energies. At higher energies, the present model and the DFT calculations [6,7] yield basically the same results. To simulate experimentally this atomic case let us assume the C_{60} molecule to be simply an ensemble of 60 independent carbon atoms, in which case the cross section for C_{60} is a factor 60 larger than $W(\epsilon_0)$ for atomic carbon [13]. The experimental cross sections we obtain by this procedure [Fig. 1(a)] agree very well with the shape of the calculated $W_{\mathrm{TF}}(\epsilon_0)$ at low screening. On the other hand, all of the theoretical models shown in Fig. 1(a) are clearly at variance with the measured $W(\epsilon_0)$ for C_{60} (note the measured and the calculated cross sections are on an absolute scale). Figure 1(b) sheds light on the underlying reasons for the shortcomings of the

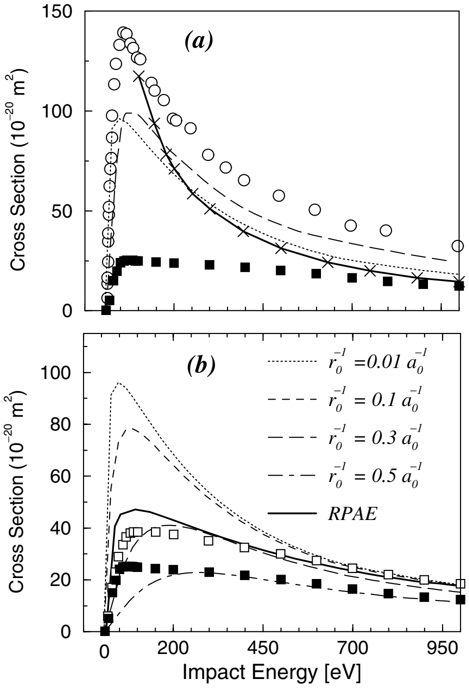

FIG. 1. (a) The total ionization cross section [Eq. (2)] for the electron impact single ionization of C_{60} as a function of projectile energy. The *absolute* experimental data (full squares) for the production of stable C_{60}^{+} ions [2,3] are shown along with the experimental electron-impact total ionization cross sections for atomic carbon (open circles) [13] multiplied by a factor of 60 (cf. text). The solid line with crosses is the result of the DFT calculations [6], whereas the dashed line is due to the model of Ref. [5]. The dotted line indicates the present calculations with very small screening ($r_0^{-1} = 0.01$ a.u.). (b) The RPAE results (solid line) are shown together with calculations employing the Thomas-Fermi model of screening with varying values of the screening length, as shown in the figure. Full squares as in (a), whereas the open squares are the *absolute* experimental total counting cross section for the emission of one electron from the initially neutral cluster (cf. text for details) [2,3].

theories shown in Fig. 1(a): As alluded to in the introduction, with increasing screening the region where scattering may take place shrinks. This results in a suppression of the ionization cross section with increasing screening length, as is evident from Fig. 1(b). This effect is not a simple scaling down of $W(\epsilon_0)$, but the shape is also affected. The peak of $W(\epsilon_0)$ is shifted to higher energies and $W(\epsilon_0)$ is generally flattened. In fact, for extremely high screening the cross section is very small and shows basically very weak dependence on ϵ_0. This can be understood from the behavior of the form factor of the potential U_{TF} which for large screening is independent of ϵ_0, i.e., $U_{\mathrm{TF}}(q) \propto r_0^2 = \mathrm{const}, \forall\ \epsilon_0$ [14]. Another extreme limit that shows up in Fig. 1 (cf. also Fig. 2) is that when ϵ_0 is very large the electronic density of the cluster cannot react within the very short passage time of the electron through the interaction region and hence only small deviations between all the models are observed in the high energy regime.

The full numerical RPAE calculations for the cross section $W_{\mathrm{RPAE}}(\epsilon_0)$ confirm the trends we pointed out by means of the locally screened potential U_{TF}. In fact, by comparing the $W_{\mathrm{RPAE}}(\epsilon_0)$ and $W_{\mathrm{TF}}(\epsilon_0)$ one may deduce a rough estimate of the screening length which is of importance for the consideration of the relaxation time due to electron-electron collisions [15]. We obtain a qualitative agreement between $W_{\mathrm{RPAE}}(\epsilon_0)$ and $W_{\mathrm{TF}}(\epsilon_0)$ when $r_0^{-1} = 0.3$ a.u. is used to evaluate $W_{\mathrm{TF}}(\epsilon_0)$, however, it should be stressed that we were not able to reproduce correctly the RPAE calculations by simply adjusting r_0, as can be concluded from Fig. 1(b).

For a comparison of $W_{\mathrm{RPAE}}(\epsilon_0)$ with the experiments we recall the remarks of Ref. [5] that, experimentally the electron impact on C_{60} may lead not only to the formation of stable C_{60}^{+} but also may produce unstable C_{60}^{+} that within a certain lifetime, not resolved by the experiment, decay subsequently into various fragmentation channels. Therefore, we show in Fig. 1(b) the experimental total counting rates, i.e., the total electron-impact ionization cross sections for the emission of one electron from C_{60} along with the experimental total cross section for the ionization of C_{60} and for the formation of the stable C_{60}^{+} ion. We regard the agreement between the parameter-free $W_{\mathrm{RPAE}}(\epsilon_0)$ and the experimental results as satisfactory, in view of the fact that the RPA is the first order approximation to the two-point particle-hole Green function, as outlined in the introduction.

To study the interplay between quantum-size effects and the nonlocal screening as described by RPAE we calculated within the spherical jellium model the cross section $W_{\mathrm{RPAE}}(\epsilon_0)$ for Li clusters with varying sizes. For a judicious conclusions we normalized the cross sections to the number of electrons in the respective cluster. Figures 2(a) and 2(b) reveal a striking influence of charge density fluctuation on $W(\epsilon_0)$, in particular at low energies: The RPAE model predicts a suppression of $W_{\mathrm{RPAE}}(\epsilon_0)$ with an increasing cluster size due the increasing phase space for the particle-hole creation [cf. inset of Fig. 2(a)]. In contrast the neglect of charge density fluctuations results in increased peak values of $W(\epsilon_0)$ for larger clusters. Furthermore, according to the RPAE, the peak in $W(\epsilon_0)$ is considerably broadened and shifted towards higher energies when the cluster size is increased (for the cluster with a radius $R_{\mathrm{Li}} = 4a_0$ the peak is at $\epsilon_0 \approx 200$ eV whereas this peak is shifted to $\epsilon_0 \approx 700$ eV for $R_{\mathrm{Li}} = 10a_0$) [cf. Fig. 2(a) and inset]. As explained above, this is consistent with the behavior of $W(\epsilon_0)$ with increased screening length [14]. In contrast, the neglect of the particle-hole (de)excitations leads to cross sections with the peak positions being shifted towards lower energies as the cluster size grows [cf. Fig. 2(b) and inset]. For small clusters or for $\epsilon_0 \gg 1$ there is hardly an influence of charge density fluctuations [cf. heavy solid lines in Figs. 2(a) and 2(b)].

Summarizing the above results, we have seen how the particle-hole (de)excitations suppress and modify the

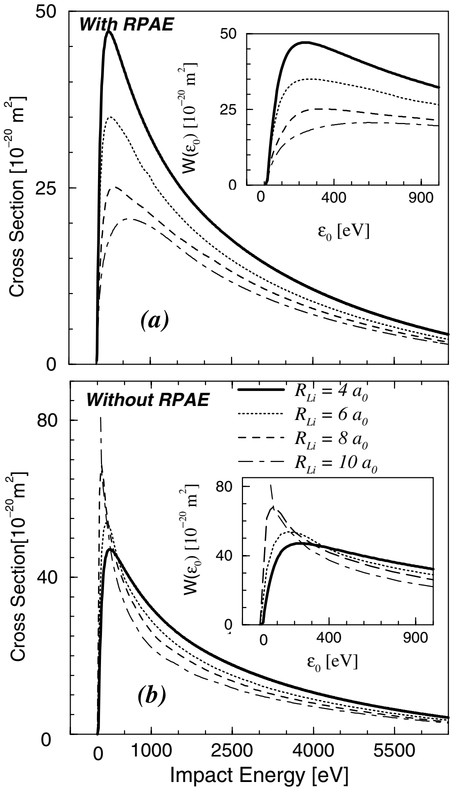

FIG. 2. The total electron-impact cross section for the ionization of spherical Li clusters with varying radius size R_{Li}. (a) shows the RPAE calculations. (b) shows the results when the particle-hole (de)excitation is neglected [the first term of Eq. (1)]. The insets in (a) and (b) highlight the low-energy region.

ionization cross sections for the electron scattering from neutral metal clusters. The simple Thomas-Fermi (TF) model of screening provided a useful tool to obtain global views on the role of delocalization of the electrons. The more elaborate random phase approximation confirmed and specified more precisely the understanding gained from the TF model. We also envisaged the interrelation between quantum-size and screening effects. From a formal point of view, we note that to treat scattering processes in isolated few charged particle systems, such as in atoms or small molecules, one has to deal with the infinite-range tail of the Coulomb interaction that precludes the use of standard methods [16] and induces multiple scattering between the collision partners up to very large distances. In contrast, the presence of the screening in systems with a large number of delocalized active electrons renders possible the use of standard scattering theory but on the considerable expense of actually calculating the nonlocal screening properties of the medium, e.g., as described by the polarization propagator Π. The crossover between the two cases is marked by a breakdown of the RPAE for dilute systems, where other methods such as the ladder approximation become more appropriate. In any case one has to bear in mind that, both from a practical and a conceptual point of view, approximate methods that perform well for few particle scattering may not be suitable for the treatment of delocalized many-particle systems (and vice versa).

We thank P. Bruno and S. Keller for helpful comments.

---

*Electronic address: okidun@mpi-halle.de

†Electronic address: jber@mpi-halle.de

[1] A. L. Fetter and J. D. Walecka, *Quantum Theory of Many-Particle Systems,* (McGraw-Hill, New York, 1971).

[2] S. Matt *et al.,* J. Chem. Phys. **105**, 1880 (1996).

[3] V. Foltin *et al.,* Chem. Phys. Lett. **289**, 181 (1998).

[4] V. Tarnovsky *et al.,* J. Phys. B **31**, 3043 (1998).

[5] H. Deutsch *et al.,* J. Phys. B **29**, 5175 (1996).

[6] S. Keller and E. Engel, Chem. Phys. Lett. **299**, 165 (1999).

[7] S. Keller, Eur. Phys. J. D **13**, 51 (2001).

[8] J. L. Martins *et al.,* Chem. Phys. Lett. **180**, 457 (1991).

[9] M. Brack, Rev. Mod. Phys. **65**, 677 (1993).

[10] F. Calogero, Nuovo Cimento **33**, 352 (1964).

[11] V. Babikov, *Method of the Phase Functions in Quantum Mechanics* (Nauka, Moskow, 1971).

[12] O. Kidun and J. Berakdar, in *Many-Particle Spectroscopy of Atoms, Molecules, Clusters and Surfaces* (Kluwer Academic/Plenum Publishers, New York, 2001).

[13] E. Brook *et al.,* J. Phys. B **11**, 3115 (1978).

[14] This behavior and the rough positions of the peaks in $W(\epsilon_0)$ can be explained analytically if we write $T_{\mathrm{TF}} = \int d^3\boldsymbol{p}_1\, d^3\boldsymbol{p}_2 \langle \boldsymbol{k}_1\boldsymbol{k}_2 | U_{\mathrm{TF}} | \boldsymbol{p}_1\boldsymbol{p}_2 \rangle B$, where $B = \langle\, \boldsymbol{p}_1\boldsymbol{p}_2 \,|\, \phi_\nu \boldsymbol{k}_0 \rangle$, and assume B to vary slowly with $\boldsymbol{p}_1, \boldsymbol{p}_2$ on the scale of the variation of the form factor of U_{TF}.

[15] A. Domps *et al.,* Phys. Rev. Lett. **81**, 5524 (1998).

[16] J. P. Taylor, *Scattering Theory* (John Wiley, Inc., New York, 1972).

Surface Science 507–510 (2002) 662–665

SURFACE SCIENCE

www.elsevier.com/locate/susc

Excitation spectra of free fullerene clusters

Oleg Kidun *, Jamal Berakdar

Max-Planck Institut fuer Mikrostrukturphysik, Weinberg 2, D06120 Halle/Saale, Germany

Abstract

In this work we study the single electron emission from fullerene clusters upon the impact of low-energy electrons. The calculations of the quantum ground states of the fullerene are performed within the Hartree–Fock and the jellium shell model. The interaction between the incoming projectile and knocked out electrons is described on the basis of random phase approximation with exchange, which leads to the concept of screening of the inter-electronic interaction. We compare the results of the calculations with available experimental data for the ionization of C_{60} by electron impact and show that neglect of polarization leads to results at variance with experimental finding. © 2002 Elsevier Science B.V. All rights reserved.

Keywords: Jellium models; Many body and quasi-particle theories; Electron density, excitation spectra calculations; Electron bombardment; Electron emission; Electron–solid interactions

The aim of this work is the investigation of the single ionization of the fullerene cluster from its (single-particle) ground state $|\phi_{2j}\rangle$ upon the impact of an electron with wave vector $\boldsymbol{k}_0$. In the final channel two electrons recede from the residual cluster to emerge with asymptotic momenta $\boldsymbol{k}_1$ and $\boldsymbol{k}_2$. The transition amplitude for such a reaction is given by

$$T(\boldsymbol{k}_0,\boldsymbol{k}_1,\boldsymbol{k}_2,\phi_v) = E_0\langle \boldsymbol{k}_1\boldsymbol{k}_2|V_{12}\Pi|\phi_{2j}\boldsymbol{k}_0\rangle \qquad (1)$$

E_0 is the total kinetic energy of the two electrons and $\Pi = G_0 + G_0 V\Pi$ is the total Green operator of the projectile–cluster system with the total potential V. The interaction between the projectile and the knocked-out electron is designated by V_{12}. Here we report on the calculation of the first-order term of Eq. (1) as well as of the next terms due to the electron–hole excitations. In the presence of the external electron with momentum $\boldsymbol{k}_0$ the self-consistent cluster potential changes. Taking into account the polarization of the electronic cloud, we write the amplitude of the process as a sum of two terms. The "direct" one corresponds to the excitation of the cluster's electron labeled by index "2" from the jth bound state ϕ_{2j} to the continuum state with the asymptotic momentum $\boldsymbol{k}_2$. The second "correlation" term describes correction, which appears from electron–hole excitations. Thus, in the random phase approximation with exchange (RPAE) the matrix element reads

$$\begin{aligned} T &\sim \left\langle \boldsymbol{k}_1\boldsymbol{k}_2|V_{\mathrm{eff}}|\phi_{2j}\boldsymbol{k}_0\right\rangle \\ &= \left\langle \boldsymbol{k}_1\boldsymbol{k}_2|V_{12}|\phi_{2j}\boldsymbol{k}_0\right\rangle \\ &\quad + \sum_{\varepsilon_\alpha \leqslant \varepsilon_{\mathrm{F}} < \varepsilon_\beta} \left(\frac{\left\langle \boldsymbol{\alpha}\boldsymbol{k}_2|V_{\mathrm{eff}}|\phi_{2j}\boldsymbol{\beta}\right\rangle \left\langle \boldsymbol{\beta}\boldsymbol{k}_1\left|\frac{1}{r_{13}}\right|\boldsymbol{k}_0\boldsymbol{\alpha}\right\rangle}{\varepsilon_0 - \left(\varepsilon_\alpha - \varepsilon_\beta - \mathrm{i}\delta\right)} \right. \\ &\quad \left. - \frac{\left\langle \boldsymbol{\beta}\boldsymbol{k}_2|V_{\mathrm{eff}}|\phi_{2j}\boldsymbol{\alpha}\right\rangle \left\langle \boldsymbol{\alpha}\boldsymbol{k}_1\left|\frac{1}{r_{13}}\right|\boldsymbol{k}_0\boldsymbol{\beta}\right\rangle}{\varepsilon_0 + \left(\varepsilon_\alpha - \varepsilon_\beta - \mathrm{i}\delta\right)} \right) \end{aligned} \qquad (2)$$

---

[*] Corresponding author. Tel.: +49-345-5582613; fax: +49-345-5511223.

E-mail address: okidun@mpi-halle.de (O. Kidun).

PII: S0039-6028(02)01332-8

V_{eff} being an effective interelectron interaction, $1/r_{13}$—bare Coulomb between impact and intermediate electrons; α, β are the intermediate electron's and hole's states with the energies ε_α, ε_β; ε_0 and ε_{F} are the initial energy of the projectile and the Fermi energy respectively. The different terms in the sum describe electron–hole excitation and deexcitation.

The differential electron-impact ionization cross-section is to be summed over ionization events from all the initial bound states ϕ_{2j} accessible within the energy conservation, i.e.

$$\frac{\mathrm{d}^6\sigma}{\mathrm{d}^3\mathbf{k}_1\,\mathrm{d}^3\mathbf{k}_2} = \frac{(2\pi)^4}{|k_0|}\sum_j \left|T(\mathbf{k}_0,\mathbf{k}_1,\mathbf{k}_2,\phi_{2j})\right|^2 \times \delta(\varepsilon_0 - (\epsilon_j^{\text{ion}} + k_1^2/2 + k_2^2/2)) \qquad (3)$$

The quantum states of the fullerene cluster are constructed within the Hartree–Fock approximation and within the spherical jellium model. The potential of C_{60}, which is a superposition of atomic potentials, is replaced by a potential of a fullerene shell. The latter is formed by delocalized valence electrons of carbon atoms and is modelled by a potential well: $V(r) = V_0$ within the region $R - \Delta < r < R + \Delta$, and $V = 0$ elsewhere. Here $R \approx 6.7a_0$ is the radius of the fullerene, the thickness of the shell is $2\Delta \approx 2a_0$, a_0 being the Bohr radius. The height of the well was chosen such that the experimental value of the electron affinity of C_{60} and the number of valence electrons are correctly reproduced.

Numerical calculation of the Hartree–Fock states is based on the non-local variable phase approach [1–3]. This method allows to find the eigen functions and eigen values through the scattering phase function and through the poles of the scattering amplitude in the complex plane of the wave vector of the particle. Such a choice of numerical realization of the self-consistent procedure allows to accelerate its convergency significantly.

For this purpose we look at the scattering of the spinless particle with the energy $E = k^2$ and orbital momentum ℓ in the nonlocal potential $V(r, r')$:

$$\frac{\mathrm{d}^2}{\mathrm{d}r^2}u_\ell(r) + \left(k^2 - \frac{\ell(\ell+1)}{r^2}\right)u_\ell(r) = \int_0^\infty \mathrm{d}r'\,V_\ell(r,r')u_\ell(r') \qquad (4)$$

After replacement of the radial part $u_\ell(r)$ of the wave function by the partial amplitude and phase functions $\alpha_\ell(r)$ and $\delta_\ell(r)$:

$$u_\ell(r) = \alpha_\ell(r)\cdot F(\delta_\ell(r))$$
$$\mathrm{d}u_\ell(r) = \alpha_\ell(r)\cdot \mathrm{d}G(\delta_\ell(r))$$

where

$$F(\delta_\ell(r)) = \cos\delta_\ell(r)j_\ell(kr) - \sin\delta_\ell(r)n_\ell(kr)$$
$$\mathrm{d}G(\delta_\ell(r)) = \cos\delta_\ell(r)\mathrm{d}j_\ell(kr) - \sin\delta_\ell(r)\mathrm{d}n_\ell(kr) \qquad (5)$$

the Schrödinger second order differential (4) transforms to the system of the first order Riccati-type equations:

$$\frac{\mathrm{d}}{\mathrm{d}r}\delta_\ell(r) = \left(-\frac{2}{k}\right)F^2(\delta_\ell(r))\int_0^r \mathrm{d}r'\,V(r,r') \times \exp\left[-\int_{r'}^r \frac{\mathrm{d}G(\delta_\ell(r''))}{F(\delta_\ell(r''))}\right]$$
$$\frac{\mathrm{d}}{\mathrm{d}r}\alpha_\ell(r) = \alpha_\ell(r)\frac{\sin\delta_\ell(r)\cdot j_\ell(kr) + \cos\delta_\ell(r)\cdot n_\ell(kr)}{F(\delta_\ell(r))} \times \frac{\mathrm{d}}{\mathrm{d}r}\delta_\ell(r) \qquad (6)$$

$j_\ell(kr)$, $n_\ell(kr)$—Riccati–Bessel functions are regular and irregular solutions of the free Schrödinger equation. For the local potential $V(r)$, $\delta_{\ell(r)}$ and $\alpha_{\ell(r)}$ have clear physical interpretation: they are the asymptotic scattering phase and the asymptotic amplitude of the wave function built for cutoff at r potential.

The eigen energies are calculated by finding the poles of the partial scattering amplitude in the imaginary half-axis of the wave vector $k = \mathrm{i}\kappa$, $\kappa \in \Re$. It is related to the scattering phase $f_\ell = (1/k)\mathrm{e}^{\mathrm{i}\delta_\ell}\sin\delta_\ell$. After some algebra, Volterra-type equation for f_ℓ, corresponding to the system (6), can be derived

$$\frac{\mathrm{d}(\mathrm{i}\cdot f_\ell(r))}{\mathrm{d}r} = \left(-\frac{2}{\kappa}\right)\frac{1}{\beta^2}F^2(f_\ell(r))\int_0^r \mathrm{d}r'\,V_\ell(r,r') \times \exp\left\{\int_{r'}^r \frac{\mathrm{i}\cdot f_\ell(r'')\cdot \mathrm{d}q_\ell(\kappa r'') + \beta^2\mathrm{d}p_\ell(\kappa r)}{F(f_\ell(r''))}\right\} \qquad (7)$$

$$F(f_\ell(r)) = \mathrm{i}\cdot f_\ell(r)\cdot q_\ell(\kappa r) + \beta^2 p_\ell(\kappa r)$$

where p_ℓ and q_ℓ are modified Riccati–Bessel functions of the real argument κr; $\beta = (\mathrm{i})^{\ell+1}$. Initial condition for the integration is $f_\ell(r = 0) = 0$. The condition for the bound state is condition for the poles of $f_\ell(r \to \infty)$. In practical calculation the regularization of this equation can be made in two different ways: by the replacement $\mathrm{i}\cdot f_\ell = 1/\phi$ or by the replacement $\mathrm{i}\cdot f_\ell = \tan\gamma$. Then the eigen state exists at zeros of ϕ or for $\gamma = (2n+1)\pi/2$, $n \in \mathscr{Z}$. In this work we used the regularization of the first kind.

Due to the spherical symmetry the Hartree–Fock total wave function was constructed from $2(2\ell+1)$ degenerate single-electron orbitals. The latter form several sub-bands characterized by different number of nodes of the radial wave functions. The lowest sub-band orbitals with the orbital momenta $0 \leqslant \ell \leqslant 7$ do not have nodes on radial axis, the next ones ($0 \leqslant \ell \leqslant 5$) have one node, and highest sub-bands occupied orbitals (with $0 \leqslant \ell \leqslant 3$ and $0 \leqslant \ell \leqslant 2$)—two and three nodes respectively. All shells are closed and the total number of the electrons is equal to 240.

To get a qualitative insight into the role of screening for the shape of the cross section we compare our RPAE calculations with the calculations in intuitively transparent approximation: Due to the presence of a large number of mobile electrons on the surface of the fullerene the interaction of the incident electron with the cluster electrons is screened. A simple model to account for this effect is the Thomas–Fermi approach which yields a local screening of the electron–electron interaction described by the one-parameter Yukawa potential: $V(r_{12}) = \exp(-\lambda r_{12})/r_{12}$, where λ is the inverse screening length. The results of our calculations are presented in Fig. 1a, where the total cross section of the process $\sigma(\varepsilon_0)$ is given as a function of the impact energy. Dashed curves correspond to different values of the inverse screening length, solid curve is the RPAE result.

Despite their conceptual simplicity, these models of electronic correlation yield encouraging results. We compare them with available experimental data [4] together with the calculation of work [5], where the bare Coulomb interaction was taken into account and the (e, 2e) total cross section was calculated in the plane wave Born approximation, and with the semi-empirical model calculation [6] (see Fig. 1b). When contrasted with calculations that neglect screening effect, the account of it results in a flattening of the total ionization cross section at lower impact energies. This effect can be traced back to the fact that for the unscreened Coulomb

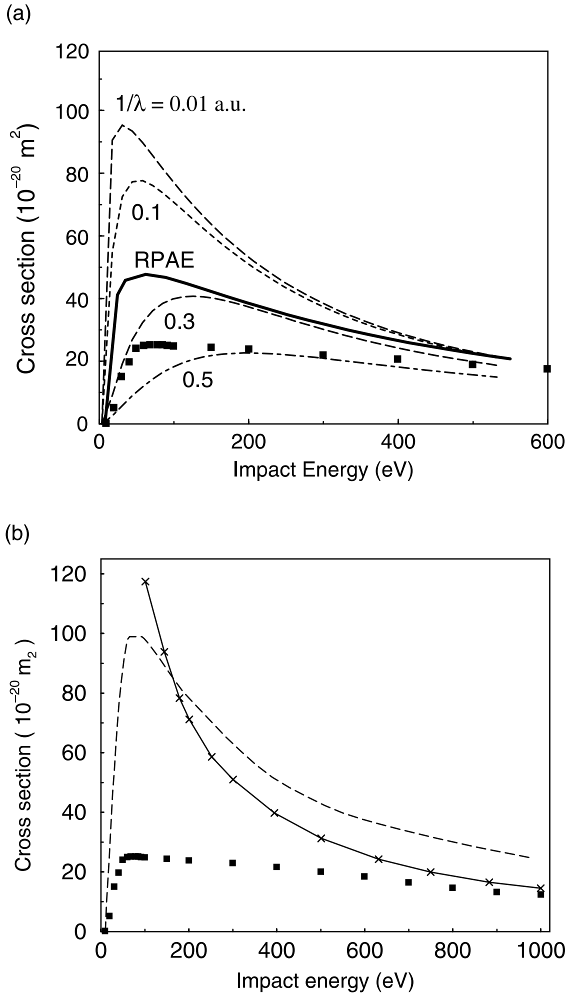

Fig. 1. Integrated electron-impact single ionization cross section of C_{60} as a function of the projectile energy: (a) Present calculations in Thomas–Fermi model (dashed curves) with different values of the inverse screening length and in the RPAE (solid curve). (b) Solid line: calculation in the plane wave Born approximation for the jellium-shell model [5]; dashed line: result of semi-empirical model calculation [6]; (a) and (b) symbols: experimental cross section for production of C_{60}^{+} ions [4].

interaction the main contribution to the cross sections originates from far collisions, whereas in case of screening there is a cut-off impact parameter beyond which the contribution of collisions to the cross section diminishes.

References

[1] F. Calogero, Nuovo Cimento 27 (1) (1963) 261; F. Calogero, Nuovo Cimento 33 (2) (1964) 352.

[2] V. Babikov, Method of the phase functions in quantum mechanics. Moskow, Nauka, 1971.

[3] O. Kidun, J. Berakdar, in: Many-Particle Spectroscopy of Atoms, Molecules, Clusters and Surfaces, 2001, pp. 395–404.

[4] V. Foltin, M. Foltin, S. Matt, P. Scheier, K. Becker, H. Deutsch, T.D. Mark, Chem. Phys. Lett. 289 (1–2) (1998) 181–188.

[5] S. Keller, E. Engel, Chem. Phys. Lett. 299 (2) (1999) 165–170.

[6] H. Deutsch, K. Becker, J. Pittner, V. Boniacic-Koutecy, S. Matt, T.D. Mark, J. Phys. B 29 (1996) 5175.

Manifestations of Electronic Correlations in the Diffraction of Electron Pairs from Crystals

J. Berakdar,* S. N. Samarin, R. Herrmann, and J. Kirschner
Max-Planck-Institut für Mikrostrukturphysik, Weinberg 2, 06120 Halle, Germany

(Received 23 March 1998)

The energy-sharing spectra of correlated electron pairs ejected from Cu(001) and Fe(110) surfaces reveal characteristic structures associated with diffraction of the pair from the lattice. It is demonstrated theoretically and experimentally that (1) the momentum-space *positions* of these new features are determined by the change of the center-of-mass wave vector of the pairs as compared to the reciprocal lattice vector, and (2) the relative *intensities* of the peaks and the *shapes* of the individual peaks are dependent on the internal correlation of the pairs. Possible pathways for the pair creation are envisaged at various diffracted beams. [S0031-9007(98)07432-8]

PACS numbers: 79.20.Kz

An electronic system distorted externally by a photon or a charged particle impact can integrally respond by the simultaneous emission of two electrons into the vacuum. The vacuum states of these two correlated electrons can be then determined using an angular and energy-resolved coincidence technique. The spectra of low-energy electron pairs, the subject of this study, carry the signature of their mutual correlations and their coupling to other degrees of freedom of the environment while in the high energy regime information on the initial-momentum components of the pair can be extracted from the recorded spectra [1–4]. These observations have been made in diverse areas of physics, such as plasma, atomic, molecular, and condensed matter physics [3,5,6]. For pair emission from localized electronic states, such as atomic and molecular orbitals, it turns out that the spectra are dominated by the interelectronic interaction of the pair, in particular at lower energies (with respect to the initial orbital energies) [6]. Thus, an adequate theoretical description of these phenomena must go beyond an independent particle description. For delocalized electronic states, as present in metallic crystals and surfaces, it is established that delocalization does not preclude correlations. E.g., in transition metals the d electrons are delocalized, yet correlation between them is far from weak.

In this work it is shown theoretically and experimentally that an electron pair can be regarded as a "two-electron quasiparticle." The scattering of this quasi-single-particle from a crystal potential results in characteristic diffraction pattern that is, for the first time, experimentally observed. The positions of the diffraction peaks are governed by a von Laue–like diffraction condition for the center-of-mass wave vector of the electron pair. The relative intensities of the diffraction maxima are largely determined by the internal degree of freedom of the pair, i.e., by interelectronic correlations.

The experimental setup used for the angular and energy-resolved detection of the pairs, i.e., for the projection of the two-electron initial state onto the two-electron vacuum state, is schematically depicted in Fig. 1. A more detailed description can be found in Refs. [7–9]. The sample surface defines the x-y plane, while the z axis coincides with the surface normal. In the z-x plane two position sensitive microchannel plate electron detectors are located at a distance of 160 mm to the sample surface, such that the relative angle between the detector axes and the surface normal is given by $\pm\alpha$. The angular acceptance of each electron detector within the scattering plane is $\pm 13.2°$. A parallel electron beam of about 1 mm diameter impinges onto the sample surface including the angle γ with the surface normal. For investigating the Cu(001) sample, the angles α and γ are chosen to be 40° and 0°, respectively, while in the case of Fe(110) (BCC), α was set to be 50° and $\gamma = 5°$. Correlated electron pairs emitted from the sample upon excitation by a primary electron are detected in coincidence. Their energies have been measured using a time-of-flight technique. In the range of electron energies detected here, we achieve an energy resolution of $\Delta E = 0.4$–0.8 eV. Standard cleaning procedure of the surface is applied before each measurement under a base pressure in the range of 10^{-11} mbar.

The probability for the two electrons to be detected with asymptotic momenta $\mathbf{k}_1$ and $\mathbf{k}_2$ is derived from an

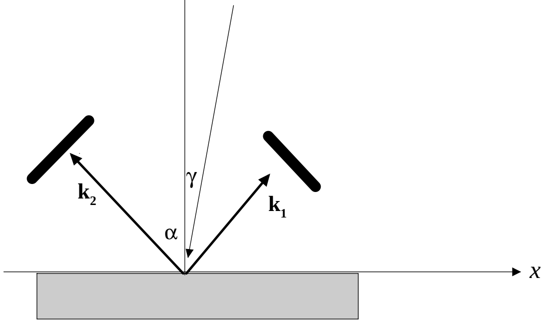

FIG. 1. A schematic representation of the experimental setup as described in the text.

excitation amplitude, $\mathcal{T}$, that is, to leading order, a sum of direct electron pair excitation amplitude, T_{ee}, and an amplitude, T_{ec}, that involves the scattering of the pair from the crystal potential W_{ec} [10,11] (i.e., atomic units [a.u.] are used throughout)

$$\mathcal{T} = T_{ee} + T_{ec}\,. \tag{1}$$

To emphasize the quasi-single-particle nature of the correlated pair we canonically transform to a wave vector representation $\mathbf{K}^- \otimes \mathbf{K}^+$ where $\mathbf{K}^+ = \mathbf{k}_1 + \mathbf{k}_2$ is the center-of-mass wave vector of the pair, and $\mathbf{K}^- = (\mathbf{k}_1 - \mathbf{k}_2)/2$ characterizes the interelectronic wave vector, i.e., the internal degree of freedom of the pair. The direct pair emission amplitude has the form

$$T_{ee} = \langle \mathbf{K}^-, \mathbf{K}^+ | W_{ee} | \mathbf{k}_0, \chi_{\epsilon(\mathbf{k})} \rangle\,, \tag{2}$$

where $|\mathbf{k}_0, \chi_{\epsilon(\mathbf{k})}\rangle$ is the state vector describing the pair as initially prepared by the experiment. In the present work $|\mathbf{k}_0, \chi_{\epsilon(\mathbf{k})}\rangle$ consists of an excited electronic vacuum state with wave vector $\mathbf{k}_0$ and a bound state $|\chi_{\epsilon(\mathbf{k})}\rangle$ with energy ϵ and wave vector $\mathbf{k}$. These two states are then coupled via a screened (renormalized) Coulomb interaction W_{ee}. The transition amplitude T_{ec} that describes scattering from the semi-infinite crystal can be deduced to

$$T_{ec} = \iint d^3\mathbf{p}\, d^3\mathbf{q} \langle \mathbf{K}^-, \mathbf{K}^+ | W_{ee} g_{ee}^- | \mathbf{p}, \mathbf{q} \rangle \times \langle \mathbf{p} | W_{ec} | \mathbf{k}_0 \rangle \langle \mathbf{q} | \chi_{\epsilon(\mathbf{k})} \rangle\,. \tag{3}$$

Here g_{ee}^- is the propagator in the interelectronic Coulomb interaction, W_{ec} is the interaction potential between the projectile and the lattice, and $|\mathbf{q}\rangle \otimes |\mathbf{p}\rangle$ is a complete set of plane waves. For the numerical calculations presented here we approximate W_{ec} by nonoverlapping muffin-tin ionic potentials V^{ion} ($W_{ec} = \sum_i V_i^{\text{ion}}$). The quality of this approximation is discussed in Ref. [12]. The form factor $\tilde{W}_{ec} := \langle \mathbf{p} | W_{ec} | \mathbf{k}_0 \rangle$ can then be reduced to

$$\tilde{W}_{ec} = \frac{N\sqrt{2\pi}f}{A_{uc}} \sum_{\ell} e^{-iK_z r_{\perp,\ell}} \sum_{\mathbf{g}_\|} \delta^{(2)}(\mathbf{g}_\| - \mathbf{K}_\|) \tilde{V}^{\text{ion}}(\mathbf{K})\,. \tag{4}$$

In Eq. (4) $\tilde{V}^{\text{ion}}(\mathbf{K})$ is the Fourier transform of V^{ion}, N is the number of ionic cores illuminated by the electron beam, A_{uc} is the volume of the two-dimensional unit cell, $\mathbf{g}_\|$ is the surface reciprocal lattice vector, ℓ enumerates the atomic layers with shortest distance $r_{\perp,\ell}$ with respect to the origin, $\mathbf{K} = \mathbf{p} - \mathbf{k}_0$, and $f = \exp(i\mathbf{p} \cdot \mathbf{r}_1)$ with $\mathbf{r}_1$ referring to the position of the bound electron.

The decisive point is that due to Bloch's theorem, which relies only on the two-dimensional periodicity of W_{ec}, regardless of it's actual functional form, the transition amplitudes T_{ec} and T_{ee} can be expressed as

$$T_{ec} = C \sum_{\ell, \mathbf{g}_\|} \delta^{(2)}[\mathbf{g}_\| - (\mathbf{K}_\|^+ - \mathbf{K}_{0,\|})] \times \mathcal{L}(\mathbf{g}_\|, \ell, \mathbf{K}^+, \mathbf{K}^-, \mathbf{k})\,, \tag{5}$$

whereas T_{ee} is given by

$$T_{ee} = \delta^{(2)}(\mathbf{K}_{0,\|} - \mathbf{K}_\|^+)\, \mathcal{L}'. \tag{6}$$

In Eq. (6) $\mathbf{K}_0 = \mathbf{k}_0 + \mathbf{k}$ is the initial wave vector of the pair. The functions $C, \mathcal{L}, \mathcal{L}'$ depend on the description of the momentum-space wave function $\langle \mathbf{q} | \chi_{\epsilon(\mathbf{k})} \rangle$ of the bound electron. For a jellium-state momentum distribution and free interelectronic propagation, Eqs. (5) and (6) can be evaluated in closed form [10].

Equation (5) has important implications:

(1) Only the pair center-of-mass wave vector enters in the von Laue-like diffraction condition, expressed by the delta function. This is equivalent to a diffraction of a quasiparticle located at the pair's center of mass when the parallel component of its wave vector is changed by $\mathbf{g}_\|$ during the collision. We note that in LEED studies (Low Energy Electron Diffraction) diffraction occurs when the change in the wave vector of the incident electron equals $\mathbf{g}_\|$ [12,13]. The decisive difference to the pair's diffraction is that a fixed $\mathbf{K}^+$ does not imply fixed $\mathbf{k}_1, \mathbf{k}_2$ since a momentum exchange of the two electrons (the internal coordinate $\mathbf{K}^-$ changes then) does not necessarily modify $\mathbf{K}^+$. Therefore, a definite change in $\mathbf{K}^+$ does not fix the amount of change in the wave vector of the incoming projectile.

(2) While $\mathbf{K}^+$ determines the *positions* of the diffraction peaks, the functional dependence of $\mathcal{L}$ on $\mathbf{K}^-$, which characterizes the strength of electronic correlations (in momentum space W_{ee} depends only on $|\mathbf{K}^-|$), controls the *intensity* of the individual diffraction peaks. Furthermore, the *shape* of the individual peaks is influenced by the interelectronic correlation.

(3) The distribution of the wave vector $\mathbf{k}_\|$ of the initially bound Bloch electron results in a smear-out effect of the diffraction pattern even in the case where $\mathbf{K}^+$ and $\mathbf{k}_0$ are experimentally sharply resolved.

(4) Conversely, in case $\mathbf{K}_\|^+, \mathbf{g}_\|$ and $\mathbf{k}_{0,\|}$ are well defined, the position and widths of the diffraction peaks reflects the character of $\mathbf{k}_\|$.

To substantiate the above statements we performed, using the setup depicted in Fig. 1, three sets of measurements where, for a fixed incident E_i and total excess energies $E_{\text{tot}} = (k_1^2 + k_2^2)/2$ of the pair, we scan the electrons' energy sharing. As shown in Fig. 1, $\mathbf{k}_0, \mathbf{k}_1, \mathbf{k}_2$ lie in the x-z plane, i.e., $\mathbf{K}_\|^+$ possesses only one nonvanishing component K_x^+ along the x axis. As indicated above, it is this component that is relevant for the pair diffraction, and hence we investigate the energy sharing as function of K_x^+. Since $E_{\text{tot}} = K^{+^2}/2m + K^{-^2}/2m_\mu$, where $m = 2$ is the total mass of the pair and $m_\mu = 0.5$ is their reduced mass, the value of K_x^+ is generally restricted to $0 \leq K_x^+ \leq \sqrt{4E_{\text{tot}}}$. In the arrangement of Fig. 1 the condition

$$-\sin\alpha\sqrt{2E_{\text{tot}}} \leq K_x^+ \leq \sin\alpha\sqrt{2E_{\text{tot}}} \tag{7}$$

has to be imposed. In Fig. 2 the results are presented for a Cu(001) monocrystal. The cross section is then proportional to $|\mathcal{T}|^2$ [Eq. (1)]. An integration over $\mathbf{k}_\|$ (weighted with the density of states) is, however, necessary as it is not experimentally resolved [10]. Furthermore, an average of the spin degrees of freedom has been performed.

Since $\gamma = 0$ in Fig. 2, the whole experimental arrangement, i.e., the scattering plane, spanned by $\mathbf{k}_1$ and $\mathbf{k}_2$, and the crystal is invariant under 180° rotation around $\hat{\mathbf{z}}$ (note that $\mathbf{k}_0 \parallel \hat{\mathbf{z}}$ lies in the scattering plane and is the bisector of the relative angle $\cos^{-1}\hat{\mathbf{k}}_1 \cdot \hat{\mathbf{k}}_2$). Thus, the spectrum depicted in Fig. 2 is symmetric with respect to $K_x^+ = 0$. Furthermore $\mathcal{L}, \mathcal{L}'$ are symmetric with respect to $K_x^+ = 0$; hence structures left and right to $K_x^+ = 0$ are modified in the same way by $\mathcal{L}, \mathcal{L}'$.

For illustration, assuming $\mathbf{k}_\parallel = 0$, the positions of the first diffraction maxima [hereafter referred to as the $(-1,0)\,(1,0)$ maxima] are indicated by arrows. The theoretical and experimental data (Fig. 2) clearly show the onset of the $(1,0)$, and $(-1,0)$ diffraction peaks. The abrupt decrease of these peaks at the wings is due to the cutoff condition (7). The structure in the middle is due to the specular beam $(0,0)$. This is clearly demonstrated by analyzing separately the contributions $|T_{ee}|$ and $|T_{ec}|$ to the total transition amplitude (1). By far the major contribution originates from T_{ec} [Eq. (5)], i.e., from events where the pair is back-reflected from the crystal potential. Nonetheless, at the specular beam the amplitude T_{ee} [Eq. (6)] provides an observable contribution to the total transition amplitude $|\mathcal{T}| = |T_{ec} + T_{ee}|$ (cf. Fig. 2). The contribution of $|T_{ee}|$ [Eq. (6)] to the $(-1,0)$ and $(1,0)$ peaks vanishes identically. This is in line with Eq. (6) and supports the identification of these peaks as $(-1,0)$ and $(1,0)$ diffraction maxima of the pair. As suggested above, the width of the structure corresponding to the $(0,0)$ diffraction is determined by the initial momentum components of the pair. Since k_0 is fixed by the experiment, the initial momentum distribution of the pair is given by that of the bound electron with its maximum value being the Fermi wave vector k_F. I.e., each of the diffraction peaks has an extension of $K_x^+ = \pm k_F$. This is consistent with the experimental findings of Figs. 2–4. We note however, that the cutoff condition (7) has to be superimposed on the widths of the diffraction peaks, in particular on those at the wings of the spectra.

Going down with E_{tot} (and E_i) the variation interval of K_x^+ shrinks according to Eq. (7). In fact, at $E_i = 34$ eV and $E_{\text{tot}} = 27$ eV (see Fig. 3) only the structure in the middle of Fig. 2 is captured by the region in which K_x^+ is allowed. To demonstrate the sensitivity of the spectra

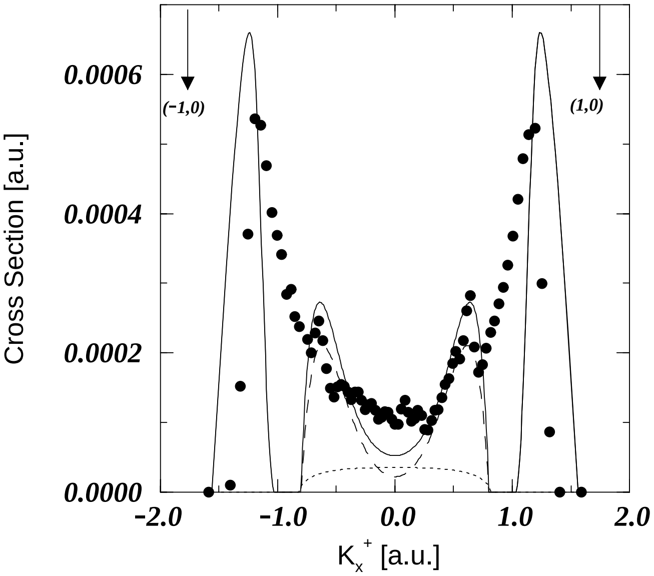

FIG. 2. For a fixed incident energy $E_i = 85$ eV and fixed excess energy $E_{\text{tot}} = 79$ eV, the excess energy-sharing of the escaping electrons is depicted as function of $K_x^+ = k_{1,x} + k_{2,x}$. The experiment has been performed on a Cu(001) crystal in normal incidence, corresponding to $\gamma = 0$ in Fig. 1, Furthermore, we choose $\alpha = 40°$ (cf. Fig. 1). Depicted are the separate contributions of amplitudes for direct pair emission [$|T_{ee}|$ as given by Eq. (6)] (dotted curve) and the amplitude for the pair's scattering from the lattice potential [$|T_{ec}|$ as defined by Eq. (5)] (dashed curve). Calculations using the coherent sum $|\mathcal{T}| = |T_{ee} + T_{ec}|$ (solid curve) are also shown. The calculations are performed for infinite energy and angular resolution of the detectors; for clarity the theoretical $(-1,0)$ and $(1,0)$ diffracted peaks are scaled down by 2. The positions of the $(1,0)$ and $(-1,0)$ diffracted beams are indicated (see text). The experimental data (full dots) are on relative scale.

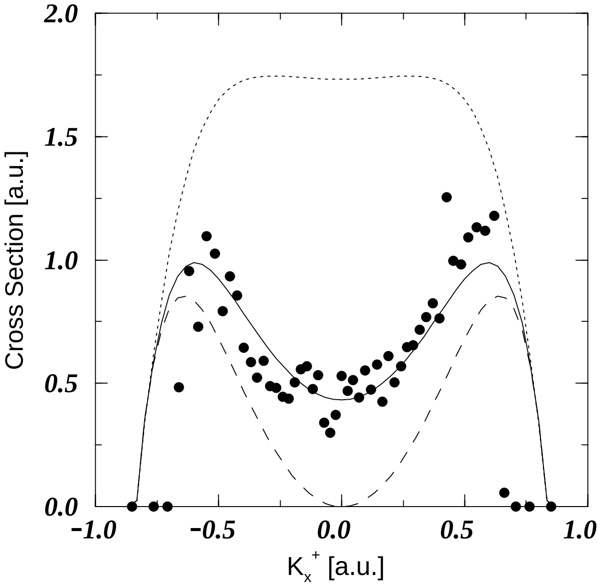

FIG. 3. The same as in Fig. 2, however, the incident energy is lowered to $E_i = 34$ eV and $E_{\text{tot}} = 27$ eV. For the calculations we employ the coherent sum, $\mathcal{T}$, of the amplitudes for the direct pair emission and the pair's scattering from the crystal potential, i.e., $\mathcal{T} = T_{ee} + T_{ec}$ [Eq. (1)]. The singlet σ^s (dotted curve) and the triplet σ^t (dashed curve) scattering cross sections are shown along with their statistical average, $0.25\sigma^s + 0.75\sigma^t$ (solid curve). The finite experimental resolution has not been taken into account. The spin nonresolved experimental data (full dots) are relative and have been normalized to theory at one point.

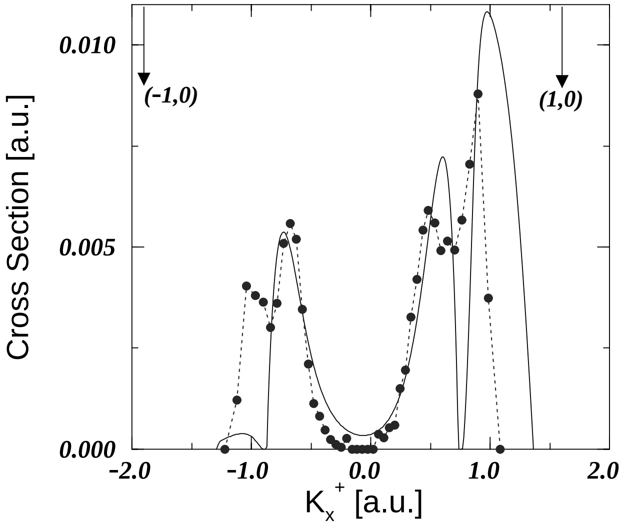

Fig. 4. The experimental results (full dots) for a Fe(110) (BCC) sample at an incident energy of 50 eV and $E_{\text{tot}} = 44$ eV. The incident beam is tilted with respect to the normal by an angle of $\gamma = 5°$ and $\alpha = 50°$ (cf. Fig. 1). Theoretical results (solid curve) are obtained by evaluating $|\mathcal{T}| = |T_{ee} + T_{ec}|$ [Eq. (1)].

to the interelectronic coupling we investigate the singlet (dotted curve in Fig. 3) and the triplet (dashed curve in Fig. 3) scattering contribution to the spin nonresolved spectrum (solid curve in Fig. 3). Because of symmetry requirement the triplet scattering must vanish when the two electron emerge with the same energies, i.e., for $K_x^+ = 0$. In fact, inspecting Fig. 3 we can deduce that the minimum in the spin-averaged spectrum around $K_x^+ = 0$ is primarily due to the diminishing triplet contribution at $K_x^+ = 0$. The same has been observed for the cases of Figs. 2 and 4. Further investigations (not shown here for space limitations) have shown that the absolute magnitude of the spectra is strongly dependent on the amount of screening of the interelectronic Coulomb interaction.

In the last example (Fig. 4) performed for Fe(110) the crystal and the scattering plane do not have a common symmetry axis. This is reflected in a break of symmetry of the spectra. The initial wave-vector distribution of the pair $K_{0,x}$ is then modified in a preferential direction determined by $k_{0,x} = 0.17$ a.u. This is of prime importance when determining the change of the wave vector of the pair during the collision that in turn decides the diffraction pattern. E.g., the positions of the $(-1,0)$ and $(1,0)$ diffraction peaks in Fig. 4 are not symmetric with respect to $K_x^+ = 0$, in contrast to Figs. 2 and 3. Hence, only a reminiscence of $(-1,0)$ diffraction is seen in the spectra shown in Fig. 4. An interplay of this effect with the scattering dynamics, described by the now asymmetric functions $\mathcal{L}, \mathcal{L}'$ in Eqs. (5) and (6), leads to the relative heights of the peaks as observed in Fig. 4.

From an analysis, analogous to that done in Fig. 2, we conclude in cases of Figs. 3 and 4 that pair emission at the $(-1,0)$ and $(1,0)$ beams is solely due to the amplitude T_{ec} Eq. (5). The pair generation around the specular beam $(0,0)$ is dominated by (5) as well, however, interference with the amplitude T_{ee} [Eq. (6)] is evident. Investigating the sum over ℓ in Eq. (5) we deduce that in this present case of Figs. 2–4 correlated pairs are predominantly generated in the two topmost atomic layers.

---

*Email Address: jber@mpi-halle.de

[1] I. E. McCarthy and E. Weigold, Rep. Prog. Phys. **54**, 789 (1991).
[2] M. A. Coplan, J. H. Moore, and J. P. Doering, Rev. Mod. Phys. **66**, 98 (1994).
[3] M. Vos and I. E. McCarthy, Rev. Mod. Phys. **67**, 713 (1995).
[4] A. S. Kheifets, S. Iacobucci, A. Ruoccoa, R. Camilloni, and G. Stefani, Phys. Rev. B **57**, 7360 (1998).
[5] *Electron Impact Ionization,* edited by T. D. Mark and G. H. Dunn (Springer-Verlag, Vienna, 1985).
[6] *Coincidence Studies of Electron and Photon Impact Ionization,* edited by C. T. Whelan and H. R. J. Walters (Plenum Press, New York, London, 1997), and references therein.
[7] J. Kirschner, O. M. Artamonov, and A. N. Terekhov, Phys. Rev. Lett. **69**, 1711 (1992).
[8] J. Kirschner, O. M. Artamonov, and S. N. Samarin, Phys. Rev. Lett. **75**, 2424 (1995).
[9] O. M. Artamonov, S. N. Samarin, and J. Kirschner, Appl. Phys. A **65**, 535 (1997).
[10] J. Berakdar and M. P. Das, Phys. Rev. A **56**, 1403 (1997).
[11] H. Gollisch, G. Meinert, Xiao Yi, and R. Feder, Solid State Commun. **102**, 317 (1997).
[12] J. B. Pendry, *Low Energy Electron Diffraction* (Academic Press, London, 1974).
[13] M. A. van Hove, W. H. Weinberg, and C.-M. Chan, *Low Energy Electron Diffraction,* in Springer Series in Surface Science (Springer, Berlin, 1986).

PERGAMON

Solid State Communications 112 (1999) 587–591

solid
state
communications

www.elsevier.com/locate/ssc

Pair correlation in two-electron emission from surfaces

J. Berakdar[a,*], H. Gollisch[b], R. Feder[b]

[a]*Max-Planck-Institut für Mikrostrukturphysik, Weinberg 2, 06120 Halle, Germany*
[b]*Theoretische Festkörperphysik, Universität Duisburg, D-47048 Duisburg, Germany*

Received 23 July 1999; accepted 28 July 1999 by P. Dederichs

Abstract

An electron pair emitted from a crystalline surface system is represented by a relativistic two-electron scattering state, which contains the pair correlation mediated by a screened Coulomb interaction. This state is obtained from the solutions of two one-electron Dirac equations with potentials, which incorporate the electron–electron interaction as a dynamical screening of the usual effective one-electron potentials. Numerical applications to the electron pair emission due to low-energy electron impact on a He atom and on a clean W(001) surface demonstrate that pair correlation effects can be quite strong and significantly improve the agreement of calculated results with experimental data. © 1999 Elsevier Science Ltd. All rights reserved.

Keywords: A. Metals; A. Surfaces and interfaces; D. Electron–electron interactions; E. Electron emission spectroscopies

The simultaneous two-electron emission induced by electron impact on atomic and solid targets, so-called (e,2e) spectroscopy, has a long history of success for high-energy primary electrons (cf. e.g. [1–3] and references therein). For low-energy primary electrons (with less than a few 100 eV) impinging on a crystalline surface and momentum-resolved pair observation in the reflection mode, substantial experimental and theoretical progress was made only fairly recently [4–10]. Good overall agreement between experimental data and their calculated counterparts was achieved and details of the (e,2e) mechanism were thence revealed.

In the existing theoretical treatments (cf. [6,8,9]), the two ejected electrons are described by an anti-symmetrized product of single-particle states. Whilst a "pair correlation" due to exchange (Pauli principle) is thus incorporated, the Coulomb interaction between the two ejected electrons has not been taken into account. On the other hand, the Coulomb pair correlation is known to be vital for photon-induced two-electron emission [11,12]. We therefore explore in the present work its potential importance in the low-energy (e,2e) process by formulating a theoretical method and applying it numerically to the prototype surface W(001).

To incorporate the Coulomb interaction between the two ejected electrons, at least, an effective "quasi *two*-particle" theory is needed. The initial asymptotic state of the system is an anti-symmetrized direct product of two single quasi-particle states, which represent the projectile electron and an individual valence electron, i.e. $|1,2\rangle = |1\rangle \otimes |2\rangle$. The states $|1\rangle$ and $|2\rangle$ are solutions of a Dirac equation involving optical potentials V_1 and V_2, respectively, which incorporate the interaction with the nuclei and all the other ground state electrons. We recall (cf. e.g. [9]) that for a semi-infinite crystalline system with lattice periodicity parallel to the surface relativistic one-electron states $|i\rangle$ are characterized by energies, E_i, surface-parallel two-dimensional wave vectors $\mathbf{k}_i^{\parallel}$ and spin labels σ_i. The number i in $|i\rangle$ is thus an abbreviation for the set of quantum numbers $(E_i, \mathbf{k}_i^{\parallel}, \sigma_i)$. For the relativistic LEED (low energy electron diffraction) state $|1\rangle$, the set $(E_1, \mathbf{k}_1^{\parallel}, \sigma_1)$ is dictated by the experimental conditions and is equivalent to the three-dimensional wave vector $\mathbf{k}_1$ and the spin alignment at the electron gun. Even if the primary beam is unpolarized, states $|1\rangle$ with $\sigma_1 = \pm$ have to be employed and finally summed over. The same holds in any case for the valence states $|2\rangle$.

For the electron–electron interaction U considered as a perturbation, standard scattering theory gives the transition amplitude for the initial state $|1,2\rangle$ to go over into the two-electron excited state $|3,4\rangle$ as

$$W(1,2;3,4) = \langle 3,4|U|1,2\rangle. \tag{1}$$

---

* Corresponding author. Fax: + 49-345-55-11223.
E-mail address: jber@mpi-halle.de (J. Berakdar)

PII: S0038-1098(99)00365-8

Strictly speaking, $|3,4\rangle$ is an eigenstate of a two-electron Dirac equation involving the total potential

$$V_{\text{tot}} = V_3 + V_4 + U, \tag{2}$$

where V_3 and V_4 are one-particle optical potentials, and with asymptotic boundary conditions such that an electron with momentum $\mathbf{k}_3$ and spin alignment σ_3 arrives at one detector and an electron with momentum $\mathbf{k}_4$ and spin alignment σ_4 at the other detector. Obviously, an exact solution of this non-separable many-body equation is not possible. On the other hand, if we neglect in Eq. (2) the interaction term U, the state $|3,4\rangle$ reduces to an anti-symmetrized direct product of two independent time-reversed LEED states, $|3\rangle$ and $|4\rangle$, as was done in previous work [8,9]. Since these (uncoupled) LEED states $|3\rangle$ and $|4\rangle$ are calculated using one-particle optical potentials V_3 and V_4, respectively, each of them contains—within the framework of a local spin density approximation to exchange and correlation terms—the exchange and correlation with all the other “passive electrons”.

The interaction U between the two active electrons must be included in a dynamic way that reflects the dependence of the mutual coupling on the electrons’ positions relative to each other. For example, the interaction between the two electrons is strongest when they escape close to each other, whereas this interaction diminishes when the electrons are far apart.

To implement this dynamical coupling, we first identify the electron pair interaction U as a Coulomb potential, which is screened by the ground state electrons of the semi-infinite crystal. Since the calculation of a realistic dielectric function $\epsilon(\mathbf{r},\mathbf{r}')$ for such a highly inhomogeneous electron gas is beyond the scope of this work, we adopt the Thomas–Fermi form $U(\mathbf{r}_3,\mathbf{r}_4) = \exp(-r_{34}/\lambda)/r_{34}$, where $\mathbf{r}_3$ and $\mathbf{r}_4$ are the positions of the two active electrons and $\mathbf{r}_{34} = \mathbf{r}_3 - \mathbf{r}_4$. To obtain a physically reasonable estimate of the screening length, λ, we start from the Thomas–Fermi expression (at $T = 0$) $\lambda = (4\pi e^2 N(E_F))^{(-1/2)}$, where $N(E_F)$ is the total density of states at the Fermi energy E_F. Rather than approximating $N(E_F)$ by a non-interacting homogeneous electron gas value, as is frequently done, we take it from a self-consistent electronic structure calculation for the actual crystal. Employing the simple Thomas–Fermi form appears reasonable in this work, firstly because it is our aim to get first and perhaps only semi-quantitative results on pair correlation effects, and secondly, because it led to rather good agreement between theory and experiment in a recent (e,2e) study on W(001) [9].

With this approximation for U, we return to the potential V_{tot} (Eq. (2)). We express the one-electron potentials V_3 and V_4 as lattice sums over potentials w_3 and w_4 residing in muffin tin spheres around the lattice sites. Inside each sphere, we then have the total potential $W_{\text{tot}} = w_3 + w_4 + U$. With the above Thomas–Fermi expression for U, this can easily be reformulated as

$$W_{\text{tot}} = w_3 + \frac{Z_3}{r_3} + w_4 + \frac{Z_4}{r_4} \tag{3}$$

where

$$Z_j = a_j^{-1} \exp\left(-\frac{a_j}{2\lambda} r_j\right), \qquad j = 3, 4, \tag{4}$$

with $a_j = 2r_{34}/r_j$. The interpretation of Eq. (3) is straightforward. Owing to the electronic correlation, the single-particle potentials $w_j, j = 3, 4$ are augmented by the term Z_j/r_j. This means that the inter-electronic correlation is subsumed into a dynamic non-local screening of the electron core interaction.

The strength of this screening is determined by the functions Z_j, as given by Eq. (4). In fact, the augmented electron core potentials $\bar{w}_j = w_j + Z_j/r_j$ may even turn repulsive when the two electrons are “on top of each other” ($r_{34} \to 0$).. If the two electrons are far away from each other ($r_i \gg r_j$, $i \neq j \in [3,4]$) the screening strengths Z_3 and Z_4 become negligible and we end up with two independent particles ($\bar{w}_j \to w_j$). Furthermore, if one of the electrons approaches closely the ionic sites its motion becomes dominated by the corresponding ionic potential w_j. This is readily deduced from the relation $\lim_{r_j \to 0} \bar{w}_j \to w_j$.

Our dynamic screening expression in Eq. (3) is, for the above-defined U, merely a rearrangement of the interaction terms in Eq. (2). Its direct numerical implementation is extremely difficult. In the present exploratory study, we therefore approximate the dynamical screening strengths Z_j by $\bar{Z}_j = \bar{a}_j^{-1} \exp(-(\bar{a}_j/2\lambda) r_j)$ with $\bar{a}_3 = 2v_{34}/v_3$ and $\bar{a}_4 = 2v_{34}/v_4$, where $\mathbf{v}_3$ and $\mathbf{v}_4$ are velocities of the two emitted electrons and $\mathbf{v}_{34} = \mathbf{v}_3 - \mathbf{v}_4$. The approximation $\bar{Z}_j \approx Z_j$ amounts to assuming $\mathbf{r}_3 \propto \mathbf{v}_3$ and $\mathbf{r}_4 \propto \mathbf{v}_4$; this means that the potential Eq. (2) is exactly diagonalized when the particles proceed along trajectories where the positions are proportional to the velocities. Whilst inside the solid this is of course not the case, we feel that the above approximation is of a semi-quantitative value if we choose the two velocities $\mathbf{v}_i = \mathbf{k}'_{i0}/m$—with $i = 3, 4$—where $\mathbf{k}'_{i0}$ is the wave vector of the 00 LEED beam inside the crystal, which is obtained from the wave vector $\mathbf{k}_{i0}$ outside the crystal (and in particular at the detector) by refraction at the surface potential barrier.

To assess the quality of the above approach we evaluate at first the amplitude Eq. (1) for an atomic helium target in its ground state. This should give a direct insight into the single-site behavior of the dynamic screening. In this case the states $|3(\bar{Z}_3(\mathbf{v}_3, \mathbf{v}_4))\rangle$ and $|4(\bar{Z}_4(\mathbf{v}_3, \mathbf{v}_4))\rangle$ are derived from the corresponding Schrödinger equation for one particle moving in the electrostatic field of He$^+$ with an effective screening of this field given by $\bar{Z}_j(\mathbf{v}_3, \mathbf{v}_4)$, $j = 3, 4$. The electron–electron interaction is assumed unscreened, i.e. $\lambda \to \infty$. The cross-section with appropriate flux normalization is readily obtained from the transition amplitude, Eq. (1) [6]. Fig. 1 shows the cross-section at 2 eV above the single

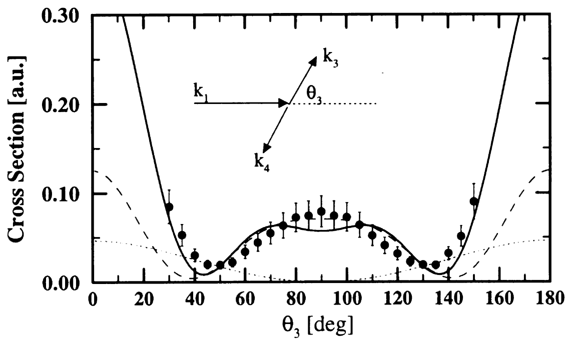

Fig. 1. The cross-section for the emission of two equal-energy electrons following the collision of an electron with an atomic He($^1S^e$) target. The excess energy of the pair is 2 eV. The angular correlation pattern is depicted as a function of the angle of the interelectronic axis with respect to the beam direction (see inset). The calculations with (continuous line) and without (dashed curve) dynamical screening are shown along with the results of the first Born approximation (dotted line) (see text for more details). The experimental data are taken from Ref. [14] where comparison with other theoretical methods can be found.

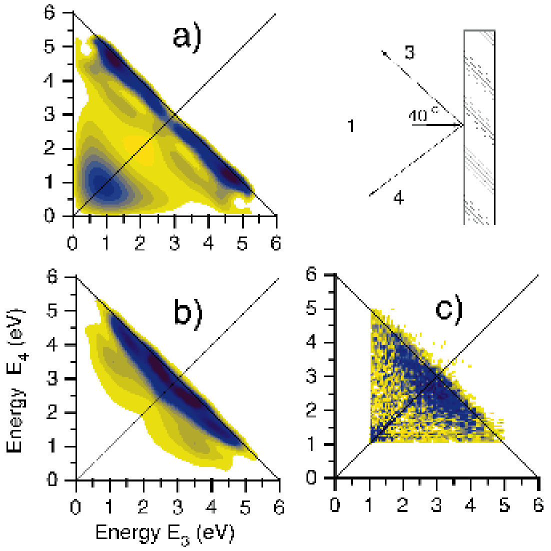

Fig. 2. Spin-averaged intensity for the two-electron emission from a W(001) surface following the impact of a 10.6 eV electron along the surface normal (chosen as the *z*-axis), i.e. polar angle of incidence $\theta_1 = 0$. The direction [100] defines the *x* axis. The emitted electrons are detected in the *x*–*z* plane, i.e. their azimuthal angles are $\phi_3 = 0$ and $\phi_4 = 180°$, and the polar angles are set to $\theta_3 = \theta_4 = 40°$. The contour plots in the (E_3,E_4)-plane show calculated results without Coulomb pair correlation (panel a) and with pair correlation according to Eq. (3) (panel b), in comparison with experimental data (panel c) [15]. For outgoing pair energies indicated by the solid counter-diagonal lines, the corresponding valence electron energy is the Fermi energy. Along the diagonal lines, the two outgoing electrons have equal energies.

ionization threshold of He as a function of the interelectronic axis with respect to the incident beam direction. As shown in the inset, both electrons escape with the same energy (1 eV) and opposite to each other, i.e. $\hat{\mathbf{k}}_3\cdot\hat{\mathbf{k}}_4 = -1$. The absolute experimental data are well reproduced by the present theory. To highlight the effect of correlation we also show in Fig. 1 the results neglecting the dynamic screening, i.e. we discard U in Eq. (2). This leads to results clearly at variance with the experimental finding. Furthermore, the importance of the coupling to the ionic core can be demonstrated by switching off U and V_3, i.e. one electron moves in the field of the residual ion whereas the second one is considered as free. This inadequate (cf. Fig. 1) procedure amounts to the well-known first Born approximation. The geometry depicted in Fig. 1 is in so far remarkable as in this situation the electronic correlation is minimal (at fixed total excess energy of 2 eV). Thus for situations where the electrons are detected close to each other in velocity space we can expect an even more striking effect of the pair correlation.

Having established the usefulness of the above method for single-site reactions we turn now to its application to (e,2e) spectroscopy from the clean crystal surface W(001), which was recently studied in detail experimentally and by calculations without the Coulomb pair correlation [9]. Employing a relativistic layer-KKR method [13] we numerically calculate the correlated time-reversed LEED states $\langle 3(\bar{Z}_1(\mathbf{v}_3,\mathbf{v}_4))|$ and $\langle 4(\bar{Z}_2(\mathbf{v}_3,\mathbf{v}_4))|$, each of which depends on the velocities $\mathbf{v}_3$ and $\mathbf{v}_4$ of the *two* electrons—chosen above as velocities of the 00 LEED beams inside the crystal—and their mutual relative velocity. For the screening length λ of the electron–electron interaction (cf. earlier) we obtained, with the aid of a self-consistent LMTO calculation for W, the value $\lambda = 0.48\,Å$. The cross-section is then calculated as in [9]. It essentially involves absolute squares of transition amplitudes (cf. Eq. (1)) summed over all spin labels σ_i (with $i = 1,\ldots,4$), since we wish to make contact with experiments without any spin resolution.

For the experimental conditions used in [9]—with primary electron energies between 16 and 24 eV and an angle of 80° between the directions of the two outgoing electrons—we find only rather small pair correlation effects, and the fairly good agreement between experiment and theory, which was reached in [9], remains practically unchanged. For different conditions, however, quite drastic effects emerge.

Firstly, we retained the coplanar geometry with the large angle between the two detected electrons, but lowered the primary energy to 10.6 eV, which implies a maximal total energy of the pair of 6 eV. The intensity distribution calculated without Coulomb pair correlation, i.e. for $Z_3 = 0 = Z_4$ in Eq. (3), is shown in Fig. 2a. For total pair energies between 5 and 6 eV, the intensity is small for $E_3 = E_4$ and has maxima around $(E_3,E_4) = (4.8, 1.0)$ and (1.0,4.8). In contrast, the spectra obtained with pair correlation (Fig. 2b) are maximal closer to and around $E_3 = E_4$. This is

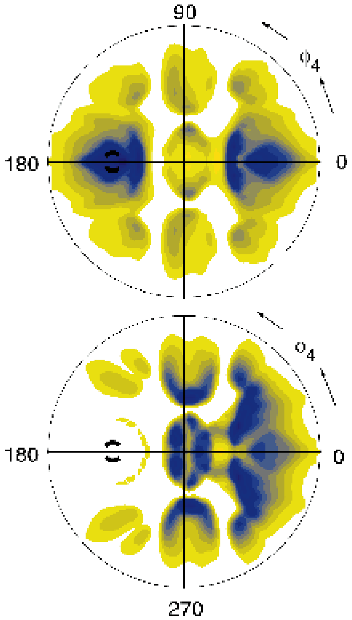

Fig. 3. Calculated spin-averaged angular distributions of two electrons emitted from W(001) upon impact of electrons with primary energy 17.2 eV. The polar and azimuthal angles of the incident electron are $\theta_1 = 88°$ (i.e. grazing incidence) and $\phi_1 = 0°$. The two outgoing electrons are detected with equal energies $E_3 = E_4 = 6$ eV. One electron detector is fixed at a direction defined by $\theta_3 = 47°$ and $\phi_3 = 180°$. The coincident emission rate is scanned as a function of the angles θ_4 and ϕ_4 of the other electron detector, which correspond to the radial and angular coordinates in the contour plots. The Coulomb pair correlation between the two outgoing electrons is switched off in the upper panel and taken into account according to Eq. (3) in the lower panel. The broken circle around $\theta_4 = 47°$ and $\phi_4 = 180°$ marks the direction of parallel escape of the two electrons, i.e. the centre of the “pair correlation hole”.

understandable from the fact that the Coulomb interaction can transfer energy from the one escaping electron to the other. Close to the threshold, around $(E_3, E_4) = (1, 1)$, where refraction implies a very small angle between $\mathbf{v}_3$ and $\mathbf{v}_4$, the electron–electron interaction is seen to prevent pair emission. Comparison with experimental data [15] (cf. Fig. 2c) shows that the inclusion of pair correlation significantly improves the agreement for total pair energies between 4 and 6 eV. As for the intensity around $(E_3, E_4) = (1, 1)$, we recall from [9] that this feature in experimental data is likely to arise from two accidentally time-correlated secondary electrons. Altogether, our calculations predict a strong influence of the pair correlation, which is substantiated by experimental findings.

The dependence of correlation effects on the angle between the two outgoing electrons is demonstrated in Fig. 3, where the detection direction of one electron is fixed and that of the other sweeps over the entire hemisphere. Comparison of the calculated results in the upper half of Fig. 3 with those in the lower half shows that the inter-electronic coupling results in a drastic modification of the angular distribution pattern. Without correlation, the emission probability is seen (cf. upper half of Fig. 3) to be maximal when the two electrons escape into the same direction and with the same velocity. This unphysical result is remedied by the pair interaction (cf. lower half of Fig. 3), which carves a considerable “pair correlation hole” around the position where electrons are close to each other in velocity space. For regions where the two electrons emerge with diverging directions, the effect of the pair correlation becomes less and less visible.

In conclusion, we have presented a theoretical formalism for including the Coulomb pair correlation in the calculation of *two-electron* scattering states from single atoms and from crystalline surface systems. This has been achieved through position-dependent dynamical screening of the usual effective one-electron potentials. For the actual evaluation of transition amplitudes, the position dependence has been approximated by a velocity dependence. Numerical results for an atomic target and for a crystal surface demonstrate that pair correlation effects can be important in two-electron emission upon low-energy electron impact. The application of the present formalism to electron pair emission due to the absorption of a VUV photon [11], a reaction forbidden in the absence of the pair correlation [12], is currently in progress.

Acknowledgements

We would like to thank S.N. Samarin for making available the experimental data shown in Fig. 2c.

References

[1] I.E. McCarthy, E. Weigold, Rep. Prog. Phys. 54 (1991) 789.
[2] M. Vos, I.E. McCarthy, Rev. Mod. Phys. 67 (1995) 713.
[3] C.T. Whelan, H.R.J. Walters (Eds.), Electron Coincidence Studies of Electron and Photon Impact Ionization Plenum, New York, 1997.
[4] J. Kirschner, O.M. Artamonov, S.N. Samarin, Phys. Rev. Lett. 75 (1995) 2424.
[5] O.M. Artamonov, S.N. Samarin, J. Kirschner, Appl. Phys. A 65 (1997) 535.
[6] J. Berakdar, M.P. Das, Phys. Rev. A. 56 (1997) 1403.
[7] J. Berakdar, S.N. Samarin, R. Herrmann, J. Kirschner, Phys. Rev. Lett. 81 (1988) 3535.
[8] H. Gollisch, G. Meinert, Xiao Yi, R. Feder, Solid State Commun. 102 (1997) 317.
[9] R. Feder, H. Gollisch, D. Meinert, T. Scheunemann, O.M. Artamonov, S.N. Samarin, J. Kirschner, Phys. Rev. B 58 (1998) 16418.
[10] A.S. Kheifets, S. Iacobucci, A. Ruoccoa, R. Camilloni, G. Stefani, Phys. Rev. B 57 (1998) 7380.

[11] R. Herrmann, S.N. Samarin, H. Schwabe, J. Kirschner, Phys. Rev. Lett. 81 (1998) 2148.

[12] J. Berakdar, Phys. Rev. B 58 (1908) 9808.

[13] R. Feder (Ed.), Polarized Electrons in Surface Physics World Scientific, Singapore, 1985.

[14] T. Rösel, J. Röder, L. Frost, K. Jung, H. Ehrhardt, S. Jones, D.H. Madison, Phys. Rev. A 46 (1992) 2539.

[15] S.N. Samarin, private communication.

Probing the Spin Polarization in Ferromagnets

Jamal Berakdar*
Max-Planck-Institut für Mikrostrukturphysik, Weinberg 2, 06120 Halle, Germany

(Received 30 August 1999)

The emission of correlated electrons from an itinerant ferromagnet following the impact of a polarized electron beam is analyzed in terms of irreducible tensorial parameters that can be measured. Under favorable conditions, specified in this work, these parameters are related to the spin polarization in the ferromagnet. The formal results are illustrated by numerical studies of the polarized electron pair emission from a Fe(110) surface, and a novel technique for the investigation of magnetic properties of ferromagnets is suggested.

PACS numbers: 79.20.Kz, 72.10.–d, 75.30.Ds

The electronic and magnetic properties of low dimensional systems with long-range magnetic order, such as ultrathin ferromagnetic films and magnetic surfaces, are currently under intensive investigations [1]. This is due to the fundamental and technological importance of such materials. Magnetic systems with reduced symmetry can be explored by a variety of techniques [1]. Low-energy spin-polarized electron spectroscopy is particularly suitable as the penetration depth is on the order of a few atomic layers [2]. In this method one resolves the quantum states of the incoming and outgoing electrons to extract the accessible information on the sample under investigation. On the other hand, a promising technique emerged in recent years where an electron pair, resolved in energy and momentum, is detected following the impact of an unpolarized electron beam upon a non-magnetic sample [3–6]. As demonstrated successfully for a variety of materials [3–5], the electron pair carries, under favorable conditions, direct signature of the Bloch spectral function which is a central quantity as far as the electronic structure is concerned. However, these studies [3,4] have been performed at higher energies (≈20 keV) and the role of the spin polarization has not been yet addressed. Very recently, however, it has been demonstrated by a pioneering experiment [7] that the electron-pair emission depends strongly on the spin polarization of the electron beam and the magnetization of the sample. Thus, it seems timely to inspect theoretically the low-energy polarized electrons emission from ferromagnets. We conclude the following: (i) the electrons' spectra are quantified fully by a set of irreducible tensorial components; (ii) under certain circumstances specified below, the electron-pair spectrum is directly related to the spin-resolved spectral function of the surface.

For a theoretical formulation we consider a reaction in which two electrons are simultaneously emitted from a ferromagnet with a defined magnetization direction $\hat{\mathbf{M}}$ after the impact of a monoenergetic spin-polarized electron beam. The spins of the electrons in the incoming beam and in the sample are assumed to be good quantum numbers. A corresponding experiment resolves the asymptotic wave vectors of the impinging and the two emitted (vacuum) electrons which we label $\mathbf{k}_1$ and $\mathbf{k}_1'$, $\mathbf{k}_2'$, respectively. No spin analysis of the outgoing electrons is performed. The target surface is described by the state vectors $|\phi_{\epsilon,\alpha,s_2,m_{s_2}}\rangle$, where ϵ is the ground state energy, m_{s_2} is the projection of the spin $\mathbf{s}_2$ of the ground state along a quantization axis, and α denotes all other quantum numbers. The spin polarization of the incoming beam with projection m_{s_1} of the electron's spin $\mathbf{s}_1$ is characterized by the density matrix $\rho^{s_1}_{m_{s_1}m_{s_1}}$, whereas the population of the magnetic sublevels of the state $|\phi_{\epsilon,\alpha,s_2,m_{s_2}}\rangle$ is given by the density matrix $\bar{\rho}^{s_2}_{m_{s_2}m_{s_2}}$. The scattering probability is related to (atomic units, a.u., are used throughout)

$$W(\mathbf{k}_1',\mathbf{k}_2';\mathbf{k}_1) = C \sum_{m_{s_1'},m_{s_2'},m_{s_1},m_{s_2}} \sum\!\!\!\!\!\!\int_{\alpha} \mathcal{M}(\mathbf{k}_1',\mathbf{k}_2',m_{s_1'},m_{s_2'};\alpha,m_{s_2},\mathbf{k}_1,m_{s_1})\rho^{s_1}_{m_{s_1}}m_{s_1}\bar{\rho}^{s_2}_{m_{s_2}}m_{s_2}(\epsilon,\alpha)$$
$$\times\, \mathcal{M}^*(\mathbf{k}_1',\mathbf{k}_2',m_{s_1'},m_{s_2'};\alpha,m_{s_2},\mathbf{k}_1,m_{s_1})\delta(E_f - E_i)\,, \qquad (1)$$

where E_f is the final-state total energy. The initial-state total energy E_i is $E_i = E_{\mathbf{k}_1} - \epsilon$, while $E_{\mathbf{k}_1}$ is the energy of the projectile beam and $C = (2\pi)^4/k_1$. All energies are measured with respect to the vacuum level. The transition amplitude $\mathcal{M}(\mathbf{k}_1',\mathbf{k}_2',m_{s_1'},m_{s_2'};\alpha,m_{s_2},\mathbf{k}_1,m_{s_1})$ is given by $\mathcal{M} = \langle\psi_{\mathbf{k}_1',\mathbf{k}_2',m_{s_1'},m_{s_2'}}|\mathcal{T}|\phi_{\epsilon,\alpha,s_2,m_{s_2}}\varphi_{\mathbf{k}_1,s_1m_{s_1}}\rangle$, where $\varphi_{\mathbf{k}_1,s_1m_{s_1}}$ is a spinor vacuum state describing the incoming beam. The emitted electrons with spin projections $m_{s_1'}, m_{s_2'}$ are represented by the state vector $|\psi_{\mathbf{k}_1',\mathbf{k}_2',m_{s_1'},m_{s_2'}}\rangle$, whereas $\mathcal{T}$ is the transition operator. In Eq. (1) the density matrices are diagonal. Furthermore, we adopt $\hat{\mathbf{M}}$ as a joint quantization axis for $\mathbf{s}_1$ and $\mathbf{s}_2$. For convenience we express the electrons' final state in the total spin space as $|\psi_{\mathbf{k}_1',\mathbf{k}_2',m_{s_1'},m_{s_2'}}\rangle = \sum_{SM_S}\langle SM_S\,|\,s_1'm_{s_1}', s_1'm_{s_1}'\rangle|\Psi_{\mathbf{k_1}',\mathbf{k_2}';SM_S}\rangle$, where S is the total spin and M_S is its projection.

To disentangle geometrical from dynamical properties, we expand the density matrices in state multipoles (statistical tensors) ρ_{pq} [8],

$$\rho^{s_1}_{m_{s_1} m_{s_1}} = \sum_{p_1=0}^{2s_1} (-)^{p_1 - s_1 - m_{s_1}} \langle s_1 - m_{s_1}; s_1 m_{s_1} \mid p_1 q_1 = 0 \rangle \rho_{p_1 q_1 = 0}\,. \tag{2}$$

$$\bar{\rho}^{s_2}_{m_{s_2} m_{s_2}}(\epsilon, \alpha) = \sum_{p_2=0}^{2s_2} (-)^{p_2 - s_2 - m_{s_2}} \langle s_2 - m_{s_2}; s_2 m_{s_2} \mid p_2 q_2 = 0 \rangle \bar{\rho}_{p_2 q_2 = 0}(\epsilon, \alpha)\,. \tag{3}$$

Substituting Eqs. (2) and (3) into the general expression (1) yields

$$W = \sum\!\!\!\!\!\!\!\int_{\alpha} \sum_{p_1=0}^{2s_1} \sum_{p_2=0}^{2s_2} \rho_{p_1 q_1 = 0} \bar{\rho}_{p_2 q_2 = 0}(\epsilon, \alpha) \Lambda^{p_1, p_2}_{q_1 = 0, q_2 = 0} \delta(E_f - E_i)\,, \tag{4}$$

where

$$\Lambda^{p_1, p_2}_{q_1=0, q_2=0} = C \sum_{m_{s_1}} (-)^{p_1 - s_1 - m_{s_1}} \langle s_1 - m_{s_1}; s_1 m_{s_1} \mid p_1 q_1 = 0 \rangle \sum_{m_{s_2}} (-)^{p_2 - s_2 - m_{s_2}} \langle s_2 - m_{s_2}; s_2 m_{s_2} \mid p_2 q_2 = 0 \rangle$$
$$\times \sum_{SM_S} \mathcal{M}(\mathbf{k}_1', \mathbf{k}_2', SM_s; \alpha, m_{s_2}, \mathbf{k}_1, m_{s_1}) \mathcal{M}^*(\mathbf{k}_1', \mathbf{k}_2', SM_s; \alpha, m_{s_2}, \mathbf{k}_1, m_{s_1})\,. \tag{5}$$

The decisive point is that the sum over m_{s_1} (m_{s_2}) in Eq. (5) defines the component (along $\hat{\mathbf{M}}$) of a spherical tensor of rank p_1 (p_2) [9]. This mathematical observation yields important information as to the transformation behavior of $\Lambda^{p_1, p_2}_{0,0}$: $\Lambda^{p_1=0, p_2}_{0,0}$ $(\Lambda^{p_1, p_2=0}_{0,0})$ is a *scalar* with respect to spin rotations generated by $\mathbf{s}_1$ $(\mathbf{s}_2)$, i.e., it represents spin averaged quantities in the $\mathbf{s}_1$ $(\mathbf{s}_2)$ spin space, whereas the components $\Lambda^{p_1=\mathrm{odd}, p_2}_{0,0}$ $(\Lambda^{p_1, p_2=\mathrm{odd}}_{0,0})$ can be regarded as a spin *orientation* in the $\mathbf{s}_1$ $(\mathbf{s}_2)$ spin space (for $p_1 = 1$ it is a polar vector) and, hence, changes sign upon spin reflection, i.e., $\Lambda^{p_1=\mathrm{odd}, p_2}_{0,0}(-m_{s_1}) = -\Lambda^{p_1=\mathrm{odd}, p_2}_{0,0}(m_{s_1})$ $[\Lambda^{p_1, p_2=\mathrm{odd}}_{0,0}(-m_{s_2}) = -\Lambda^{p_1, p_2=\mathrm{odd}}_{0,0}(m_{s_2})]$. The tensorial components with even p_1 values are alignment parameters, i.e., they describe the deviations in the spectra from the unpolarized case. The above formalism is easily generalized [9] to the case of strong spin-orbit coupling and/or multielectron emission. For two electrons, Eq. (4) reduces to

$$W = \sum\!\!\!\!\!\!\!\int_{\alpha} \left\{ \Lambda^{0,0}_{0,0} \left[\rho_{00} \bar{\rho}_{00} + \rho_{00} \bar{\rho}_{10} \frac{\Lambda^{0,1}_{0,0}}{\Lambda^{0,0}_{0,0}} + \rho_{10} \bar{\rho}_{00} \frac{\Lambda^{1,0}_{0,0}}{\Lambda^{0,0}_{0,0}} + \rho_{10} \bar{\rho}_{10} \frac{\Lambda^{1,1}_{0,0}}{\Lambda^{0,0}_{0,0}} \right] \delta(E_f - E_i) \right\}. \tag{6}$$

The first term of the sum in Eq. (6) is the pair emission rate averaged over the spin orientation of the incoming electron beam and the spin polarization of the sample. The second term describes the spin asymmetry due to the inversion of the magnetization while the incoming electron beam is being *unpolarized*. The third term is the spin asymmetry in the electron-pair emission from *unpolarized targets* when inverting the spin polarization of the electron beam. In the absence of explicit spin interactions in the *transition operator* $\mathcal{T}$, e.g., spin-orbit coupling, the parameters $\Lambda^{1,0}_{0,0}$ and $\Lambda^{0,1}_{0,0}$ vanish. The last term of Eq. (7) is related to the electron-pair emission from spin-polarized samples by spin-polarized electrons. It is a polar vector both in the $\mathbf{s}_1$ and the $\mathbf{s_2}$ spin spaces, i.e., $\Lambda^{1,1}_{0,0}(-m_{s_1}, m_{s_2}) = -\Lambda^{1,1}_{0,0}(m_{s_1}, m_{s_2}) = \Lambda^{1,1}_{0,0}(m_{s_1}, -m_{s_2})$. The explicit forms of $\Lambda^{1,1}_{0,0}$ and $\Lambda^{0,0}_{0,0}$ are derived from Eq. (5) to be

$$\Lambda^{1,1}_{0,0} = \frac{C}{2} \sum_{S=0}^{1} \sum_{M_s} \{ |\mathcal{M}(\mathbf{k}_1', \mathbf{k}_2', SM_s; \mathbf{k}_1, \alpha, \downarrow, \Downarrow)|^2 - |\mathcal{M}(\mathbf{k}_1', \mathbf{k}_2', SM_s; \mathbf{k}_1, \alpha, \uparrow, \Downarrow)|^2$$
$$+ |\mathcal{M}(\mathbf{k}_1', \mathbf{k}_2', SM_s; \mathbf{k}_1, \alpha, \uparrow, \Uparrow)|^2 - |\mathcal{M}(\mathbf{k}_1', \mathbf{k}_2', SM_s; \mathbf{k}_1, \alpha, \downarrow, \Uparrow)|^2 \}\,, \tag{7}$$

$$\Lambda^{0,0}_{0,0} = \frac{C}{2} \sum_{S=0}^{1} \sum_{M_s} \{ |\mathcal{M}(\mathbf{k}_1', \mathbf{k}_2', SM_s; \mathbf{k}_1, \alpha, \downarrow, \Downarrow)|^2 + |\mathcal{M}(\mathbf{k}_1', \mathbf{k}_2', SM_s; \mathbf{k}_1, \alpha, \uparrow, \Downarrow)|^2$$
$$+ |\mathcal{M}(\mathbf{k}_1', \mathbf{k}_2', SM_s; \mathbf{k}_1, \alpha, \uparrow, \Uparrow)|^2 + |\mathcal{M}(\mathbf{k}_1', \mathbf{k}_2', SM_s; \mathbf{k}_1, \alpha, \downarrow, \Uparrow)|^2 \}\,. \tag{8}$$

The projections of the spins of the sample state and the electron beam parallel (antiparallel) to the quantization axis are labeled, respectively, by the arrows $\Uparrow$ $(\Downarrow)$ and $\uparrow$ $(\downarrow)$. In the total spin space, Eqs. (7) and (8) are expressed in terms of the singlet and the triplet partial cross sections, $X^{(S=0)}$ and $X^{(S=1)}$, respectively, i.e.,

$$\Lambda^{1,1}_{0,0} = \frac{C}{2} [X^{(S=1)}(\mathbf{k}_1', \mathbf{k}_2'; \mathbf{k}_1; \alpha) - X^{(S=0)}(\mathbf{k}_1', \mathbf{k}_2'; \mathbf{k}_1; \alpha)]\,, \tag{9}$$

$$\Lambda_{0,0}^{0,0} = \frac{C}{2}\,[3X^{(S=1)}(\mathbf{k}_1', \mathbf{k}_2'; \mathbf{k}_1; \alpha) + X^{(S=0)}(\mathbf{k}_1', \mathbf{k}_2'; \mathbf{k}_1; \alpha)] =: 2X^{\mathrm{tot}}. \quad (10)$$

$X^{(S=0)}$ and $X^{(S=1)}$ are determined by the matrix elements, $T^{(S)}(\mathbf{k}_1', \mathbf{k}_2'; \mathbf{k}_1, \alpha)$, of the singlet ($S = 0$) and triplet ($S = 1$) transition operators $\mathcal{T}^S = (\mathbf{1} + (-1)^S \mathcal{P}_{12})\mathcal{T}$. Here, $\mathcal{P}_{12}$ is a permutation operator that interchanges the two emitted electrons. Thus, one obtains the symmetry property $T^{(S)}(\mathbf{k}_1', \mathbf{k}_2'; \mathbf{k}_1; \alpha) = (-1)^S T^{(S)}(\mathbf{k}_2', \mathbf{k}_1'; \mathbf{k}_1, \alpha)$; i.e., in situations where an interchange of the electrons does not modify the ionization dynamics the triplet scattering amplitude and, hence, $X^{(S=1)} = C|T^{(S=1)}|^2$ vanishes. An example will be shown below. Until this point the electronic and structural properties of the sample have not been yet specified. For perfect clean surfaces the integral over α in Eq. (6) implies summation over the surface Bloch wave vector $\mathbf{k}_{2\|}$ and over the surface layers. The Bloch theorem imposes a conservation law for the surface components of the *total* wave vector of the emitted electrons $\mathbf{K}_\|^+ = \mathbf{k}_{1\|}' + \mathbf{k}_{2\|}'$ [10]; i.e., the change of $\mathbf{K}_\|^+$ from its initial value $\mathbf{k}_{1\|} + \mathbf{k}_{2\|}$ (before the collision) is restricted to a multiple of the surface reciprocal lattice vector $\mathbf{g}_\|$. This fact can be used to perform the integrals over $\mathbf{k}_{2\|}$ in Eq. (6) which reduces then to a summation over the surface layers, indexed by l, and over $g_\|$, i.e.,

$$W \propto \sum_{\mathbf{g}_\|, l} \{2X^{\mathrm{tot}}(\mathbf{k}_1', \mathbf{k}_2'; \mathbf{k}_1, \mathbf{g}_\|, l)\,[\rho_{00}\bar{\rho}_{00}(\epsilon, \mathbf{\Lambda}_\|, l) + \rho_{10}\bar{\rho}_{10}(\epsilon, \mathbf{\Lambda}_\|, l) A^s(\mathbf{k}_1', \mathbf{k}_2'; \mathbf{k}_1, \mathbf{g}_\|, l)] \times \delta(E_f - E_i)\}, \quad (11)$$

where $\mathbf{\Lambda}_\| = \mathbf{K}_\|^+ - \mathbf{g}_\| - \mathbf{k}_{1\|}$. The "exchange scattering asymmetry" has been defined as

$$A^s := \frac{X^{(S=1)}(\mathbf{k}_1', \mathbf{k}_2'; \mathbf{k}_1, \mathbf{g}_\|, l) - X^{(S=0)}(\mathbf{k}_1', \mathbf{k}_2'; \mathbf{k}_1, \mathbf{g}_\|, l)}{3X^{(S=1)}(\mathbf{k}_1', \mathbf{k}_2'; \mathbf{k}_1, \mathbf{g}_\|, l) + X^{(S=0)}(\mathbf{k}_1', \mathbf{k}_2'; \mathbf{k}_1, \mathbf{g}_\|, l)}\,. \quad (12)$$

To calculate the terms in Eq. (11), the state multipoles ρ_{10} and $\bar{\rho}_{10}$ are needed. These can be obtained by inverting the relations (2) and (3). In the standard representation, the density operators of the beam and the surface are linearly expanded in terms of the Pauli matrices $\boldsymbol{\sigma}$ as $\rho^{s_1} = \mathbf{1} + \mathbf{P}_1 \cdot \boldsymbol{\sigma}$ and $\bar{\rho}^{s_2} = w_0(\mathbf{k}_{2\|}, l, \epsilon)\,(\mathbf{1} + \mathbf{P}_2 \cdot \boldsymbol{\sigma})$, where $w_0(\mathbf{k}_{2\|}, l, \epsilon)$ is the spin-averaged Bloch spectral function of the layer l, and $\mathbf{P}_1$ and $\mathbf{P}_2$ are the polarization vectors. The sample polarization is given by $P_2 = [w(\mathbf{k}_{2\|}, l, \epsilon, \Uparrow) - w(\mathbf{k}_{2\|}, l, \epsilon, \Downarrow)]/[w_0(\mathbf{k}_{2\|}, l, \epsilon)]$. Here $w(\mathbf{k}_{2\|}, l, \epsilon, m_{s_2})$ stands for the spin and layer resolved Bloch spectral function. Thus we obtain $\rho_{00}\bar{\rho}_{00} = [w_0(\mathbf{k}_{2\|}, l, \epsilon)]/2$ and $\rho_{10}\bar{\rho}_{10} = [w_0(\mathbf{k}_{2\|}, l, \epsilon)]P_1P_2/2$, and Eq. (11) reduces to

$$W \propto \sum_{\mathbf{g}_\|, l} w_0(\mathbf{\Lambda}_\|, l, \epsilon) X^{\mathrm{tot}}[1 + \mathcal{A}]\delta(E_f - E_i)\,. \quad (13)$$

The asymmetry function $\mathcal{A}$ has been introduced as

$$\mathcal{A} = P_1\,\frac{\sum_l [w(\mathbf{\Lambda}_\|, l, \epsilon, \Uparrow) - w(\mathbf{\Lambda}_\|, l, \epsilon, \Downarrow)] \sum_{\mathbf{g}_\|} X^{\mathrm{tot}} A^s \delta(E_f - E_i)}{\sum_{l'} w_0(\mathbf{\Lambda}_\|, l', \epsilon) \sum_{\mathbf{g}_\|'} X^{\mathrm{tot}} \delta(E_f - E_i)} = \frac{W(\uparrow\Uparrow) - W(\downarrow\Uparrow)}{W(\uparrow\Uparrow) + W(\downarrow\Uparrow)}\,. \quad (14)$$

Thus, for the calculation of the tensorial parameters two major ingredients are needed: (i) The spin and layer-resolved spectral function of the sample which can be obtained from the trace of the imaginary part of the corresponding Green function and (ii) the matrix element of the singlet and triplet transition operators. Now we calculate the terms in Eq. (13) for a Fe(110) surface. The Bloch spectral functions used here are provided by two independent calculations: (i) The scalar relativistic full-potential linearized augmented plane-wave method [11,12] and (ii) the full relativistic layer Korringa-Kohn-Rostoker method [2,13]. For the calculations of the transition matrix element we approximate the $\mathcal{T}$ operator by $\mathcal{T} = U_{\mathrm{surf}} + U_{ee}(\mathbf{1} + G_{ee}^- U_{\mathrm{surf}})$, where U_{ee} is the electron-electron interaction, G_{ee}^- is the Green function of the electron pair, and U_{surf} is the surface scattering potential. For U_{surf} we employ, for a given layer, a linear combination of nonoverlapping muffin-tin potentials [10].

As stated above, for certain geometries, the triplet scattering amplitude vanishes due to symmetry and, hence, A^s tends to -1 [cf. Eq. (12)]. Thus, if a monolayer or a bulk system is considered the magnetic asymmetry P_2 can be scanned by determining $W(\uparrow\Uparrow)$ and $W(\downarrow\Uparrow)$. This yields a direct (relative) estimate of the population of the spin states in the sample. For multilayered systems, we have to consider the weighting factor X^{tot} in Eq. (14). An example is shown in Fig. 1 for a Fe(110) sample. The two electrons are detected with fixed *equal* energies in the x-z plane and at *symmetric* positions with respect to the z direction while the incident beam direction is varied in the z-y plane. The experiment, in the geometry of Fig. 1, is invariant under a 180° rotation with respect to the z direction. This rotation can be regarded as an interchange of $\mathbf{k}_1'$ by $\mathbf{k}_2'$ and, since $T^{(S=1)}(\mathbf{k}_1', \mathbf{k}_2'; \mathbf{k}_1, \alpha) = -T^{(S=1)}(\mathbf{k}_2', \mathbf{k}_1'; \mathbf{k}_1, \alpha)$, the triplet scattering ($X^{(S=1)} = C|T^{(S=1)}|^2$) vanishes.

The energies ϵ in Eq. (14) are determined by $\epsilon = E_1' + E_2' - E_{\mathbf{k}_1}$, where E_1' and E_2' are the energies of the vacuum electrons. Thus we tune E_1', E_2', and $E_{\mathbf{k}_1}$ such that ϵ coincides with the Fermi energy E_F. Now by varying $\beta = \cos^{-1}\hat{\mathbf{z}} \cdot \hat{\mathbf{k}}_1$ we scan P_2 along

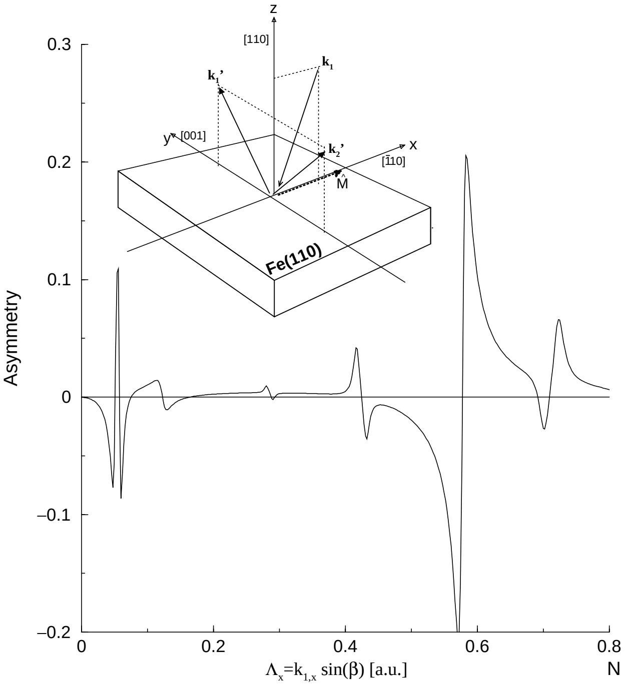

FIG. 1. The asymmetry, as given by Eq. (14), for the emission of two equal-energy electrons from a magnetized Fe(110) surface following the impact of a polarized electron beam with an energy of 35 eV. The total energy of the pair is fixed to $E_1' + E_2' = 30.15$ eV. The two electrons are detected in the y-z plane at symmetric position $\cos^{-1}\hat{\mathbf{z}} \cdot \hat{\mathbf{k}}_1' = 40° = \cos^{-1}\hat{\mathbf{z}} \cdot \hat{\mathbf{k}}_1'$ left and right to the z axis (cf. inset) and $\hat{\mathbf{M}} \parallel x$. The angle of incidence $\beta = \cos^{-1}\hat{\mathbf{z}} \cdot \hat{\mathbf{k}}_1$ is varied in the x-z plane, as shown by the inset. In this geometry, the triplet scattering vanishes and $\mathcal{A}$ can be related to P_2. The predominant contributions to $\mathcal{A}$ originate from the first and second surface layers.

the Γ-N direction in the Brillouin zone, as shown in Fig. 1. Alternatively, one may fix the direction $\mathbf{\Lambda}_{\parallel} = \mathbf{k}_{1\parallel}$ and image $P_2(\epsilon)$ by varying, e.g., the incident energy. For a polarized homogeneous electron gas, one scans (as function of energy) the relative difference between the occupied density of states of the majority and minority bands.

Away from the points of high symmetry (cf. Fig. 1) the scattering dynamics, as described by $X^{(S=0)}$ and $X^{(S=1)}$ become dominant. An example is shown in Fig. 2 for $\beta = 0$. Again at the Γ point ($\mathbf{k}_{1\parallel}' = -\mathbf{k}_{2\parallel}'$) the asymmetry $\mathcal{A}$, and in particular its sign, is determined solely by P_2. The For highly asymmetric energy sharing the scattering exchange asymmetry A^s is small which leads to a reduced asymmetry $\mathcal{A}$, as seen in Fig. 2.

I would like to thank X. Qian, W. Hübner, A. Ernst, and N. Fominykh for communicating their results on the spectral functions and also S. N. Samarin, J. Henk, J. Kirschner, and P. Bruno for valuable discussions.

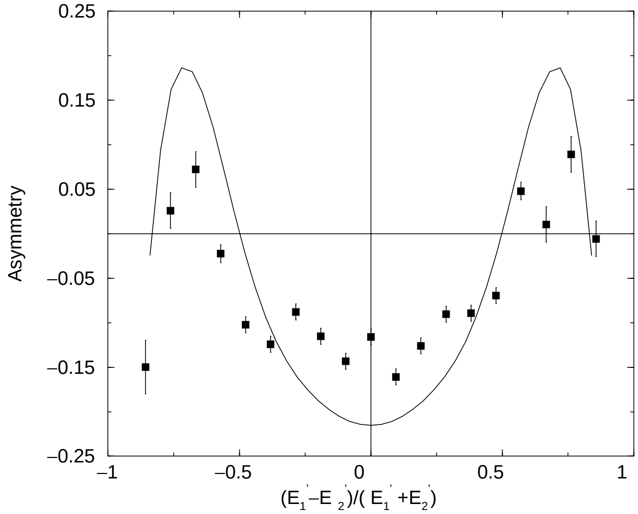

FIG. 2. The spin asymmetry $\mathcal{A}$ as a function of the energy sharing $(E_1' - E_2')/(E_1' + E_2')$ for a fixed total energy $(E_1' + E_2') = 21$ eV. The incident electron has an energy 26 eV and a polarization degree of ≈65%. This is the same target as in Fig. 1, however, we choose $\beta = 0$ and the two electron detectors to lay in the x-z plane. As in Fig. 1, the detectors are positioned at $\cos^{-1}\hat{\mathbf{z}} \cdot \hat{\mathbf{k}}_1' = 40° = \cos^{-1}\hat{\mathbf{z}} \cdot \hat{\mathbf{k}}_1'$. The theoretical results are averaged over the angular resolution of the detectors. The experimental data are courtesy of Ref. 7. The spectral functions are calculated within the scalar relativistic full-potential linearized augmented plane-wave method [11].

*Email address: jber@mpi-halle.de

[1] A. Hubert and R. Schäfer, *Magnetic Domains: The Analysis of Magnetic Microstructures* (Springer-Verlag, Berlin, 1998).
[2] *Polarized Electrons in Surface Physics*, edited by R. Feder (World Scientific, Singapore, 1985).
[3] I. E. McCarthy and E. Weigold, Rep. Prog. Phys. **54**, 789 (1991).
[4] M. Vos and I. E. McCarthy, Rev. Mod. Phys. **67**, 713 (1995).
[5] A. S. Kheifets, S. Iacobucci, A. Ruoccoa, R. Camilloni, and G. Stefani, Phys. Rev. B **57**, 7380 (1998).
[6] J. Kirschner, O. M. Artamonov, and S. N. Samarin, Phys. Rev. Lett. **75**, 2424 (1995).
[7] S. N. Samarin and J. Kirschner (private communication).
[8] U. Fano, Rev. Mod. Phys. **29**, 76 (1957).
[9] J. Berakdar (unpublished).
[10] J. Berakdar, S. N. Samarin, R. Herrmann, and J. Kirschner, Phys. Rev. Lett. **81**, 3535 (1998).
[11] X. Qian and W. Hübner (private communication); Phys. Rev. B (to be published).
[12] P. Blaha, K. Schwarz, P. Sorantin, and S. B. Trickey, Comput. Phys. Commun. **59**, 399 (1990).
[13] E. Tamura, in *Applications of Multiple Scattering Theory to Materials Science*, edited by W. H. Butler, P. H. Dederichs, A. Gonis, and R. L. Weaver (Materials Research Society, Pittsburgh, Pennsylvania, 1992), pp. 347.

Visualizing Spin-Dependent Electronic Collisions In Ferromagnets

S. N. Samarin, J. Berakdar,* O. Artamonov, and J. Kirschner
Max-Planck-Institut für Mikrostrukturphysik, Weinberg 2, 06120 Halle, Germany

(Received 22 November 1999)

This work demonstrates experimentally and theoretically that the coincident two-electron emission from a ferromagnetic surface, upon the impact of a polarized electron, carries detailed information on the spin-dependent electronic collisions in ferromagnets. The analysis of the calculated and the measured two-electron spectra reveals the potential of the electron-pair emission technique for the study of (a) surface magnetism and (b) spin-dependent electron scattering dynamics in ferromagnets.

PACS numbers: 79.20.Kz, 72.10.–d, 75.30.Ds

Magnetic systems with reduced dimensionality, such as ultrathin ferromagnetic films and magnetic surfaces are in the focus of current experimental and theoretical investigations [1,2]. These studies are driven by the fundamental importance of such materials and by their technological potential for magnetic storage and recording media as well as by the prospects of the fabrication of artificially synthesized devices. A number of dynamical features of magnetic systems are primarily controlled by the spin-dependent excitation spectrum [2]. Examples of such properties are the response characteristics and the spin dependence of the mean-free path of excited electrons. Thus, experimental techniques that probe the spin-dependent excitation of magnetic systems are of considerable value. One of the established methods that serves this purpose is the spin polarized electron energy loss spectroscopy (SPEELS). As low energy electrons can penetrate only the first few atomic layers, SPEELS can be employed to investigate the elementary excitations of magnetic systems with reduced symmetry [3]. For example, the Stoner spectrum (electron hole pair spectrum) has been successfully explored by SPEELS [4,5]. The Stoner excitation involves, at least, a two state transition: A majority band electron interacts with an incoming polarized electron (of opposite spin projection) and goes over into a vacuum state. Upon this interaction, the projectile electron loses energy and occupies an empty state in the minority band. This collision process is called exchange scattering. In SPEELS only one (the excited majority band electron) of the two participating electronic states is resolved. Obviously, valuable details of the exchange scattering dynamics are obscured by averaging over the second electron not detected by SPEELS. Therefore, we designed an experiment which measures the two-electron coincident emission rate from a magnetic surface following the impact of a polarized electron, while the energies (E_1, E_2) and the emission angles of the two emitted electrons as well as the energy E_0 and the angle of incidence of the electron beam are being determined (cf. Fig. 1). Hence, the wave vectors $\mathbf{k}_0$ and $\mathbf{k}_1, \mathbf{k}_2$ of the impinging and two receding electrons are measured in coincidence. The escaping electrons are detected using two time of flight (TOF) detectors [6]. The sample normal, the incident electron beam, and the axes of the TOF detectors are chosen to be in the same plane. The polarization vector $\mathbf{P}_e$ of the incident beam and the magnetization direction of the sample, a bcc Fe(110) single crystal, are both perpendicular to the scattering plane (cf. Fig. 1). As a source of spin polarized electrons we used a strained GaAs multilayer photocathode activated by Cs deposition and oxygen exposure. Photoelectrons generated from the photocathode by the circularly polarized light of the laser diode were deflected by a 90° deflector to convert the longitudinally polarized beam into a transversely polarized one. The average count rate of coincidence was 1 event per second. For reasonable statistics a typical spectrum takes an acquisition time of about 270 hours. This long term measurement requires the stability of electronics, constant incident current, and good vacuum conditions. To reduce the influence of the possible instabilities the polarization of the incident beam is inverted every 5 seconds and the data for each polarization are stored in two different files. In spite of the UHV conditions ($\approx 5 \times 10^{-11}$ mbar) the cleanliness of the sample surface has to be ensured regularly (by Ar^+ ion sputtering followed by an annealing and, if necessary, oxygen treatment to remove the carbon from the surface). The surface properties were monitored

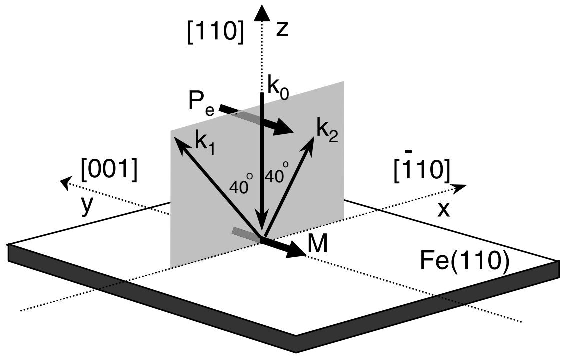

FIG. 1. The experimental setup as used for the coincident measurements. The direction of the magnetization $\mathbf{M}$, the spin polarization vector of the incoming beam $\mathbf{P}_e$ as well as the wave vectors of the incoming and the two emitted electrons $\mathbf{k}_0$ and $\mathbf{k}_1$ and $\mathbf{k}_2$ are indicated. The electron detectors are positioned at 40° to the left and to the right of the z axis.

0031-9007/00/85(8)/1746(4)$15.00

using Auger electron spectroscopy and low-energy electron diffraction. The experiment requires a high degree of polarization of the incident beam and a single domain magnetization of the sample. To guarantee that these conditions are given we employed SPEELS and measured the energy loss spectra (the Stoner spectrum) for an electron beam polarization parallel and antiparallel to the magnetization in the same geometry of Fig. 1 while one of the TOFs is being switched off. The asymmetry A, derived from the two intensities for the opposite spin projections of the incident beam, is measured before and after the coincidence experiments and is used as an indicator for the stability of the experimental setup.

As illustrated in Figs. 1 and 2, the energy and wave vector balance impose the conditions

$$E_0 + \epsilon = E_1 + E_2 , \tag{1}$$

$$\mathbf{k}_{0,\parallel} + \mathbf{q}_{\parallel} + \mathbf{g}_{\parallel} = \mathbf{k}_{1,\parallel} + \mathbf{k}_{2,\parallel} . \tag{2}$$

Here, ϵ is the energy of the valence band electron and $\mathbf{q}_{\parallel}$ is its (surface) Bloch wave vector. The surface reciprocal lattice vector is denoted by $\mathbf{g}_{\parallel}$. Since the quantities E_0, E_1, E_2 and $\mathbf{k}_0, \mathbf{k}_{1,\parallel}, \mathbf{k}_{2,\parallel}$ are determined experimentally [cf. Figs. 1 and 2] we can control, via Eqs. (1) and (2), the values of ϵ and $\mathbf{q}_{\parallel}$; i.e., we can perform the experiment in a certain region of the (magnetic) surface Brillioun zone. For example, by lowering E_2 while keeping E_1 and E_0 fixed we can zoom in deeper levels of conduction band [cf. Figs. 2(a) and 2(b)]. Equivalently, one can scan $\mathbf{q}_{\parallel}$ by varying, e.g., $\mathbf{k}_{0,\parallel}$ for given $\mathbf{k}_{1,\parallel}$, $\mathbf{k}_{2,\parallel}$, and $\mathbf{g}_{\parallel}$.

The role of the exchange scattering in the present experiment is illustrated in Figs. 2(a)–2(d). In the reaction shown in Fig. 2(a) the impinging electron escapes as the fast electron, i.e., $E_1 > E_2$. This process is called the direct scattering and proceeds with an amplitude f. In contrast, as illustrated in Fig. 2(c), the incoming electron may *exchange* as much energy and momentum with the initially bound one that it emerges as the slower one ($E_1 < E_2$). This scattering process is precisely the one active in the case of the aforementioned Stoner excitation. It is usually referred to as the exchange process and is quantified with an amplitude g. Intuitively one can expect that $|f| \gg |g|$ for $E_0 \approx E_1$ and $E_1 \gg E_2 \ll E_0$.

Our experiment does not resolve the electron spin projections in the final state, i.e., we cannot distinguish between the processes shown in Figs. 2(a) and 2(c). Thus, the coincident rate for antiparallel [Fig. 2(a)] or parallel [Fig. 2(b)] alignment of the spins of the incoming and the bound electron is proportional to $|f|^2 + |g|^2$ and $|f - g|^2$, respectively. This is because the processes shown in Figs. 2(a) and 2(c) can be distinguished experimentally while the processes shown in Figs. 2(b) and 2(d) are experimentally identical, and hence f and g are added coherently. Theoretically, to sum over the (final-state) spin quantum numbers we couple the electrons' spins to the (conserved) total spin of the electron pair S and end up with two spin channels: the singlet channel ($S = 0$) and the triplet channel ($S = 1$). The singlet (triplet) cross section $X^{(S=0)}$ ($X^{(S=1)}$) can then be expressed in terms of f and g [7]. The experiment (Fig. 1) measures a spin asymmetry $\mathcal{A}$; i.e., for a certain magnetization direction $\mathbf{M}$, we register the electron-pair emission rate W for antiparallel [$W(\downarrow\uparrow)$] and parallel [$W(\uparrow\uparrow)$] alignment of the polarization vector of the incoming beam with $\mathbf{M}$ (cf. Fig. 1) and evaluate $\mathcal{A}$ as

$$\mathcal{A}(\mathbf{k}_1, \mathbf{k}_2; \mathbf{k}_0) = \frac{W(\downarrow\uparrow) - W(\uparrow\uparrow)}{W(\downarrow\uparrow) + W(\uparrow\uparrow)} . \tag{3}$$

For a gaseous atomic target with a defined spin polarization P_a (taken as a quantization axis) the asymmetry $\mathcal{A}$ is directly expressible in terms of $X^{(S=0/1)}$ (and hence in terms of f and g) as [7] $\mathcal{A} = P_a P_e A^{(s)}$, $A^{(s)} = (X^{(S=0)} - X^{(X=1)})/(X^{(S=0)} + 3X^{(S=1)}) = (2|f| \times |g| \cos\delta)/(|f|^2 + |g|^2 + |f + g|^2)$, where δ is the phase difference between the amplitudes f and g. This relation for $\mathcal{A}$ implies that $\lim_{(|g|/|f|) \to 0} A \to 0$, as discussed and shown experimentally below. For magnetized surfaces, the spin polarization of electronic states is dependent on the binding energy ϵ and on $\mathbf{q}_{\parallel}$; i.e., the theory has to consider the spin resolved Bloch spectral functions w rather then the density of states. The influence

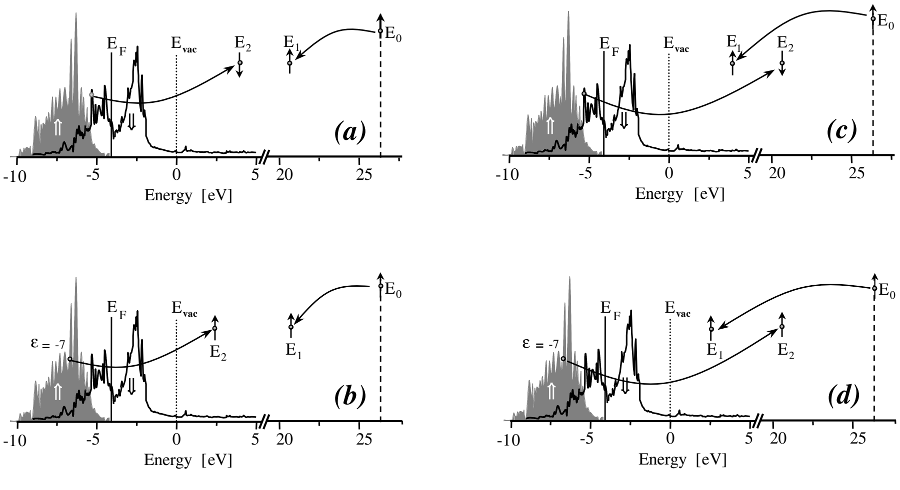

FIG. 2. An illustration of the direct (a),(b) and the exchange (c),(d) scattering (see text for details). The energies of the incoming and the two escaping electrons are denoted by E_0 and E_1, E_2. The vacuum and the Fermi levels are shown as E_{vac} and E_{F}. ϵ is the initial binding energy of the ejected electron. The surface density of states of the majority band (referred to by $\Uparrow$) and the minority band (indicated by $\Downarrow$) are shown.

of the crystal structure on the scattering dynamics is encompassed in f and g. The *exchange* induced asymmetry $\mathcal{A}$ has the form [8] (other spin asymmetries [8] are negligible within the accuracy of the present experiment)

$$\mathcal{A}(\mathbf{k}_1, \mathbf{k}_2; \mathbf{k}_0) = P_e \frac{\sum_{l,\mathbf{g}_\parallel} A_l^{(m)} A_{l,\mathbf{g}_\parallel}^{(s)} \mathcal{B}_{l,\mathbf{g}_\parallel}}{\sum_{l',\mathbf{g}'_\parallel} \mathcal{B}_{l',\mathbf{g}'_\parallel}}. \tag{4}$$

Here, the atomic layers parallel to the surface are indexed by l. In Eq. (4) $A^{(m)}$ describes the *sample's magnetic asymmetry,* whereas the dynamical aspects of the spin-dependent collisions are contained in the *exchange scattering asymmetry* $A^{(s)}$. The spin averaged intensity is referred to as $\mathcal{B}$. This interpretation follows from the definitions of $A^{(m)}$, $A^{(s)}$, and $\mathcal{B}$

$$A_l^{(m)} = \frac{w(\mathbf{q}_\parallel, l, \epsilon, \Downarrow) - w(\mathbf{q}_\parallel, l, \epsilon, \Uparrow)}{w_0(\mathbf{q}_\parallel, l, \epsilon)}, \tag{5}$$

$$A_{l,\mathbf{g}_\parallel}^{(s)} = \frac{X^{(S=0)}(\mathbf{k}_1, \mathbf{k}_2; \mathbf{k}_0, \mathbf{g}_\parallel, l) - X^{(S=1)}(\mathbf{k}_1, \mathbf{k}_2; \mathbf{k}_0, \mathbf{g}_\parallel, l)}{3X^{(S=1)}(\mathbf{k}_1, \mathbf{k}_2; \mathbf{k}_0, \mathbf{g}_\parallel, l) + X^{(S=0)}(\mathbf{k}_1, \mathbf{k}_2; \mathbf{k}_0, \mathbf{g}_\parallel, l)}, \tag{6}$$

$$\mathcal{B}_{l,\mathbf{g}_\parallel} = w_0(\mathbf{q}_\parallel, l, \epsilon)\left[\frac{3}{4} X^{(S=1)} + \frac{1}{4} X^{(S=0)}\right], \tag{7}$$

where $w(\mathbf{q}_\parallel, l, \epsilon, \Uparrow)$ and $w(\mathbf{q}_\parallel, l, \epsilon, \Downarrow)$ are the Bloch spectral functions of, respectively, the majority and the minority bands. The spin averaged Bloch spectral function is w_0.

The calculational scheme for $A^{(m)}$, $A^{(s)}$, and $\mathcal{B}$ of Ref. [8] is employed for the subsequent numerical study. $A^{(m)}$ is derived from band structure calculations within the scalar relativistic full potential linearized augmented plane wave method [9], whereas $A^{(s)}$ and $\mathcal{B}$ are calculated from the layer dependent transition matrix elements.

Equations (5)–(7) demonstrate the versatile potential of the pair emission technique for material and scattering dynamics studies: (a) In case of unpolarized electrons and provided $X^{(S=1)}$ and $X^{(S=0)}$ are sufficiently known, the Bloch spectral functions w_0 can be mapped using Eq. (7). This is documented in Refs. [10,11] for diverse systems; (b) the magnetic asymmetry $A^{(m)}$ [i.e., Eq. (6)] in the spin-split band structure can be visualized by using polarized electron beam and choosing a geometrical arrangement under which the triplet channel is closed [8] ($X^{(S=1)} = 0$) in which case $A^{(s)} = 1$ [cf. Eq. (6)]; (c) conversely in the case that the spin polarized band structure is known, e.g., from reliable *ab initio* calculations, $A^{(m)}$ can be deduced from Eq. (5) and the spin scattering dynamics, which is embedded in $A^{(s)}$, can be extracted from the measured asymmetry $\mathcal{A}$ [Eq. (4)].

The present experimental setup does not yet allow one to explore in full detail all these facets of the pair emission technique. In particular, the averaging over the present angular resolution involves an integration over $\mathbf{q}_\parallel$ that extends basically over the entire surface Brillouin zone. The $\mathbf{q}_\parallel$ integration of the Bloch spectral functions [cf. Eq. (5)] yields the surface spin split density of states $\rho(\epsilon, \Uparrow)$, $\rho(\epsilon, \Downarrow)$ that are depicted in Fig. 2. For the interpretation of the data we employ thus $A^{(m)} \approx [\rho(\epsilon, \Downarrow) - \rho(\epsilon, \Uparrow)]/[\rho(\epsilon, \Downarrow) + \rho(\epsilon, \Uparrow)]$.

In Figs. 3(a) and 3(b) the asymmetry $\mathcal{A}$ is scanned as a function of the energy sharing within the electron pair for a fixed total energy $E = E_1 + E_2$. According to Eq. (1) the energy of the valence band state ϵ is then fixed (E_0 is constant). When the two electrons escape with equal energies $E_1 = E_2$ the triplet scattering $X^{(S=1)}$ vanishes due to symmetry [8], and hence for $E_1 = E_2$ we obtain $A^{(s)} = 1$, as experimentally verified in a recent work [7]. Therefore, in this situation ($E_1 = E_2$), the *magnitude* and *sign* of the asymmetry $\mathcal{A}$ are dictated merely by $A^{(m)}(\epsilon)$ which in Fig. 3(a) amounts to $A^{(m)}(\epsilon = -5.3 \text{ eV}) \approx +60\%$. This interpretation can be substantiated experimentally by shifting ϵ deeper into the band [cf. Figs. 2(a) and 2(b)] in which case $A^{(m)}$ changes sign. This results, as shown in Fig. 3(b) ($\epsilon = -7$ eV and $A^{(m)} \approx -40\%$), in an inverted sign of $\mathcal{A}$ as compared to the case of a positive $A^{(m)}$.

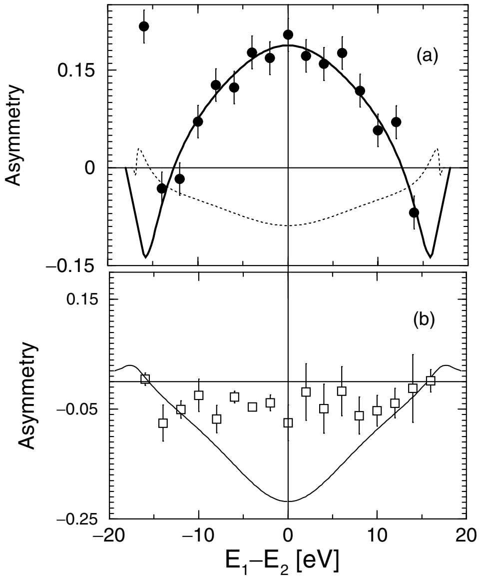

FIG. 3. (a) The measured (full dots) and calculated spin asymmetry $\mathcal{A}$ as a function of the energy sharing $E_1 - E_2$ for a fixed total energy $E = E_1 + E_2 = 17.7 \pm 0.7$ eV. The surface (bulk) electronic band structure has been employed for the calculations shown by the solid (dotted) line. The incident electron energy is $E_0 = 23$ eV; i.e., ϵ is just below E_F [cf. Fig. 2(a)]. The sample and the scattering geometry are as shown in Fig. 1. The theoretical results are averaged over the angular and the excess energy (E) resolution of the detectors. (b) The same as in (a) except that the energies are chosen as $E_0 = 26$ eV and $E = 19 \pm 1$ eV; i.e., ϵ is well below E_F [cf. Fig. 2(b)]. The experimental findings (open squares) are shown along with the (surface) calculations (solid curve).

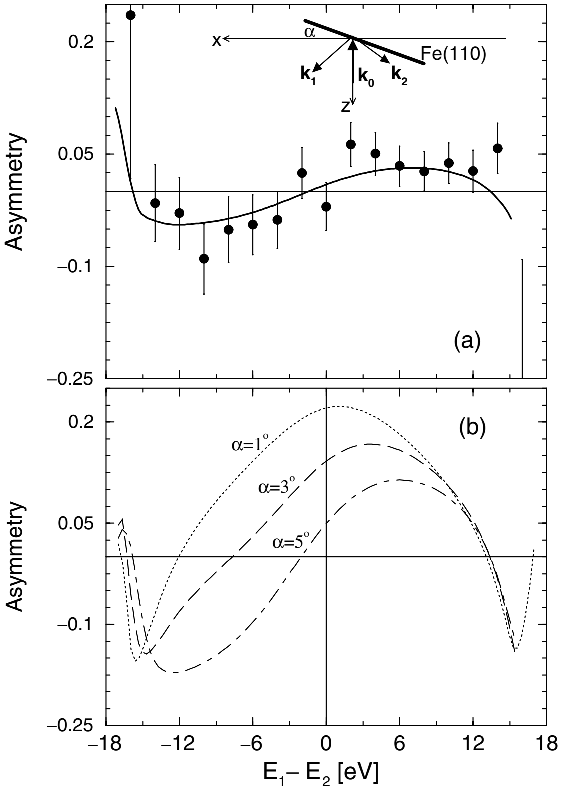

FIG. 4. (a) The measured (full dots) and calculated (solid curve) asymmetry for the same sample, incident, and excess energies as in Fig. 3(a) ($E_0 = 23$ eV, $E = 17.7 \pm 0.7$ eV); however, the sample is tilted with respect to the incident beam by an angle $\alpha = 5°$, as shown in the inset. The calculations (solid curve) are averaged over the angular and energy resolution of the experiment, as done in Fig. 3(a). (b) The same situation as in (a) but $\mathcal{A}$ is calculated for different angles α (from $\alpha = 1$ to $\alpha = 5°$, as depicted on the curves). The excess energy is $E = 18$ eV. The curves are averaged only over the angular resolution of the detectors.

Since ϵ is constant in Fig. 3(a) (and hence $A^{(m)}$ is constant) the variation of $\mathcal{A}$ is due to the spin-dependent scattering dynamics which is dictated by $A^{(s)}$. Thus the structure of $\mathcal{A}$, as depicted in Figs. 3(a) and 3(b), can be understood as follows: At $E_1 = E_2$ the triplet cross section vanishes in which case $A^{(s)}$ attains its highest value (unity). This structure is a peak (minimum) when $A^{(m)} > 0$ ($A^{(m)} < 0$). The decline in $\mathcal{A}$ for $E_1 > E_2$ or $E_2 < E_1$ is due to a dominance of the direct scattering amplitude $|f|$ [Fig. 2(a)] over the exchange one $|g|$ [Fig. 2(c)]; i.e., it is more likely for the fast incoming electron to escape as the fast electron than for it to lose almost its whole energy and emerge as the slower one. As deduced above $\lim_{(|g|/|f|)\to 0} A^{(s)} = (|f||g|\cos\delta)/(|f|^2|g|^2 + |f||g|\cos\delta) \to 0$, and hence the asymmetry in Figs. 3(a) and 3(b) decreases with increasing deviations from $E_1 = E_2$.

Figure 3(a) shows the asymmetry as calculated using a surface and a bulk electronic band structure. The model employing bulk spectral functions is clearly at variance with the data. This is comprehensible as in our experiment *two* low-energy electrons have to escape the surface and hence the surface sensitivity is increased as compared to SPEELS.

The special symmetry of the experimental arrangement depicted in Fig. 1 implies a symmetrical $\mathcal{A}$ with respect to $E_1 = E_2$ (in our case, spin orbit effects are negligibly small). This symmetry is broken by tilting the sample as shown in the inset of Fig. 4. Since ϵ is fixed, $A^{(m)}$ has a fixed constant value in Fig. 4. Therefore, the structure of $\mathcal{A}$ is related to that of $A^{(s)}$. To explore the origin of the shape of $\mathcal{A}$ in Fig. 4(a) we carried out numerical calculations [Fig. 4(b)] for varying angle of incidence, ranging from the symmetric case of Fig. 3(a) to that of Fig. 4(a) (in the single atom case $\mathcal{A}$ remains unchanged). As seen in Fig. 4(b), with increasing values of α, the broad peak in Fig. 3(a) at $E_1 = E_2$ diminishes to the small positive hump around $E_1 - E_2 \approx 8$ eV in Fig. 4(a). Its origin can still be related to a small triplet contribution. The negative dip in Fig. 3(a) at the left wing develops to the broad valley at $E_1 - E_2 \approx 12$ eV in Fig. 4(a). This trend illustrates the subtle dependence of the scattering dynamics on the propagation directions of the electrons through the surface.

The present Letter illustrates evidently that the utilization of the coincident two-electron emission technique renders possible a novel insight into the spin-dependent electronic scattering at surfaces. Future refinement of the present study will yield yet more precise information on the spin polarization $A^{(m)}$ of the surface electronic states in a well-defined region of the surface magnetic Brillouin zone.

The technical assistance of H. Schwabe and A. Wiessner is gratefully acknowledged.

---

*Corresponding author.
Email address: jber@mpi-halle.de

[1] A. Hubert and R. Schäfer, *Magnetic Domains: The Analysis of Magnetic Microstructures* (Springer-Verlag, Berlin, 1998).
[2] *Ultrathin Magnetic Structures,* edited by B. Heinrich and J. A. C. Bland (Springer-Verlag, Heidelberg, 1994).
[3] *Polarized Electrons in Surface Physics,* edited by R. Feder (World Scientific, Singapore, 1985).
[4] J. Kirschner, D. Rebenstorff, and H. Ibach, Phys. Rev. Lett. **53**, 698 (1984).
[5] D. L. Abraham and H. Hopster, Phys. Rev. Lett. **62**, 1157 (1989).
[6] O. M. Artamonov, S. N. Samarin, and J. Kirschner, Appl. Phys. A **65**, 535 (1997).
[7] M. Streun, G. Baum, W. Blask, and J. Berakdar, Phys. Rev. A **59**, R4109 (1999).
[8] J. Berakdar, Phys. Rev. Lett. **83**, 5150 (1999).
[9] X. Qian and W. Hübner, Phys. Rev. B **60**, 16 192 (1999).
[10] I. E. McCarthy and E. Weigold, Rep. Prog. Phys. **54**, 789 (1991).
[11] A. S. Kheifets, S. Iacobucci, A. Ruoccoa, R. Camilloni, and G. Stefani, Phys. Rev. B **57**, 7380 (1998).

PHYSICAL REVIEW B, VOLUME 65, 104425

Spin-correlation imaging of electrons in ferromagnets

A. Morozov, J. Berakdar, S. N. Samarin, F. U. Hillebrecht, and J. Kirschner
Max-Planck-Institut für Mikrostrukturphysik, Weinberg 2, 06120 Halle, Germany

(Received 27 August 2001; published 26 February 2002)

The angular and energy dependencies of the exchange interaction between the electrons in an itinerant ferromagnetic surface can be mapped out by exciting two interacting spin-polarized electrons into the vacuum and resolving at the same time the energies and emission angles of the two electrons. From a tensorial symmetry analysis it is deduced that the recorded two-particle spectra carry detailed information on the spin-split electronic structure that can be extracted under favorable conditions. To substantiate these statements we present and analyze experimental results and numerical calculations for a ferromagnetic iron surface.

DOI: 10.1103/PhysRevB.65.104425 PACS number(s): 75.30.Ds, 34.80.Nz, 34.80.Dp, 79.20.Kz

I. INTRODUCTION

The fermionic nature of electrons dictates that the quantum-mechanical wave function of a multielectron system has to be antisymmetric with respect to exchange of the states of two individual electrons. This symmetry requirement has profound consequences as to the properties of correlated electronic systems. In particular, the exchange ‘‘coupling’’ between electrons is essential for the ferromagnetic state of matter. Therefore, experimental and theoretical approaches that expose details of the energy and angular dependencies of the exchange interaction are of considerable value for fundamental and applied research. The obstacles encountered in such studies are of a technical as well as of a theoretical/conceptual nature: To investigate the influence of the exchange interaction one should be able to control experimentally the states, i.e., the quantum numbers, of at least two electrons and then change the spin state of one of these electrons while monitoring the change in the properties of the system.

Experimentally, this can be realized by measuring the two-particle excitation spectrum of a ferromagnet upon the impact of a single polarized electron. Features related to the exchange interaction are studied by observing the dependence of the spectrum on the electrons’ spin projections. It is clear from the outset that such measurements put high demands on the experiment as one has to utilize a multiparticle coincidence technique using a spin-polarized beam to resolve and control the two electrons’ quantum numbers. Such a method is hampered by low counting rates as compared to conventional single-particle spectroscopic techniques. Nevertheless, since the exchange coupling is a many-body effect it is indispensable to use many-particle techniques to trace the various facets of this interaction, such as the energy and angular dependencies of the exchange-influenced pair-correlation function. Correspondingly, a theoretical treatment has to deal with the excited states of a fermionic many-body system to describe the propagation of two hot electrons that interact with each other and with the surface and emerge eventually into the vacuum with well-defined wave vectors and with a given total spin of the electron pair.

The experimental approach used in this work can be regarded as an extension of the well-established spin-polarized electron energy-loss spectroscopy (SPEELS) as applied to the study of the electron-hole pair excitations in ferromagnets, known as the Stoner spectrum.[1–5] The Stoner excitation of a ferromagnetic surface involves a two-state transition: A majority band electron interacts with the incoming polarized electron (of opposite spin projection) and is promoted to a highly excited state. If this state lies above the vacuum level, the electron may escape such that it can be detected by a suitable detector. Due to this interaction, the projectile electron loses energy and relaxes into an unoccupied (hot-electron) state in the minority band. Therefore, an observer monitoring the spin state and the energy loss of the incoming polarized electron beam registers (using SPEELS) a spin-flip event at a certain energy loss determined by the characteristics of the unoccupied density of states of the minority band. In a SPEELS experiment only one (the excited majority band electron) is detected while the mechanism that triggered the transition is an exchange process that involves, at least, two electrons. To map out the details of the exchange-dependent electron-electron scattering one needs to resolve the energies and emission angles of the two electrons which are excited upon the interaction of one single energetic, spin-polarized electron with a single domain ferromagnet. The dependence of the spectrum on the spin projection of the projectile electron and/or the magnetization direction of the sample yields direct information on the spin-dependent electronic interactions. If spin-orbit interactions are deemed small it suffices to determine the spin states of the electrons prior to the collision as the total spin is conserved (this does not exclude the possibility for the individual electrons to exchange their spin projections via exchanging their energies and emission angles. The latter exchange process is mediated by the spin-independent electron-electron interaction).

In this work we conducted this type of experiment on an Fe(110) single-crystal surface with a well-defined magnetization direction. The experiment allows one to set the energy and spin polarization of the incoming electron beam. The measurement determines the energy and angle-resolved coincidence rate of electron pairs emitted after excitation by a single electron. Furthermore, in order to address the influence of the exchange interaction directly, the relative orientation of sample magnetization and incident-beam polarization is switched between parallel and antiparallel.

As deduced from a tensorial symmetry analysis, the spin-dependent two-particle spectrum can be classified according

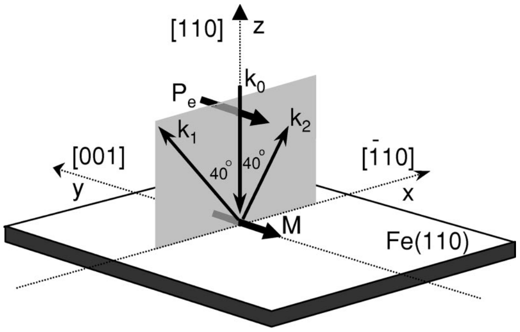

FIG. 1. The experimental setup as used for the coincidence measurements. The direction of the magnetization **M**, the spin-polarization vector of the incoming beam $\mathbf{P}_1$, as well as the wave vectors of the incoming and the two emitted electrons $\mathbf{k}_0$ and $\mathbf{k}_1$, $\mathbf{k}_2$ are indicated. The electron detectors are positioned at 40° to the left and to the right of the z axis.

to the symmetry of the interactions involved in the excitation process (exchange and spin-orbit interactions). The mathematical treatment yields a prescription to disentangle and measure the various terms related to a specific symmetry class. For the calculations of the two-particle spectrum we utilize a numerical method which employs a realistic spin-split surface electronic band structure combined with a Green-function technique to propagate the two excited, correlated electrons into the vacuum in the presence of the scattering from the surface crystal potential.

The results of this work show a strong dependence of the two-electron coincidence signal on the direction of the spin polarization of the incoming beam. The origin of this spin asymmetry is revealed by an analysis of its rotational properties (in the two-electron spin space). From this analysis we conclude that, within the resolution of the present setup, the spin asymmetry measured for the Fe(110) surface is induced by the exchange coupling. It depends on the mutual angle of the two escaping electrons as well as on their relative energies and on the crystal orientation, providing thus detailed information on the influence of the exchange interaction on excited electrons at surfaces. A brief account of the present studies and first results has been published in Refs. 6 and 7.

II. EXPERIMENTAL DETAILS

The experimental realization of the coincident measurement is depicted in Fig. 1. A pulsed spin-polarized electron beam with wave vector $\mathbf{k}_0$ impinges onto a clean ferromagnetic surface, in our study, bcc Fe(110). The time structure in combination with the very low average current of the incoming beam ensure that only single electrons interact with the sample. A fraction of the scattering events leads to the emission of two electrons with energies E_1, E_2 and emission angles θ_1, θ_2 with respect to the incoming beam direction.

Hence, the experiment measures simultaneously the wave vectors $\mathbf{k}_0$ and $\mathbf{k}_1$, $\mathbf{k}_2$ of the impinging and two ejected electrons. The escaping electrons are detected by two position sensitive time-of-flight (TOF) detectors. The sample normal, the incident electron beam, and the axes of the TOF detectors are in the same plane. The polarization vector $\mathbf{P}_1$ of the incident beam and the magnetization direction of the sample are both perpendicular to the scattering plane (cf. Fig. 1). As a source of spin-polarized electrons we used a strained GaAs multilayer photocathode activated by Cs deposition and oxygen exposure. Photoelectrons generated from the photocathode by the circularly polarized light of a laser diode are deflected by a 90° deflector to convert the longitudinally polarized beam into a transversely polarized one. At an electron pulse frequency of 500 MHz, the average coincidence count rate was 30 events per s. To obtain a data set with statistics suitable for the detailed analysis presented in this paper, a typical spectrum took an acquisition time of about 100 h. This long term measurement requires good vacuum conditions to maintain a clean sample surface, and good stability of the incident-beam polarization. To reduce the influence of the possible instabilities the polarization of the incident beam is inverted every 5 s and the data for each polarization are stored in two different files. In spite of the UHV conditions ($\approx 5.10^{-11}$ mbar) the cleanliness of the sample surface has to be restored regularly. This was done by Ar^+ ion sputtering followed by annealing and, if necessary, oxygen treatment to remove the carbon from the surface. The surface properties were monitored by Auger electron spectroscopy and low-energy electron diffraction. The experiment requires a high degree of polarization of the incident beam and single domain magnetization of the sample. To monitor these conditions we measured the energy-loss spectra (the Stoner spectrum) for an electron-beam polarization parallel and antiparallel to the magnetization in the same geometry of Fig. 1 with one of the TOF detectors switched off.[8] The asymmetry A, derived from the two intensities for the opposite spin projections of the incident beam, is measured before and after the coincidence experiments and is used as an indicator for the stability of the experimental setup.

The energy and wave-vector balance imposes the conditions

$$E_0 + \epsilon = E_1 + E_2, \tag{1}$$

$$\mathbf{k}_{0\parallel} + \mathbf{q}_{\parallel} + \mathbf{g}_{\parallel} = \mathbf{k}_{1\parallel} + \mathbf{k}_{2\parallel}. \tag{2}$$

Here, ϵ is the energy of the valence-band electron and $\mathbf{q}_{\parallel}$ is its (surface) Bloch wave vector. The surface reciprocal-lattice vector is denoted by $\mathbf{g}_{\parallel}$. Since the quantities E_0, E_1, and E_2 and $\mathbf{k}_0$, $\mathbf{k}_{1\parallel}$, and $\mathbf{k}_{2\parallel}$ are determined experimentally (cf. Fig. 1) we can control, via Eqs. (1) and (2), the values of ϵ and $\mathbf{q}_{\parallel}$, i.e., we can perform the experiment in a certain region of the (magnetic) surface Brillouin zone. Lowering E_2 while keeping E_1 and E_0 fixed we can zoom in to deeper levels of the conduction band. Equivalently, one can scan $\mathbf{q}_{\parallel}$ by varying, e.g., $\mathbf{k}_{0\parallel}$ for given $\mathbf{k}_{1\parallel}$, $\mathbf{k}_{2\parallel}$, and $\mathbf{g}_{\parallel}$. The experiment (Fig. 1) measures a spin asymmetry $\mathcal{A}$, i.e., for a certain magnetization direction **M**, hereafter denoted by $\Downarrow^{\mathrm{M}}$, we register the electron-pair emission rate W for antiparallel and parallel alignment of the polarization vector of the incoming beam with **M** (cf. Fig. 1) and evaluate $\mathcal{A}$ as

$$\mathcal{A}(\mathbf{k}_1,\mathbf{k}_2;\mathbf{k}_0)=\frac{W(\uparrow\Downarrow^{\mathrm{M}})-W(\downarrow\Downarrow^{\mathrm{M}})}{W(\uparrow\Downarrow^{\mathrm{M}})+W(\downarrow\Downarrow^{\mathrm{M}})}. \tag{3}$$

III. THEORETICAL CONSIDERATIONS

For a theoretical formulation we describe the incoming polarized electron beam as a (microcanonical) ensemble and quantify it by the density operator ρ^{s_1} with matrix elements $\rho^{s_1}_{m_{s_1}m_{s_1}}$. Here m_{s_1} is the projection of the electron's spin $\mathbf{s}_1$ along an appropriately chosen quantization axis (e.g., the magnetization direction). The density matrix is chosen to be diagonal. This is not a restriction since it can always be diagonalized by an appropriate unitary transformation. In the standard representation the density operator ρ^{s_1} is expanded linearly in terms of the Pauli matrices σ as

$$\rho^{s_1}=\mathbf{1}+\mathbf{P}_1\cdot\sigma, \tag{4}$$

where $\mathbf{P}_1$ is the polarization vector of the beam. Analogously, the electrons in the exchange-split conduction band are characterized by the density matrix $\overline{\rho}^{s_2}_{m_{s_2}m_{s_2}}$ where s_2 is the spin of the electron and m_{s_2} labels the corresponding magnetic sublevels. The density operator $\overline{\rho}^{s_2}$ is expressed as

$$\overline{\rho}^{s_2}=w_0(\mathbf{k}_{2\parallel},l,\epsilon)(\mathbf{1}+\mathbf{P}_2\cdot\sigma), \tag{5}$$

where $w_0(\mathbf{k}_{2\parallel},l,\epsilon)$ is the spin-averaged Bloch spectral function of the layer l and $\mathbf{P}_2$ characterizes the polarization of the band states, for its value is defined as

$$P_2=\frac{w(\mathbf{k}_{2\parallel},l,\epsilon,\Uparrow)-w(\mathbf{k}_{2\parallel},l,\epsilon,\Downarrow)}{w_0(\mathbf{k}_{2\parallel},l,\epsilon)}. \tag{6}$$

Here $w(\mathbf{q}_{\parallel},l,\epsilon,\Uparrow)$ and $w(\mathbf{q}_{\parallel},l,\epsilon,\Downarrow)$ are the Bloch spectral functions of, respectively, the majority and the minority bands. The spin-averaged Bloch spectral function is denoted by w_0. These samples' spectral functions are obtained from the trace of the imaginary part of the corresponding single-particle Green function of the surface. For the calculations of the (ground-state) electronic properties of the sample we utilized the full-potential linearized augmented plane-wave method[9] and compared the results with those obtained from a self-consistent layer-resolved Korringa-Kohn-Rostoker method.[10] Both methods are based on density-functional theory within the local-density approximation. The density matrix $\rho^{\mathcal{S}}$ of the combined electron-surface system, long before the collision, is obtained from the direct product $\rho^{\mathcal{S}}=\rho^{s_1}\otimes\overline{\rho}^{s_2}$.

For the calculations of the pair-emission probability we note that the experiment resolves the asymptotic wave vectors of the impinging and the two emitted (vacuum) electrons (cf. Fig. 1). However, no spin analysis of the outgoing electrons is performed in the final channel. Such a spin analysis is redundant in the absence of spin-orbit interaction, as shown below.

The cross section W for the simultaneous emission of two electrons with wave vectors $\mathbf{k}_1$ and $\mathbf{k}_2$ in response to the impact of a projectile electron with wave vector $\mathbf{k}_0$ is given by

$$W(\mathbf{k}_2,\mathbf{k}_1;\mathbf{k}_0)=C\sum_{\substack{m_{s_1'},m_{s_2'}\\ m_{s_1},m_{s_2}}}\;\sum\!\!\!\!\!\!\!\int_{\alpha}\; T\rho^{\mathcal{S}}T^{\dagger}\,\delta(E_f-E_i). \tag{7}$$

Here $m_{s_1'},m_{s_2'}$ denote the spin projections of the final-state electrons and α stands for all the quantum numbers needed to quantify uniquely the quantum-mechanical state of the system which are not resolved by the experiment. $C=(2\pi)^4/k_0$ is a kinematical factor that originates from the normalization to the incoming electron flux current density.

In Eq. (7) T denotes the matrix elements of the transition operator $\mathcal{T}$ of the total system consisting of the projectile electron and the magnetic surface, i.e.,

$$\begin{aligned}&T(\mathbf{k}_1,m_{s_1'},\mathbf{k}_2,m_{s_2'};\mathbf{k}_0,m_{s_1},\alpha,m_{s_2})\\&\quad=\langle\psi_{\mathbf{k}_1,\mathbf{k}_2,m_{s_1'},m_{s_2'}}(1,2)|\mathcal{T}|\phi_{\epsilon,\alpha,s_2,m_{s_2}}(2)\varphi_{\mathbf{k}_0,s_1m_{s_1}}(1)\rangle.\end{aligned} \tag{8}$$

$\varphi_{\mathbf{k}_0,s_1m_{s_1}}$ is a spinor vacuum state describing the incoming beam. The ground state of the surface is to be described by the single-particle, spin-resolved orbital $\phi_{\epsilon,\alpha,s_2,m_{s_2}}(2)$ which is characterized by the energy ϵ, the spin state s_2,m_{s_2}, and the collective quantum numbers α. The emitted electrons with spin projections $m_{s_1'},m_{s_2'}$ are represented by the two-particle state vector $|\psi_{\mathbf{k}_1,\mathbf{k}_2,m_{s_1'},m_{s_2'}}(1,2)\rangle$.

To leading order in the electron-electron and the electron-crystal interaction the operator $\mathcal{T}$ can be approximated by[11] $\mathcal{T}\approx U_{surf}+U_{ee}(\mathbf{1}+G^{-}_{ee}U_{surf})$ where U_{ee} is the electron-electron interaction, G^{-}_{ee} is the Green function within the potential U_{ee}, and U_{surf} is the surface scattering potential. For a given atomic layer of the surface the potential U_{surf} is cast in a nonoverlapping muffin-tin form. For the electronic interaction U_{ee} we employ a screened Coulomb potential with the screening length determined according to the Thomas-Fermi theory. In T we discard any spin-orbit effects. The justification for the neglect of spin-orbit interaction can be checked experimentally, as explained below.

A. Tensorial recoupling

Having sketched the general calculational scheme it is advantageous to analyze the transformational properties of the spectrum (7) using group theory. This analysis is generally valid and does not rely on the specific approximation to $\mathcal{T}$. To this end and to disentangle geometrical from dynamical features we express the density matrices (4) and (5) in terms of the statistical tensors $\rho_{p_1q_1}$ and $\overline{\rho}_{p_2q_2}$,[12]

$$\rho^{s_1}_{m_{s_1}m_{s_1}} = \sum_{p_1=0}^{2s_1} (-)^{p_1-s_1-m_{s_1}} \times \langle s_1 - m_{s_1}; s_1 m_{s_1} | p_1 q_1 = 0\rangle \rho_{p_1 q_1=0}, \tag{9}$$

$$\overline{\rho}^{s_2}_{m_{s_2}m_{s_2}}(\epsilon,\alpha) = \sum_{p_2=0}^{2s_2} (-)^{p_2-s_2-m_{s_2}} \times \langle s_2 - m_{s_2}; s_2 m_{s_2} | p_2 q_2 = 0\rangle \overline{\rho}_{p_2 q_2=0}(\epsilon,\alpha). \tag{10}$$

We recall here that the density matrices are both diagonal due to the assumption that there exists a common quantization axis, therefore, only the components along the axes $\rho_{p_1 q_1=0}$ and $\overline{\rho}_{p_2 q_2=0}$ appear in Eqs. (9) and (10) [in Eqs. (9) and (10) $\langle \cdots | \cdots \rangle$ denotes Clebsch-Gordon coefficients].

Substituting Eqs. (9) and (10) into the general expression (7) yields

$$W = \sum\!\!\!\!\!\!\!\int_{\alpha} \sum_{p_1=0}^{2s_1} \sum_{p_2=0}^{2s_2} \rho_{p_1 q_1=0} \overline{\rho}_{p_2 q_2=0}(\epsilon,\alpha) \Lambda^{p_1,p_2}_{q_1=0,q_2=0} \times \delta(E_f - E_i), \tag{11}$$

where

$$\Lambda^{p_1,p_2}_{q_1=0,q_2=0} = \sum_{m_{s_1}} (-)^{p_1-s_1-m_{s_1}} \langle s_1 - m_{s_1}; s_1 m_{s_1} | p_1 q_1 = 0\rangle \times \sum_{m_{s_2}} (-)^{p_2-s_2-m_{s_2}} \langle s_2 - m_{s_2}; s_2 m_{s_2} | p_2 q_2 = 0\rangle \times \mathcal{F}_\alpha(m_{s_1}, m_{s_2}), \tag{12}$$

$$\mathcal{F}_\alpha(m_{s_1},\alpha,m_{s_2}) = C \sum_{\substack{m_{s'_1}\\ m_{s'_2}}} T(\mathbf{k}_1, m_{s'_1}, \mathbf{k}_2, m_{s'_2}; \mathbf{k}_0, m_{s_1}, \alpha, m_{s_2}) \times T^\dagger(\mathbf{k}_1, m_{s'_1}, \mathbf{k}_2, m_{s'_2}; \mathbf{k}_0, m_{s_1}, \alpha, m_{s_2}). \tag{13}$$

The complete dynamical information on the two-particle emission are encompassed in $\Lambda^{p_1,p_2}_{q_1,q_2}$ whereas the geometry of the ground state is described by the state multipoles.

The importance of the above recoupling scheme follows from the conclusion that the sum over m_{s_1} (m_{s_2}) in Eq. (13) defines the component along the quantization axis (the magnetization direction) of a spherical tensor of rank p_1 (p_2) while the dependence of the sum on $m_{s'_1}$ $(m_{s'_2})$ is considered parametrically. This is readily deduced from the fact that for given spin projections $m_{s'_1}$ and $m_{s'_2}$ the m_{s_1} (m_{s_2}) behavior of T is given by the dependence on the magnetic sublevels of an angular momentum state, namely, by the m_{s_1} (m_{s_2}) dependence of the spin part of $|\varphi_{\mathbf{k}_1,s_1 m_{s_1}}(1)\rangle$ $[|\phi_{\epsilon,\alpha,s_2,m_{s_2}}(2)\rangle]$. Thus $T(\mathbf{k}_1, m_{s'_1}, \mathbf{k}_2, m_{s'_2}; \mathbf{k}_0, m_{s_1}, \alpha, m_{s_2})$ may be regarded as the m_{s_1} (m_{s_2}) component of a spherical tensor of rank s_1 (s_2). Furthermore, the complex conjugate can be written in the form $T^*(s_1, m_{s_1}) = (-)^{\delta - m_{s_1}} \mathcal{W}(s_1, -m_{s_1})$. This relation is a definition for the tensor $\mathcal{W}$, and resembles formally the definition of the adjoint of a tensor operator where the phase δ is chosen arbitrarily under the constraint that $\delta - m_{s_1}$ must be an integer.[13] Thus we choose $\delta - m_{s_1} = p_1 - s_1 - m_{s_1}$ (note that $p_1 = 0 \cdots 2s_1$ and $s_1 - m_{s_1}$ are always integers). The tensor product of $T(s_1, m_{s_1})$ and $T^\dagger(s_1, m_{s_1})$, which is again a spherical tensor, is then given by

$$[T(s_1, m_{s_1}) \wedge T^\dagger(s_1, m_{s_1})]^{p_1}_{q_1=0} = \sum_{m_{s_1}} (-)^{p_1-s_1-m_{s_1}} \langle s_1 - m_{s_1} s_1 m_{s_1} | p_1 0\rangle \times \mathcal{W}(s_1, -m_{s_1}) T(s_1, m_{s_1}).$$

Comparing this result with Eq. (13) it is obvious that for a given p_2 the parameter $\Lambda^{p_1,p_2}_{q_1=0,q_2=0}$ can be regarded as the component along the quantization axis of a spherical tensor of rank p_1. The same argument applies to the dependence on p_2, i.e., for a given p_1 we can treat $\Lambda^{p_1,p_2}_{q_1=0,q_2=0}$ as the $\hat{\mathbf{M}}$ component of the spherical tensor with rank p_2.

This mathematical analysis yields important information as to the transformation behavior of the tensorial components $\Lambda^{p_1,p_2}_{0,0}$: $\Lambda^{p_1=0,p_2}_{0,0}$ $(\Lambda^{p_1,p_2=0}_{0,0})$ is a *scalar* with respect to spin rotations generated by $\mathbf{s}_1$ $(\mathbf{s}_2)$, i.e., it represents spin-averaged quantities in the $\mathbf{s}_1$ $(\mathbf{s}_2)$ spin space, whereas the components $\Lambda^{p_1=odd,p_2}_{0,0}$ $(\Lambda^{p_1,p_2=odd}_{0,0})$ can be regarded as spin *orientation* in the $\mathbf{s}_1$ $(\mathbf{s}_2)$ spin space (for $p_1 = 1$ it is a vector) and hence changes sign upon spin reflection, i.e., $\Lambda^{p_1=odd,p_2}_{0,q_0}(-m_{s_1}) = -\Lambda^{p_1=odd,p_2}_{0,0}(m_{s_1})$ $[\Lambda^{p_1,p_2=odd}_{0,q_0}(-m_{s_2}) = -\Lambda^{p_1,p_2=odd}_{0,0}(m_{s_2})]$. The tensorial components with even p_1 values are alignment parameters, i.e., they describe the deviations in the spectra from the unpolarized case.

For the case $s_1 = 1/2$ and $s_2 = 1/2$ Eq. (11) reduces to

$$W = \sum\!\!\!\!\!\!\!\int_{\alpha} \left\{ \Lambda^{0,0}_{0,0} \left[\rho_{00}\overline{\rho}_{00} + \rho_{00}\overline{\rho}_{10} \frac{\Lambda^{0,1}_{0,0}}{\Lambda^{0,0}_{0,0}} + \rho_{10}\overline{\rho}_{00} \frac{\Lambda^{1,0}_{0,0}}{\Lambda^{0,0}_{0,0}} + \rho_{10}\overline{\rho}_{10} \frac{\Lambda^{1,1}_{0,0}}{\Lambda^{0,0}_{0,0}} \right] \delta(E_f - E_i) \right\}. \tag{14}$$

As stated above, the first term of the sum in Eq. (14) yields the pair-emission rate averaged over the spin orientation of the incoming electron beam and the spin polarization of the sample. The second term describes the spin asymmetry due to the inversion of the magnetization while the incoming electron beam is *unpolarized* . The third term is the spin asymmetry in the electron-pair emission from *unpolarized targets* when inverting the spin polarization of the electron beam.[14] In the absence of explicit spin interactions in the transition operator $\mathcal{T}$, e.g., spin-orbit coupling, the parameters $\Lambda_{0,0}^{1,0}$ and $\Lambda_{0,0}^{0,1}$ vanish. In the present experiment on the Fe(110) sample we measured the parameters $\Lambda_{0,0}^{0,1}$ and $\Lambda_{0,0}^{1,0}$ and found them to be zero in the particular geometry of Fig. 1 and within the accuracy of our setup. In this context we note that with the same setup it has been possible to determine a finite value of $\Lambda_{0,0}^{1,0}$ when a tungsten sample is employed,[15] due to the enhanced strength of spin-orbit interaction as compared to the case of Fe(110).

Therefore, the present study is devoted to the last term of Eq. (14). This parameter is relevant for the description of the electron-pair emission from an exchange-split ferromagnetic surface induced by spin-polarized electrons. $\Lambda_{0,0}^{1,1}$ is a polar vector both in the $\mathbf{s}_1$ and $\mathbf{s_2}$ spin spaces, i.e.,

$$\begin{aligned}
\Lambda_{0,0}^{1,1}(-m_{s_1},m_{s_2}) &= -\Lambda_{0,0}^{1,1}(m_{s_1},m_{s_2}),\\
\Lambda_{0,0}^{1,1}(m_{s_1},-m_{s_2}) &= -\Lambda_{0,0}^{1,1}(m_{s_1},m_{s_2}),\\
\Lambda_{0,0}^{1,1}(-m_{s_1},-m_{s_2}) &= \Lambda_{0,0}^{1,1}(m_{s_1},m_{s_2}).
\end{aligned} \tag{15}$$

The explicit forms of $\Lambda_{0,0}^{1,1}$ and $\Lambda_{0,0}^{0,0}$ are derived from Eq. (13) to be

$$\Lambda_{0,0}^{1,1}=\frac{1}{2}\{\mathcal{F}(\downarrow,\Downarrow)+\mathcal{F}(\uparrow,\Uparrow)-\mathcal{F}(\uparrow,\Downarrow)-\mathcal{F}(\downarrow,\Uparrow)\}, \tag{16}$$

$$\Lambda_{0,0}^{0,0}=\frac{1}{2}\{\mathcal{F}(\downarrow,\Downarrow)+\mathcal{F}(\uparrow,\Uparrow)+\mathcal{F}(\uparrow,\Downarrow)+\mathcal{F}(\downarrow,\Uparrow)\}. \tag{17}$$

To expose the symmetry properties of the total wave function that are imposed by the Pauli principle we transform $\mathcal{F}$ and T, as given by Eq. (8), into the total-spin (S) space and obtain (we assume separable spin and spatial degrees of freedom)

$$\begin{aligned}
\mathcal{F}(m_{s_1},m_{s_2}) &= C\sum_{SM_S}|\langle s_1 m_{s_1};s_2 m_{s_2}|SM_S\rangle|^2\\
&\quad\times X^{(S)}(\mathbf{k}_1,\mathbf{k}_2;\mathbf{k}_0,\alpha),
\end{aligned} \tag{18}$$

$$\begin{aligned}
X^{(S)}(\mathbf{k}_1,\mathbf{k}_2;\mathbf{k}_0,\alpha) &= |\langle \Psi^{(S)}_{\mathbf{k}_1,\mathbf{k}_2}(1,2)\chi_{SM_S}(1,2)|\mathcal{T}|\\
&\quad\times\Phi(S)(1,2)\chi'_{SM_S}(1,2)\rangle|^2.
\end{aligned} \tag{19}$$

Here we introduced the total-spin-resolved cross section $X^{(S)}$ and the normalized two-particle spin wave function as $|\chi'_{SM_S}\rangle$. The spatial parts of the two-electron state in the initial and the final channels are denoted by, respectively, $|\Psi^{(S)}_{\mathbf{k}_1,\mathbf{k}_2}(1,2)\rangle$ and $|\Phi(S)(1,2)\rangle$, i.e.,

$$|\Psi^{(S)}_{\mathbf{k}_1,\mathbf{k}_2}(1,2)\rangle=\frac{1}{\sqrt{2}}\{|\psi_{\mathbf{k}_1,\mathbf{k}_2}(1,2)\rangle+(-)^S|\psi_{\mathbf{k}_2,\mathbf{k}_1}(1,2)\rangle\}. \tag{20}$$

From this relation we deduce an important feature of the triplet state ($S=1$) and the corresponding triplet transition amplitude: In cases where an exchange of $\mathbf{k}_1$ and $\mathbf{k}_2$ does not affect the experiment, e.g., when $\mathbf{k}_1=\mathbf{k}_2$, the triplet scattering vanishes.

To understand the polarized multielectron emission it is useful to introduce the direct- (f) and the exchange- (g) scattering amplitudes. These are defined as

$$f=\langle\psi_{\mathbf{k}_1,\mathbf{k}_2}(1,2)|\mathcal{T}|\phi_{\epsilon,\alpha}(2)\varphi_{\mathbf{k}_0}(1)\rangle, \tag{21}$$

$$g=\langle\psi_{\mathbf{k}_2,\mathbf{k}_1}(1,2)|\mathcal{T}|\phi_{\epsilon,\alpha}(2)\varphi_{\mathbf{k}_0}(1)\rangle. \tag{22}$$

In physical terms f, the direct-scattering amplitude, can be interpreted as a measure for the probability that the projectile electron, labeled (1) and incident with wave vector $\mathbf{k}_0$, is scattered into the asymptotic (detector) state that is characterized by the wave vector $\mathbf{k}_1$ while the other electron (2) is being excited into the asymptotic state with the wave vector $\mathbf{k}_2$. Analogously, the exchange-scattering amplitude g describes the probability that electron (1) is scattered into the state $\mathbf{k}_2$ while particle (2) is promoted to the state with the wave vector $\mathbf{k}_1$.

If k_0 and k_1 are very large (with respect to the Fermi wave vector) and if a small amount of momentum is being transferred to the sample during the collision, it can be expected intuitively that $|f|\gg|g|$, i.e., the fast incoming electron is the one electron which emerges swiftly. In other words, in this case the electrons are distinguishable via their highly asymmetric energies and hence, as shown below, the spin asymmetry vanishes in this case.

From Eqs. (20) and (18) we deduce the relations

$$X^{(S=0)}(\mathbf{k}_1,\mathbf{k}_2;\mathbf{k}_0,\alpha)=C|f+g|^2, \tag{23}$$

$$X^{(S=1)}(\mathbf{k}_1,\mathbf{k}_2;\mathbf{k}_0,\alpha)=C|f-g|^2. \tag{24}$$

Equation (18) yields a relation that links the single-electron spin-resolved cross section $\mathcal{F}(m_{s_1},m_{s_2})$ with the triplet and singlet cross sections, namely,

$$\mathcal{F}(\uparrow,\Uparrow)=\mathcal{F}(\downarrow,\Downarrow)=X^{(S=1)}=C|f-g|^2, \tag{25}$$

$$\mathcal{F}(\downarrow,\Uparrow)=\mathcal{F}(\uparrow,\Downarrow)=\frac{1}{2}[X^{(S=1)}+X^{(S=0)}]=C|f|^2+C|g|^2. \tag{26}$$

Equations (16) and (17) reexpressed in terms of the singlet and the triplet partial cross sections, $X^{(S=0)}$ and $X^{(S=1)}$, read

$$\Lambda_{0,0}^{1,1}=\frac{1}{2}[X^{(S=1)}(\mathbf{k}_1,\mathbf{k}_2;\mathbf{k}_0;\alpha)-X^{(S=0)}(\mathbf{k}_1,\mathbf{k}_2;\mathbf{k}_0,\alpha)], \tag{27}$$

$$\begin{aligned}
\Lambda_{0,0}^{0,0} &= \frac{1}{2}[3X^{(S=1)}(\mathbf{k}_1,\mathbf{k}_2;\mathbf{k}_0,\alpha)+X^{(S=0)}(\mathbf{k}_1,\mathbf{k}_2;\mathbf{k}_0,\alpha)]\\
&=:2X_{av}.
\end{aligned} \tag{28}$$

Evidently, these two equations can as well be expressed in terms of the direct- and exchange-scattering amplitudes f and g. In Eq. (28) we introduced the spin-averaged cross section X_{av}.

B. Calculational scheme

For perfect clean surfaces the average over α in Eq. (14) implies summation over the surface Bloch wave vector $\mathbf{q}_\parallel$ and over the surface layers. The Bloch theorem for two interacting particles imposes a conservation law [cf. Eq. (2)] for the surface components of the *total* wave vector of the emitted electrons $\mathbf{K}_\parallel^+ = \mathbf{k}_{1\parallel} + \mathbf{k}_{2\parallel}$,[11] i.e., the change of $\mathbf{K}_\parallel^+$ from its initial value $\mathbf{k}_{0\parallel} + \mathbf{q}_\parallel$ (before the collision) is restricted to a multiple of the surface reciprocal-lattice vector $\mathbf{g}_\parallel$. This fact can be used to perform the integrals over $\mathbf{q}_\parallel$ in Eq. (14). Therefore, Eq. (14) reduces to a summation over the surface layers, indexed by l, and over $\mathbf{g}_\parallel$, i.e.,

$$W \propto \sum_{\mathbf{g}_\parallel, l} \{2X_{av}(\mathbf{k}_1,\mathbf{k}_2;\mathbf{k}_0,\mathbf{g}_\parallel,l)[\rho_{00}\overline{\rho}_{00}(\epsilon,\mathbf{\Lambda}_\parallel,l) - \rho_{10}\overline{\rho}_{10}(\epsilon,\mathbf{\Lambda}_\parallel,l)A^s(\mathbf{k}_1,\mathbf{k}_2;\mathbf{k}_0,\mathbf{g}_\parallel,l)]\delta(E_f - E_i)\}, \tag{29}$$

where

$$\mathbf{\Lambda}_\parallel = \mathbf{K}_\parallel^+ - \mathbf{g}_\parallel - \mathbf{k}_{0\parallel}. \tag{30}$$

We recall that spin interactions in the transition operator $\mathcal{T}$ have been neglected, in which case the parameters $\Lambda_{0,0}^{0,1}$ and $\Lambda_{0,0}^{1,0}$ vanish identically. In Eq. (29) we introduced the "exchange-scattering asymmetry" as

$$A^s := \frac{X^{(S=0)}(\mathbf{k}_1,\mathbf{k}_2;\mathbf{k}_0,\mathbf{g}_\parallel,l) - X^{(S=1)}(\mathbf{k}_1,\mathbf{k}_2;\mathbf{k}_0,\mathbf{g}_\parallel,l)}{X^{(S=0)}(\mathbf{k}_1,\mathbf{k}_2;\mathbf{k}_0,\mathbf{g}_\parallel,l) + 3X^{(S=1)}(\mathbf{k}_1,\mathbf{k}_2;\mathbf{k}_0,\mathbf{g}_\parallel,l)} = \frac{|f||g|\cos\delta}{|f|^2 + |g|^2 - |f||g|\cos\delta}. \tag{31}$$

In the last equation we reexpressed the cross sections in terms of the direct- $[f = f(\mathbf{k}_1,\mathbf{k}_2;\mathbf{k}_0,\mathbf{g}_\parallel,l)]$ and the exchange- $[g = g(\mathbf{k}_1,\mathbf{k}_2;\mathbf{k}_0,\mathbf{g}_\parallel,l)]$ scattering amplitudes and their relative phase δ. Thus, Eq. (31) reveals the spin asymmetry as the result of a quantum interference of the two amplitudes f and g.

Two conclusions follow directly from Eq. (31): (i) For a given layer the asymmetry A^s assumes unity value if $X^{(S=1)} = 0$. As stated above this is the case if the experiment is invariant under an exchange of $\mathbf{k}_1$ and $\mathbf{k}_2$. The function A^s varies between 1 and $-1/3$. The experimentally relevant quantity is, however, the value A^s weighted with the pair-emission cross section X_{av} [cf. Eqs. (29) and (34)], i.e., in cases where the cross section diminishes, e.g., for emission from atomic layers whose positions with respect to the surface are beyond the electron's inelastic mean free path, the pair-emission cross section and the spin asymmetry are not measurable (in the way proposed in this paper). (ii) In the cases $|f| \gg |g|$, $|f| \ll |g|$, or $f \perp g$ the spin asymmetry vanishes as the interference between f and g is then negligible.

To calculate the terms in Eq. (29) the state multipoles ρ_{10} and $\overline{\rho}_{10}$ are needed. These can be obtained by inverting the relations (9) and (10) as

$$\rho_{pq} = \sum_{m_s} (-)^{p-s-m_s} \langle s - m_s; s m_s | pq \rangle \rho^s_{m_s m_s}. \tag{32}$$

From this equation it is clear that even for pure states (fully spin-polarized states) all state multipoles are generally finite.

Since we have neglected spin-dependent interactions only the multipoles ρ_{00}, ρ_{01}, $\overline{\rho}_{00}$, and $\overline{\rho}_{01}$ are required. From Eqs. (9), (10), and (32) we deduce $\rho_{00}\overline{\rho}_{00} = [w_0(\mathbf{q}_\parallel,l,\epsilon)]/2$ and $\rho_{10}\overline{\rho}_{10} = [w_0(\mathbf{q}_\parallel,l,\epsilon)]P_1P_2/2$. Equation (29) can thus be written in the form

$$W \propto \sum_{\mathbf{g}_\parallel, l} w_0(\mathbf{\Lambda}_\parallel,l,\epsilon)X_{av}[1 + \mathcal{A}]\delta(E_f - E_i), \tag{33}$$

where the asymmetry function $\mathcal{A}$ is defined by the relation

$$\mathcal{A} = P_1 \frac{\sum_l [w(\mathbf{\Lambda}_\parallel,l,\epsilon,\Downarrow) - w(\mathbf{\Lambda}_\parallel,l,\epsilon,\Uparrow)] \sum_{\mathbf{g}_\parallel} X_{av}A^s\delta(E_f - E_i)}{\sum_{l'} w_0(\mathbf{\Lambda}_\parallel,l',\epsilon) \sum_{\mathbf{g}'_\parallel} X_{av}\delta(E_f - E_i)} = \frac{W(\uparrow\Uparrow) - W(\downarrow\Uparrow)}{W(\uparrow\Uparrow) + W(\downarrow\Uparrow)}. \tag{34}$$

This result for the asymmetry admits a simple structure in some limiting situations:

For atomic gaseous targets the sample's polarization vector $\mathbf{P}_2$ is a constant, experimentally determined quantity, namely, the polarization P_a of the atomic beam. Therefore, $\mathcal{A}$ reduces to $\mathcal{A} = P_aP_eA^{(s)}$.

For a spin-polarized homogeneous electron gas (Stoner model) P_2 is directly related to the density of states $\rho_{\Uparrow,\Downarrow}$ and therefore $\mathcal{A} = P_1[(\rho_\Downarrow - \rho_\Uparrow)/(\rho_\Downarrow + \rho_\Uparrow)]A^{(s)}$.

For bulk sensitive studies, e.g., for a high-energy electron beam ($E_0 > 1$ keV), the three-dimensional translational symmetry of the sample results in a simplified form of Eq. (34), namely,

$$\mathcal{A} = P_1P_2 \frac{\sum_{\mathbf{g}} X_{av}A^s\delta(E_f - E_i)}{\sum_{\mathbf{g}'} X_{av}\delta(E_f - E_i)}. \tag{35}$$

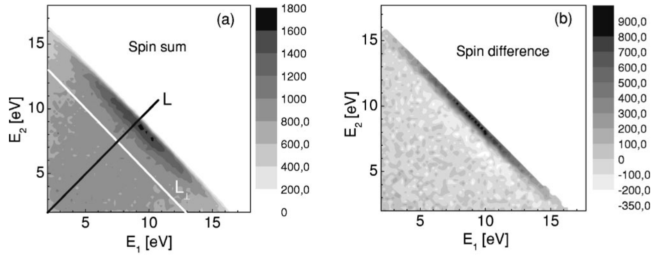

FIG. 2. (a) The coincident two-electron spectrum measured in the geometry of Fig. 1. The incident energy is $E_0 = 22.6$ eV and the data are summed for two polarizations of the incoming electron beam. The data set was integrated over the whole area of the detectors, therefore the emission angles are determined within the range $\theta_1 = 40° \pm 15°$ and $\theta_2 = 40° \pm 15°$. Along the line L, the two electrons escape with equal energies. Along the lines perpendicular to L the electron pairs have a constant total energy $E_{\mathrm{tot}} = E_1 + E_2 = \mathrm{const}$. The absolute values of the spectra are not determined whereas the absolute magnitude and the sign of the spin asymmetry is measured. (b) The difference between two spectra obtained when $\mathbf{P}_1$ is parallel to $\hat{\mathbf{M}}$ and $\mathbf{P}_1$ is antiparallel to $\hat{\mathbf{M}}$.

Here $\mathbf{g}$ is a three-dimensional reciprocal-lattice vector and the polarization vector P_2 is given by $P_2 = [w(\mathbf{\Lambda}, \epsilon, \Downarrow) - w(\mathbf{\Lambda}, \epsilon, \Uparrow)]/[w_0(\mathbf{\Lambda}, \epsilon)]$. In this context it should be noted that, except for some highly symmetric situations, in the high-energy regime A^s might be very small due to the dominance of direct scattering.

IV. COMPARATIVE ANALYSIS OF EXPERIMENTAL AND THEORETICAL RESULTS

We conducted the experiment for a series of impact energies from $E_0 = 20$ eV up to $E_0 = 37.6$ eV in the geometry shown in Fig. 1. The two-dimensional distributions of coincidence events for $E_0 = 22.6$ eV are shown in Fig. 2(a) as a function of the energies of the two electrons E_1 and E_2. In this graph, the two data sets obtained with different electron-beam polarizations with respect to the sample magnetization are summed up. We recall that the emission angles θ_1 and θ_2 are also measured, however, the data depicted in Fig. 2 are integrated over the whole solid angle of detection. The position of the Fermi level E_F is shown as well as the line L along which the two electrons have equal energies. Figure 2(b) shows the difference in the spectrum associated with reversal of the spin polarization of the electron beam. Equivalently, one can also plot the electrons' energy dependence of the asymmetry $\mathcal{A}$. The line L is of a special importance as it corresponds to the Γ point for $\theta_1 = \theta_2$, as can be seen from Eq. (2) $[\mathbf{k}_{0\|} = 0, \mathbf{k}_{1\|} = -\mathbf{k}_{2\|}]$. Different points on L correspond to different binding energies ϵ of the conduction-band electrons [cf. Eq. (1)]. On the other hand, in the highly symmetric geometry of the setup shown in Fig. 1 and along the line L $(E_1 = E_2)$ the complete experiment and in particular the sample's properties are invariant under a 180° rotation with respect to the $z \| \mathbf{k}_0$ direction. Such a symmetry operation is, however, equivalent to an exchange of $\mathbf{k}_1$ and $\mathbf{k}_2$. Therefore, along the line L in Figs. 2(a) and 2(b) the triplet scattering vanishes [cf. Eqs. (20)–(22) and (24)] and therefore the term A^s (31) becomes unity. This means that the spin asymmetry $\mathcal{A}$ (34) in this situation reflects the properties of the electronic band structure of the sample. The scattering dynamics plays no role due to symmetry (as far as the quantity $\mathcal{A}$ is concerned).

The above statements apply strictly speaking along the line L only. In our experiment, however, we have to integrate over a finite detection solid angle in order to obtain reasonable statistics, i.e., in the geometry of Fig. 1 and along the line L the electrons are emitted into a solid angle Ω_θ with an aperture Δ_θ. The sampling over Ω_θ implies an averaging over $\hat{\mathbf{k}}_1$ and $\hat{\mathbf{k}}_2$ within a certain range. From Eq. (2) it follows that this procedure corresponds to an integration in a certain region in the Brillouin zone around the Γ point. It should be stressed, however, that in the case of a finite angular resolution the coincident signal cannot be directly related to the sample's electronic structure since the triplet scattering is then generally finite and the term A^s [Eq. (31)] is not simply a constant (except for $\theta_1 = \theta_2$, $E_1 = E_2$ where $A^s = 1$). The quantitative shape of A^s away from the highly symmetric points $\theta_1 = \theta_2$ and $E_1 = E_2$ is strongly dependent on the scattering dynamics (embedded in $\Lambda^{p_1, p_2}_{q_1, q_2}$) whose modeling poses a real challenge, even for simple few-body systems.[16,17]

The asymmetry A^s has its unity maximum value at $\theta_1 = \theta_2$ and $E_1 = E_2$. Thus, any angular sampling (Δ_θ) will decrease the unity value of A^s. This argument is, however, not valid for $\mathcal{A}$, since the angular integration procedure involves different electronic states of the conduction band whose spin polarization is not known *a priori* and depends on the material under investigation. For the present case we observed in the theoretical results that angular integration reduces the values of the spin asymmetries $\mathcal{A}$.

In Fig. 3 we assess the above statements by contrasting theoretical with experimental spectra along the line L in Fig. 2. In Figs. 3(a)–3(c) the angular integration for each of the TOF detectors is $\Delta_\theta = 15°$ whereas in Figs. 3(a′)–3(c′) the angular integration is decreased to $\Delta_\theta = 7.5°$. In all cases the angular resolution is accounted for by the theory. As stated above for the strict conditions $\theta_1 = \theta_2$ and $E_1 = E_2$ the spin asymmetry $\mathcal{A}$ [Eq. (34)] is an image of the spin polarization P_2 [cf. Eq. (6)] at the respective point in the Brillouin zone. Therefore, the value of $\mathcal{A}$ should not depend on the incident energy E_0 of the beam (since P_2 is independent of E_0). For the theoretical results we observe the general trend that the finite angular resolution has the effect of decreasing the value $\mathcal{A}$ {due to the decreased value of A^s [Eq. (31)], as explained above}. Improving on the angular resolution $[\Delta_\theta = 15°$ in Figs. 3(a)–3(c) and $\Delta_\theta = 7.5°$ in Figs. 3(a′)–3(c′)$]$ increases the averaged value of A^s and possibly enhances the value of $\mathcal{A}$. These expectations are basically confirmed by the theoretical results in the region around the Fermi level (1 eV below E_F) (cf. Fig. 3): The theoretical $\mathcal{A}$ increases substantially when the angular resolution is improved and the value and sign of $\mathcal{A}$ do not depend on E_0 near the Fermi energy. While the agreement between theory and experiment can be regarded as satisfactory up to 2 eV below E_F, large deviations are observed for the electron-pair emission from levels deeper in the band. For these levels the experimental

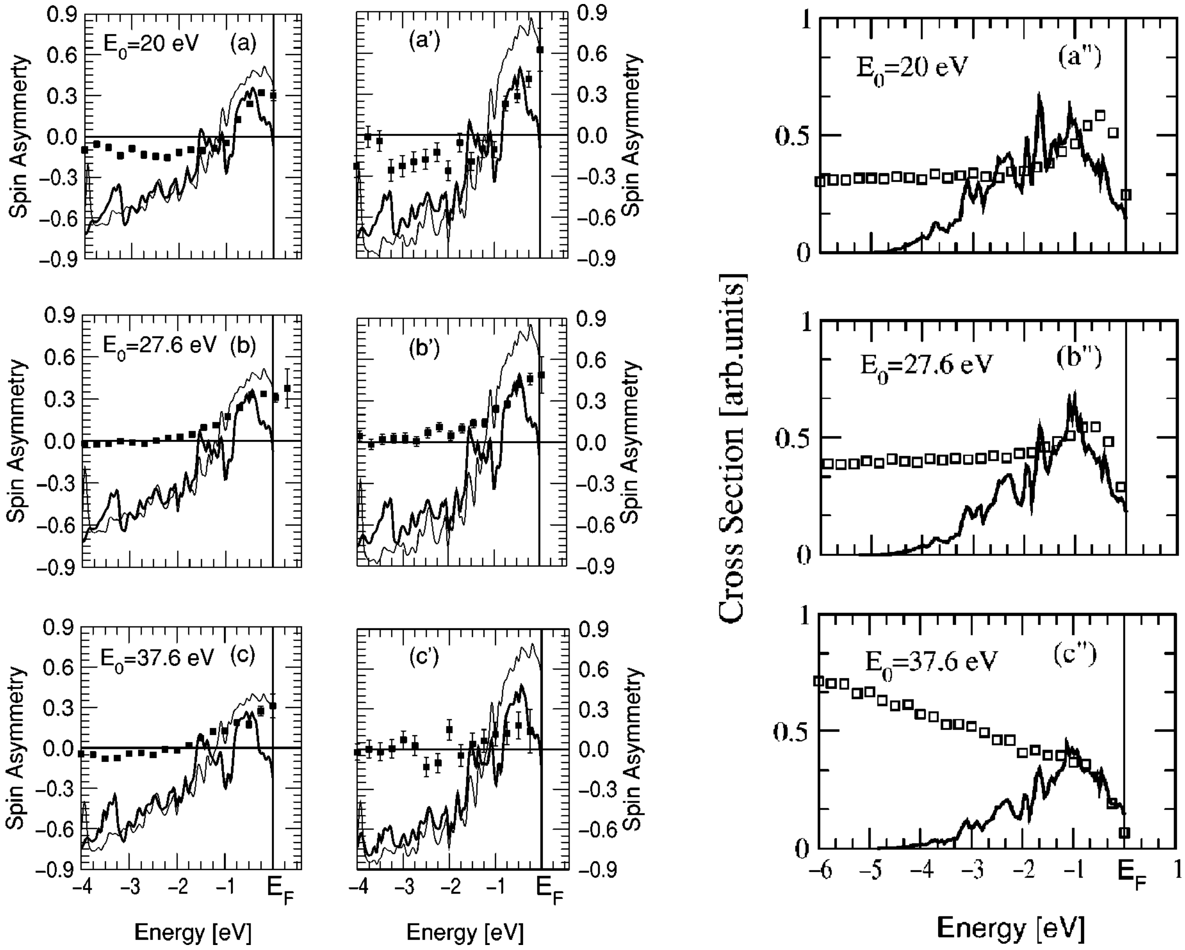

FIG. 3. With the same geometry as in Figs. 1 and 2 we scan the spin asymmetry $\mathcal{A}$ in the electron-pair-emission cross section along the line of equal energies of the electrons, i.e., along the line labeled L in Fig. 2(a). The asymmetry $\mathcal{A}$ is plotted as a function of the energy $\epsilon = E_{\mathrm{tot}} - E_0$. According to Eq. (1) ϵ corresponds to the binding energy of the ground-state electrons and hence the Fermi energy is at $\epsilon = 0$. The sets (a)–(c) and (a″)–(c″) show, respectively, the spin asymmetry in the electron-pair spectrum and the spin-averaged spectrum for three different incident energies E_0 of the incoming electrons [$E_0 = 20$ eV in (a), (a′), and (a″), $E_0 = 27.6$ eV in (b), (b′), and (b″), and $E_0 = 23.6$ eV in (c), (c′), and (c″)]. In (a)–(c) and (a″)–(c″) the angular integration for each of the detectors is $\theta_{1/2} = (40 \pm 15)°$, whereas in (a′)–(c′) the solid angle of the integration area was restricted to $\theta_{1/2} = (40 \pm 7.5)°$. Full squares with error bars are experimental data whereas the solid lines are the theoretical results.

results are also different for different incident energies E_0 and therefore they cannot be related directly to the ground-state electronic band structure. To get insight into the origin of these discrepancies we discuss the main limitations of our theoretical approach: In the present theory, when we derive the single-particle Green function, we do not employ a proper expression for the self-energy operator which would generally have the effect of (a lifetime) broadening and an energetic shifting of the quasiparticle states.[18] In our calculations we assume the imaginary part of the self-energy to be merely a spin-independent constant (0.02 eV). Therefore, our theory yields an energetic spreading of the bound states which is very narrow. For a given Bloch wave vector, when we energy-scan the Brillouin zone, e.g., as is done in Fig. 3, we encounter only narrow states centered around specific energies, and hence we see the spiky structure of the theoretical curves shown in Fig. 3 (note, however, that in Fig. 3 we accounted for the finite experimental angular resolution which results in a certain broadening of the peaks). An additional shortcoming of the present theory is that we do not account for a dynamic, multiple inelastic scattering of the electron pair from other electrons in the sample (the electron-electron scattering within the electron pair is treated properly). This is justifiable when the emission of the electron pair is from states around the Fermi level, for the energy conservation (1) pins down the energetic position of the bound electron [$\epsilon = (E_1 + E_2) - E_0$]. For states deep in the band this determination of the initial binding energy of the ejected electrons is no longer unique. This is because, on their way out to the vacuum, the excited electrons may scatter inelastically from other target electrons which further propagate in the sample and remain undetected. This leads to a spin decoherence of the excited electrons since, as we have shown in this paper, the electron-electron inelastic scattering is strongly spin dependent (due to the exchange coupling).

These statements are in line with the behavior of the experimental and theoretical results shown in Figs. 3(a)–3(c) and Figs. 3(a″)–3(c″). In the latter figures the spin-averaged electron-emission rate corresponding to the geometry of Figs. 3(a)–3(c) is depicted. In contrast to theory, the experiments show a considerable increase in the coincidence rate for very low electron energies, i.e., for large negative initial binding energies $[\epsilon=(E_1+E_2)-E_0]$. In fact the extent of the experimental spectra [not fully shown in Figs. 3(a″)–3(c″)] goes beyond the conduction bandwidth. On the other hand these slow electrons might have been originally fast (at the time of their creation) and suffered one or more inelastic electronic collisions before escaping into the vacuum. This additional channel, not accounted for theoretically, leads to an increase in the cross sections for the emission of two slow electrons (or from levels deep in the band). Due to the spin decoherence associated with these inelastic processes the spin asymmetry, as shown in Figs. 3(a)–3(c), diminishes when the contribution of such inelastically scattered electron pairs becomes a sizable part of the recorded coincidence spectra. This argument gains support by correlating the behavior of the experiments in Figs. 3(a)–3(c) and Figs. 3(a″)–3(c″), e.g., with increasing impact energy E_0 the contribution of the inelastic, energy-loss processes of the electron pairs increases, while in this case the spin asymmetry decreases. As expected, the theory shows hardly a dependence on E_0 of the spectra in Figs. 3(a) and 3(c″).

In Fig. 2 we highlighted the importance of the equal-energy line L and showed in Fig. 3 the electron-pair spectrum along L. For events along this line, the binding energy ϵ of valence electron removed from the Γ point varies. If we consider lines $L_\perp$ in Fig. 2 which are perpendicular to L, we consider events at fixed binding energy ϵ [this is because in this case $E_{\mathrm{tot}}=E_1+E_2$ is constant and due to Eq. (1), $\epsilon=E_{\mathrm{tot}}-E_0$]. The electron-pair spectrum along $L_\perp$ is an energy pair-correlation function. It is a measure of the probability that the first electron will escape with energy E_1 and the other electron will emerge with energy $E_2=E_{\mathrm{tot}}-E_1$. This probability will strongly depend on the strength of the correlation between these two electrons. In particular, the spin asymmetry in this spectrum is intimately related to the strength of the exchange interaction as quantified by the amplitude g [Eq. (22)]. If g vanishes (distinguishable electrons) the spin asymmetry diminishes. Therefore it is of interest to analyze $\mathcal{A}$ along the line $L_\perp$, as done in Fig. 4 for three different total energies of the electron pair for a fixed incident energy $E_0=22.6$ eV. When the two electrons escape with equal energies $E_1=E_2$ (the crossing point of the lines $L_\perp$ and L) the triplet scattering $X^{(S=1)}$ vanishes, as explained above. Therefore, for $E_1=E_2$ we obtain $A^{(s)}=1$. In this situation ($E_1=E_2$), the *magnitude* and *sign* of the asymmetry $\mathcal{A}$ are dictated merely by $P_2(\epsilon)$. Since $P_2(\epsilon)$ may be positive or negative, $\mathcal{A}$ may have a different sign depending on E_{tot} (or on $\epsilon=E_{\mathrm{tot}}-E_0$). In general, the shape of $\mathcal{A}$ as depicted in Fig. 4 can be understood from the following arguments emerging from the analysis of our theoretical results: For $E_1=E_2$, the triplet cross section vanishes, and therefore $A^{(s)}$ reaches its highest value (unity). This structure is at a peak (minimum) when $P_2>0$ ($P_2<0$). The decrease in $\mathcal{A}$ for $E_1>E_2$ or $E_2<E_1$ is due to a dominance of the direct-scattering amplitude $|f|$ over the exchange amplitude $|g|$, i.e., it is more likely that the fast incoming electron will escape as the fast electron than it is for it to lose almost all its energy and emerge as the slow one. As deduced above, $\lim_{(|g|/|f|)\to 0}A^{(s)}=(|f||g|\cos\delta)/(|f|^2|g|^2-|f||g|\cos\delta)\to 0$, and hence the asymmetry in Fig. 4 decreases with increasing deviation from $E_1=E_2$.

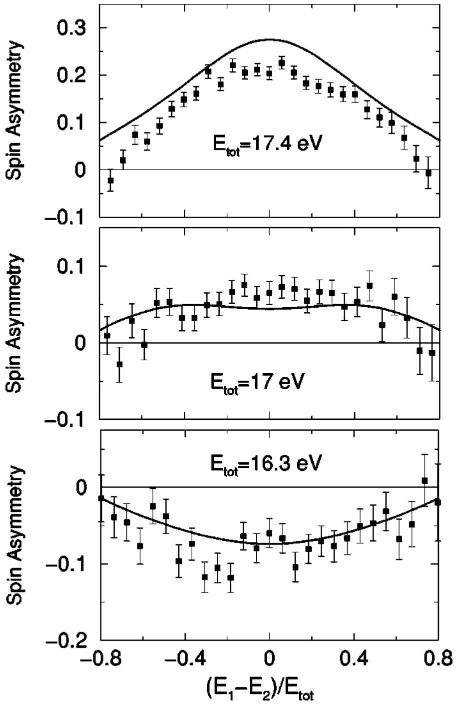

FIG. 4. For a fixed total energy E_{tot} and a fixed energy $\epsilon=E_{\mathrm{tot}}-E_0$ of the initially bound electron we measure (full squares) and calculate (solid lines) the spin asymmetry $\mathcal{A}$ (34) as a function of the energy sharing of E_{tot} between the two emitted electrons. The zero point indicates the position of equal-energy sharing. Three sets are shown corresponding to three different values of E_{tot} as indicated in the figures. The experimental data are obtained from Fig. 2 by taking cuts along the lines perpendicular to L, the position marking equal energies. Theoretical results have been averaged over the solid angle, as stated in Fig. 2.

V. CONCLUSIONS

In this work we presented a theoretical and experimental analysis of the correlated electron-pair emission from magnetic surfaces induced by the impact of polarized electrons. We employed a tensorial symmetry analysis to disentangle geometrical from dynamical properties and to classify the spectra according to their symmetry properties. We also described a calculational model for the two-particle spectrum and performed numerical calculations using a realistic electronic band structure of the sample. Under certain conditions worked out in this study, the present two-particle coincidence technique allows for an insight into the spin-split electronic band structure of the sample and is also suitable to investigate the electrons' exchange scattering at surfaces.

ACKNOWLEDGMENTS

The technical assistance of H. Schwabe and A. Wiessner is gratefully acknowledged.

[1] J. Kirschner, D. Rebenstorff, and H. Ibach, Phys. Rev. Lett. **53**, 698 (1984).

[2] M. Plihal, D. L. Mills, and J. Kirschner, Phys. Rev. Lett. **82**, 2579 (1999).

[3] D. L. Abraham and H. Hopster, Phys. Rev. Lett. **62**, 1157 (1989).

[4] H. Ibach and D. L. Mills, *Electron Energy Loss Spectroscopy and Surface Vibrations* (Academic Press, New York, 1982).

[5] *Polarized Electrons in Surface Physics*, edited by R. Feder (World Scientific, Singapore, 1985).

[6] J. Berakdar, Phys. Rev. Lett. **83**, 5150 (1999).

[7] S. N. Samarin, J. Berakdar, O. Artamonov, and J. Kirschner, Phys. Rev. Lett. **85**, 1746 (2000).

[8] S. Samarin, O. Artamonov, J. Berakdar, A. Morozov, and J. Kirschner, Surf. Sci. **482**, 618 (2001).

[9] P. Blaha, K. Schwarz, P. Sorantin, and S. B. Trickey, Comput. Phys. Commun. **59**, 399 (1990); X. Qian and W. Hübner, Phys. Rev. B **60**, 16 192 (1999).

[10] E. Tamura, in *Application of Multiple Scattering Theory to Materials Science*, edited by W. H. Butler, P. H. Dederichs, A. Gonis, and R. L. Weaver, Mater. Res. Soc. Symp. Proc. No. 253 (Materials Research Society, Pittsburgh, 1992), p. 347.

[11] J. Berakdar, S. N. Samarin, R. Herrmann, and J. Kirschner, Phys. Rev. Lett. **81**, 3535 (1998).

[12] U. Fano, Rev. Mod. Phys. **29**, 76 (1957).

[13] D. M. Brink and G. R. Satchler, *Angular Momentum*, 3rd ed. (Clarendon Press, Oxford, 1994).

[14] H. Gollisch, X. Yi, T. Scheunemann, and R. Feder, Phys. Rev. B **60**, 8055 (1999).

[15] S. Samarin, O. Artamonov, A. Morozov, and J. Kirschner (unpublished).

[16] M. Streun, G. Baum, W. Blask, and J. Berakdar, Phys. Rev. A **59**, R4109 (1999).

[17] J. Lower, E. Weigold, J. Berakdar, and S. Mazevet, Phys. Rev. Lett. **86**, 624 (2001).

[18] L. Hedin, J. Phys. C **11**, R489 (1999); **11**, R528 (1999); P. Fulde, *Electron Correlation in Molecules and Solids*, Springer Series in Solid-State Sciences, Vol. 100 (Springer-Verlag, Berlin, 1991).

PHYSICAL REVIEW B VOLUME 58, NUMBER 15 15 OCTOBER 1998-I

Emission of correlated electron pairs following single-photon absorption by solids and surfaces

Jamal Berakdar
Max-Planck Institute for Microstructure Physics, Weinberg 2, 06120 Halle, Saale, Germany

(Received 23 March 1998)

The simultaneous emission of two electrons from condensed matter following the absorption of a linearly polarized photon is studied in the first order-perturbation theory for the radiation field, and within the dipole approximation. The double emission from localized and delocalized electronic states is considered. It is shown that spectra of the emitted pairs obey propensity rules expressed by the scalar product of the center-of-mass vector momentum of the pair and the photon's polarization vector. Furthermore, it is shown that diffraction of the pair from the lattice occurs when the pair's center-of-mass wave vector changes by a lattice reciprocal vector during the photoemission. For semi-infinite solids with delocalized valence electrons, an initial state is constructed from single-particle orbitals. Following the absorption of the photon the valence-band electron pair propagates into the vacuum within the screened electron-electron Coulomb potential. Numerical results for a clean Cu crystal are analyzed for photon polarization parallel and perpendicular to the surface.
[S0163-1829(98)09439-9]

I. INTRODUCTION

Over the last few decades angular- and spin-resolved ultraviolet single-photoemission spectroscopy (ARUPS) emerged as a powerful and widely used method to investigate the electronic structure of crystalline materials.[1,2] This development has been driven by the growing demand for a detailed knowledge of technologically relevant physical properties of solids and their surfaces, e.g., catalytic reactions are mainly controlled by the electronic and geometric structure of surfaces.

Theoretical treatments of ARUPS are of special importance as they provide the linkage between the photocurrent measurements and the corresponding band structure.[1–3] A standard successful scheme for band-structure calculations relies on density-functional theory (DFT),[4] in which the electronic many-body problem is solved in a one-electron picture. *Spatially* uncoupled *single-particle* states are then determined self-consistently using an approximate expression for the exchange and correlation term.[5] Many aspects of the emission process are described within this single-particle picture, as a transition from an occupied one-electron orbital to a state describing the propagation of the photoelectron. The complicated many-body nature of the solid is then collectively subsumed in the screening and decay of the photoelectron, and the hole left behind. These screened, decaying quasiparticles can still be described by a single-particle wave equation. Experimental evidence for many-body effects shows up as subsidiary features in the photoelectron spectra.

In contrast, and as explicitly shown in the present work, a simultaneous two-orbital excitation by one photon is prohibited if *spatial* coupling between these orbitals is absent. Therefore, dealing with this process, the description of the electron-electron interaction must go beyond regarding it as a collective, spatially independent perturbation of the single-particle orbitals. Thus it seems worthwhile to employ double photoemission (DPE) as an investigative tool for strongly correlated systems, such as Mott insulators, ferromagnetic materials with *d* and *f* levels, and high-temperature superconductors. In fact, as shown in this paper, to some extent DPE can be regarded as single photoemission of a ''quasiparticle'' formed by the electron pair. In addition to the known features of ARUPS, the spectra of this photoemitted ''quasiparticle'' reveal a dependence on the pair's internal degree of freedom that characterizes the mutual interaction of the two emitted electrons. Therefore, DPE experiments are expected to provide a direct insight into the influence of electronic correlation on initial and final many-body states.

In atomic and molecular physics, the explicit dependence of DPE on the interelectronic correlation is well established.[6] The first experiment of this kind on a He($^1S^e$) target was performed in 1993,[7] followed by a series of experiments on different targets at a variety of scattering geometries.[8–12] The theoretical treatments stimulated by these experiments revealed the strong dependence of this reaction on the detail of mutual electronic coupling,[8,13,15,14,16] as well as on properties of the radiation field.[17,18] Very recently DPE from He($^1S^e$) with circularly polarized photons has been observed.[19,20]

DPE from Ni(001) and Cu(001) has just been reported.[21] Thus it is appropriate to consider DPE theoretically from solids and surfaces. Starting from the first-order perturbation theory and the dipole approximation for the photon field, a formal expression for the cross section of DPE is derived (transition rate normalized to the incoming photon-flux density). Subsequently, DPE from localized bulk states is studied and propensity rules are inferred. DPE from delocalized valence electrons is then investigated, and the selection rules in this case are discussed. Numerical examples for DPE from a clean Cu crystal are presented for *p* and *s* polarizations. Atomic units (a.u.) are used throughout.

II. THEORETICAL FRAMEWORK

For the derivation of the transition amplitude for simultaneous electron ejection, it is instructive to specify the properties of the radiation field. In what follows we assume a large photon density, so that the electromagnetic field can be treated classically (an upper limit for the photon density of concern here is given below). We operate in the Coulomb gauge, i.e., $\nabla\cdot\mathbf{A}=0$, so that, in vacuum, we can set $\Phi=0$, where **A** and Φ are the field vector and scalar potentials, respectively. It should be noted from the outset, however, that near a surface **A** may change rapidly which invalidates the assumption $\nabla\cdot\mathbf{A}=0$ unless the dielectric constant ϵ is unity.[22,23] To avoid this case the photon energies have to be well above the plasmon energies.[24] For **A** we assume a monochromatic, plane-wave solution with a wave vector **k**, which is related to the photon frequency ω via $k=\alpha\omega$, where α is the fine-structure constant. The energy density ρ of the (classical) radiation field averaged over the period $T=2\pi/\omega$ is given by $\rho=\omega^2A^2/(2\pi)$. Thus the energy-flux density, i.e., the intensity I, is given by $I=\rho/\alpha$. For a low-intensity field we can set $A^2\approx 0$ (for $A\approx 0.01$ and a photon energy of 50 eV we arrive at a maximum intensity $I\approx 5\times 10^{17}$ W/m^2). We assume the unperturbed system to be described by the Hamiltonian H, and to be in the stationary state $|i\rangle$ with energy ϵ_i, i.e.,

$$(H-\epsilon_i)|i\rangle=0. \tag{1}$$

Under the time-dependent action of the photon field the system performs, within a time lap τ, a transition into vacuum states $|f\rangle$ which lay within the interval β and $\beta+d\beta$, where β stands for collective quantum numbers that specify the final channel.

In a time-dependent first-order perturbation treatment (only photoabsorption is considered here), a transition probability dw_{if} can be derived.[25] Thus we can define a transition rate $dP_{if}=dw_{if}/\tau$ that can be deduced to

$$dP_{if}=(2\pi)^2\frac{I\alpha}{\omega^2}\sum_{\alpha_i}|\langle f|\tilde{W}_0|i\rangle|^2\delta(E_f-E_i)d\beta, \tag{2}$$

where E_f is the total energy in the final channel and $E_i=\omega+\epsilon_i$. Equation (2) sums over the unresolved quantum numbers α_i in the initial state. The perturbation $\tilde{W}_0$ in Eq. (2) amounts to

$$\tilde{W}_0=A\sum_{j=1}^{N}\exp[i(\mathbf{k}\cdot\mathbf{r}_j)]\hat{\mathbf{e}}\cdot\mathbf{p}_j, \tag{3}$$

where $\mathbf{p}_j$ are the one-particle momentum operators and $\hat{\mathbf{e}}$ is the polarization vector.

As the differential cross section $d\sigma/d\beta$ we define the transition rate normalized to the incoming flux density I/ω, i.e.,

$$d\sigma=\omega dP_{if}/I. \tag{4}$$

In this work we consider moderate photon energies (<500 eV), and we can thus operate within the dipole approximation. In this case Eq. (4) reduces to

$$d\sigma=4\pi^2\frac{\alpha}{\omega}\sum_{\alpha_i}|M_{fi}|^2\delta(E_i-E_f)d\beta, \tag{5}$$

where the dipole-matrix element is given by

$$M_{fi}=\sum_{j}^{N}\langle f|\hat{\mathbf{e}}\cdot\mathbf{p}_j|i\rangle. \tag{6}$$

By making use of the canonical commutation relations $-i[\mathbf{r}_j,H]=\mathbf{p}_j$, and assuming that $|i\rangle$ and $|f\rangle$ are eigenfunctions of the *same* Hamiltonian H, the *velocity form* Eq. (5) can be converted into the *length form*

$$d\sigma=4\pi^2\alpha\omega\sum_{\alpha_i}\left|\sum_{j}^{N}\langle f|\mathbf{r}_j|i\rangle\right|^2\delta(E_f-E_i)d\beta. \tag{7}$$

In practice, $|i\rangle$ and $|f\rangle$ are derived using different approximate procedures for H, and thus the velocity and length forms yield, in general, different predictions. Conversely, equivalent cross sections, calculated within the length and velocity forms, mean merely that the same approximations have been made in the initial and final channel, but they say, however nothing about the quality of these approximations. Nevertheless, it is desirable to choose $|i\rangle$ and $|f\rangle$ as eigenstates of the same (approximate) Hamiltonian to preclude spurious transitions in the absence of the perturbation $\tilde{W}_0$.

Regardless of the form in which the dipole operator is presented, its mathematical structure is always a sum of single-particle operators. This has the following important consequence: If we assume $|i\rangle$ and $|f\rangle$ to be written in terms of orthonormal single-particle orbitals $\phi_j(\mathbf{r}_j)$, in the simplest case as

$$\langle\mathbf{r}_1\cdots\mathbf{r}_N|i\rangle=\prod_{j}^{N}\phi_{i,j}(\mathbf{r}_j),$$

$$\langle\mathbf{r}_1\cdots\mathbf{r}_N|f\rangle=\prod_{j}^{N}\phi_{f,j}(\mathbf{r}_j), \tag{8}$$

then the matrix element (6) is finite for single-orbital excitation, only, e.g., single photoemission. In other words, DPE is prohibited in a single-particle picture. This is readily concluded in the simplest case of two orbital excitation ϕ_l,ϕ_k, which is the minimal requirement for DPE:

$$\begin{aligned}M_{fi}&=\langle\phi_{f,k}\phi_{f,l}|\hat{\mathbf{e}}\cdot\mathbf{p}_l|\phi_{i,k}\phi_{i,l}\rangle+\langle\phi_{f,k}\phi_{f,l}|\hat{\mathbf{e}}\cdot\mathbf{p}_k|\phi_{i,k}\phi_{i,l}\rangle\\&=\langle\phi_{f,k}|\phi_{i,k}\rangle\langle\phi_{f,l}|\hat{\mathbf{e}}\cdot\mathbf{p}_l|\phi_{i,l}\rangle\\&\quad+\langle\phi_{f,l}|\phi_{i,l}\rangle\langle\phi_{f,k}|\hat{\mathbf{e}}\cdot\mathbf{p}_k|\phi_{i,k}\rangle\\&=\delta_{i,f}(\langle\phi_{f,k}|\hat{\mathbf{e}}\cdot\mathbf{p}_k|\phi_{i,k}\rangle+\langle\phi_{f,l}|\hat{\mathbf{e}}\cdot\mathbf{p}_l|\phi_{i,l}\rangle),\end{aligned} \tag{9}$$

where $\phi_{i,k},\phi_{i,l}$ ($\phi_{f,k},\phi_{f,l}$) are the participating single particle orbitals in the initial (final) channel. From Eq. (9) it follows that DPE is a direct signature of coupling between single-particle orbitals, at least those of the electrons simultaneously detected in the final state, i.e., the two photoelectrons must be correlated in initial and/or final state. This conclusion is also valid for an antisymmetrized product of spatially independent single-particle orbitals. It should be stressed that Eq. (9) and the single-particle nature of the perturbation [Eq. (3)] do not mean that the photon can only be absorbed by one electron, and the other electron is emitted by means of coupling or inelastic scattering with the former one. To see this, let us assume the holes created by the process to be long lived on the scale of the characteristic interaction time τ and neglect any phonon excitation. In this case a frozen-core approximation is appropriate. In addition, if the photoelectrons are represented by the correlated initial (final) state $\psi_i(\mathbf{r}_l,\mathbf{r}_k)$ $[\psi_f(\mathbf{r}_l,\mathbf{r}_k)]$ we can always canonically transform to the coordinate system $\mathbf{r}^+=(\mathbf{r}_l+\mathbf{r}_k)/2$, $\mathbf{r}^-=\mathbf{r}_l-\mathbf{r}_k$. In this case the photoabsorption matrix element (6) takes on the (length) form $M_{fi}=\langle\psi_f(\mathbf{r}^+,\mathbf{r}^-)|\hat{\mathbf{e}}\cdot\mathbf{r}^+|\psi_i(\mathbf{r}^+,\mathbf{r}^-)\rangle/2$ which means that the photon is absorbed by the center-of-mass coordinate $\mathbf{r}^+$ of the two-electron system. This *simultaneous* photoabsorption is fundamentally distinct from the process of single photoemission accompanied by secondary vacuum-electron creation.

III. DOUBLE PHOTOEMISSION FROM LOCALIZED ELECTRONIC STATES

In the rest of this work we assume a frozen-core approximation, i.e., only the degrees of freedom of the two emitted electrons are affected by the photoabsorption process. To obtain an insight into the structure of the matrix element M_{fi}, we consider first the DPE of localized electrons, e.g., core electronic states or valence-band electrons of insulators. The initial state can then be described by a tight-binding two-electron wave function, whereas the vacuum motion of the electrons is assumed to be free and characterized by the momenta $\mathbf{k}_a$ and $\mathbf{k}_b$, as measured in a coincidence experiment (uncorrelated final-state Bloch waves lead basically to the same conclusion). Equation (6) can be written in the form

$$\begin{aligned}M_{fi}(\mathbf{k}_a,\mathbf{k}_b)=C\sum_l\int\int d^3\mathbf{r}_a d^3\mathbf{r}_b\\ \times\exp(-i\mathbf{k}_a\cdot\mathbf{r}_a-i\mathbf{k}_b\cdot\mathbf{r}_b)\exp[i(\mathbf{k}'_a+\mathbf{k}'_b)\cdot\mathbf{R}_l]\\ \times[\hat{\mathbf{e}}\cdot(\mathbf{p}_a+\mathbf{p}_b)]\phi_i(\mathbf{r}_a-\mathbf{R}_l,\mathbf{r}_b-\mathbf{R}_l).\qquad(10)\end{aligned}$$

where $\mathbf{R}_l$ designates the core sites, and ϕ_i describes the localized two-electron initial state with Bloch wave vectors $\mathbf{k}'_a$ and $\mathbf{k}'_b$. The constant C derives from the normalization of the initial- and final-state wave functions. After some elementary manipulation the magnitude of $M_{fi}(\mathbf{k}_a,\mathbf{k}_b)$ is reduced to

$$|M_{fi}|^2=|C|^2\delta^{(3)}_{(\mathbf{q}_i-\mathbf{q}_f,\mathbf{G})}|M_{fi}^{atom}|^2,\qquad(11)$$

where $\mathbf{q}_i=\mathbf{k}'_a+\mathbf{k}'_b,\mathbf{q}_f=\mathbf{k}_a+\mathbf{k}_b$ are the wave vectors of the pair's center of mass in the initial and final states, respectively, and $\mathbf{G}$ is a bulk reciprocal-lattice vector. The atomic matrix element M_{fi}^{atom} is given by

$$\begin{aligned}M_{fi}^{atom}(\mathbf{k}_a,\mathbf{k}_b)=\int\int d^3\mathbf{r}\,d^3\mathbf{r}'\exp(-i\mathbf{k}_a\cdot\mathbf{r}-i\mathbf{k}_b\cdot\mathbf{r}')\\ \times[\hat{\mathbf{e}}\cdot(\mathbf{p}_a+\mathbf{p}_b)]\phi_i(\mathbf{r},\mathbf{r}').\qquad(12)\end{aligned}$$

In momentum-space representation

$$\begin{aligned}M_{fi}^{atom}(\mathbf{k}_a,\mathbf{k}_b)=\int\int d^3\mathbf{p}\,d^3\mathbf{p}'\langle\mathbf{k}_a,\mathbf{k}_b|\hat{\mathbf{e}}(\mathbf{p}_a+\mathbf{p}_b)|\mathbf{p},\mathbf{p}'\rangle\\ \times\langle\mathbf{p},\mathbf{p}'|\phi_i\rangle\\ =\hat{\mathbf{e}}\cdot(\mathbf{k}_a+\mathbf{k}_b)\tilde{\phi}_i(\mathbf{k}_a,\mathbf{k}_b).\qquad(13)\end{aligned}$$

In Eq. (13) $|\mathbf{p},\mathbf{p}'\rangle$ denotes a complete set of plane waves, and $\tilde{\phi}_i(\mathbf{k}_a,\mathbf{k}_b)$ is the double Fourier transform of the initial state. Note that Eqs. (12) and (13) do not factorize in single-particle contributions due to the correlated state $\phi_i(\mathbf{r},\mathbf{r}')$. From Eqs. (11)–(13), three important conclusions are drawn.

(a) According to the von Laue-like conditions in Eq. (11), diffraction of the pair occurs when the center-of-mass momentum of the pair changes by a reciprocal bulk vector due to the emission process. This (and the selection rules stated below) is equivalent to assuming the pair as a quasiparticle with momentum $\mathbf{k}_a+\mathbf{k}_b$ (the pair's center-of-mass momentum) and performing single photoemission of this quasiparticle.

(b) The selection rules for M_{fi}^{atom} can be summarized in the equation $\hat{\mathbf{e}}\cdot(\mathbf{k}_a+\mathbf{k}_b)=0$, i.e., double photoemission is forbidden if the momentum of the two-electron center of mass is perpendicular to the polarization vector $\hat{\mathbf{e}}$ or if $\mathbf{k}_a=-\mathbf{k}_b$. In addition the structure of $\tilde{\phi}_i(\mathbf{k}_a,\mathbf{k}_b)$, which is very much dependent on the symmetry of the investigated core level, imposes additional restrictions on the DPE spectra. These conclusions remain valid if we allow for mutual repulsion of the outgoing electrons, but disregard the final-channel coupling to the cores. This can be deduced in a similar manner as in Eq. (22). In cases where the motion of the vacuum electrons is influenced by the core potentials, atomic selection rules for the double photoionization applies.[13,16,17]

(c) If the magnetic sublevels of the two-electron orbital ϕ_i are statistically populated (which is usually the case), then $|M_{fi}|^2$, and hence the cross section, shows in general a *circular dichroism* with respect to inversion of the helicity of the incoming radiation. This is readily deduced from the analysis performed in Refs. 17 and 18. Note that, in the absence of a preferential orientation of the initial state and a spin analysis of the photoelectrons, as assumed in this work, the aforementioned dichroism vanishes identically for single photoemission.[18]

IV. DOUBLE PHOTOEMISSION OF DELOCALIZED ELECTRONIC STATES

In this section we consider double photoemission from *s-p* bonded (simple) metal surfaces like Na and Al. In this case the cores scatter the conduction-band electrons only weakly. The momentum distribution of the conduction-band electrons can then, to a good approximation, be simulated by jellium states. In the jellium model the ionic cores are smeared to a uniform constant positive ‘‘background charge.’’ The electrons are bound to the metal half-space $(z<0)$ by the step-potential barrier V_0 (at $z=0$)

$$V_0=\epsilon_F+W,\qquad(14)$$

where ϵ_F is the Fermi energy and W is the work function. Within the metal volume V the conduction-band electrons are treated as free particles. The density of states ρ_{DOS} is given by that of the free-electron gas (apart from a factor 2 due to electronic spin states) $\rho_{DOS}=V/(4\pi^3)$. As the binding potential V_0 is steplike, the single-particle jellium wave function $\phi_{\epsilon_j(\mathbf{k}'_j),\mathbf{k}'_j}(\mathbf{r}_j)$, with binding energy $\epsilon_j(\mathbf{k}'_j)$ and wave vector $\mathbf{k}'_j$, can be represented in terms of reflection and transmission coefficients:

$$\phi_{\epsilon_j(\mathbf{k}'_j),\mathbf{k}'_j}(\mathbf{r}_j)=\frac{1}{\sqrt{V}}\exp(i\mathbf{k}'_{j,\parallel}\cdot\mathbf{r}_{j,\parallel}) \times\begin{cases} e^{i\mathbf{k}'_{j,z}z_j}+\mathrm{R}e^{-i\mathbf{k}'_{j,z}z_j} & z<0,\\ Te^{-\gamma z_j} & z>0,\end{cases} \tag{15}$$

where $\mathbf{k}'_{j,z}$ and z_j are, respectively, the components of $\mathbf{k}'_j,\mathbf{r}_j$ with respect to the normal of the surface (pointing into the vacuum), and $\mathbf{k}'_{j,\parallel},\mathbf{r}_{j,\parallel}$ are the corresponding components parallel to the surface. The reflection and transmission coefficients R and T are given by

$$R=\frac{\mathbf{k}'_{j,z}-i\gamma}{\mathbf{k}'_{j,z}+i\gamma},\quad T=\frac{2\mathbf{k}'_{j,z}}{\mathbf{k}'_{j,z}+i\gamma} \tag{16}$$

and $\gamma=\sqrt{2V_0-\mathbf{k}'^2_j}$.

As in the jellium model the electrons are considered to be quasifree, for the two-electron initial state $|i\rangle$ we employ a (singlet) symmetrized direct product of two jellium single-particle states, i.e.,

$$|\psi_{\epsilon_i;\mathbf{k}'_a,\mathbf{k}'_b}(\mathbf{r}_a,\mathbf{r}_b)\rangle\approx\frac{1}{\sqrt{2}}[|\phi_{\epsilon_a,\mathbf{k}'_a}(\mathbf{r}_a)\rangle\otimes|\phi_{\epsilon_b,\mathbf{k}'_b}(\mathbf{r}_b)\rangle +|\phi_{\epsilon_a,\mathbf{k}'_a}(\mathbf{r}_b)\rangle\otimes|\phi_{\epsilon_b,\mathbf{k}'_b}(\mathbf{r}_a)\rangle]. \tag{17}$$

The total binding energy ϵ_i of this state is $\epsilon_i=\epsilon_a(\mathbf{k}'_a)+\epsilon_b(\mathbf{k}'_b)$ with parabolic dispersion for the *single* particle states. State (17) is energetically favored with respect to its antisymmetric (triplet) counterpart.

As the initial state [Eq. (17)] does not contain any interelectronic coupling, it is essential to incorporate the interelectronic interaction in the final state. To this end we note that the asymptotic two-electron vacuum state $|\mathbf{k}_a,\mathbf{k}_b\rangle$, that is defined by the measured momenta $\mathbf{k}_a$ and $\mathbf{k}_b$, where $E_f=E_a+E_b$ and $E_a=k_a^2/2$, $E_b=k_b^2/2$ are the electrons' energies, is an eigenstate of the two-electron kinetic-energy operator K, i.e.,

$$K|\mathbf{k}_a,\mathbf{k}_b\rangle=\tfrac{1}{2}(\mathbf{p}_a^2+\mathbf{p}_b^2)|\mathbf{k}_a,\mathbf{k}_b\rangle=E_f|\mathbf{k}_a,\mathbf{k}_b\rangle. \tag{18}$$

The final state $|f\rangle$ is then obtained by the time-reversed evolution (back to the time of absorption) mediated by the Møller operator $\Omega^-=(1+G^-V)$,[26] i.e.,

$$|f\rangle=[1+G^-(H-K)]|\mathbf{k}_a,\mathbf{k}_b\rangle=(1+G^-V)|\mathbf{k}_a,\mathbf{k}_b\rangle, \tag{19}$$

where G^- is the resolvant (Green operator) of total Hamiltonian H which satisfies the Dyson equation

$$G^-=G_0^-+G_0^-VG^-, \tag{20}$$

and G_0 is the Green operator of the noninteracting system (with outgoing wave boundary conditions). Contrasting the state vector (19) with that used in single photoemission,[1] it can be said that $|f\rangle$ is the time-reversed low-energy electron-diffraction (LEED) state of the coupled electron pair.[24]

From Eqs. (19) and (20), it is evident that, after absorption of the photon, the two electrons interact with all degrees of freedom of the system, described by H (such as diffraction from the lattice, elastic, and inelastic collisions and collective excitations) before emerging with the asymptotic momenta $\mathbf{k}_a$ and $\mathbf{k}_b$. These interactions are basically contained in the complex two-particle self-energy V that appears in Eqs. (20) and (19).[3,27,28] The non-Hermitian character of V accounts for damping processes of the photoelectron flux and energetic shifts in the quasi-particle spectrum. Considering the difficulties encountered in adequately estimating the *single*-particle self energy,[3] it is obvious that calculating the two-particle self-energy is a very delicate problem. Hence, we replace it in the rest of this work by the (real) potential. In addition, as the electron-electron interaction V_{ee} is inevitable for coherent DPE we regard this interaction as the ''strong'' potential with respect to the surface-photoelectron coupling, i.e., we employ the approximation $V\approx V_{ee}$. For V_{ee} we assume a screened Coulomb potential, with the screening constant derived from the Thomas-Fermi model.[29] Under these circumstances Eq. (19) reduces to

$$|f\rangle\approx(1+G_{ee}^-V_{ee})|\mathbf{k}_a,\mathbf{k}_b\rangle, \tag{21}$$

with G_{ee}^- being the propogator within the potential V_{ee}. With Eqs. (21) and (17), we can now obtain an estimate of the transition probability M_{fi}, given by Eq. (6). Since V_{ee} and G_{ee} are dependent on interelectronic degrees of freedom only, properties of M_{fi} are most transparent in the representation $\mathbf{r}^+\otimes\mathbf{r}^-$ that, as previously mentioned, can be canonically mapped onto $\mathbf{r}_a\otimes\mathbf{r}_b$ $[\mathbf{r}^+=(\mathbf{r}_a+\mathbf{r}_b)/2,\mathbf{r}^-=\mathbf{r}_a-\mathbf{r}_b]$. Equation (6) reads

$$\begin{aligned} M_{fi}(\mathbf{k}^-,\mathbf{k}^+)&=\int\int d^3\mathbf{q}^-d^3\mathbf{q}^+\langle\mathbf{k}^-,\mathbf{k}^+|(1+V_{ee}G_{ee}^+)(\hat{\mathbf{e}}\cdot\mathbf{p}^+)|\mathbf{q}^-,\mathbf{q}^+\rangle\langle\mathbf{q}^-,\mathbf{q}^+|\psi\rangle\\ &=\hat{\mathbf{e}}\cdot\mathbf{k}^+\left[\tilde{\psi}(\mathbf{k}^+,\mathbf{k}^-)+\int d^3\mathbf{q}^-\langle\mathbf{k}^-|V_{ee}G_{ee}^+|\mathbf{q}^-\rangle\langle\mathbf{q}^-,\mathbf{k}^+|\psi\rangle\right], \end{aligned} \tag{22}$$

where $\mathbf{k}^-=(\mathbf{k}_a-\mathbf{k}_b)/2$, $\mathbf{k}^+=\mathbf{k}_a+\mathbf{k}_b$, and $|\mathbf{q}^-,\mathbf{q}^+\rangle$ is a complete set in the space reciprocal to $\mathbf{r}^+\otimes\mathbf{r}^-$.

According to Eq. (22) the propensity rules $\hat{\mathbf{e}}\cdot\mathbf{k}^{+}=0$, as discussed in Sec. III, apply. As it is clear from the derivation of Eq. (22) these rules do not depend on the structure of the initially bound state $|\psi\rangle$. They are rather an immediate consequence of the approximation made to arrive at Eq. (21).

V. CALCULATION OF THE DIPOLE-MATRIX ELEMENT

In spite of the simple analytical structure of the wave function (17), the evaluation of the transition amplitude (22) is mathematically involved and, till now, only possible within the approximation $G_{ee}^{+}\approx G_{0}^{+}$, i.e., in LEED language, within the kinematical approximation.[30] The derivation of M_{fi} is presented in the Appendix. The final result can be written as

$$M_{fi}(\mathbf{k}_a,\mathbf{k}_b)=\langle\mathbf{k}_a,\mathbf{k}_b|(1+V_{ee}G_0^{+})[\hat{\mathbf{e}}\cdot(\mathbf{p}_a+\mathbf{p}_b)]|\psi_{\epsilon_i}\rangle=T_{\mathrm{spe}}+T_{\mathrm{dpe}}, \tag{23}$$

where

$$\begin{aligned}T_{\mathrm{spe}}&=\langle\mathbf{k}_a,\mathbf{k}_b|\hat{\mathbf{e}}\cdot(\mathbf{p}_a+\mathbf{p}_b)|\psi_{\epsilon_i}\rangle\\&=-(\hat{\mathbf{e}}\cdot\mathbf{k}_a+\hat{\mathbf{e}}\cdot\mathbf{k}_b)\,\delta^{(2)}(\mathbf{k}'_{a,\parallel}-\mathbf{k}_{a,\parallel})\,\delta^{(2)}(\mathbf{k}'_{b,\parallel}-\mathbf{k}_{b,\parallel})\frac{\pi\sqrt{2}}{V}[L_{\mathbf{k}'_a}(\mathbf{k}_a)L_{\mathbf{k}'_b}(\mathbf{k}_b)+L_{\mathbf{k}'_b}(\mathbf{k}_a)L_{\mathbf{k}'_a}(\mathbf{k}_b)]\end{aligned} \tag{24}$$

and

$$\begin{aligned}T_{\mathrm{dpe}}&=\langle\mathbf{k}_a,\mathbf{k}_b|V_{ee}G_0^{+}[\hat{\mathbf{e}}\cdot(\mathbf{p}_a+\mathbf{p}_b)]|\psi_{\epsilon_i}\rangle\\&=\hat{\mathbf{e}}\cdot(\mathbf{k}_a+\mathbf{k}_b)\,\delta^{(2)}[(\mathbf{k}'_{a,\parallel}+\mathbf{k}'_{b,\parallel})-(\mathbf{k}_{a,\parallel}+\mathbf{k}_{b,\parallel})]\frac{1}{\sqrt{8}\pi V}[I(\epsilon_a,\mathbf{k}'_a,\epsilon_b,\mathbf{k}'_b;\mathbf{k}_a,\mathbf{k}_b)+I(\epsilon_b,\mathbf{k}'_b,\epsilon_a,\mathbf{k}'_a;\mathbf{k}_a,\mathbf{k}_b)].\end{aligned} \tag{25}$$

The functions $I(\epsilon_a,\mathbf{k}'_a,\epsilon_b,\mathbf{k}'_b;\mathbf{k}_a,\mathbf{k}_b)$ and $L_{\mathbf{k}'_j}(\mathbf{k}_j)$, $j=a,b$, are given by Eqs. (A9) and (A4), respectively. Equations (24) and (25) reflect the basic difference between single and simultaneous double photoemission: Term (24) contains no final-state correlation of the pairs. The DPE is then regarded as two independent single photoemission processes. Consequently, the surface components of the wave vectors of the *individual* electrons is conserved during the ejection, and for each absorption process the selection rules for the single photoemission apply. In contrast, as a result of including electronic correlation in Eq. (25) only the surface component of the pair's center-of-mass wave vector is invariant during the reaction. Under this constraint the surface components of the wave vectors of the individual electrons may well not be conserved (due to momentum exchange). As mentioned in the preceding sections, the amplitude [Eq. (24)] must vanish, for initial- and final-state electronic correlation are disregarded. In fact extensive numerical calculations have shown that $|T_{\mathrm{spe}}|$ is negligible with respect to $|T_{\mathrm{dpe}}|$ (typically six order of magnitudes smaller).

Double emission probabilities

In a recent double photoemission experiment[21] on Cu(001) and Ni(001), the coincidence rate has been measured as function of $\mathbf{k}_a$, $\mathbf{k}_b$, and ω. The Bloch wave vectors of the initially bound electronic states were not specified [actually a Bloch wave vector of the electron pair is a more appropriate designation of these states (cf. Eq. (25)]. Thus, Eq. (5) yields

$$\begin{aligned}d\sigma=4\pi^2\frac{\alpha}{\omega}\int\int d^3\mathbf{k}'_a d^3\mathbf{k}'_b\rho(\mathbf{k}'_{\mathbf{a}})\\\times F(\mathbf{k}'_{\mathbf{a}},T)\rho(\mathbf{k}'_{\mathbf{b}})F(\mathbf{k}'_{\mathbf{b}},T)|M_{fi}|^2\delta(E_i-E_f)\\\times d^3\mathbf{k}_b d^3\mathbf{k}_a d^3\mathbf{k}_{\mathrm{rec}},\end{aligned} \tag{26}$$

where $\mathbf{k}_{\mathrm{rec}}$ is related to the recoil momentum of the crystal (free electrons cannot absorb the photon). The one-particle density of states at the temperature T is referred to as $\rho(\mathbf{k}'_j), j=a,b$, and $F(\mathbf{k}'_j,T)$ is the Fermi distribution. The initial total energy E_i can be estimated assuming the conduction band of the pair as being formed of independent bands of the single electrons, i.e., $E_i=\omega-2W-\epsilon_a(\mathbf{k}'_{\mathbf{a}})-\epsilon_b(\mathbf{k}'_{\mathbf{b}})$. (In contrast to atomic systems, this approximation is reasonable due to the collective screening of the electron-electron interaction). In Eq. (26) the dependence of σ on $\mathbf{k}_{\mathrm{rec}}$ is fixed by the conservation of linear momentum.

For the approximate initial state [Eq. (17)] which leads to the matrix element (23) and at $T=0$, Eq. (26) simplifies to

$$d\sigma=\frac{V^2\alpha}{4\pi^4\omega}\left[\int_{k'_a\leqslant k_F}\int_{k'_b\leqslant k_F}d^3\mathbf{k}'_{\mathbf{a}}d^3\mathbf{k}'_{\mathbf{b}}|M_{fi}|^2\times\delta(E_i-E_f)\right]d^3\mathbf{k}_b d^3\mathbf{k}_a, \tag{27}$$

where k_F is the Fermi momentum for the single-particle band. The six-dimensional integral in Eq. (27) can be analytically reduced to three-dimensional ones that have been performed numerically.

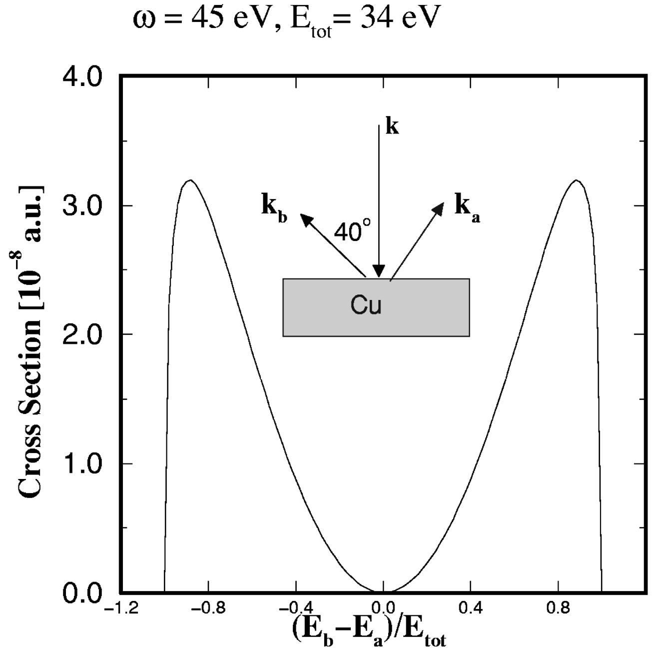

FIG. 1. The double-photoemission cross section [Eq. (27)] as function of the energy sharing of two electrons emitted from a clean Cu monocrystal upon the absorption of a linearly polarized photon. The photon's wave vector **k** is normal to the surface, whereas the electron detectors are fixed at 40° to the left and right of **k** (see the inset). The photon incident energy is $\omega = 45$ eV, and the total excess energy of the pair is chosen as $E_{\mathrm{tot}} = E_a + E_b = 34$ eV.

Employing Eq. (27), we consider the energy sharing of the two-photoelectron pair emitted from Cu(001) for *s*-photon polarization (see the inset in Fig. 1). As the electron detectors have the same relative angles with respect to the wave vector of the photons (the inset in Fig. 1), the vector momentum of the pair $\mathbf{k}_a + \mathbf{k}_b$ is perpendicular to the surface, and hence to the polarization vector, for equal-energy electrons. Consequently, double photoemission is forbidden for $k_a = k_b$, as is obvious from Eq. (25). The corresponding experiment[21] shows an evident decrease of the cross section at $k_a = k_b$. However, these data cannot be directly compared with the predictions of Fig. 1, since another competing channel for the double emission is not considered here, namely, that of single photoelectron emission followed by electron-electron inelastic collision. In contrast to gaseous targets, like in atomic physics, this channel is expected to be quite strong for metallic samples due to the much higher density of the active electrons.

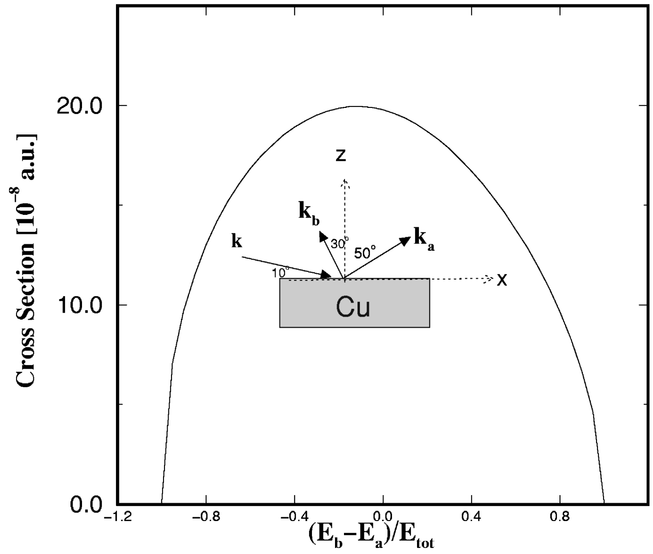

FIG. 2. Same energies as Fig. 1; however, as demonstrated by the inset, the photon beam is now in grazing incidence (10° with respect to the surface). One of the electron detectors (say detector *a*) is fixed right to the surface normal at an angle of 50°, whereas the other detector is positioned left the surface normal at an angle of 30°. The coordinate system and the geometry are sketched in the inset.

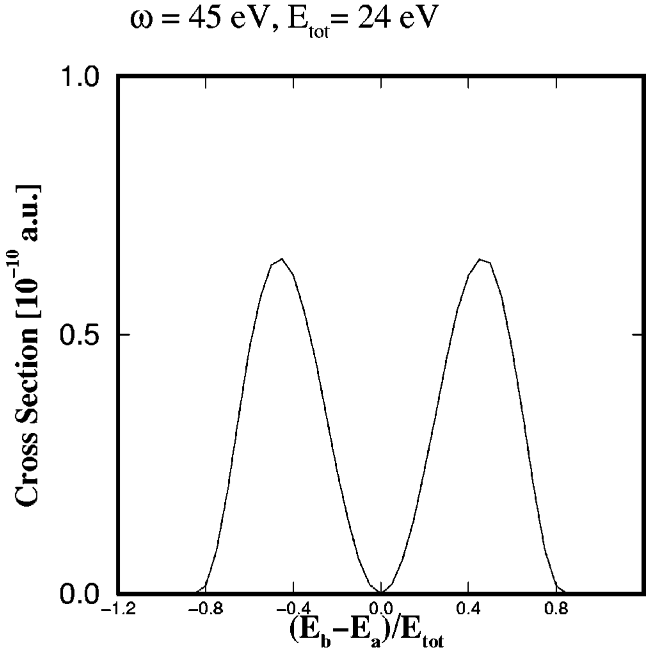

FIG. 3. Same geometry as in Fig. 1, with the same incident photon energy; however, the total excess energy of the pair is lowered to $E_{\mathrm{tot}} = 24$ eV.

In the second example we consider the case of Fig. 1 for grazing photon incidence, i.e., for nearly *p* polarization. As is evident from Eq. (25), the factor $\hat{\mathbf{e}} \cdot (\mathbf{k}_a + \mathbf{k}_b)$ implies a maximum intensity when the center-of-mass momentum is parallel to the polarization vector, which is clearly confirmed by Fig. 2.

For the two-electron band, we define a Fermi energy $E_F = 2\epsilon_F$. In Fig. 1, the double emission occurred from states just below E_F. For double emission from the bottom of the two-electron band, we observe a squeezing of the distribution toward equal energy sharing, as seen in Fig. 3. This effect has also been experimentally observed. Till now I have no profound explanation for this trend that also showed up in equivalent calculations for Al and Ni targets.

VI. CONCLUSION

In this work a theory has been presented for the treatment of one-photon–two-electron excitation from solids and surfaces. It has been argued that this process is a footprint of electron-electron coupling in the final and/or initial state.

From the mathematical analysis, it has been inferred that the pairs' spectra are subject to certain selection rules that lead to vanishing emission intensity when the vector momentum of the pair is perpendicular to the polarization vector. In addition, it has been shown that the excited pair undergoes a diffraction from the lattice when their center-of-mass vector momentum changes by multiples of a reciprocal vector. Starting from single-particle jellium states for the delocalized conduction electrons, the optical transition amplitude has been derived analytically. Numerical examples for clean Cu crystal have been presented.

ACKNOWLEDGMENTS

I am indebted to Professor J. Kirschner, Ralf Herrmann, and Serguei Samarin for many enlightening discussions and suggestions.

APPENDIX: ANALYTICAL EVALUATION OF DIPOLE-TRANSITION AMPLITUDE

In this appendix I derive an expression for the transition amplitude M_{fi} [Eq. (6)] using the approximate initial and final states, given by Eqs. (17) and (21), respectively. For the electron-electron interaction V_{ee} I assume a screened Coulomb potential with a screening constant λ, i.e.,

$$V_{ee}=\frac{\exp(-\lambda|\mathbf{r}_a-\mathbf{r}_b|)}{|\mathbf{r}_a-\mathbf{r}_b|}. \tag{A1}$$

Upon inserting a complete set of plane waves $|\mathbf{q}_1,\mathbf{q}_2\rangle$, M_{fi} can be written in the form

$$\begin{aligned}M_{fi}(\mathbf{k}_a,\mathbf{k}_b)&=\int\int d^3\mathbf{q}_1 d^3\mathbf{q}_2\langle\mathbf{k}_a,\mathbf{k}_b|(1+V_{ee}G_{ee}^{+})\\&\quad\times[\hat{\mathbf{e}}\cdot(\mathbf{p}_a+\mathbf{p}_b)]|\mathbf{q}_1,\mathbf{q}_2\rangle\langle\mathbf{q}_1,\mathbf{q}_2|\psi_{\epsilon_i}\rangle\\&=\hat{\mathbf{e}}\cdot(\mathbf{k}_a+\mathbf{k}_b)\tilde{\psi}(\mathbf{k}_a,\mathbf{k}_b)+M_{fi}^{ab}+M_{fi}^{ba},\end{aligned} \tag{A2}$$

where the double Fourier transform $\tilde{\psi}(\mathbf{k}_a,\mathbf{k}_b)$ is easily constructed from the Fourier transform of the single-particle jellium wave functions $\tilde{\phi}(\mathbf{k}_j), j=a,b$,

$$\tilde{\phi}_{\mathbf{k}'_j}(\mathbf{k}_j)=i\sqrt{\frac{2\pi}{V}}\delta^{(2)}(\mathbf{k}'_{j\parallel}-\mathbf{k}_{j\parallel})L_{\mathbf{k}'_j}(\mathbf{k}_j), \tag{A3}$$

where

$$L_{\mathbf{k}'_j}(\mathbf{k}_j)=\left(\frac{1}{\mathbf{k}_{j,z}-\mathbf{k}'_{j,z}+i\delta}+\frac{R_j}{\mathbf{k}_{j,z}+\mathbf{k}'_{j,z}+i\delta}-\frac{T_j}{\mathbf{k}_{j,z}-i\gamma_j}\right). \tag{A4}$$

The infinitesimal real variable $\delta>0$ has been introduced to account for the finite extension of the surface in the direction $z<0$, and can be set to zero (infinite extension) in the final result. Formally, the first term in expression (A2) should vanish, since initial and final states are combinations of independent single-particle states. In fact, numerical investigations have shown that magnitude of this term is negligibly small with respect to the terms $|M_{fi}^{mn}|;\ m,n=a,b$.

The terms $|M_{fi}^{mn}|;\ m\neq n\in\{a,b\}$ are defined as

$$M_{fi}^{mn}=\frac{1}{\sqrt{2}}\int\int d^3\mathbf{q}_1 d^3\mathbf{q}_2\langle\mathbf{k}_a,\mathbf{k}_b|V_{ee}G_{ee}^{+}[\hat{\mathbf{e}}\cdot(\mathbf{p}_a+\mathbf{p}_b)]|\mathbf{q}_1,\mathbf{q}_2\rangle\tilde{\phi}_{\epsilon_m,\mathbf{k}'_m}(\mathbf{q}_1)\tilde{\phi}_{\epsilon_n,\mathbf{k}'_n}(\mathbf{q}_2);m\neq n\in\{a,b\}. \tag{A5}$$

The two-body Green operator G_{ee}^{+} satisfies an interative integral equation similar to Eq. (20) with V being replaced by V_{ee}. That is, in a perturbative sense, the interelectronic interaction is taken into account to infinite order. Unfortunately, it has not yet been possible to evaluate Eq. (A5) with the full G_{ee}^{+}. Thus we replace G_{ee}^{+} by the free Green operator G_0^{+}, and V_{ee} is treated to first order [this approximation is less severe than in atomic and molecular reactions since the potential (A1) is screened]. The expressions (A5) are obtained from the integral

$$\begin{aligned}J&=\int\int d^3\mathbf{q}_1 d^3\mathbf{q}_2\langle\mathbf{k}_a,\mathbf{k}_b|V_{ee}G_0^{+}(\hat{\mathbf{e}}\cdot\mathbf{p}_a)|\mathbf{q}_1,\mathbf{q}_2\rangle\tilde{\phi}_{\epsilon_a,\mathbf{k}'_a}(\mathbf{q}_1)\tilde{\phi}_{\epsilon_b,\mathbf{k}'_b}(\mathbf{q}_2)\\&=\lim_{\eta\to 0^+}\int\int d^3\mathbf{q}_1 d^3\mathbf{q}_2(\hat{\mathbf{e}}\cdot\mathbf{q}_1)\langle\mathbf{k}_a,\mathbf{k}_b|V_{ee}|\mathbf{q}_1,\mathbf{q}_2\rangle\frac{\tilde{\phi}_{\epsilon_a,\mathbf{k}'_a}(\mathbf{q}_1)\tilde{\phi}_{\epsilon_b,\mathbf{k}'_b}(\mathbf{q}_2)}{k_a^2+k_b^2-q_1^2-q_2^2-i\eta}\\&=\frac{\lim_{\eta\to 0^+}}{2\pi^2}\int\int d^3\mathbf{q}_1 d^3\mathbf{q}_2(\hat{\mathbf{e}}\cdot\mathbf{q}_1)[(\mathbf{q}_2-\mathbf{k}_b)^2+\lambda^2]^{-1}(k_a^2+k_b^2-q_1^2-q_2^2-i\eta)^{-1}\\&\quad\times\tilde{\phi}_{\epsilon_a,\mathbf{k}'_a}(\mathbf{q}_1)\tilde{\phi}_{\epsilon_b,\mathbf{k}'_b}(\mathbf{q}_2)\delta^{(3)}(\mathbf{q}_1+\mathbf{q}^2-\mathbf{k}_a-\mathbf{k}_b).\end{aligned} \tag{A6}$$

Writing $\hat{\mathbf{e}}\cdot\mathbf{q}_1=-i\lim_{\beta\to 0}\partial_\beta\exp(i\beta\hat{\mathbf{e}}\cdot\mathbf{q}_1)$, and using the δ function to perform one of the integration, Eq. (A6) reduces to

$$J=\frac{\lim_{\eta,\beta\to 0^+}}{i2\pi^2}\partial_\beta\int d^3\mathbf{q}[(\mathbf{q}_2-\mathbf{k}_b)^2+\lambda^2]^{-1}[-2q^2-2\mathbf{k}_a\cdot\mathbf{k}_b+2\mathbf{q}\cdot(\mathbf{k}_a+\mathbf{k}_b)-i\eta]^{-1}\tilde{\phi}_{\epsilon_a,\mathbf{k}'_a}(\mathbf{q})\tilde{\phi}_{\epsilon_b,\mathbf{k}'_b}(\mathbf{\Lambda})\exp(i\beta\hat{\mathbf{e}}\cdot\mathbf{q}_1), \tag{A7}$$

where $\Lambda:=\mathbf{k}_a+\mathbf{k}_b-\mathbf{q}$. Making use of Eq. (A3), and upon some elementary algebraic manipulation, Eq. (A7) is transformed to the one-dimensional integral on the real axis:

$$J=\frac{\lim_{\eta,\beta,\delta\to 0^+}}{i2\pi V}\partial_\beta[\exp(i\beta\hat{\mathbf{e}}_\parallel\cdot\mathbf{k}'_{a,\parallel})\,\delta^{(2)}(\mathbf{k}'_{a,\parallel}+\mathbf{k}'_{b,\parallel}-\mathbf{k}_{a,\parallel}+\mathbf{k}_{b,\parallel})I]. \tag{A8}$$

The integral I can be written as the sum of nine one-dimensional integrals

$$I(\epsilon_a,\mathbf{k}'_a,\epsilon_b,\mathbf{k}'_b;\mathbf{k}_a,\mathbf{k}_b)\coloneqq\sum_{j=1}^{9}\int_{-\infty}^{\infty}d\mathbf{q}_z II_j(q_z,\epsilon_a,\mathbf{k}'_a,\epsilon_b,\mathbf{k}'_b;\mathbf{k}_a,\mathbf{k}_b), \tag{A9}$$

where

$$II_1=\exp(i\beta\hat{\mathbf{e}}_z q_z)A^{-1}(q_z)B^{-1}(q_z)(q_z-k'_{a,z}+i\delta)^{-1}(q_z-k_{a,z}-k_{b,z}+k'_{b,z}-i\delta)^{-1}, \tag{A10}$$

$$II_2=R_b\exp(i\beta\hat{\mathbf{e}}_z q_z)A^{-1}(q_z)B^{-1}(q_z)(q_z-k'_{a,z}+i\delta)^{-1}(q_z-k_{a,z}-k_{b,z}-k'_{b,z}-i\delta)^{-1}, \tag{A11}$$

$$II_3=-T_b\exp(i\beta\hat{\mathbf{e}}_z q_z)A^{-1}(q_z)B^{-1}(q_z)(q_z-k'_{a,z}+i\delta)^{-1}(q_z-k_{a,z}-k_{b,z}+i\gamma_b)^{-1}, \tag{A12}$$

$$II_4=R_a\exp(i\beta\hat{\mathbf{e}}_z q_z)A^{-1}(q_z)B^{-1}(q_z)(q_z+k'_{a,z}+i\delta)^{-1}(q_z-k_{a,z}-k_{b,z}+k'_{b,z}-i\delta)^{-1}, \tag{A13}$$

$$II_5=R_aR_b\exp(i\beta\hat{\mathbf{e}}_z q_z)A^{-1}(q_z)B^{-1}(q_z)(q_z+k'_{a,z}+i\delta)^{-1}(q_z-k_{a,z}-k_{b,z}-k'_{b,z}-i\delta)^{-1}, \tag{A14}$$

$$II_6=-R_aT_b\exp(i\beta\hat{\mathbf{e}}_z q_z)A^{-1}(q_z)B^{-1}(q_z)(q_z+k'_{a,z}+i\delta)^{-1}(q_z-k_{a,z}-k_{bz}+i\gamma_b)^{-1}, \tag{A15}$$

$$II_7=-T_a\exp(i\beta\hat{\mathbf{e}}_z q_z)A^{-1}(q_z)B^{-1}(q_z)(q_z-i\gamma_a)^{-1}(q_z-k_{a,z}-k_{b,z}+k'_{b,z}-i\delta)^{-1}, \tag{A16}$$

$$II_8=-T_aR_b\exp(i\beta\hat{\mathbf{e}}_z q_z)A^{-1}(q_z)B^{-1}(q_z)(q_z-i\gamma_a)^{-1}(q_z-k_{a,z}-k_{b,z}-k'_{b,z}-i\delta)^{-1}, \tag{A17}$$

$$II_9=T_aT_b\exp(i\beta\hat{\mathbf{e}}_z q_z)A^{-1}(q_z)B^{-1}(q_z)(q_z-i\gamma_a)^{-1}(q_z-k_{a,z}-k_{b,z}+i\gamma_b)^{-1}. \tag{A18}$$

The functions $A(q_z)$ and $B(q_z)$ possess the forms

$$A(q_z)=(k_{a,z}-q_z)^2+(\mathbf{k}_{a,\parallel}-\mathbf{k}'_{a,\parallel})^2+\lambda^2, \tag{A19}$$

$$B(q_z)=q_z^2-q_z(k_{a,z}+k_{b,z})+\mathbf{k}_a\cdot\mathbf{k}_b+\mathbf{k}'^2_{a,\parallel}-\mathbf{k}'_{a,\parallel}\cdot(\mathbf{k}_{a,\parallel}+\mathbf{k}_{b,\parallel}) +i\eta/2. \tag{A20}$$

To evaluate the integrals $II_j, j=1,\ldots,9$ we convert q_z to a complex variable, and consider the improper contour integrals

$$I=\sum_{j=1}^{9}\lim_{\rho\to\infty}\oint_{\partial G_\rho}dq_z II_j(q_z). \tag{A21}$$

The compact domain G is chosen as the upper half of the complex plane, i.e., $G=\{q_z|\,\mathscr{I}(q_z)>0,|q_z|<\rho\}$. From the preceding analytical expressions of II_j it is readily deduced that only isolated singularities of II_j occur in G, i.e., $II_j(q_z)$ are meromorphic in G. Integral (A9) can thus be evaluated via calculus of residues.

The poles of $II_1(q_z)$ are deduced to

$$z_{11}^{\pm}=k_{a,z}\pm i\sqrt{(\mathbf{k}_{a,\parallel}-\mathbf{k}'^2_{a,\parallel})+\lambda^2}, \tag{A22}$$

$$z_{21}^{\pm}=-b/2\pm\sqrt{\rho_z}(\cos\varphi/2+i\sin\varphi/2), \tag{A23}$$

$$z_{41}=k_{a,z}+k_{b,z}-\mathbf{k}'_{b,z}+i\delta, \tag{A24}$$

where $b\coloneqq k_{a,z}+k_{b,z}$, $\rho_z\coloneqq\sqrt{(b^2-4d)^2+\eta^2/4}$, $d\coloneqq\mathbf{k}_a\cdot\mathbf{k}_b+k'^2_{a,\parallel}-\mathbf{k}'_{a,\parallel}\cdot(\mathbf{k}_{a,\parallel}+\mathbf{k}_{b,\parallel})$, and $\sin\varphi=-\eta/(2\rho_z)<0$. In G the function II_1 possesses the poles z_{11}^{+},z_{21}^{-}, and z_{41}. The poles of II_2 in G are $z_{12}^{+}\equiv z_{11}^{-}$, $z_{22}^{-}\equiv z_{21}^{-}$, and z_{42}, where $z_{42}=k_{a,z}+k_{b,z}+\mathbf{k}'_{b,z}+i\delta$. The singularities of II_3 in G are $z_{13}^{+}\equiv z_{11}^{-}$ and $z_{23}^{-}\equiv z_{21}^{-}$. The poles of II_4 in G are deduced to $z_{14}^{+}\equiv z_{11}^{-}$, $z_{24}^{-}\equiv z_{21}^{-}$, and $z_{44}\equiv z_{41}$. II_5 possesses in G poles

$z_{15}^{+}\equiv z_{11}^{-}$, $z_{25}^{-}\equiv z_{21}^{-}$, and $z_{45}\equiv z_{42}$. II_6, in G, has the poles $z_{16}^{+}\equiv z_{11}^{-}$, and $z_{26}^{-}\equiv z_{21}^{-}$. The singularities of II_7 in G are $z_{17}^{+}\equiv z_{11}^{-}$, $z_{27}^{-}\equiv z_{21}^{-}$, $z_{37}=i\gamma_a$, and z_{47}, where $z_{47}=z_{41}$. The singularities of II_8 that occurr in G are $z_{18}^{+}\equiv z_{11}^{-}$, $z_{28}^{-}\equiv z_{21}^{-}$, $z_{38}\equiv z_{37}$, and $z_{48}\equiv z_{42}$. Finally, the poles of II_9 in G are $z_{19}^{+}\equiv z_{11}^{-}$, $z_{29}^{-}\equiv z_{21}^{-}$, and $z_{39}\equiv z_{38}$.

The integral I can then be written in closed form

$$I=2\pi i\sum_{j=1}^{9}\sum_{\nu}\operatorname{Res}_{\nu j}II_j(q_z). \tag{A25}$$

Upon substitution of Eq. (A25) into Eq. (A8), and performing the derivatives and the limits, an analytical, however complicated, expression for the dipole-transition amplitude (A5) is obtained (within the approximation $G_{ee}^{+}\approx G_0^{+}$).

---

[1] *Angle-Resolved Photoemission: Theory and Current Application*, edited by S. D. Kevan, Studies in Surface Science and Catalysis (Elsevier, Amsterdam, 1992).

[2] S. Hüfner, *Photoelectron Spectroscopy*, in Springer Series in Solid-State Science Vol. 82 (Springer-Verlag, Berlin, 1995).

[3] J. Braun, Rep. Prog. Phys. **59**, 1267 (1996).

[4] P. Hohenberg and W. Kohn, Phys. Rev. B **136**, 864 (1964).

[5] R. M. Dreizler and E. K. U. Gross, *Density Functional Theory* (Springer-Verlag, Berlin, 1990).

[6] V. Schmidt, *Electron Spectrometry of Atoms using Synchrotron Radiation*, Cambridge Monographs on Atomic, Molecular and Chemical Physics (Cambridge University Press, Cambridge, 1997).

[7] O. Schwartzkopf, B. Krässig, J. Elmiger, and V. Schmidt, Phys. Rev. Lett. **70**, 3008 (1993).

[8] P. Lablanquie, J. Mazeau, L. Andric, P. Selles, and A. Huetz, Phys. Rev. Lett. **74**, 2192 (1995).

[9] A. Huetz, L. Andric, A. Jean, P. Lablanquie, P. Selles, and J. Mazeau, in *The Physics of Electronic and Atomic Collisions*, Proceedings of XIX ICPEAC, Whistler, edited by L. Dube' *et al.*, AIP Conf. Proc. No. 360 (AIP, New York, 1995).

[10] G. Dawber, L. Avaldi, A. G. McConkey, H. Rojas, M. A. McDonald, G. C. King, F. Heiser, R. Hentgens, O. Gessner, and A. Rüdel, J. Phys. B **28**, L271 (1995).

[11] J. Viefhaus, L. Avaldi, F. Heiser, R. Hentgens, O. Gessner, A. Rüdel, M. Wiedenhöft, K. Wieliczek, and U. Becker, J. Phys. B **29**, L729 (1996).

[12] R. Dörner, J. Feagin, C. L. Cocke, H. Bräuning, O. Jagutzki, M. Jung, E. P. Kanter, H. Khemliche, S. Kravis, V. Mergel, M. H. Prior, H. Schmidt-Böcking, L. Spielberger, J. Ullrich, M. Unverzagt, and T. Vogt, Phys. Rev. Lett. **77**, 1024 (1996).

[13] F. Maulbetsch and J. S. Briggs, J. Phys. B **28**, 551 (1995).

[14] M. Pont and R. Shakeshaft, Phys. Rev. A **51**, R2676 (1995).

[15] A. K. Kazansky and V. N. Ostrovsky, J. Phys. B **26**, 2231 (1993).

[16] A. W. Malcherek, F. Maulbetsch, and J. S. Briggs, J. Phys. B **29**, 4127 (1996).

[17] J. Berakdar and H. Klar, Phys. Rev. Lett. **69**, 1175 (1992); J. Phys. B **26**, 4219 (1993).

[18] J. Berakdar, H. Klar, A. Huetz, and P. Selles, J. Phys. B **26**, 1463 (1993).

[19] J. Viefhaus, L. Avaldi, G. Snell, M. Wiedenhöft, R. Hentgens, A. Rüdel, F. Schäfers, D. Menke, U. Heinzmann, A. Engelns, J. Berakdar, H. Klar, and U. Becker, Phys. Rev. Lett. **77**, 3975 (1996).

[20] V. Mergel, M. Achler, R. Dörner, KH. Khayyat, T. Kambara, Y. Awaya, V. Zoran, B. Nyström, L. Spielberger, J. H. McGuire, J. Feagin, J. Berakdar, Y. Azuma, and H. Schmidt-Böcking, Phys. Rev. Lett. **80**, 5301 (1998).

[21] R. Herrmann, S. N. Samarin, H. Schwabe, and J. Kirschner, Phys. Rev. Lett. (to be published).

[22] P. J. Feibelman, Surf. Sci. **46**, 558 (1974).

[23] H. J. Levinson, E. W. Plummer, and P. J. Feibelman, Phys. Rev. Lett. **43**, 942 (1979).

[24] J. B. Pendry, in *Photoemission and the Electronic Properties of Surfaces*, edited by B. Feuerbacher, B. Fitton, and R. Willis (Wiley, New York, 1978), p. 87.

[25] L. D. Landau and E. M. Lifschitz, *Lehrbuch der theoretischen Physik Vol. III: Quantenmechanik* (Akademie Verlag, Berlin, 1979).

[26] J. P. Taylor, *Scattering Theory* (Wiley, New York, 1972).

[27] W. Nolting, *Viel-Teilchen-Theorie*, 2nd ed. (Verlag Zimmermann-Neufang, Ulmen, 1992).

[28] G. D. Mahan, *Many-Particle Physics*, 2nd ed. (Plenum, New York, 1993).

[29] C. Kittel, *Introduction to Solid State Physics*, 3rd ed. (Wiley, New York, 1966).

[30] J. B. Pendry, *Low Energy Electron Diffraction* (Academic, London, 1974).

PERGAMON

Solid State Communications 113 (2000) 665–669

solid
state
communications

www.elsevier.com/locate/ssc

Theory of two-electron photoemission from surfaces

N. Fominykh[a,*], J. Henk[a], J. Berakdar[a], P. Bruno[a], H. Gollisch[b], R. Feder[b]

[a]Max-Planck-Institut für Mikrostrukturphysik, Weinberg, 2, D-06120 Halle (Saale), Germany
[b]Theoretische Festkörperphysik, Universität Duisburg, D-47048 Duisburg, Germany

Received 6 December 1999; accepted 13 December 1999 by P. Dederichs

Abstract

A general theoretical approach to double photoemission from solid surfaces is formulated in terms of two-electron Green functions and two-electron states. By incorporating the screened Coulomb interaction between the two outgoing electrons in a dynamically screened effective one-electron potential, approximate expressions for the two-photoelectron current are derived, which essentially consist of elements well-known from one-electron photoemission theory. © 2000 Elsevier Science Ltd. All rights reserved.

Keywords: A. Surfaces and interfaces; C. Surface electron diffraction (LEED, RHEED); D. Electron–electron interactions; D. Electronic band structure; E. Photoelectron spectroscopies

1. Introduction

Traditionally, the basic conceptual framework for dealing with many-electron systems is the independent electron model. The electronic structure is described mostly by means of a self-consistent field, based on the Hartree–Fock or the Kohn–Sham equations. Although the effective-field approach has long served for the interpretation of photoemission spectra [1,2], its central assumption of a single-particle wave function is, in general, of limited applicability, e.g. it fails in narrow-band systems with strong correlation between valence electrons [3]. The basic quantity relevant to the many-body effects is the correlation energy which, within density functional theory, is thought to reach its exact value at the exact ground-state density. However, the main question—to what extent the motion of the electrons is interrelated—is to be addressed by means of many-particle wave functions rather than by static properties such as the correlation energy. On the experimental side, double photoelectron emission (DPE) from solids and surfaces [4] is perfectly suited for the study of the correlated dynamics. Detecting simultaneously two electrons after the absorption of one photon, this process is one of the few known that in principle cannot be described within the single-particle picture. If the initial-state and the final-state wave functions are taken as products of orthogonal one-electron wave functions, the transition-matrix element for double photoionization vanishes [5]. Thus, the inter-electronic correlation plays a major role in determining the characteristics of doubly excited states. In other words, quantities used for the theoretical formulation of the problem (wave functions, propagators, etc.) have to be of at least two-particle nature. On the other hand, realizing that all features of scattering within a crystal intrinsically complicate the problem, it would be essential to seek for an extension of the well-established one-step single-electron photoemission (SPE) framework [6–8] to the case of DPE. In the present Paper we follow both of these pathways.

In Section 2 we present a general formulation of the DPE in terms of two-particle states and Green functions. Section 3 deals with schemes for calculating correlated two-particle states in a solid. In particular, the pair interaction is formulated in terms of dynamical screening. This approximation is used in Section 4 to derive expressions for the DPE photo: current, which are directly connected with established SPE theory.

2. General expression for the two-electron photocurrent

We consider a process in which an incident photon with

---

[*] Corresponding author.
E-mail address: fom@mpi-halle.de (N. Fominykh).

[1] We use atomic units, $\hbar = m = e = 1$.

PII: S0038-1098(99)00568-2

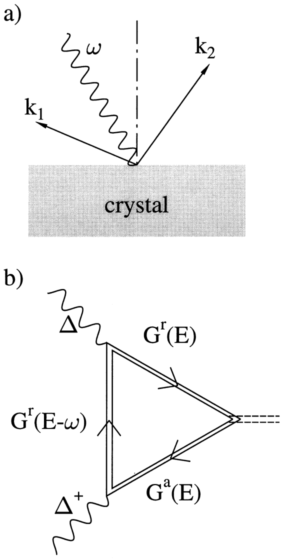

Fig. 1. Two-electron photoemission. (a) Sketch of the experimental geometry. A photon with energy ω impinges onto the surface. Two outgoing electrons with momenta $\vec{k}_1$ and $\vec{k}_2$ are detected in coincidence. (b) Diagrammatic representation of the photocurrent expression (Eqs. (1) and (2)). Wavy lines represent the photon, double straight lines with arrows correspond to retarded and advanced two-electron Green functions G^{r} and G^{a} at the final and initial state energies E and $E - \omega$. The double dashed line symbolizes the emitted (and detected) electron pair.

energy ω knocks two electrons out of a semi-infinite solid with periodicity parallel to the surface.[1] The subsequent detection of both outgoing electrons in coincidence allows the simultaneous determination of their kinetic energies E_1 and E_2 as well as the surface-parallel wave-vector components $\vec{k}_1^{\|}$ and $\vec{k}_2^{\|}$ (cf. Fig. 1a). The plane waves at the detectors are fully described by their momentum $\vec{k}_j$, $j = 1, 2$, since the normal component $k_j^{\perp}$ is related to E_j by $k_j^{\perp} = \sqrt{2E_j - (\vec{k}_j^{\|})^2}$. Assuming the sudden approximation for the DPE process, the photon field affects only those degrees of freedom of the two electrons, which can be distinguished by the detection process. We restrict ourselves to the pair interaction between these two 'active' electrons, thus neglecting three-body and higher order terms as well as explicit many-body effects with or between the 'passive' (ground state) electrons.

In analogy to the well-known Green-function formulation of SPE by Caroli et al. [9], we express the DPE current in the dipole approximation in terms of the two-particle Green function G,

$$J(\vec{k}_1\vec{k}_2) = -\frac{1}{\pi}\langle\Psi|\Delta \mathrm{Im}\, G^r(E-\omega)\Delta^{\dagger}|\Psi\rangle, \tag{1}$$

where $|\Psi\rangle$ can be viewed as a time-reversed LEED state for two correlated electrons, e.g. it has the (experimentally set) boundary conditions of plane waves $|\vec{k}_1\rangle$ and $|\vec{k}_2\rangle$ taken at the detector positions and is propagated by the advanced Green function G^{a} from inside the solid towards the detectors,

$$|\Psi\rangle = G^a|\vec{k}_1\vec{k}_2\rangle. \tag{2}$$

The kinetic energy of the outgoing electron pair is $E = E_1 + E_2$, its surface-parallel momentum $\vec{K}^{\|} = \vec{k}_1^{\|} + \vec{k}_2^{\|}$. In Eq. (1), Δ is the two-particle dipole operator, i.e. the sum of two single-particle dipole operators [5], and $-\mathrm{Im}\, G^{\mathrm{r}}(E-\omega)/\pi$ is the non-local density of two-particle states.

Eq. (1) can be represented by the diagram in Fig. 1b, which is the two-particle analogue of the lowest order diagram of the SPE theory. Interactions between the 'active' electron pair and the other electrons of the solid are thus taken into account to the extent that they are incorporated in the on-the-total-energy-shell Green function G.

If the imaginary self-energy part is set to zero, e.g. assuming an infinite two-particle life-time, $\mathrm{G}^{\mathrm{r}}(E)$ in Eq. (1) can be written in terms of two-particle states $|\Phi_i\rangle$ with energies E_i and further quantum numbers denoted by the compound index i,

$$-\frac{1}{\pi}\,\mathrm{Im}\, G^r(E) = \sum_i |\Phi_i\rangle\delta(E - E_i)\langle\Phi_i|, \tag{3}$$

where the summation over i is understood as integration in the case of continuous quantum numbers. Inserting Eq. (3) into the DPE expression (1) simplifies this to Fermi's 'golden rule',

$$J(\vec{k}_1\vec{k}_2) = \sum_i |\langle\Psi|\Delta|\Phi_i\rangle|^2\delta(E - \omega - E_i). \tag{4}$$

The summation over unresolved quantum numbers contained in i accounts for all initial two-particle states that are compatible with energy conservation and symmetry requirements imposed by the dipole transition to the particular final state. As was shown in Ref. [5], conservation of the surface-parallel component of the momentum in the SPE translates in DPE into the same but for the two-particle momentum $\vec{K}^{\|}$. This means that the two-particle momenta are conserved modulo reciprocal surface-lattice vectors. In Eq. (1), G^{r} can be restricted to these values of $\vec{K}_i^{\|}$. Note that due to the Coulomb interaction, single-particle momenta are in general not 'good quantum numbers' in the DPE process.

In order to evaluate the above DPE current formulae, ways have to be found to actually calculate the two-particle Green function or the two-particle states involved. We address this problem in Section 3.

3. Two-electron states

The Hamiltonian H for two electrons inside the semi-infinite solid consists of the kinetic energy K, the electron–electron interaction U, and the crystal potential $W, H = K + U + W$. Due to the simultaneous occurrence of two difficulties—the many-body and the scattering problem—we have to decide about the sequence of treating U and W. Paying tribute to the fact that DPE is due to the electron–electron interaction U, we assign the latter to the reference Hamiltonian $H_{\mathrm{int}} = K + U$. In this way the crystal potential is kept as a perturbation. In the absence of W, the operator $G_{\mathrm{int}}U$ promotes the uncorrelated two-particle state $|\Phi^0\rangle$, which is an eigenfunction of K, to the correlated one

$$|\Phi^1\rangle = (1 + G_{\mathrm{int}}U)|\Phi^0\rangle, \tag{5}$$

the latter being an eigenfunction of H_{int}. G_{int}, the resolvent of H_{int}, is the propagator of the internal motion of the electron pair. The reference state $|\Phi^1\rangle$ is perturbed by the crystal potential W and evolves into the state

$$|\Phi\rangle = (1 + G_{\mathrm{int}}T)|\Phi^1\rangle. \tag{6}$$

The transition operator T describes the dynamic response of the system upon the action of W and obeys the Lippmann–Schwinger equation $T = W + WG_{\mathrm{int}}T$.

Despite the fact that $|\Phi^1\rangle$ in Eq. (5) is a quasi-single-particle subject to the scattering in the crystal, the internal and external motions are not separable due to the presence of G_{int} in Eq. (6). If U is negligible, the problem reduces to scattering of independent particles. If this is not the case, use of Eq. (6) in order to evaluate physically relevant quantities requires further approximations, e.g. application of the perturbation expansion of G_{int} with respect to U. This would allow for a systematic treatment of correlation effects. In the above formulation, our scheme is general and applicable for both initial and final two-particle states of the DPE process.

As an alternative to the above, we consider an approach for the calculation of the final two-particle state $|\Psi\rangle$, which uses single-particle scattering states of the semi-infinite system as reference states for the electron–electron interaction. These states are well-known from LEED and SPE theories and can be calculated by multiple-scattering methods (cf. e.g. Ref. [6]). Taking the Coulomb interaction U as a perturbation, $|\Psi\rangle$ then assumes the form

$$|\Psi\rangle = (1 + GU)|\psi_1\psi_2\rangle. \tag{7}$$

$|\psi_1\rangle$ and $|\psi_2\rangle$ are single-particle time-reversed LEED states which are plane waves $|\vec{k}_1\rangle$ and $|\vec{k}_2\rangle$, respectively, at the detectors.

A rigorous evaluation of Eq. (7) is however complicated. A computationally viable approximation has recently been proposed in the context of pair emission by electron impact, (e,2e) [10,11]. Taking U as a Thomas–Fermi-like screened Coulomb interaction, this two-particle potential was approximated by a sum of two single-particle potentials. This amounts to a dynamical screening. Each electron moves in an effective single-particle potential $\tilde{w}_j$, $j = 1, 2$, which is the usual quasi-particle potential w of LEED theory augmented by a dynamical screening term depending on the other electron. Denoting by g_j and $\tilde{g}_j$ the single-particle Green functions for electron j in the potentials w and $\tilde{w}_j$,, respectively, our approximation takes the operator form

$$(1 + GU)(1 + g_1 w)(1 + g_2 w) \approx (1 + \tilde{g}_1\tilde{w}_1)(1 + \tilde{g}_2\tilde{w}_2). \tag{8}$$

The time-reversed LEED states $|\tilde{\psi}_j\rangle$ can then be written as

$$|\tilde{\psi}_j\rangle = (1 + \tilde{g}_j^a\tilde{w}_j)g_j^0|\vec{k}_j\rangle = \tilde{g}_j^a|\vec{k}_j\rangle, \tag{9}$$

in analogy to Eq. (2). They can readily be calculated by employing $\tilde{w}_j$ in standard multiple-scattering computer codes. The two-particle final state is then simply an antisymmetrized product of these single-particle states,

$$|\Psi\rangle = A(|\tilde{\psi}_1\rangle \otimes |\tilde{\psi}_2\rangle), \tag{10}$$

where operator A is antisymmetrizator.

4. Double photoemission from wide valence bands

In contrast to narrow-band systems, the ground state of metals with sp-valence bands consists in good approximation of independent quasi-electrons moving in an effective external potential. Hence, pair correlation can be neglected in our initial two-particle state. Since the screening of single electrons by the ground state electrons decreases with increasing energy, one can expect non-negligible pair correlation in the final state, which we approximate as described above.

In order to evaluate the general photocurrent expression Eq. (1) we first express the two-particle spectral density $-\mathrm{Im}\, G^{\mathrm{r}}/\pi$ in terms of retarded single-particle Green functions g^{r}. Straightforward calculation yields

$$\mathrm{Im}\, G^r(12, 1'2'; E) = -\tfrac{1}{\pi}\int \mathrm{d}\, E'(\mathrm{Im}\, g^{\mathrm{r}}(11'; E')$$
$$\times\, \mathrm{Im}\, g^{\mathrm{r}}(22'; E - E') - \mathrm{Im}\, g^{\mathrm{r}}(12'; E')\, \mathrm{Im}\, g^{\mathrm{r}}(21'; E - E')). \tag{11}$$

We thus have a convolution involving a direct product plus an exchange product, in which the co-ordinates $1'$ and $2'$ are interchanged. Note that by taking the trace of Eq. (1) the density of two-particle states N is obtained as a convolution of single-particle densities n,

$$N(E) = \int \mathrm{d}\, E' n(E') n(E - E'). \tag{12}$$

We now substitute Eq. (11) and the final two-particle state, Eq. (10), into Eq. (1). Using the decomposition of the two-particle dipole operator into two single-particle operators, we eventually obtain the DPE current as

$$J(\vec{k}_1\vec{k}_2) \sim \frac{1}{\pi^2}\int_{E_{\min}}^{E_{\mathrm{F}}} \mathrm{d}\, E'(I_{\mathrm{d}}(E') - I_e(E')) \tag{13}$$

where $E_{\min} = E - \omega - E_{\mathrm{F}}$ is the lowest occupied single-particle level allowed by energy conservation. $I_{\mathrm{d}}(E)$ is the

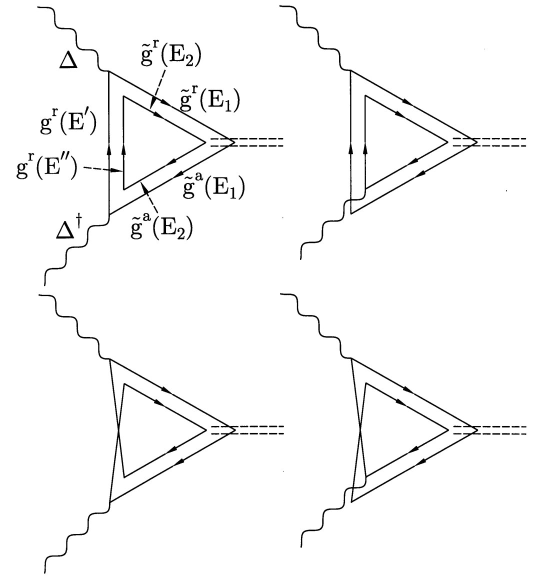

Fig. 2. Diagrammatic representation of the approximate two-electron photocurrent in terms of one-electron Green functions g and $\tilde{g}$. The upper (lower) two diagrams correspond to the first two direct (exchange) terms given in Eq. (14) (its analogue with $|\tilde\psi_1\rangle$ and $|\tilde\psi_2\rangle$ interchanged). The symbols are as in Fig. 1b except that single straight lines with arrows represent one-electron Green functions.

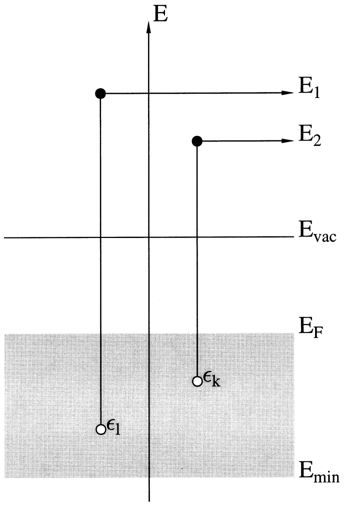

Fig. 3. Energy diagram of the approximate DPE process as depicted in Fig. 2. Initial states with energies ϵ_l and ϵ_k are excited to time-reversed LEED states with kinetic energies E_1 and E_2 (relative to the vacuum level E_{vac}), respectively. The energy region available for the initial states (grey area) is given by the Fermi energy E_F and E_{min} (see text).

direct intensity term defined as

$$\begin{aligned} I_d(E') = {} & \langle\tilde\psi_1|\Delta \mathrm{Im}\, g^r(E')\Delta^\dagger|\tilde\psi_1\rangle\langle\tilde\psi_2|\mathrm{Im}\, g^r(E'')|\tilde\psi_2\rangle \\ & + \langle\tilde\psi_1|\Delta \mathrm{Im}\, g^r(E')|\tilde\psi_1\rangle\langle\tilde\psi_2|\mathrm{Im}\, g^r(E'')\Delta^\dagger|\tilde\psi_2\rangle \\ & + \langle\tilde\psi_1|\mathrm{Im}\, g^r(E')\Delta^\dagger|\tilde\psi_1\rangle\langle\tilde\psi_2|\Delta \mathrm{Im}\, g^r(E'')|\tilde\psi_2\rangle \\ & + \langle\tilde\psi_1|\mathrm{Im}\, g^r(E')|\tilde\psi_1\rangle\langle\tilde\psi_2|\Delta \mathrm{Im}\, g^r(E'')\Delta^\dagger|\tilde\psi_2\rangle \quad (14) \end{aligned}$$

where $E'' = E - \omega - E'$. The exchange contribution I_e consists of four terms like those of I_d but in each term $|\tilde\psi_1\rangle\langle\tilde\psi_2|$ is exchanged by $|\tilde\psi_2\rangle\langle\tilde\psi_1|$.

Expressing the single-particle final states in terms of Green functions, cf. Eq. (9), the four individual parts of I_d and those of I_e can be represented by eight diagrams, four typical ones of which are shown in Fig. 2. The exchange terms in the lower row are seen to arise from the direct terms in the upper row by 'crossing' the two Green functions associated with the single-particle initial states.

In order to recover the 'golden rule' form of the DPE current, we assume infinite life-time of the particles and express the retarded Green functions g^r in terms of eigenstates of the single-particle Hamiltonian,

$$g^r(E') = \lim_{\eta\to 0^+} \sum_k \frac{|\phi_k\rangle\langle\phi_k|}{E' - \epsilon_k - i\eta}. \quad (15)$$

In other words, the two-particle initial states Φ_j with energies E_j are replaced by anti-symmetrized products of single-particle states ϕ_k and ϕ_l with energies $\epsilon_k + \epsilon_l = E_j$, cf. Eq. (11). Note that for a given E_j the energies ϵ_k and ϵ_l are not fixed but range from $E_{min} = E_j - E_F$ to the Fermi energy E_F. Eventually applying Dirac's identity, we arrive at

$$J(\vec{k}_1\vec{k}_2) = \sum_{kl}^{occ} |M_{kl}^{(1)} + M_{kl}^{(2)} - M_{lk}^{(1)} - M_{lk}^{(2)}|^2 \delta(E - \omega - \epsilon_k - \epsilon_l), \quad (16)$$

where the matrix elements $M_{kl}^{(1)}$ and $M_{kl}^{(2)}$ are defined as

$$M_{kl}^{(1)} = \langle\tilde\psi_1|\Delta|\phi_k\rangle\langle\tilde\psi_1|\phi_l\rangle \quad (17)$$

$$M_{kl}^{(2)} = \langle\tilde\psi_2|\Delta|\phi_k\rangle\langle\tilde\psi_1|\phi_l\rangle. \quad (18)$$

The single-particle energy levels involved in Eq. (16) are illustrated by Fig. 3, in which the grey region depicts the initial state energy integration range contained in the k and l summations.

Each matrix element M is a product of a single-particle transition-matrix element and an overlap integral between 'the other' single-particle initial and final states. These overlap integrals do not vanish in general because the effective single-particle Hamiltonian is different for initial and final states due to the electron–electron interaction. This allows the following interpretation: when one electron absorbs the photon, the effective potential changes such that the 'shake-up' of the other one becomes possible. We further note that in the present approximation the individual surface-parallel momenta are conserved, since when two electrons are uncoupled there is no longer a mechanism responsible for the momentum transfer within a pair.

From the above analytical expressions as well as from the diagrams it is evident that the two-particle photocurrent has been reduced to single-particle constituents. These can be evaluated using standard procedures of one-electron photoemission theory with some modifications.

5. Conclusion

In conclusion, we have developed a multiple-scattering formalism for the treatment of correlated electron-pair emission from surfaces upon the absorption of a single VUV photon. By transforming the electron–electron interaction from position into momentum space the two-photoelectron current has been approximated in terms of single-electron Green functions and transition-matrix elements. Numerical evaluation of the formulae, which we derived in this work, is currently in progress.

Acknowledgements

We are grateful to A. Ernst, D. Meinert, S. Samarin, T. Scheunemann, and G. Tatara for helpful discussions.

References

[1] M. Cardona, L. Ley (Eds.), Photoemission in solids I, (no.26) Topics in Applied PhysicsSpringer, Berlin, 1978.
[2] S.V. Kevan (Ed.), Angle-resolved Photoemission: Theory and Current Applications Elsevier, Amsterdam, 1992.
[3] F. Manghi, V. Bellini, C. Arcangeli, Phys. Rev. B 56 (1997) 7149.
[4] R. Herrmann, S. Samarin, H. Schwabe, J. Kirschner, Phys. Rev. Lett. 81 (1998) 2148.
[5] J. Berakdar, Phys. Rev. B 58 (1988) 9808.
[6] R. Feder (Ed.), Polarized Electrons in Surface Physics Advanced Series in Surface ScienceWorld Scientific, Singapore, 1985.
[7] J. Pendry, Surf. Sci. 57 (1976) 679.
[8] J. Braun, Rep. Prog. Phys. 59 (1996) 1267.
[9] C. Caroli, D. Lederer-Rozenblatt, B. Roulet, D. Sanit-James, Phys. Rev. B 8 (1973) 4552.
[10] R. Feder, H. Gollisch, D. Meinert, T. Scheunemann, O.M. Artamonov, S.N. Samarin, J. Kirschner, Phys. Rev. B 58 (1998) 16 418.
[11] J. Berakdar, H. Gollisch, R. Feder, Sol. State Commun. 112 (1999) 587.

VOLUME 89, NUMBER 8 PHYSICAL REVIEW LETTERS 19 AUGUST 2002

Spectroscopy of the Electron-Electron Interaction in Solids

N. Fominykh, J. Berakdar,[*] J. Henk, and P. Bruno
Max-Planck Institut für Mikrostrukturphysik, Weinberg 2, 06120 Halle, Germany

(Received 26 March 2002; published 2 August 2002)

The spectrum of a photoexcited electron pair carries detailed information on the electron-electron interaction in metals. This is deduced from the results of a theoretical model presented here for the treatment of the double-photoelectron emission from surfaces. Main features in the two-particle spectra are assigned to (a) the exchange-correlation interaction, (b) the electronic band structure, (c) the photoelectron diffraction, and (d) the specific experimental setup. Comparison with experiments is made and common features and differences to the atomic case are pointed out.

DOI: 10.1103/PhysRevLett.89.086402 PACS numbers: 71.20.–b, 32.80.Rm, 33.55.Ad, 79.20.Kz

In recent years, angular and spin-resolved ultraviolet (UV) single-photoelectron spectroscopy [1] has witnessed an impressive refinement in resolution, allowing for a yet more detailed study of material properties. Currently this technique is intensively applied to unravel features governed by many-body effects, such as superconductivity [2,3], correlated excitations in low-dimensional systems [4–6], and the influence of electronic correlation on the spectrum [7,8]. Single-particle techniques have, however, a principle limitation in exposing the details of electronic correlation: An external perturbation introduced to probe the sample may excite simultaneously many degrees of freedom of the specimen; e.g., interacting electrons share the energy of a UV photon and the compound as a whole is then excited. Resolving the excited state of *one* of the electrons, as in single-photoelectron emission (SPE), yields integral information on the influence of the coupling to the surrounding medium. Obviously, more details are revealed on how and whether the particles are interacting if the states of *two* photoexcited particles are measured. For example, the *double*-photoelectron emission (DPE) is forbidden in the absence of correlation [9]; in case the DPE reaction may take place, the measured two-particle spectra provide direct insight into the energy and the angular dependence of the pair-correlation functions (cf. below).

In atomic and molecular physics, this kind of correlation spectroscopy has recently been realized and is currently under intensive experimental and theoretical research (cf. [10–12] for earlier references). While electronic correlation has some striking manifestations in solids [13], it is only recently that fully resolved DPE measurements from surfaces have been conducted [14]. The main experimental obstacle in this case are the low-counting coincidence rates of two *correlated* electrons as compared to the large amount of (background) uncorrelated secondary electrons. With the development of a new generation of detectors [15], it is, however, conceivable that the DPE technique for solids will undergo major advances in the near future.

On the theoretical side, an adequate treatment of electronic correlation, in particular, of the interaction between the photoexcited electron pair, is a prerequisite for the description of DPE [9,16,17]. An important step in this direction is the recent development of a version of the density-functional theory (DFT) that describes the ground state in terms of correlated many-particle densities [18,19]. For the calculation of DPE spectra, one needs, however, in addition to the correlated ground state, an expression for the correlated two-particle state.

This Letter provides the first theory for DPE from solids with a realistic *ab initio* calculation of the (single-particle) electronic structure of the sample. Correlated two-particle states are generated upon the coupling of two single-particle states via a model potential of the screened Coulomb type. The goals of this work are (i) the calculation of both SPE and DPE spectra within the same approach to contrast conclusively the information obtained from both techniques and to assess the reliability of the single-particle part of the DPE theory, (ii) the analysis of how the electron-electron interaction manifests itself in the DPE spectra, (iii) the study of the DPE surface sensitivity (compared to SPE) and of the dependence of DPE on the photoelectron energies and emission angles, (iv) the comparison of theory with available experiments, and (v) the analysis of differences and similarities to DPE from single atoms.

Theory.—Within the one-step model of SPE, the current $J^{(1)}$ [20] of photoelectrons emitted with a surface-parallel wave vector $\boldsymbol{k}_\parallel$ and an energy ϵ, upon the absorption of a UV photon with energy ω, is given by

$$J^{(1)} \propto -\mathrm{Im}\langle\Psi^{(1)}|\Delta g^r(\epsilon-\omega)\Delta^\dagger|\Psi^{(1)}\rangle. \tag{1}$$

The final state $|\Psi^{(1)}\rangle = g^a|\boldsymbol{k}_\parallel, \epsilon\rangle$ is obtained by propagating (back) the detector state $|\boldsymbol{k}_\parallel, \epsilon\rangle$ using the advanced Green function g^a. The photohole state is described by the retarded Green function g^r, and Δ is the dipole operator of the incident radiation. In the one-step DPE process, one photon ejects *two* electrons with wave vectors $\boldsymbol{k}_{1\parallel}$ and $\boldsymbol{k}_{2\parallel}$ and energies E_1 and E_2 from the occupied states of a metal surface. The double-photoelectron current $J^{(2)}$ can be approximated by [16]

$$J^{(2)} \propto \int_{E_{\mathrm{min}}}^{E_{\mathrm{F}}} \langle\Psi^{(2)}|\Delta \mathrm{Im} g^r(\epsilon)\mathrm{Im} g^r(E-\omega-\epsilon)\Delta^\dagger|\Psi^{(2)}\rangle d\epsilon, \tag{2}$$

where E_F is the Fermi energy, $E = E_1 + E_2$, and $E_{\mathrm{min}} = E - \omega - E_F$. The correlated two-particle final state $|\Psi^{(2)}\rangle = G^a|\boldsymbol{k}_{1\|}, E_1; \boldsymbol{k}_{2\|}, E_2\rangle$ is obtained from the uncorrelated detector states $|\boldsymbol{k}_{1\|}, E_1; \boldsymbol{k}_{2\|}, E_2\rangle = |\boldsymbol{k}_{1\|}, E_1\rangle \otimes |\boldsymbol{k}_{2\|}, E_2\rangle$ via the two-particle Green function G^a. The occupied nonlocal density related to electron j is determined by $\mathrm{Im}\, g^r(\boldsymbol{k}_{j\|}, \epsilon_j)$, $j = 1, 2$.

To elucidate the features of DPE as compared to SPE, we employ a calculational scheme for the currents $J^{(1)}$ and $J^{(2)}$ in which the single-particle states are evaluated simultaneously. The ground-state single-particle electronic structure is obtained from an *ab initio* linear muffin-tin orbital method based on the local density approximation of DFT. For the photoemission calculations, we utilize the layer Korringa-Kohn-Rostoker (LKKR) method [21].

The explicit incorporation of the mutual interaction U between the two excited photoelectrons is indispensable for an adequate description of DPE [9]. Here, this is achieved as follows: For a nearly free electron metal, U is screened with a screening length λ dependent on the density of states $N(E_F)$ [$\lambda = 1/\sqrt{4\pi N(E_F)}$; for Cu, $\lambda \approx 2.66$ Bohr]. In the long-wavelength limit, U depends only on the coordinate difference $\boldsymbol{r}_1 - \boldsymbol{r}_2$, namely, $U(\boldsymbol{r}_1, \boldsymbol{r}_2) = e^{(-|\boldsymbol{r}_1 - \boldsymbol{r}_2|/\lambda)}/|\boldsymbol{r}_1 - \boldsymbol{r}_2|$. To determine the two-particle state $|\Psi^{(2)}\rangle$, we first employ the LKKR method and obtain the single-particle states $|\psi_j(\boldsymbol{k}_j)\rangle = g^r|\boldsymbol{k}_{j\|}, \epsilon_j\rangle$, $j = 1, 2$. Using the procedure developed in [22], $|\psi_1(\boldsymbol{k}_1)\rangle$ and $|\psi_2(\boldsymbol{k}_2)\rangle$ are then coupled to each other via U to determine the state $|\Psi^{(2)}\rangle$ [and subsequently the current $J^{(2)}$, Eq. (2)]. In this way, single-particle and two-particle photocurrents are calculated within the same scheme allowing a sensible comparison. From the functional form of U, it is clear that $J^{(2)}$ depends not only on the energies and emission directions of the photoelectrons, as in the SPE case, but also on the mutual angle between the photoelectrons: If the electrons are close to each other, U provides a strong coupling, whereas U (and, hence, the DPE signal [9]) is strongly suppressed when the photoelectrons are separated at distances larger than λ. This general statement is quantified below by numerical results.

Reliability of the SPE part.—Figure 1(a) shows a measured angular distribution of the SPE intensity from Cu(001) [23]. Our calculations for $J^{(1)}$ [Fig. 1(b)] agrees with the experiments which indicates an adequate treatment of the single-particle part of the problem.

Symmetry of the angular distribution.—The SPE angular distributions reflect the $4mm$ symmetry of the Cu(001) surface [Figs. 1(a) and 1(b)]. In contrast, the presence of a second photoelectron in DPE dictates a different symmetry of the angular distribution. In Figs. 1(c) and 1(d), the DPE current is depicted as a function of $\boldsymbol{k}_\|$ of one electron, while $\boldsymbol{k}_\|$ of the other electron is fixed. If this "fixed" electron is detected in off-normal emission, the symmetry is reduced [to m in Fig. 1(d)]. However, if the fixed electron is detected with $\boldsymbol{k}_\| = 0$, the distributions of DPE and SPE show the same symmetry [$4mm$ in Fig. 1(c)].

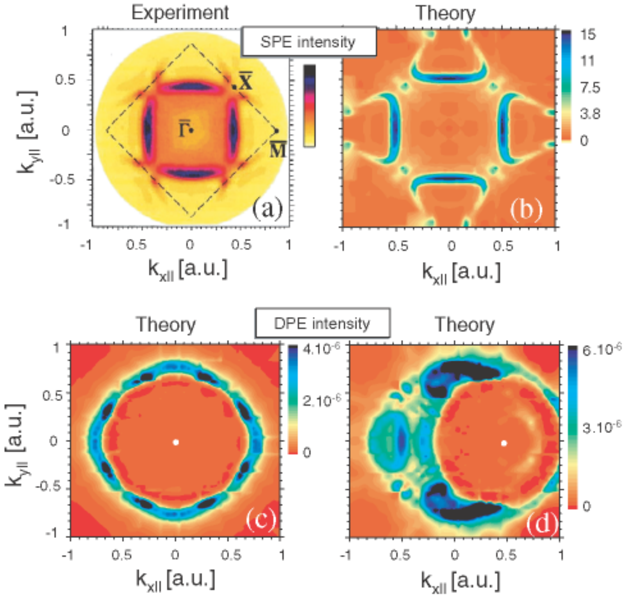

FIG. 1 (color online). Angular distribution of photoemission from the Fermi level of Cu(001). (a) Experimental single-photoelectron emission (SPE) intensity vs surface-parallel wave vector $\boldsymbol{k}_\| = (k_{x\|}, k_{y\|})$. The photon energy of the unpolarized light is $\omega = 21.2$ eV. (b) Theoretical results corresponding to case (a) with light incident normally to the surface. (c) and (d) Double-photoemission (DPE) intensities for photoelectrons having equal energies of 16 eV and $\omega = 42.4$ eV. One electron is detected at a fixed direction marked by the white dot [at 0° (c) and 30° (d) polar angle]. The DPE intensity is then scanned as a function of $\boldsymbol{k}_\|$ of the other photoelectron.

Exchange-correlation hole.—The most notable structure in the DPE angular distributions is the intensity minimum centered at $\boldsymbol{k}_\|$ of the fixed electron [Figs. 1(c) and 1(d)]. This "hole" is a direct manifestation of exchange and correlation between the two photoelectrons. The former is accounted for by the antisymmetry of the two-particle state, whereas the latter is mediated by the potential U. The high intensity surrounding the hole can be explained by the competition of two factors: (i) the electron-electron repulsion and the exchange interaction prevent the two electrons from escaping with comparable wave vectors within a proximity determined by the screening length. Therefore, the extent of the hole is a qualitative measure of the strength of the electron-electron interaction [for specified $(\boldsymbol{k}_{1\|}, E_1; \boldsymbol{k}_{2\|}, E_2)$]. (ii) If the two electrons are well separated from each other, the electron-electron interaction U becomes negligible and the DPE signal diminishes, for the DPE process is forbidden in the absence of U [9]. Combining these two effects, the distribution of the intensity around the direction of the fixed electron becomes comprehensible.

Both the shape and the extent of the correlation hole depend on the photoelectron energies: At low energies, it is large and dominates the distribution, whereas at higher ones, it is limited to a small region [cf. Figs. 1(d) and 2(d)]. This behavior can be understood from the properties of U as reflected in the transition-matrix elements [Eq. (2)].

In those regions where the two electrons are far away from each other (U is then weak), one observes a remote reminiscence of the DPE spectra to the corresponding SPE distributions; e.g., the influence of the single-electron diffraction is observable, slightly distorted due to the presence of the second (fixed) electron (Fig. 2).

Surface sensitivity.—Since *two* electrons have to escape the surface, DPE is expected to be more surface sensitive than SPE. In a crude model, the escape probability p for a single electron decays exponentially with the distance from the surface, $p \sim \exp(-z/\ell)$, where ℓ is the escape depth. The escape probability for two electrons is then $\exp(-2z/\ell)$; i.e., the escape depth is effectively halved. Hence, in SPE theory one has to sum up contributions from deep layers (typically from the first 15 surface layers) to obtain $J^{(1)}$, as is evident from Figs. 2(a) and 2(c). In DPE, both the shape and the magnitude of the photocurrent are determined by including contributions from the first two to four surface layers [Figs. 2(b) and 2(d)].

Photoelectron diffraction.—DPE experiments from crystal surfaces reported in Refs. [14] show pronounced features in the distributions of the electron-pair total energy ($E = E_1 + E_2$) between the two electrons [Fig. 3(a)]. To uncover the origin of structures occurring in the corresponding theoretical spectra [Fig. 3(b)], it is constructive to contrast with the results of the present theory for the double photoionization of the ground state [He($^1S^e$)] of the helium atom [Fig. 3(c)]. For the "single-site" DPE from atomic He, the cross section vanishes if $\boldsymbol{k}_1 + \boldsymbol{k}_2$ is perpendicular to the polarization vector of the incoming photon [12], which occurs in Fig. 3(c) at $E_1 = E_2$. This propensity rule holds for solids, too, but in the absence of photoelectron diffraction [9]. Indeed, we argue here that the photoelectron diffraction is the reason for the finite photocurrent $J^{(2)}$ at $E_1 = E_2$ found for Ni(001) in Figs. 3(a) and 3(b): For a periodic surface, the electronic states are eigenstates of the lattice translations; i.e., they can be expanded into plane waves. Hence, the effect of the lattice can be investigated by varying the number n of plane waves included in the expansion of the photoelectron states. The inset of Fig. 3(b) shows the DPE current for $E_1 = E_2$ and $\theta_1 = \theta_2$ vs n. Indeed, $J^{(2)}$ decreases rapidly with decreasing n and saturates at about $n \approx 20$. This behavior corroborates both the propensity rule and the explanation of the finite DPE photocurrent at $E_1 = E_2$.

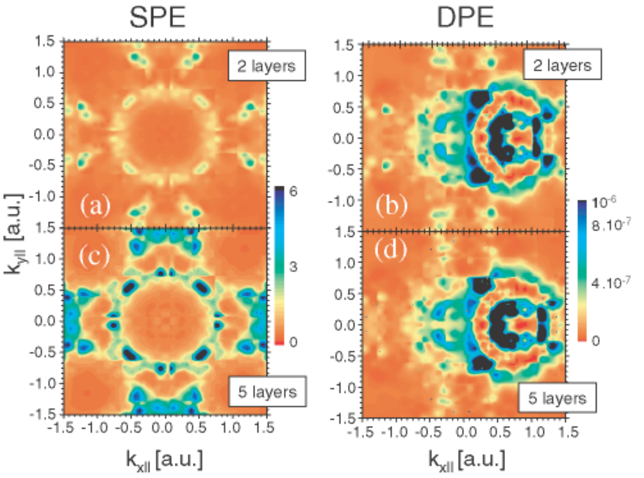

FIG. 2 (color online). Surface sensitivity of SPE [(a) and (c)] and DPE [(b) and (d)] from Cu(001). The setups are chosen as in Figs. 1(b) and 1(d), respectively, but the photoelectron energies are increased to 36 eV. The photon energy is 41 eV for SPE and 82 eV for DPE. In (a) and (b) [(c) and (d)] the contributions to the photocurrent from the two (five) outermost surface layers are depicted.

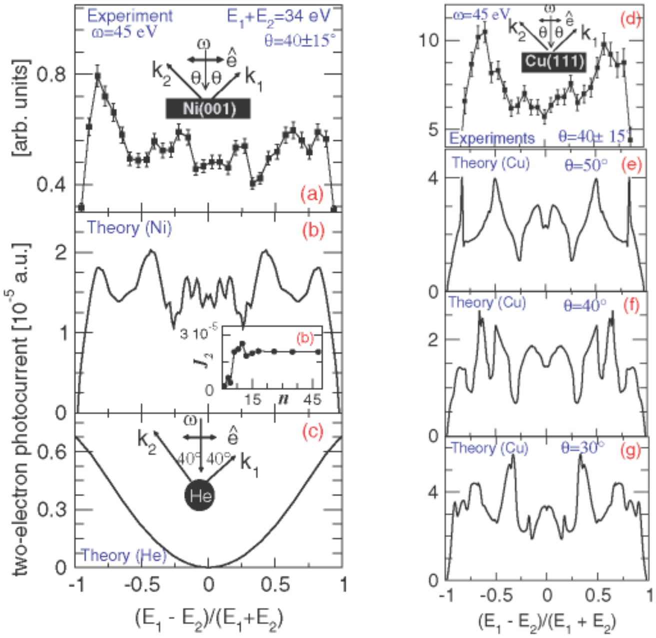

FIG. 3 (color online). (a) Experimental DPE intensity from Ni(001) [14]. The wave vectors $\boldsymbol{k}_1$ and $\boldsymbol{k}_2$ of the emitted electrons and the linear polarization vector of the light $\hat{\boldsymbol{e}}$ are coplanar (cf. inset). The total energy of the electron-pair is fixed as $E = E_1 + E_2 = 34 \pm 1$ eV with $\omega = 45$ eV. The DPE current is scanned as a function of the energy sharing $(E_1 - E_2)/E$. The electron detectors are fixed at symmetric positions (40° polar angle) and have an angular resolution of ±15°. (b) Theoretical results corresponding to case (a), with account for the experimental angular resolution. Inset: DPE current $J^{(2)}$ (at $E_1 = E_2$) vs number n of plane waves included in the expansion of the photoelectron wave. (c) As in (b), but for a single He atom in state $^1S^e$; ω is adjusted to compensate for the double ionization threshold of He. For the ground state the two-electron wave function of Ref. [24] is employed. (d) As in (a), but for Cu(111). (e)–(g) Theoretical results corresponding to (d) but with varying escape angles $\theta_1 = \theta = \theta_2$ [$\theta = 50°$ (e), $\theta = 40°$ (f), $\theta = 30°$ (g)].

Density-of-states effect.—Assuming parabolic dispersion of the photoelectron states in the vacuum (which means $dE_j = k_j\,dk_j$; $j = 1, 2$), one obtains for the fully resolved DPE current in spherical coordinates $J^{(2)}(\theta_1, \varphi_1, E_1; \theta_2, \varphi_2, E_2) = CJ^{(2)}(\boldsymbol{k}_1, \boldsymbol{k}_2)$, where $C = k_1 k_2$, and φ_1 as well as φ_2 are azimuthal angles [9,12]. In the atomic case, the density of states (DOS) for one photoelectron in the field of the residual ion behaves as $1/k_j$ for $k_j \longrightarrow 0$ (and $k_i \gg k_j$) [25]; i.e., for one electron the DOS diverges at the ionization threshold. This DOS effect combined with the kinematical factor $C = k_1 k_2$ leads, in general, to a finite DPE current from atoms when the energy of one of the electrons diminishes. In contrast, for surfaces, the DOS is finite at the vacuum level ($\boldsymbol{k}_j \approx 0$) and, hence, the DPE current $[k_1\, k_2\, J^{(2)}(\boldsymbol{k}_1, \boldsymbol{k}_2)]$ vanishes if E_1 or E_2 is very small. This profound difference between atoms and solids is confirmed by our calculations: In contrast to DPE from surfaces (Fig. 3), for He$(^1S^e)$ the DPE current is finite for $E_1 \longrightarrow 0$ or $E_2 \longrightarrow 0$ [Fig. 3(c)].

Band-structure effect.—In Fig. 3, both the photon energy ω and the electron-pair energy $E = E_1 + E_2$ are fixed. This specifies the initial binding energy of the electron pair as $\epsilon = \omega - E$. For atoms, ϵ pins down the initial state to a specific, discrete level. For surfaces, the electronic structure is dependent not only on the energy ϵ_i, but also on the Bloch wave vectors $\boldsymbol{q}_{i\parallel}$. When varying $(E_1 - E_2)/E$ (for fixed E, ω, and hence fixed ϵ), one scans through different $\boldsymbol{k}_{i\parallel}$ [Figs. 3(e)–3(g)]. Therefore, the relevant $\boldsymbol{q}_{i\parallel}$ and the associated electronic levels appear as sharp peaks in $J^{(2)}$ at certain $(E_1 - E_2)/E$ [16]. A similar effect arises due to the energy integration in Eq. (2) which involves several single-particle levels. In consequence, the structure of the initial-state spectral density is reflected as pronounced maxima and minima in the DPE spectra. In contrast, the smooth spectral density of the jellium model results in smooth DPE spectra [9].

Concerning the comparison with experiments, it should be remarked that the shape of the DPE spectrum changes substantially within the experimental angular resolution [Figs. 3(e)–3(g)]. This is due to the fact that, with increasing polar angles, the allowed range for the initial $\boldsymbol{k}_{i\parallel}$ is stretched and different initial states contribute to the photocurrent. For $\theta \longrightarrow 0$, the DPE current vanishes at $E_1 = E_2$ due to the electron-electron repulsion, whereas for $\theta \longrightarrow \pi/2$, it decreases due to the weakening of the electron-electron interaction [cf. also Figs. 1(c) and 1(d)].

In conclusion, we present pilot results to highlight the general aspects and the power of DPE from surfaces as a novel tool for electronic-correlation imaging.

We thank J. Kirschner, S. Samarin, A. Morozov, R. Dörner, M. Hattas, G. Stefani, R. Gotter, A. Ernst, R. Feder, and H. Gollisch for enlightening discussions.

---

*Electronic address: jber@mpi-halle.de

[1] S. Hüfner, *Photoelectron Spectroscopy* (Springer, New York, 1995).

[2] A. Lanzara *et al.*, Nature (London) **412**, 510 (2001).

[3] T. Yokoya *et al.*, Science **294**, 2518 (2001).

[4] Y. D. Chuang *et al.*, Science **292**, 1509 (2001).

[5] P. Segovia *et al.*, Nature (London) **402**, 504 (1999).

[6] S. Maekawa *et al.*, Rep. Prog. Phys. **64**, 383 (2001).

[7] A. Marini *et al.*, Phys. Rev. Lett. **88**, 016403 (2002).

[8] L. Hedin, J. Phys. Condens. Matter **11**, R489 (1999).

[9] J. Berakdar, Phys. Rev. B **58**, 9808 (1998).

[10] P. Selles *et al.*, Phys. Rev. A **65**, 032711 (2002); A. S. Kheifets and I. Bray, *ibid.* **65**, 012710 (2002); S. Senz and N. Chandra, *ibid.* **652**, 052702 (2000); A. Knapp *et al.*, Phys. Rev. Lett. **89**, 033004 (2002); J. Colgan *et al.*, J. Phys. B **34**, L457 (2001); M. Walter *et al.*, *ibid.* **33**, 2907 (2000).

[11] J. B. West *et al.*, J. Phys. B **34**, 4169 (2001); C. Dawson *et al.*, *ibid.* **34**, L525 (2001); P. Bolognesi, *ibid.* **34**, 3193 (2001); M. Achler *et al.*, *ibid.* **34**, 965 (2001); T. Masuoka, J. Chem. Phys. **115**, 264 (2001); S. A. Collins *et al.*, Phys. Rev. A **64**, 062706 (2001); S. Rioual *et al.*, Phys. Rev. Lett. **86**, 1470 (2001); A. Huetz *et al.*, *ibid.* **85**, 530 (2000).

[12] J. S. Briggs and V. Schmidt, J. Phys. B **33**, R1 (2000); G. C. King and L. Avaldi, *ibid.* **33**, R215 (2000); J. Berakdar and H. Klar, Phys. Rep. **340**, 473 (2001).

[13] P. Fulde, *Electron Correlation in Molecules and Solids* (Springer, Berlin, 1991).

[14] R. Herrmann *et al.*, Phys. Rev. Lett. **81**, 2148 (1998); J. Phys. IV (France) **9**, 127 (1999); H. W. Biester *et al.*, Phys. Rev. Lett. **59**, 1277 (1987).

[15] J. Kirschner and M. Hattas (private communication).

[16] N. Fominykh *et al.*, Solid State Commun. **113**, 665 (2000).

[17] N. Fominykh *et al.*, in *Correlations, Polarization and Ionization in Atomic Systems*, AIP Conf. Proc. No. 604 (AIP, New York, 2002), p. 210.

[18] A. Gonis *et al.*, Phys. Rev. B **56**, 9335 (1997); Phys. Rev. Lett. **77**, 2981 (1996).

[19] P. Ziesche, Int. J. Quantum Chem. **60**, 1361 (1996); Phys. Lett. A **195**, 213 (1994).

[20] C. Caroli *et al.*, Phys. Rev. B **8**, 4552 (1973).

[21] A. Gonis, *Theoretical Materials Science* (Materials Research Society, Pittsburgh, 2000).

[22] J. Berakdar *et al.*, Solid State Commun. **112**, 587 (1999).

[23] Th. Straub *et al.*, Phys. Rev. B **55**, 13 473 (1997).

[24] R. Bonham and D. Kohl, J. Chem. Phys. **45**, 2471 (1966).

[25] J. Berakdar *et al.*, J. Phys. B **26**, 3891 (1993).

Surface Science 507–510 (2002) 229–233

SURFACE SCIENCE

www.elsevier.com/locate/susc

Double photoemission from the surface state of Cu(1 1 1)

N. Fominykh *, J. Henk, J. Berakdar, P. Bruno

Max-Planck-Institut für Mikrostrukturphysik, Weinberg 2, D-06120 Halle (Saale), Germany

Abstract

We calculate the double photoemission spectra from the occupied surface state of Cu(1 1 1). We present and discuss the regularities in the angular and energy distributions of the process. For the emission from the d-band of Cu(1 1 1), the depth of generation of correlated photoelectron pairs is estimated. © 2002 Elsevier Science B.V. All rights reserved.

Keywords: Surface electronic phenomena (work function, surface potential, surface states, etc.); Photoelectron spectroscopy; Green's function methods; Many body and quasi-particle theories

1. Introduction

Surface states (SS) of metals are recognized as an interesting candidate for the investigation of electronic correlations. Considerable attention is paid to the electron–electron interaction in the occupied and unoccupied SS [1,2], where the scattering happens between the SS electron and the ground state electrons of the system. In the present paper we discuss the application of the new type of correlation-accented techniques: the double photoemission (DPE). In this process the absorption of a single photon leads to the simultaneous excitation and emission of two photoelectrons. The distinct feature of DPE is that the spectra of the photoelectron pairs are strongly dependent on the interaction between these two excited particles [4]. In fact, the DPE process is merely inhibited in the independent-electron approximation.

DPE has been recently investigated experimentally [3]: photoelectrons were detected with energy and momentum resolution, the simultaneity of their creation was controlled by the time-of-flight technique. In previous works [7,8] we investigated the DPE from the conduction band of Cu and showed, in particular, that the density of the initial states has a profound influence in these kind of experiments. In the present work we envisage the application of the DPE technique for the investigation of the occupied surface state of Cu(1 1 1). Using the approximation for the two-particle photocurrent [5,8] we calculate the two-photoelectron emission spectra and compare them with the results of a simple model. In addition, to reveal the surface sensitivity of the DPE process, we calculate the layer-dependent DPE patterns from the d-band of the same face of copper in order to estimate the depth of generation of the photoelectron pairs.

2. Approximations and numerical realization

In single photoemission the single-particle Green function (1GF) is needed for the

---

* Corresponding author. Fax: +49-345-5511223.
E-mail address: fom@mpi-halle.de (N. Fominykh).

PII: S0039-6028(02)01217-7

description of the ground and excited states of the surface. The ground states are provided adequately by the density functional theory within the local-density approximation whereas the treatment of excited states is a more involved task [9]. In DPE the two-particle Green function (2GF) [10] is required which is a much more complicated object than its one-particle counterpart. Our approach towards the derivation of a correlated two-particle Green function that can be implemented numerically can be summarized as follows (for the details cf. [5–8]): To a zero order approximation the 2GF is an antisymmetrized product of two 1GF, each of them describes the motion of the individual photoelectrons as moving independently in the crystal potential but obeying the Pauli exclusion principle. In the ladder approximation one goes beyond this zero order approximation by allowing the interaction between the photoelectrons. In this study we assume the coupling to be mediated by a Coulomb screened potential with the screening length λ being derived from a Thomas–Fermi type approach, i.e. it depends on the density of states at the Fermi level [11]. Evaluating the terms in the ladder approximation within a realistic model of electronic band structure of the surface is difficult numerically. Therefore we designed a method in which the screened interaction potential is incorporated in an non-perturbative way into the 1GF [5–8]). As a result, the 2GF becomes an antisymmetrized product of two ‘effective’ 1GFs. Each of the 1GFs depends dynamically on the properties of the two photoelectrons.

This procedure allows to express the two-electron photocurrent through certain types of single-particle matrix elements [5–8] that resemble formally the ones encountered in single photoemission. Finally, we utilize the ab initio computer code for electron spectroscopies [12] and extend it to end up with the DPE mode.

3. Single-particle properties

In general, the Coulomb interaction is accompanied by the energy and momentum transfer within the photoelectron pair. Contrary to single photoemission process, individual surface-parallel momenta of the electrons $\mathbf{k}_{1,2}^{\parallel}$ are not conserved in the DPE event. However, one of the consequences of the approximations of our model is that the final state surface-parallel momenta of emitted electrons remain good quantum numbers. Namely, only those initial states are participating in the optical transition, which are characterized by the same irreducible representation of the translation group, as the asymptotic final states. In particular, this means that $\mathbf{k}^{\parallel}$-resolved density of states is a meaningful quantity for the rough analysis of the calculated DPE spectra.

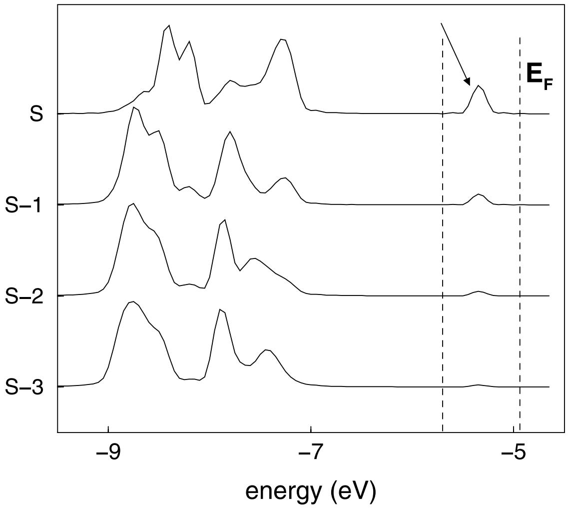

Fig. 1. Layer-resolved density of states (LDOS) of Cu(1 1 1) at $\mathbf{k}^{\parallel} = 0$. Dashed lines depict the integration range over the initial states for the DPE calculations (see text), arrow marks the position of the surface state.

So, first, we ensure that SS on Cu(1 1 1) is reproduced correctly in our single-electron calculations. This is a Shockley-type state originating from the sp-band of copper and situated at ~0.4 eV below the Fermi level [13]. Fig. 1 demonstrates the calculated Bloch spectral functions for the uppermost and few next layers of Cu(1 1 1), the SS is marked by the arrow. It decays at a depth of ~3–4 monolayers. The dispersion of the SS (Fig. 2), to a good approximation, shows a quadratic behaviour as a function of $\mathbf{k}^{\parallel}$.

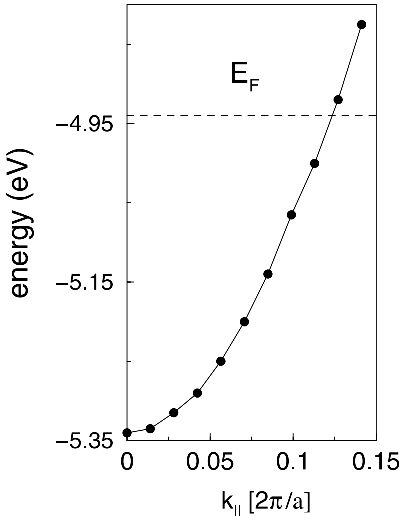

Fig. 2. Theoretical dispersion curve $E(\mathbf{k}^{\|})$ for the surface state of Cu(1 1 1).

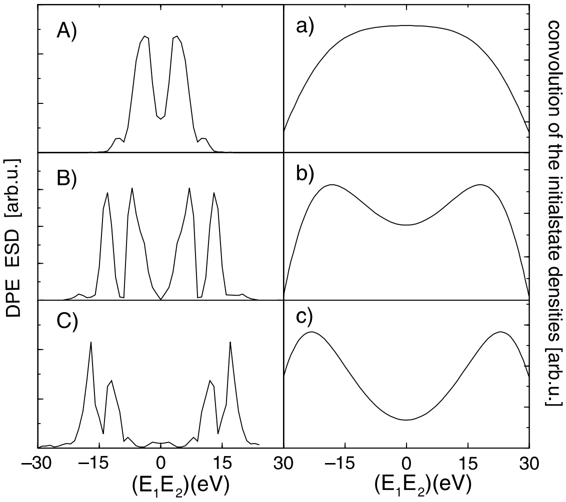

Fig. 3. (A)–(C), left column: DPE ESD from the surface state of Cu(1 1 1) for the energies $\hbar\omega = 41$ eV, $E_1 + E_2 = 30$ eV and angles $\phi_1 = \phi_2 = 0$, $\theta_1 = -\theta_2 = 30°$, 40°, 50°, respectively; (a)–(c), right column: corresponding convolution of the $\mathbf{k}^{\|}$-dependent densities of initial states of two electrons.

4. DPE energy and angular spectra

Six independent variables (energies E_1, E_2, and four angles of emission), characterizing asymptotic two-electron final state, can be combined in different ways to visualize the DPE process. Two particular situations will be considered here. At given energy and (linear) polarization of the photon DPE probability will be given: (i) as a function of the energy difference $(E_1 - E_2)$ at fixed total energy $(E_1 + E_2)$ and fixed angles (θ_1, ϕ_1), (θ_2, ϕ_2), or (ii) as a function of (θ_2, ϕ_2) for fixed (θ_1, ϕ_1) and E_1, E_2.

First mode is referred to as energy sharing distribution (ESD). It shows, how favourable for photoemission is one or another partition of the total energy between two electrons. Fig. 3 shows the examples of the ESD's from the Cu(1 1 1) SS for the energies $\hbar\omega = 41$ eV, $E_1 + E_2 = 30$ eV, and light polarization in the plane of the surface along y-axis. In this case the initial state energies E_1^{ini}, E_2^{ini} are picked out of the narrow range of approximately 1 eV width around the location of the SS, according to the energy conservation

$$E_1 + E_2 = E_1^{\text{ini}} + E_2^{\text{ini}} + \hbar\omega. \qquad (1)$$

This energy range is boundaried by the Fermi energy from above, and by $E_{\min} = E_1 + E_2 - E_{\text{F}} - \hbar\omega$ from below (shown by two dashed lines on Fig. 1). The DPE cross section is then obtained by the integration over this range. Directions of emission are set by the angles $\phi_1 = \phi_2 = 0$, $\theta_1 = -\theta_2 = 30°$, 40°, 50°. The final state energy sharing is formed, particularly, as a result of momentum transfer between electrons due to Coulomb interaction. ESD also reflects single-electron characteristics, namely, the momentum-resolved density of initial states. Finally, being the optically excited flux, it reflects the features of the dipole transition and contains a kinematical factor $K \equiv \sqrt{E_1 \cdot E_2}$. The latter leads to the zero value of the ESD at the edges, where E_1 or E_2 is equal to zero. So, each point of the ESD is related to certain E_1, E_2, corresponding $\mathbf{k}_1^{\|}$, $\mathbf{k}_2^{\|}$ and $\mathbf{k}^{\|}$-resolved densities of initial states, and factor K. We compare our results with the auxiliary function $B(\mathbf{k}_1^{\|}, \mathbf{k}_2^{\|})$ that simulate only the effect of the initial state single-particle densities. It is defined as a convolution of the corresponding $\mathbf{k}^{\|}$-resolved densities of initial states (let's denote them $A(E_i^{\text{ini}}; \mathbf{k}_i^{\|}), i = 1, 2$):

$$B(\mathbf{k}_1^{\|},\mathbf{k}_2^{\|}) = \int_{E_{\min}}^{E_F} A(E;\mathbf{k}_1^{\|}) \cdot A(E_1+E_2-E-\hbar\omega;\mathbf{k}_2^{\|})\,\mathrm{d}E. \tag{2}$$

For simplicity, $A(E;\mathbf{k}_i^{\|})$ are simulated by Gaussians, whose position move towards lower energies as a function of $\mathbf{k}_i^{\|}$ according to the dispersion curve, Fig. 2. Comparing the results, one can conclude (within the approximations made above), that the initial state densities shape the general profile of the ESD, while the fine structure should be attributed to another abovementioned aspects. For example, the minimum in the middle of ESDs, where the total energy is shared equally between the electrons, is due to the fact that the total asymptotic wave vector is then directed perpendicular to the vector of light polarization—in this situation the propensity rule [4] applies, which suppresses the dipole transition.

While ESDs are not straightforward in interpretation, DPE angular distributions (ADs) have more transparent appearance. Energies of emitted electrons are fixed there, the direction of emission of the first electron is fixed too. One should trace the DPE current as a function of emission direction of the second electron in the upper hemisphere above the surface. On the Fig. 4 we present the SPE and DPE ADs in the form of stereographic projections, where the direction perpendicular to the surface (z-axis) is a center of each circle. The energies are $\hbar\omega = 45$ eV, $E_1 = E_2 = 15$ eV, light is polarized along the normal to the surface. At these energies the range of integration over the initial states includes the region of the d-band, where the density of states is ~2.5 times higher, than that of the SS (we do not illustrate this detailedly, but only mention that the DPE intensity from the SS is approximately factor 6 lower than that from the d-band). Black-to-white scale shows the normalized intensity from zero to one, respectively. Three pictures in the left column correspond to SPE, in the right column—to DPE ADs from 2, 3 and 10 monolayers of Cu(1 1 1). In DPE ADs the first electron is emitted normally to the surface plane. Two competing features determine the angular behaviour of the process: (i) Coulomb repulsion prevents the closely lying emission directions of two electrons, (ii) far-away directions are 'suppressed' by the fact that the interaction between electrons becomes small, and so does the DPE probability, which relies entirely on the strength of this interaction. So, in Fig. 4 one can observe the dark spot around the direction of emission of first electron, which is explained by the Coulomb repulsion. Then comes the 'ring' of high intensity, where actually the most of the DPE photocurrent occurs. Towards the boundaries the intensity falls down again. This general pattern is mixed with the diffraction effects due to scattering of the electrons from the lattice. In the given geometry (the photon polarization vector and the emission direction of the 'fixed' electron are normal

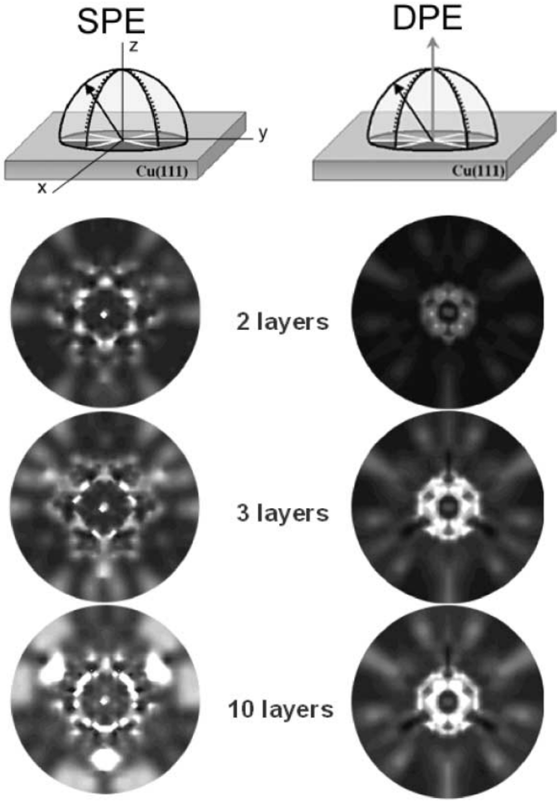

Fig. 4. Stereographically projected SPE and DPE angular patterns from the d-band of Cu(1 1 1). SPE (left column): $\hbar\omega = 22.5$ eV, $E_{\mathrm{kin}} = 15$ eV; DPE (right column): $\hbar\omega = 45$ eV, $E_1 = E_2 = 15$ eV, the 'fixed' electron is emitted normally to the surface, photon polarization vector along z-axis.

to the surface), the symmetry of the presented DPE ADs coincide with the symmetry of the copper face. However, this would be generally not true, if the emission direction of the 'fixed' electron would not coincide with the high-symmetry direction of the lattice point group (c.f. [8]). The mean angle with respect to the first electron, at which the second electron is preferentially emitted, depends on the value of the screening length λ and, hence, on the material. The larger is the screening length, the wider is the space where the electrons can interact and decline their trajectories, so the wider will be the 'ring' of high intensity. The depth of generation of correlated pairs as compared to the depth of generation of a photoelectron in SPE process is illustrated in Fig. 4. The rapidly decaying density of states of the SS does not effect much the depth of generation, since at these energies the contribution from the d-band is overwhelming. The photocurrent of both processes is calculated for different number of monolayers ($n = 2$, 3 and 10). Intensities in SPE and DPE columns (normalized in the same way within each column) differ roughly by five orders of magnitude, which is in agreement with experimental observation [14], and is in line with the knowledge on double photoionization of atomic and molecular targets [15]. Within a simple model, the probability for two electrons to escape from the surface can be estimated as a square of the single-electron escape probability. The latter, being connected to the mean free path d by exponential law $\exp(-z/d)$, gives the effective two-electron mean free path equal to $d/2$. From Fig. 4 one can indeed see that the most of the DPE signal is formed up to the third monolayer, while in the case of SPE there is still no saturation at this depth.

5. Conclusions

We have presented the results of DPE calculations from the surface state and the d-band of Cu(1 1 1). The role of initial state densities, Coulomb interaction, screening length, dipole transitions in the formation of angular and energy DPE spectra is illustrated and discussed. We perform calculations from the narrow energy band around the surface state and from the broader range, including the d-band. The nearly analytical behaviour of the SS dispersion allows to approximately single out the effect of the density of initial states on DPE energy sharing distributions. Emission from the d-band is used to illustrate the high surface sensitivity of DPE process: the depth of generation of correlated pairs is estimated to not exceed 3 monolayers.

References

[1] H. Petek, S. Ogawa, Prog. Surf. Sci. 56 (4) (1997) 239–310.
[2] J. Osma, I. Sarria, E.V. Chulkov, J.M. Pitarke, P.M. Echenique, Phys. Rev. B 59 (16) (1999) 10591–10598.
[3] R. Herrmann, S. Samarin, H. Schwabe, J. Kirschner, Phys. Rev. Lett. 81 (1998) 2148.
[4] J. Berakdar, Phys. Rev. B 58 (1998) 9808.
[5] N. Fominykh, J. Henk, J. Berakdar, P. Bruno, H. Gollisch, R. Feder, Solid State Commun. 113 (12) (2000) 665–669.
[6] J. Berakdar, H. Gollisch, R. Feder, Solid State Commun. 112 (1999) 587.
[7] N. Fominykh, J. Henk, J. Berakdar, P. Bruno, Double photoemission studies at metal surfaces, in: D.H. Madison, M. Schulz (Eds.), Correlations, Polarization and Ionization in Atomic Systems, AIP Conf. Proc., vol. 604, p. 210.
[8] N. Fominykh, J. Henk, J. Berakdar, P. Bruno, Many-particle Spectroscopy of Atoms Molecules Clusters and Surfaces, Kluwer Publishers, 2001, pp. 461-470.
[9] A. Gonis, Theoretical Materials Science: Tracing the Electronic Origins of Materials Behavior, Materials Research Society, Warrendale, Pa, 2000.
[10] A.L. Fetter, J.D. Walecka, Quantum Theory of Many-particle systems, McGraw-Hill, New York, 1971.
[11] N.W. Ashcroft, N.D. Mermin, Solid State Phys., Saunders College Publishing, 1976.
[12] J. Henk, T. Scheunemann, S.V. Halilov, E. Tamura, R. Feder, Omni—fully relativistic electron spectroscopy calculations, 1999.
[13] R. Courths, M. Lau, T. Scheunemann, H. Gollisch, R. Feder, Phys. Rev. B 63 (2001) 195110.
[14] S.N. Samarin, private communication.
[15] V. Schmidt, Electron Spectrometry of Atoms Using Synchrotron Radiation, Cambridge University Press, 1997.

8 Eidesstattliche Erklärung

Hiermit erkläre ich, dass ich die Habilitationsschrift sebstständig und ohne fremde Hilfe verfaßt und andere als die angegebenen Quellen und Hilfsmittel nicht benutzt und die den benutzten Werken wörtlich oder inhaltlich entnommenen Stellen als solche kenntlich gemacht habe.

Halle, den 30. Septemeber 2002

Dr. J. Berakdar

9 Lebenslauf

Addresse

Dr. Jamal Berakdar
Max-Planck-Institut für Mikrostrukturphysik,
Am Weinberg 2,
06120 Halle/Saale,
Tel:+49 345 5582 666
Fax:+49 345 5511223
e-mail: jber@mpi-halle.mpg.de

Persönliche Daten

Geburtsdatum	20.01.1964
Geburtsort	Damaskus
Familienstand	verheiratet, 1 Kind
Staatsangehörigkeit	deutsch

Ausbildung

November 1986	Vordiplom in Physik, Albert-Ludwigs-Universität, Freiburg im Breisgau
August 1990	Diplom in theoretischer Physik, Albert-Ludwigs-Universität, Freiburg i. Br.
Juni 1994	Dr. rer. nat. in Physik (summa cum laude), Albert-Ludwigs-Universität, Freiburg i. Br.

Berufserfahrung

Oktober 1990 - Juni 1994	Forschungs- und Lehrtätigkeit an der Fakultät für Physik, Albert-Ludwigs-Universität, Freiburg i. Br.
Juni 1994 - Dezember 1994	Assist an der Fakultät für Physik, Albert-Ludwigs-Universität, Freiburg i. Br.
1. Januar - Juni 1995	Research Associate at the Department of Applied Mathematics, Royal Holloway College, University of London, London, England
Juni 1995-April 1997	Research fellow, Atomic & Molecular Physics Laboratories, Institute of Advanced Studies, Research School of Physical Sciences and Engineering, Canberra, Austalien
April 2002 - Mai 2002	Forschungsaufenthalt am Institute for Theoretical Atomic and Molecular Physics at the Harvard-Smithsonian Center for Astrophysics, Cambridge, Massachusetts, USA.
April 1997-jetzt	Wissenschaftliches Mitglied des Max-Planck-Institutes für Mikrostrukturphysik, Halle.

Lehrtätigkeiten

Albert-Ludwigs-, Universität Freiburg i. Br., MLU-Halle	Mitarbeit im physikalischen Praktikum, Leitung und Durchführung von Übungen zu den Vorlesungen: Quantenmechanik, Elektrodynamik, klassische Mechanik und Statistik. Betreuung von Diplom- und Doktorarbeiten.